Spatiotemporal Control of Tendon Healing through Modular, Injectable Hydrogel Composites

by

Robert N. Kent III

A dissertation submitted in partial fulfillment
of the requirements for the degree of
Doctor of Philosophy
(Biomedical Engineering)
in the University of Michigan
2024

Doctoral Committee:

Associate Professor Brendon M. Baker, Chair
Associate Professor Alice H. Huang
Assistant Professor Megan L. Killian
Associate Professor Ariella Shikanov

Robert N. Kent III

rnkent@umich.edu

ORCID iD: 0000-0003-1287-6301

© Robert N. Kent III 2024

Dedication

To my parents and my sisters, who showered me with love, support,
and a healthy dose of humility throughout my life.

And to my dog, who is just such a good girl.

Acknowledgements

I would like to first thank my PhD advisor, Dr. Brendon Baker, for the heroic effort he put into molding me into a scientist. He took a big gamble when he agreed to let me join the lab, with my distant experience in cell culture, accelerated graduation timeline, and general foolish ways. Despite all of this, his teaching, inspiration, and encouragement pushed me to show up to lab every day to put cells in gels. Brendon's work ethic, patience, ambition, and creativity were core to my scientific development, and I sincerely hope to be able to emulate these traits in my future career. Brendon is also responsible for connecting me with an outstanding committee. I owe thanks to Drs. Alice Huang, Megan Killian, and Ariella Shikanov for being a persistent source of encouragement, ideas, and career advice throughout the PhD. I am grateful for their knowledge and expertise, which were critical to the development of my project. I would also like to thank Dr. Adam Abraham for his teaching, our numerous discussions about my latest data and potential next steps, and his generosity with reagents and human primary cells. Lastly, I am grateful to the many collaborators who helped to make this work possible.

I would also like to thank the Medical Scientist Training Program (MSTP) administration. First, I am deeply grateful to Justine Hein for being a vital source of support, advice, sanity, and food as I navigated this challenging program. I also owe thanks to Justine, Drs. Kathleen Collins and Ronald Koenig, Gretchen Aland, Liz Bowman, Claire Leigh-Monstevens, and Hilkka Ketola for building and maintaining the program I have grown to love over the past seven years.

I am thankful to Dan, Willy, Chris, Sam, and Harrison for putting up with me as a new graduate student and overseeing much of my early technical training in lab. I also feel lucky to have shared (almost) my entire time in the lab with Sam, Harrison, and Maggie. To Dan, Willy, Chris, Sam, Harrison, Maggie, Jingyi, Firoal, Michael, and Elizabeth: I could not have asked for a better set of lab mates. I would also like to thank the talented undergraduate students Mohamed Said, Megan Busch, Ariane Tsai, and Trevor Buck for giving me the opportunity to work with them and for generating a great deal of the data included in this thesis. Lastly, I am grateful to James Haggerty-Skeans and Michael Saunders, who have been my closest companions as we navigated the trials and tribulations of our training program.

Table of Contents

Dedication .... **ii**

Acknowledgements .... **iii**

List of Figures .... **xii**

Abstract .... **xxx**

Chapter 1: Introduction **1**

Chapter 2: Background **4**

2.1 Authors **4**

2.2 Abstract **4**

2.3 Introduction **5**

2.4 Fiber-reinforced hydrogel composite mechanics **6**

2.5 Engineered cues for effective tenogenesis and cell-mediated repair **12**

2.5.1 Tendon progenitor cell recruitment 14

2.5.2 Driving tenogenic differentiation 18

2.5.3 Templating aligned matrix deposition 21

2.5.4 Immunomodulation 22

2.6 Conclusion and future outlook **24**

Chapter 3: Physical and Soluble Cues Enhance Tendon Progenitor Cell Invasion into Injectable Synthetic Hydrogels **26**

3.1 Authors **26**

3.2 Abstract **26**

3.3 Introduction **27**

3.4 Results and discussion **30**

3.4.1 PDGF-BB drives TPC invasion into DexVS hydrogels 30

3.4.2 Fibrous topography enhances PDGF-BB-driven TPC invasion 33

3.4.3 Hybrid DexVS/HepMA microgels enable tunable release of TPC chemokines 36

3.4.4 Computational modeling predicts microgel-mediated delivery of chemokines by hybrid microgels 38

3.4.5 Microgel-delivered PDGF-BB induces TPC invasion into composite hydrogels 41

3.4.6 Microgel-delivered PDGF-BB drives TPC recruitment from the Achilles tendon 45

3.5 Conclusion **50**

3.6 Materials and methods **51**

3.6.1 Reagents 51

3.6.2 Cell isolation and culture 51

3.6.3 Polymer synthesis 52

3.6.4 Fiber segment fabrication and functionalization 53

3.6.5 Fabrication of composite hydrogels 54

3.6.6 TPC spheroid formation and encapsulation 54

3.6.7 Hybrid microgel synthesis and chemokine loading 55

3.6.8 Chemokine release characterization 56

3.6.9 Computational modeling of microgel-mediated chemokine delivery 57

3.6.10 *Ex vivo* Achilles tendon outgrowth model 58

3.6.11 Microscopy and image analysis 59

3.6.12 Statistics 60

3.7 Supplemental figures 60

Chapter 4: Engineered Microenvironmental Cues from Fiber-reinforced Hydrogel Composites Drive Tenogenesis and Aligned Collagen Deposition 65

4.1 Authors 65

4.2 Abstract.. 65

4.3 Introduction.. 67

4.4 Results and discussion 69

4.4.1 TGF-β2 and -β3 induce ScxGFP expression in TPCs 69

4.4.2 Organization of fibrous topography influences tenogenic differentiation of TPCs in 2D 72

4.4.3 TGF-β isoforms differentially regulate tenogenic vs. myofibroblastic differentiation 74

4.4.4 TGF-β3-induced tenogenesis is a mechanosensitive process dependent on actomyosin contractility 75

4.4.5 3D fiber density and alignment influence spreading and alignment of TPCs but not early tenogenesis... 78

4.4.6 Inhibition of cell contractility potentiates tenogenesis in 3D microenvironments 82

4.4.7 Topographical alignment templates de novo matrix production 83

4.4.8 Tenogenesis of human tendon-derived cells in FRHCs is donor-dependent 87

4.5 Conclusion 91

4.6 Materials and methods 92

4.6.1 Reagents 92

4.6.2 Cell isolation and culture 92

4.6.3 Polymer synthesis 93

4.6.4 2D cell culture 94

4.6.5 Fiber segment fabrication and functionalization for FHRCs 95

4.6.6 Fabrication of FRHCs 96

4.6.7 Real-time quantitative PCR 98

4.6.8 Orthohydroxyproline assay 99

4.6.9 Histology 99

4.6.10 Microscopy and image analysis 100

4.6.11 Statistics 101

4.7 Supplemental figures 102

Chapter 5: Fibrous Topographical Cues Govern a Tenogenic vs. Fibrochondrogenic Fate Switch 107

5.1 Authors 107

5.2 Abstract 107

5.3 Introduction 108

5.4 Results and discussion 109

5.4.1 TGF-β3-mediated scleraxis production is attenuated by aligned 3D cell-adhesive fibers in FRHCs 109
5.4.2 TPCs in afibrous, non-cell-adhesive hydrogels exhibit a fibrochondrogenic phenotype 111
5.4.3 hMSC chondrogenic medium and non-fibrous conditions synergistically drive fibrochondrogenic differentiation 114
5.4.4 Rac1 inhibition favors fibrochondrogenic differentiation 116
5.4.5 Fibrous topography drives ScxGFP$^+$ TPC recruitment *in vivo* but minimally impacts fibrochondrogenic differentiation 119
5.5 Conclusion 121
5.6 Materials and methods 122
5.6.1 Reagents 122
5.6.2 Cell isolation and culture 122
5.6.3 Polymer synthesis 123
5.6.4 Fiber segment fabrication and functionalization 123
5.6.5 Fabrication of FRHCs 124
5.6.6 Application of dynamic strain to FRHCs 126
5.6.7 Real-time quantitative PCR 127
5.6.8 Mouse Achilles tenotomy and FRHC implantation 128
5.6.9 Histology 130
5.6.10 Microscopy and image analysis 130
5.6.11 Statistics 131
5.7 Supplemental figures 131

Chapter 6: Conclusions and Future Directions **135**

6.1 Summary of findings **135**

6.2 Future directions **136**

6.2.1 Delayed delivery of soluble tenogenic cues 136

6.2.2 Immunomodulation 138

6.2.3 Translational considerations 139

Appendix **142**

MATLAB Scripts **142**

A1 Threshold check 142

A2 Color merge 147

A3 Nucleus counter 3D 150

A4 Donut quant 154

A5 Donut mask 156

A6 Focal adhesion quant 158

A7 Cell spheroid outgrowth quant 160

A8 Achilles ex vivo outgrowth quant 166

A9 Microgel fluorescence quant 171

A10 Perinuclear expression quant 173

A11 3D cell expression and morphology quant 180

A12 Picrosirius red quant 191

A13 Birefringence quant 194

A14 Birefringence delta and full width half max calculator 196

Bibliography 197

List of Figures

Figure 2.1: FRHC fabrication technologies. A) Fabrication schematic, scanning electron micrograph, and photograph of a 3D fibrous scaffold made from a polyurethane blend; photograph of polyurethane scaffold impregnated with an epoxy-amine hydrogel to form an FRHC. **B**) Extrusion of an aligned, ultra-high molecular weight polyethylene (UHMWPE) fiber-reinforced hydrogel composite; fibers are extruded either in a PVA/gelatin hydrogel with (FRH-PGS) or without (FRH-PG) strontium hardystonite. **C**) Alignment of cell-laden PEG dimethacrylate (PEGDM) fibers in a Teflon mold enables patterned encapsulation in a PEGDM hydrogel. **D**) SES onto a rotating mandrel generates an aligned scaffold of polycaprolactone (PCL) and gelatin methacrylate (mGLT), then mGLT fibers are dissolved in a photo-initiator solution, and UV exposure yields an FRHC; multi-layer constructs exhibit tensile moduli on the order of 10^1 Mpa. A) Adapted with permission (Agrawal et al., 2013). Copyright 2013, Elsevier. B) Adapted with permission (No et al., 2020b). Copyright 2020, American Chemical Society. C) Adapted with permission (Patel et al., 2018). Copyright 2018, Elsevier. D) Adapted with permission (G. Yang et al., 2016). Copyright 2016, Elsevier. 9

Figure 2.2: Comparison of fabrication methods and features of pure fibrous scaffolds, hydrogels, and fiber-reinforced hydrogel composites. 12

Figure 2.3: Typical vs. ideal tendon wound healing response. Following injury, a persistent pro-inflammatory response occurs, whereby M1-like macrophages invade the wound site and secrete pro-inflammatory cytokines like tumor necrosis factor (TNF)-α and interleukin (IL)-1. Myofibroblastic differentiation of invading stromal progenitors results in scar tissue formation in lieu of functional tissue regeneration. Ideally, early polarization to an M2-like phenotype and tenogenic differentiation of stromal progenitors would lead to more complete tendon regeneration.......... 14

Figure 2.4: Tunable physical microenvironmental features of an FRHC address key phases of tendon healing. Tunable crosslink density and degradability, in addition to fiber-guided cell migration, can be used to control recruitment of TPCs. Fiber composition and anisotropy can influence macrophage polarization. Finally, aligned fibrous topography templates deposition and maturation of aligned, *de novo* collagen fibrils. 16

Figure 3.1: A composite hydrogel-based scaffold providing control over soluble and physical microenvironmental cues was designed to direct the 3D migration of tendon progenitor cells (TPCs). Microgel-mediated chemokine delivery, along with contact guidance afforded by RGD-functionalized fiber segments, promoted tendon progenitor cell invasion from *ex vivo* tendons into an injectable composite hydrogel. This material strategy offers a promising route toward augmenting tendon repair and, likely, that of a range of other connective tissues. 27

Figure 3.2: PDGF-BB enhances TPC invasion into synthetic hydrogels. A) Experimental schematic; TPC spheroids were encapsulated in a 0.5 kPa DexVS/VPMS hydrogel,(D. L. Matera et al., 2020) and outgrowth proceeded for three days before fixation, with chemokine supplementation on day 1. **B**) Confocal fluorescent images of spheroid outgrowth, varying chemokine identity and concentration. Quantification of (**C**) spheroid outgrowth area (μm^2), (**D**) number of migrating cells, and (**E**) total migration distance (μm) (n = 10 spheroids, N = 2). **F**) Confocal fluorescent images of spheroids stained for Ki67, with dotted white lines delineating cytoplasmic boundaries. White arrowheads indicate Ki67^{+} nuclei in the merged panels. **G**) Quantification of the fraction of Ki67^{+} nuclei (n = 10). All data are presented as mean ± standard deviation. Asterisks indicate statistically significant comparisons, with ***p<0.001 and ****p<0.0001 by ordinary one-way ANOVA with Tukey's multiple comparisons test or Student's t-test. 32

Figure 3.3: Fibrous topography enhances TPC invasion. A) Experimental schematic; DexVS fibers were electrospun, functionalized with cell-adhesive RGD, and co-encapsulated with TPC spheroids in a DexVS/VPMS hydrogel; following encapsulation, all samples were supplemented with PDGF-BB on day 1, and outgrowth proceeded until fixation on day 3. **B**) Confocal fluorescent images of TPC spheroid outgrowth, varying fiber density and bulk stiffness. Quantification of (**C**) TPC spheroid outgrowth area (μm^2), (**D**) number of migrating cells, and (**E**) total migration distance (μm) (n = 10, N = 2). All data are presented as mean ± standard deviation. Asterisks indicate statistically significant comparisons, with **p<0.01, ***p<0.001, and ****p<0.0001 by ordinary two-way ANOVA with Tukey's multiple comparisons test. 35

Figure 3.4: Heparin content dictates soluble factor release kinetics from hybrid microgels. A) AutoCAD rendering of a microfluidic device design for generating and photo-crosslinking monodisperse DexVS/HepMA microgels. **B**) Images of varying droplet diameter as a function of channel geometry and quantification of droplet diameters (Small n = 13,827, Medium n = 476, Large n = 1,748) (solid horizontal line denotes median; dashed lines denote Q1 and Q3). **C**) PDGF-BB released from hybrid microgels over time, varying HepMA wt/v%, (**D**) DexVS wt/v%, and (**E**) microgel diameter (all n = 2) (data presented as mean ± standard deviation). Asterisks indicate statistically significant comparisons, with ***p<0.001 and ****p<0.0001 by ordinary one-way ANOVA with Tukey's multiple comparisons test. 38

Figure 3.5: Computational model predicts release kinetics from hydrogel-encapsulated microgels. A) Rendering of spatial distribution of chemokine (150-μm microgels incorporated at 2.5 v/v%) on day 3, with bulk (D_B) and microgel ($D_{\mu G}$) diffusion coefficients set to 10^{-12} and 10^{-15} $m^2 s^{-1}$. **B**) Gradient of chemokine concentration (nM mm^{-1}) over the first 20 microns adjacent to the TPC spheroid boundary across a range of D_B and $D_{\mu G}$ over a 3-day period. **C**) Renderings of model geometries with the microgel distribution in (A) and (B) (Arrangement 1) and two additional random arrangements, with cell spheroids shown in red and hybrid microgels shown in blue. **D**) Gradient quantification of arrangements in (C). **E**) Rendering of model geometry with 50-μm microgels incorporated at 2.5 v/v%. **F**) Gradient magnitude of the model in (**E**) compared to Arrangement 1 from (C). All data are presented as mean ± standard deviation. n = 6 radial directions for all gradient measurements. 40

Figure 3.6: Microgel-delivered PDGF-BB drives 3D TPC invasion. A) Experimental schematic; brightfield image of spheroids (red arrowhead) and microgels (yellow arrowheads); timeline of cell encapsulation, chemokine addition for the soluble PDGF-BB condition, and fixation. **B**) Confocal fluorescent images of TPC outgrowth in response to basal media (Vehicle), soluble PDGF-BB (sPB), and PDGF-BB released from microgels containing 1 (1% H) or 5 (5% H) wt/v% HepMA. Quantification of (**C**) TPC outgrowth area (μm^2), (**D**) number of migrating cells, and (**E**) total migration distance (μm) (n = 10, N = 2). (**F**) TPC outgrowth in response to PDGF-BB released from fluorescein-labeled microgels (5 wt/v% HepMA); orange dotted line in the 10x merge (650-μm z-range) denotes region displayed in the 40x images (100-μm z-range). All data are presented as mean ± standard deviation. Asterisks indicate statistically significant comparisons, with $^*p<0.05$, $^{**}p<0.01$, $^{***}p<0.001$, and $^{****}p<0.0001$ by ordinary one-way ANOVA with Tukey's multiple comparisons test. 43

Figure 3.7: Microgel-delivered PDGF-BB recruits Scx^+ TPCs from explanted murine Achilles tendon. **A**) Confocal fluorescent image of an axial cross-section of a mouse AT demonstrating Sca-1^+ progenitors residing in the epitenon. **B**) Experimental schematic; brightfield image of the transected tendon midsubstance encapsulated in a DexVS hydrogel. **C**) Brightfield image of an encapsulated tendon in a fibrous (inset) DexVS hydrogel containing hybrid microgels (green arrows). **D**) COMSOL model rendering of spatial distribution of PDGF-BB released from 50-μm microgels in the tendon explant model on day 10. **E**) Gradient of PDGF-BB concentration (nM mm^{-1}) over the first 20 microns adjacent to the tendon explant boundary for microgel-delivered vs. bulk-encapsulated (12 ng mL^{-1}) PDGF-BB (n = 5 radial directions). **F**) Confocal fluorescent images (axial view) of cell nuclei within and migrating from the tendon, orthogonally projected over a 500-micron stack of images, where white dotted lines mark the tissue boundary; 3D plots of nuclear centroids (red dots) outside the tissue boundary (black contours) showing the first 250 μm of tissue adjacent to the transection site for simplicity. Quantification of (**G**) number of migrating cells and (**H**) total migration distance (μm) within 500 μm of the transection site (n = 12, N = 3 [n = 4 in bPB group]). **I,** Representative confocal fluorescent image of migrating ScxGFP reporter cells, stained for Sca-1 (n = 5, N = 2). **J,** Quantification of Sca-1 and ScxGFP positivity among migrating cells. All data are presented as mean ± standard deviation. Asterisks indicate statistically significant comparisons, with $*p<0.05$ and $**p<0.01$ by ordinary one-way ANOVA with Tukey's multiple comparisons test. 50

Supplemental Figure 3.1: Blocking cell proliferation abrogates the migratory response to PDGF-BB. **A**) Confocal fluorescent images of TPC spheroid outgrowth into fibrous (2.5 v/v%) DexVS hydrogels (15 mM VPMS) after three days of culture, varying mitomycin C pre-treatment and PDGF-BB supplementation. Quantification of (**B**) TPC spheroid outgrowth area, (**C**) number of migrating cells, and (**D**) total migration distance. Asterisks indicate statistically significant comparisons, with ****p<0.0001 by ordinary two-way ANOVA with Tukey's multiple comparisons test. 60

Supplemental Figure 3.2: Bulk stiffness screen. A) Confocal fluorescent images of TPC spheroid outgrowth into nonfibrous DexVS hydrogels after three days of culture, varying VPMS crosslinker concentration. Quantification of (**B**) TPC spheroid outgrowth area, (**C**) number of migrating cells, and (**D**) total migration distance. Asterisks indicate statistically significant comparisons, with *p<0.05, **p<0.01, and ****p<0.0001 by ordinary one-way ANOVA with Tukey's multiple comparisons test. 61

Supplemental Figure 3.3: Effect of bulk functionalization with cell-adhesive ligand in fibrous hydrogels. A) Confocal fluorescent images of TPC spheroid outgrowth into fibrous (2.5 v/v%) DexVS hydrogels (15 mM VPMS) after three days of culture, with hydrogel bulk functionalization consisting of either cell-adhesive RGD or scrambled RDG peptides. Quantification of (**B**) TPC spheroid outgrowth area, (**C**) number of migrating cells, and (**D**) total migration distance. Statistical comparisons were made via Student's t-tests (α = 0.05). 62

Supplemental Figure 3.4: Soluble factor release profiles as a function of PDGF-BB loading dose and loading time. A) Fraction of loaded PDGF-BB released from DexVS microgels (5 wt/v% HepMA) with varying loading dose. **B**) Fraction of loaded PDGF-BB released from DexVS microgels (10 wt/v% HepMA) loaded at 250 ng mL^{-1}, with varying loading time. Statistical comparisons were made via ordinary one-way ANOVA with Tukey's multiple comparisons test (α = 0.05). 62

Supplemental Figure 3.5: Isolated effects of HepMA content and microgel size on TPC invasion. A) Confocal fluorescent images of 3 days of TPC spheroid outgrowth into fibrous (2.5 v/v%) DexVS hydrogels (15 mM VPMS), with non-loaded microgels containing either 0 or 5 wt/v% HepMA. Quantification of (**B**) TPC spheroid outgrowth area, (**C**) number of migrating cells, and (**D**) total migration distance. **E**) TPC spheroid outgrowth with PDGF-BB delivered from 50- or 150-μm diameter microgels (encapsulated at a density of 2.5 v/v%; PDGF-BB loaded at 500 ng mL^{-1}). Quantification of (**F**) TPC spheroid outgrowth area, (**G**) number of migrating cells, and (**H**) total migration distance. Asterisks indicate statistically significant comparisons, with $^*p<0.05$ by Student's t-test. 63

Supplemental Figure 3.6: Demonstration of injectability of composite hydrogel. Plain and composite (containing DexVS fibers and DexVS/HepMA microgels) DexVS hydrogel solutions are injected into a mold with irregular geometry through a 25-gauge needle. Confocal fluorescent images of the resulting hydrogels, orthogonally projecting over a 30-micron stack of images. .. 64

Supplemental Figure 3.7: Three-dimensional renderings of TPC outgrowth from a murine Achilles tendon. 3D renderings from confocal fluorescent images of cell nuclei migrating into composite DexVS hydrogels. Dotted white lines denote tissue boundaries. These renderings were generated from the same four images shown in Figure 3.7. 64

Figure 4.1: Fiber-reinforced hydrogel composites were employed to elucidate salient microenvironmental determinants of tenogenesis and aligned collagen deposition by tendon progenitor cells. Culture in these soft, 3D microenvironments potentiated transforming growth factor β3-mediated tenogenic differentiation of tendon progenitor cells, and fibrous topographical anisotropy templated alignment of *de novo* collagen fibrils. These findings inform the design of cell-free, injectable hydrogels for tendon tissue regeneration........ 66

Figure 4.2: TGF-β2 and -β3 induce *ScxGFP* expression in murine TPCs. **A**) Protocol schematic for isolating TPCs from *ScxGFP* mouse tail tendons; tendons were harvested and encapsulated in a type I collagen hydrogel, expanded in 3D for 10 days, then plated on polystyrene dishes for standard cell culture. **B**) ScxGFP intensity (AU) in TPCs cultured on fibronectin-coated glass for 7 days in media supplemented with a panel of putative tenogenic growth factors (n = 300-400 cells, N = 2). Boxes denote medians and span interquartile ranges; whiskers span 95% confidence intervals. **C**) Representative fluorescent images of TPC monolayers treated with basal media or supplemented with various TGF-β isoforms. **D**) Fold change in expression of canonical tenogenic genes with TGF-β3 treatment of TPC monolayers for 7 days (n = 2, N = 3). A fold change of 1 is denoted with a black, dotted line. **E**) Time-lapse imaging of ScxGFP intensity (AU) over the course of a 6-day TPC culture in media supplemented with a panel of growth factors (n = 6 fields of view [FOVs]). Statistical indicators represent comparisons between the vehicle control and TGF-β2 (*) or TGF- β3 (+). **F**) Table of growth factors and respective concentrations supplemented to culture media in (B-E). Unless stated otherwise, all data are reported as mean ± standard deviation. Asterisks indicate statistically significant comparisons, with *p<0.05, **p<0.01, ***p<0.001, and ****p<0.0001 by ordinary one-way ANOVA with Tukey's multiple comparisons test or Student's t-test........ 71

Figure 4.3: Adhesive anisotropy influences TPC tenogenesis in 2D only when cell proliferation is limited. **A**) Schematic of DexVS fiber-coated coverslip fabrication. A solution of DexVS and methacrylated rhodamine was electrospun onto coverslips mounted to a grounded, rotating mandrel, with mandrel rotation speed dictating the resulting alignment of deposited fibers; fibers were crosslinked then functionalized with cell-adhesive CGRGDS. **B**) Fluorescent images of TPCs seeded on random or aligned substrates and cultured with TGF-β3 for one week (n = 25 FOVs, N = 3). **C**) Fluorescent images of mitomycin C pre-treated TPCs in the same culture conditions as in (B) (n = 25 FOVs, N = 2). Quantification of % of TPCs expressing *ScxGFP* (**D**) without mitomycin C pre-treatment and (**E**) with mitomycin C pre-treatment. All data are reported as mean ± standard deviation. Asterisks indicate statistically significant comparisons, with ****p<0.0001 by Student's t-test (ns denotes a non-significant comparison). 73

Figure 4.4: TGF-β isoforms differentially regulate a tenogenic vs. myofibroblastic fate switch. TPCs were cultured for 7 days on aligned fiber-coated coverslips in basal media or supplemented with various isoforms of TGF-β. **A**) Fluorescent images of TPCs stained for F-actin. **B**) Quantification of F-actin intensity (AU) (n = 25 FOVs, N = 2). **C**) Fluorescent images of *ScxGFP* reporter TPCs stained for αSMA. Quantification of % of TPCs expressing (**D**) *ScxGFP* and (**E**) *αSMA* (n = 25 FOVs, N = 2). All data are reported as mean ± standard deviation. Asterisks indicate statistically significant comparisons, with ***p<0.001 and ****p<0.0001 by ordinary one-way ANOVA with Tukey's multiple comparisons test or Student's t-test. 75

Figure 4.5: Rho/ROCK inhibition promotes TGF-β-mediated tenogenesis. **A**) *ScxGFP* reporter TPCs were cultured for 7 days on aligned fiber-coated coverslips in basal media containing TGF-β3 and supplemented with various pharmacologics targeting Rho GTPase regulators of actin cytoskeleton dynamics or myosin. **B**) Fluorescent images of *ScxGFP* reporter TPCs. **C**) Quantification of % of TPCs expressing *ScxGFP* (n = 50 FOVs, N = 3). Statistical indicators represent comparisons to basal media (*) and media supplemented with TGF-β3 only (+). **D**) Fluorescent images of identical TPC cultures supplemented with TGF-β3 or TGF-β3 and Y27632 (+Y27632), fixed on days 0, 2, 4, and 6; samples were stained for F-actin and αSMA for quantitative analysis. **E**) Quantification of F-actin intensity (AU), % of TPCs expressing *ScxGFP*, and % of TPCs expressing αSMA (n = 25 FOVs, N = 2). **F**) Fluorescent images of TPC cultures fixed on day 6 and stained for vinculin. The binarized vinculin mask denotes focal adhesions and regions within which vinculin intensity was quantified. Quantification of (**G**) vinculin intensity (AU) and (**H**) average number of focal adhesions per cell (n = 10 FOVs). All data are reported as mean ± standard deviation. Asterisks indicate statistically significant comparisons, with ****p<0.0001 by ordinary one- or two-way ANOVA with Tukey's multiple comparisons test or Student's t-test (ns denotes a non-significant comparison). 77

Figure 4.6: TPC spreading and tenogenesis in fiber-reinforced hydrogel composites (FRHCs) with tunable topographical anisotropy. A) Fluorescent images of *ScxGFP* reporter TPCs encapsulated in DexVS FRHCs and cultured for 7 days in basal media or supplemented with various isoforms of TGF-β. **B**) Quantification of nuclear ScxGFP intensity (AU) and % of cells expressing αSMA (n = 10 FOVs). **C**) Schematic of microfluidic flow-alignment device used to generate FRHCs with anisotropic fibrous topography. Fluorescent images of fibers and TPCs fixed after 7 days of culture in random and flow-aligned regions of the device. Quantification of standard deviation of orientation (°) of TPC cytoskeletons and nuclei (n = 6 FOVs). **D**) Fluorescent images of TPCs cultured for 7 days with TGF-β3 in DexVS FRHCs with varying fiber density and alignment. **E**) Quantification of nuclear and cytosolic ScxGFP intensity (AU) in addition to the standard deviation of orientation (°) of TPC cytoskeletons and nuclei (n = 6 FOVs, N = 3). All data are reported as mean ± standard deviation. Asterisks indicate statistically significant comparisons, with *p<0.05, **p<0.01, ***p<0.001, and ****p<0.0001 by ordinary one- or two- way ANOVA with Tukey's multiple comparisons test (ns denotes a non-significant comparison). 81

Figure 4.7: Rho/ROCK inhibition potentiates TGF-β-mediated tenogenesis in 3D. A) Fluorescent images of *ScxGFP* reporter TPCs encapsulated in flow-aligned FRHCs and cultured for 7 days in basal media or supplemented with Y27632, TGF-β3, or both. **B**) Quantification of cytosolic and nuclear ScxGFP intensity (AU) (n = 6 FOVs, N = 2). **C**) Fold change in expression of canonical tenogenic genes by TPCs encapsulated in FRHCs and treated with Y27632, TGF-β3, or a combination for 7 days (n = 3, N = 2). A fold change of 1 is denoted with a black, dotted line. All data are reported as mean ± standard deviation. Asterisks indicate statistically significant comparisons, with *p<0.05, **p<0.01, ***p<0.001, and ****p<0.0001 by ordinary one- (soluble condition) or two-way (TGF-β3 treatment, Y27632 treatment) ANOVA with Tukey's multiple comparisons test. 83

Figure 4.8: 3D aligned fibrous topography templates *de novo* collagen deposition in FHRCs. A) Fluorescent images of *ScxGFP* reporter TPCs encapsulated in FRHCs with varying fiber alignment and cultured for 4 weeks with TGF-β3. Quantification of (**B**) standard deviation of orientation (°) of TPC cytoskeletons and nuclei, (**C**) cytosolic ScxGFP intensity, and (**D**) nuclear ScxGFP intensity (n = 6 FOVs, N = 2). **E**) Brightfield images of Picrosirius Red-stained frozen sections of 4-week TPC cultures in random and aligned FRHCs. **F**) Quantification of normalized red intensity (AU) (n = 6, N = 2). **G**) Polarized light images of random and aligned 4-week FRHC cultures over a range of angular deviation. **H**) Quantification of birefringence intensity (AU) as a function of angular deviation (°), birefringence range (AU), and full width at half maximum (°) (n = 6 FOVs, N = 2). **I**) Brightfield images of Picrosirius Red-stained sections of 4-week TPC cultures in flow-aligned FRHCs with varying fiber density. Quantification of (**J**) normalized red intensity (AU) (n = 6 FOVs), (**K**) collagen % dry weight (n = 3 hydrogels), and (**L**) birefringence intensity (AU) as a function of angular deviation (°), birefringence range (AU), and full width at half maximum (FWHM) (°) (n = 3 FOVs). All data are reported as mean ± standard deviation. Asterisks indicate statistically significant comparisons, with *$p<0.5$, **$p<0.01$, ***$p<0.001$, and ****$p<0.0001$ by ordinary one- or two-way ANOVA with Tukey's multiple comparisons test or Student's t-test (ns denotes a non-significant comparison)........... 87

Figure 4.9: Human TDCs exhibit variable capacity for tenogenesis and organized collagen deposition. **A**) Demographic information and Bonar tendinopathy scores for 3 tendon tissue donors from whom human TDCs were isolated. **B**) Fold change in expression of canonical tenogenic genes by TDCs encapsulated in FRHCs and treated with TGF-β3 or a combination of TGF-β3 and Y27632 for 7 days (n = 3 hydrogels). A fold change of 1 is denoted with a black, dotted line. **C**) Brightfield images of Picrosirius Red-stained frozen sections of 2- (Donors 1 and 2) and 4-week (Donor 3) TDC cultures in flow-aligned FRHCs. **D**) Quantification of normalized red intensity (AU) (n = 6 FOVs). **E**) Polarized light images of aligned 2-4-week FRHC cultures with TGF-β3 over a range of angular deviation. **F**) Quantification of birefringence intensity (AU) as a function of angular deviation (°), birefringence range (AU), and full width at half maximum (FWHM) (°) (n = 3 FOVs). All data are reported as mean ± standard deviation. Asterisks indicate statistically significant comparisons, with *$p<0.05$, **$p<0.01$, ***$p<0.001$, and ****$p<0.0001$ by ordinary one- or two-way ANOVA with Tukey's multiple comparisons test. 90

Supplemental Figure 4.1: Blocking cell proliferation minimally affects nuclear morphology or collective orientation. Quantifications of nuclear counts and morphology in TPCs cultured with TGF-β3 for 7 days on random and aligned, fiber-coated coverslips, with and without mitomycin C (MitC) pre-treatment. **A**) Number of nuclei per 10X FOV. **B**) Nuclear area (μm^2). **C**) Nuclear eccentricity. **D**) Standard deviation of orientation (°) of TPC nuclei. All data are reported as mean ± standard deviation, and n = 25 FOVs. Asterisks indicate statistically significant comparisons, with *p<0.05 and ****p<0.0001 by ordinary two-way ANOVA with Tukey's multiple comparisons test. 102

Supplemental Figure 4.2: Dose screens for Rho/ROCK inhibitors Y27632 and H1152. A) Fluorescent images of *ScxGFP* reporter TPCs cultured on aligned, fiber-coated coverslips for 7 days with TGF-β3, TGF-β3 and Y27632 (+Y27632), or TGF-β3 and H1152 (+H1152); inhibitors were tested at a range of doses. Quantification of (**B**) % of TPCs expressing *ScxGFP* and (**C**) number of nuclei per 10x FOV (n = 50 FOVs). All data are reported as mean ± standard deviation. Asterisks indicate statistically significant comparisons, with ****p<0.0001 by ordinary one-way ANOVA with Tukey's multiple comparisons test. 103

Supplemental Figure 4.3: Vinculin aggregation at focal adhesions during TPC tenogenesis. A) Fluorescent images of TPC cultures on aligned, fiber-coated coverslips with TGF-β3 or TGF-β3 and Y27632 (+Y27632); identical samples were fixed on days 0, 2, 4, and 6. **B**) Quantification of vinculin intensity (AU) and average number of focal adhesions (FA's) per cell (n = 10 FOVs). All data are reported as mean ± standard deviation. Asterisks indicate statistically significant comparisons, with *p<0.05 and ****p<0.0001 by Student's t-test. 104

Supplemental Figure 4.4: Screen of bulk crosslink density in FRHCs. A) Fluorescent images of *ScxGFP* reporter TPC cultures with TGF-β3 in FRHCs (2.5 v/v% fibers) with varying crosslink densities. Quantification of (**B**) cytosolic and nuclear ScxGFP intensity (AU) and (**C**) cell aspect ratio (n = 10 FOVs). All data are reported as mean ± standard deviation. Asterisks indicate statistically significant comparisons, with *p<0.05, **p<0.01, ***p<0.001, and ****p<0.0001 by ordinary one-way ANOVA with Tukey's multiple comparisons test. 104

Supplemental Figure 4.5: Rho/ROCK inhibition of TPCs in FRHCs with 30μM Y27632. A) Fluorescent images of *ScxGFP* reporter TPC cultures in flow-aligned FRHCs (2.5 v/v% fibers) with basal media or supplemented with Y27632 (30μM), TGF-β3, or both. Quantification of (**B**) cytosolic and nuclear ScxGFP intensity (AU) (n = 6 FOVs). All data are reported as mean ± standard deviation. Asterisks indicate statistically significant comparisons, with *p<0.05, **p<0.01, and ****p<0.0001 by ordinary two-way ANOVA with Tukey's multiple comparisons test. 105

Supplemental Figure 4.6: Fiber density does not impact Picrosirius Red staining in acellular FRHCs. A) Brightfield images of Picrosirius Red-stained frozen sections of random and aligned, acellular FRHCs. **B**) Quantification of normalized red intensity (AU) (n = 6 FOVs). All data are reported as mean ± standard deviation. ns denotes a non-significant comparison by Student's t-test. 105

Supplemental Figure 4.7: Bonar tendinopathy scoring for human TDC donors. A) Brightfield images of hematoxylin and eosin-stained paraffin-embedded sections of donor Achilles tendon tissues. **B**) Bonar tendinopathy scoring, where each criteria receives a grade between 0 (least tendinopathic) and 3 (most tendinopathic). 106

Supplemental Figure 4.8: Myofibroblastic differentiation of human TDCs in FRHCs. A) Fluorescent images of frozen sections of human TDC cultures in flow-aligned FRHCs (2.5 v/v% fibers) with basal media or supplemented TGF-β3. Quantification (**B**) % of TPCs expressing *αSMA* and (**C**) F-actin intensity (AU) (n = 10 FOVs). All data are reported as mean ± standard deviation. Asterisks indicate statistically significant comparisons, with *p<0.05, ***p<0.001, and ****p<0.0001 by ordinary two-way ANOVA with Tukey's multiple comparisons test. ... 106

Figure 5.1: ScxGFP expression by TPCs is attenuated by 3D fibrous topography. A) A 4-channel microfluidic chip flow-aligned DexVS FRHCs on glass coverslips. **B**) GFP-channel fluorescent images of ScxGFP reporter TPCs cultured for one week in flow-aligned DexVS hydrogels with 0 or 2.5 v/v% fibers in basal media with or without TGF-β3. **C**) Quantification of nuclear ScxGFP intensity (AU) (n = 6 FOVs, N = 2). All data are reported as mean ± standard deviation. Asterisks indicate statistically significant comparisons, with ****p<0.0001 by ordinary two-way ANOVA with Tukey's multiple comparisons test. 111

Figure 5.2: Fibrous topography limits fibrochondrogenic differentiation over four weeks of culture. A) Fluorescent images of ScxGFP reporter TPCs cultured for four weeks in flow-aligned DexVS hydrogels with 0 or 2.5 v/v% fibers with TGF-β3 supplementation. Quantification of (**B**) nuclear ScxGFP intensity, (**C**) cytosolic type I collagen intensity, (**D**) cytosolic type II collagen intensity, and (**E**) nuclear Sox9 intensity (AU) (n = 6 FOVs, N = 4). All data are reported as mean ± standard deviation. Asterisks indicate statistically significant comparisons, with ****p<0.0001 by Student's t-test (ns denotes a non-significant comparison). 113

Figure 5.3: hMSC chondrogenic medium further boosts TPC chondrogenesis in non-fibrous hydrogels. A) Fluorescent images of ScxGFP reporter TPCs cultured for two weeks in flow-aligned DexVS hydrogels with 0 or 2.5 v/v% fibers in basal media or hMSC chondrogenic medium (both with TGF-β3 supplementation). **B**) Quantification of nuclear ScxGFP intensity, cytosolic type I collagen intensity, cytosolic type II collagen intensity, and nuclear Sox9 intensity (AU) (n = 6 FOVs). All data are reported as mean ± standard deviation. Asterisks indicate statistically significant comparisons, with *p<0.05, **p<0.01, and ****p<0.0001 by ordinary two-way ANOVA with Tukey's multiple comparisons test.. 115

Figure 5.4: Rac1 inhibition favors TPC fibrochondrogenic differentiation. A) Fluorescent images of ScxGFP reporter TPCs cultured for two weeks in flow-aligned DexVS hydrogels with 0 or 2.5 v/v% fibers in basal media with TGF-β3; cultures were additionally supplemented with

DMSO, Y27632, or NSC23766. **B**) Quantification of nuclear ScxGFP intensity, cytosolic type I collagen intensity, cytosolic type II collagen intensity, and nuclear Sox9 intensity (AU) (n = 6 FOVs). All data are reported as mean ± standard deviation. Asterisks indicate statistically significant comparisons, with *p<0.05, **p<0.01, ***p<0.001, and ****p<0.0001 by ordinary two-way ANOVA with Tukey's multiple comparisons test. 117

Figure 5.5: Cyclic stretch drives fibrochondrogenic gene expression by TPCs. A) Schematic of aligned FRHC stretcher; a PDMS well is mounted to a motorized assembly, FRHCs are flow-aligned on the base of the well, and actuation results in strain parallel to the direction of flow alignment. **B**) Fold change in expression of canonical tenogenic and fibrochondrogenic genes by TPCs encapsulated in FRHCs and cultured in static or dynamic stretch conditions with TGF-β3. All data are reported as mean ± standard deviation. Asterisks indicate statistically significant comparisons, with *p<0.05, **p<0.01, and ****p<0.0001 by ordinary two-way ANOVA with Tukey's multiple comparisons test. 119

Figure 5.6: Fibrous topography drives ScxGFP$^+$ TPC recruitment to the site of injury. A) Diagram of a ScxGFP reporter mouse Achilles tenotomy followed by injection and *in situ* crosslinking of an FRHC. **B**) Intraoperative photograph of the transected Achilles during FRHC *in situ* crosslinking. **C**) Fluorescent images sectioned hindlimbs two weeks following implantation of DexVS hydrogels with 0 or 2.5 v/v% fibers. Quantification of (**D**) % ScxGFP$^+$ nuclei between the tendon stubs, (**E**) total migration distance of ScxGFP$^+$ cells from the tendon stub, and (**F**) % Sox9$^+$ nuclei between the tendon stubs (N = 3). All data are reported as mean ± standard deviation. Asterisks indicate statistically significant comparisons, with **p<0.01 by paired Student's t-test (ns denotes a non-significant comparison). 120

Supplemental Figure 5.1: Aligned fibrous topography is mirrored by cell orientation. Quantification of standard deviation of orientation (°) of TPC cytosols and nuclei after 1 week of culture in DexVS hydrogels with 0 or 2.5 v/v% fibers with TGF-β3 supplementation (n = 6 FOVs, N = 2). All data are reported as mean ± standard deviation. Asterisks indicate statistically significant comparisons, with ****p<0.0001 by ordinary two-way ANOVA with Tukey's multiple comparisons test. 131

Supplemental Figure 5.2: Biological replicates and live imaging of nuclear ScxGFP. In TPCs cultured in DexVS hydrogels (0 or 2.5 v/v% fibers) for 4 weeks, quantification of (**A**) nuclear ScxGFP intensity, (**B**) cytosolic type I collagen intensity, (**C**) cytosolic type II collagen intensity, and (**D**) nuclear Sox9 intensity (AU) (n = 6 FOVs, N = 4). **E**) Quantification of nuclear ScxGFP intensity (AU) in live-imaged samples at half-week intervals over four weeks (n = 6 FOVs). All data are reported as mean ± standard deviation. Asterisks indicate statistically significant comparisons, with *p<0.05, **p<0.01, and ****p<0.0001 by ordinary two-way ANOVA with Tukey's multiple comparisons test or paired Student's t-test (ns denotes a non-significant comparison)... 132

Supplemental Figure 5.3: TPC gene expression as a function of fibrous topography. Fold change in expression of canonical tenogenic and fibrochondrogenic genes by TPCs encapsulated in DexVS hydrogels (0 or 2.5 v/v% fibers) at (**A**) 1 week and (**B**) 4 weeks of culture (n = 2 hydrogels). All data are reported as mean ± standard deviation. Asterisks indicate statistically significant comparisons, with *p<0.05 by ordinary two-way ANOVA with Tukey's multiple comparisons test.. 133

Supplemental Figure 5.4: Validation of FRHC stretch assembly. A) Brightfield images of FRHCs after one week of culture in static and dynamic strain conditions. **B**) Photographs of a resting and stretched PDMS well, with black vertical lines spaced 1 cm apart at rest. **C**) Quantification of lateral strain (in the x direction) across the base of the PDMS well. 134

Abstract

Biomaterials providing control over microenvironmental cues pose an effective strategy for augmenting the repair of tendon, injury of which involves aberrant scar formation, chronic pain, diminished function, and heightened risk of re-injury in adults. The unknown mechanisms driving this natural, maladaptive repair process pose a major hurdle to full tendon regeneration. While adult tendons heal by scar formation, neonatal mouse tendons possess a greater regenerative capacity. As such, emulating this regenerative healing response through biomaterial-mediated, spatiotemporal control of cell recruitment, differentiation, and matrix remodeling following injury may provide an effective route toward improved tendon regeneration in adults.

Fiber-reinforced hydrogel composites are promising biomaterials for augmenting tendon regeneration that imbue the wound microenvironment with fibrous topographical cues and can be localized to an internal wound defect through minimally invasive administration. Typically composed of polymer chains crosslinked into a solid bulk by protease-responsive segments, these materials also benefit from tunable and modular inclusion of biochemical moieties in addition to tailorable mechanical properties. These synthetic scaffolds are also attractive from a manufacturing perspective because polymer and peptide synthesis are readily scalable. Positing that the microenvironmental cues defined by the natural healing response fail to properly differentiate tendon progenitor cells (TPCs) recruited to the wound site, this thesis pursued novel strategies to significantly improve the therapeutic potential of synthetic hydrogels through a fibrous, composite material approach and temporal release of biomolecules.

In this thesis, a synthetic, fiber-reinforced hydrogel composite was used to assess whether the recruitment of tendon progenitor cells can be enhanced via combined mechanical, topographical, and microparticle-delivered soluble cues. Composites were fabricated by encapsulating electrospun fiber segments in a bulk hydrogel formed from dextran vinyl sulfone crosslinked with an MMP-labile peptide. Monodisperse populations of hybrid microgels with covalently incorporated heparin were then fabricated to release platelet-derived growth factor-BB, a chemokine that potently induces TPC migration. In this material platform, recruitment of murine tendon progenitor cells into synthetic hydrogels was enhanced by fibrous topographical cues and microgel-delivered platelet-derived growth factor-BB. These cues translated effectively to an *ex vivo* model of progenitor cell recruitment from the epitenon of explanted murine Achilles tendons.

The thesis then applied 2D, and 3D engineered culture platforms to identify critical microenvironmental determinants of tenogenesis. TGF-β3 and Rho/Rho-kinase inhibition led to increased Scleraxis expression in murine tendon progenitor cells across 2D and 3D settings. Interestingly, the pro-tenogenic effect of aligned fibrous topography was unique to 2D cultures. Although fiber alignment did not increase Scleraxis expression in 3D, it drove deposition and organization of type I collagen, thereby defining mechanical anisotropy and function of regenerated tissue.

Lastly, this thesis studied the influence of fibrous topography on a tenogenic vs. fibrochondrogenic fate switch, finding that the presence of cell-adhesive fibrous topography biases tendon progenitor cells toward the former. In contrast, Rac1 inhibition and cyclic strain biased tendon progenitor cells toward a fibrochondrogenic phenotype. However, when crosslinked *in situ* in the gap of a transected murine Achilles tendon, fibers primarily influenced tendon progenitor cell recruitment and had a minimal effect on fibrochondrogenic differentiation.

The overall work presented in this dissertation develops an injectable biomaterial that can integrate a combination of physical and soluble cues to temporally orchestrate two critical phases of tendon healing: 1) recruitment of TPC populations and 2) tenogenic differentiation of TPCs leading to synthesis of *de novo* extracellular matrix with appropriate composition and organization. Moreover, the work provides insight into the microenvironmental cues regulating tenogenesis, information critical to the advancement of biomaterial therapeutics geared toward connective tissue regeneration.

Chapter 1: Introduction

The overarching goal of this thesis is to develop an injectable biomaterial strategy to improve healing of ruptured tendons. Toward this end, we developed a synthetic, fiber-reinforced hydrogel composite that provides a combination of physical and soluble cues to temporally (1) orchestrate recruitment of tendon progenitor cells (TPCs) and (2) drive tenogenic differentiation of TPCs, leading to synthesis of *de novo* extracellular matrix (ECM) comprised of mature, aligned collagen fibrils. Chapter 2 provides information on a curated list of background topics. The chapter describes the evolution of biomaterial approaches to improved tendon regeneration, which progressed from pure fibrous scaffolds to softer, fiber-reinforced composites to deliver a more pro-tenogenic microenvironment. It also outlines design criteria for these scaffolds, highlighting successful fiber-reinforced hydrogel scaffold (FRHC) approaches that address these needs. Specifically, Chapter 2 discusses the role of FRHCs in driving cell recruitment, tenogenic differentiation, organized matrix deposition, and immunomodulation. To advance the field's knowledge, the remaining chapters focus on integrating these design criteria into an injectable FRHC to achieve spatiotemporal control over tendon regeneration. Chapter 3 focuses on encouraging TPC recruitment into an injectable, synthetic FRHC. This chapter describes the fabrication of a dextran vinyl sulfone (DexVS), comprised of (1) a bulk hydrogel of DexVS crosslinked with an MMP-labile peptide and (2) electrospun DexVS fibers functionalized with a cell-adhesive RGD peptide. Using a TPC spheroid outgrowth model, this work demonstrated the synergistic, pro-migratory effects of fibrous topography and platelet-derived growth factor

(PDGF)-BB. A droplet-based microfluidic chip was also adapted to generate heparanized microparticles, and a combination of *in silico* and *in vitro* modeling characterized the pro-migratory effect of sustained, spatially organized delivery of chemotactic soluble cues. Lastly, this chapter employed an *ex vivo* model of Achilles tendon injury to show that these pro-migratory microenvironmental cues also apply to TPCs recruited from the epitenon of a transected, murine Achilles tendon.

Chapter 4 aims to interrogate the influence of microenvironmental features of an FRHC on tenogenic differentiation of TPCs. This work applied a combination of 2D and 3D engineered culture platforms to identify the salient physical and biochemical cues driving tenogenic differentiation and organized matrix deposition by murine TPCs and human TDCs. The work also highlighted a tenogenic vs. myofibroblastic fate switch as a function of TGF-β isoform, where TGF-β3 treatment, softer substrates, and actin cytoskeletal dysregulation by Rho/ROCK inhibition led to more complete tenogenic differentiation. While an aligned, fibrous topography drove tenogenesis of individualized TPCs in 2D, the impact of fiber alignment in 3D FRHCs was limited to the organization of *de novo* collagenous matrix, delineating the roles of cell spreading morphology and cellular organization in tenogenic differentiation and matrix remodeling, respectively. Lastly, this chapter showed that human TDCs exhibit heterogeneity with respect to their tenogenesis and matrix synthesis in response to TGF-β3.

Chapter 5 investigates the influence of cell-adhesive fibrous topography on tenogenic and fibrochondrogenic differentiation of TPCs encapsulated in flow-aligned DexVS FRHCs. In this chapter, the presence of cell-adhesive fibrous topography attenuated TGF-β3-mediated scleraxis (Scx) production by TPCs due to a nuanced interplay between *Scx* expression and tenogenic differentiation. Additionally, TPCs in non-fibrous hydrogels exhibited a fibrochondrogenic phenotype characterized by the co-expression of Scx and Sox9 in addition to increased production of type II collagen. Rac1 inhibition also favored fibrochondrogenic differentiation, suggesting a key mediator of cytoskeletal dynamics in response to fibrous topography. Potentially through Rac1 down-regulation, cyclic stretch, a known tenogenic cue, induced fibrochondrogenic gene expression in TPCs. Finally, in a murine tendon healing model, fibrous topography drove the recruitment of ScxGFP$^+$ TPCs but had minimal impact on nuclear Sox9 intensity, highlighting the role of fibrous topography in cell recruitment to FRHCs.

Finally, chapter 6 provides a summary of key findings from this thesis and outlines future directions including improving mass transport, influencing immune polarization, and translational considerations. The successful integration of these technologies will improve treatment of tendon injury, and it is likely that lessons learned in this context will be applicable to tissue engineering strategies for a range of connective tissues.

Chapter 2: Background

Note: this chapter contains unpublished work in preparation for submission

2.1 Authors

Robert N. Kent III, Alice H. Huang, Brendon M. Baker

2.2 Abstract

This review examines the promise of fiber-reinforced hydrogel composites (FRHCs) for augmenting tendon regeneration. Composed of reinforcing fibers embedded in a degradable hydrogel, these scaffolds provide both mechanical strength and a conducive microenvironment for biological processes required for tendon regeneration. We discuss typical properties of FRHCs, highlighting their ability to simultaneously fulfill essential mechanical and biological design criteria for a regenerative tendon scaffold. Furthermore, we describe features of FRHCs that improve specific biological aspects of tendon healing including stromal progenitor cell recruitment, early polarization to a pro-regenerative immune response, tenogenic differentiation of recruited progenitor cells, and subsequent production of a mature, aligned collagenous matrix. Finally, the review offers a perspective on clinical translation of tendon FRHCs and outlines key directions for future work.

2.3 Introduction

Tendons are a critical component of the musculoskeletal system, responsible for transmitting forces between muscles and bones. Unfortunately, they are prone to injury and degeneration, with nearly half of all musculoskeletal injuries reported in the US involving tendons or ligaments (Praemer et al., 1999). Moreover, current surgical and conservative treatment strategies result in comparably poor outcomes with regard to pain, diminished function, and elevated risk of re-injury (Lantto et al., 2016; Nilsson-Helander et al., 2010). There is a clear need for better therapies for tendon injury, motivating the development of biomaterials geared toward enhancing tendon healing and improving long-term function.

The tendon repair field has widely recognized the need for influencing the biochemical milieu at the site of injury, motivating early strategies of injection or suture-based delivery of drugs or biologics (de Vos et al., 2010; Efird et al., 2018; Padilla et al., 2021; Tempfer et al., 2018). However, these approaches failed to provide the spatiotemporally controlled cues necessary for regenerating the functional architecture of native tendon, essential to the performance of the regenerated tissue (Sharma and Maffulli, 2006; F. Wu et al., 2017a). To address this key structural requirement, initial strategies explored the use of woven fibrous scaffolds made of synthetic materials such as poly(glycolic acid) or poly(lactic-co-glycolic acid) (PLGA). Even though these woven scaffolds approached the mechanical properties of native tendon, their stiffness elicited adverse biological responses including the promotion of chondrogenic or osteogenic trans-differentiation *in vivo* (English et al., 2015). Hydrogels have therefore recently gained popularity as they allow for fine tuning of the cell-scale microenvironment that has been shown to enhance tenogenic differentiation *in vitro* (Miranda-Nieves and Chaikof, 2017; H. Yin et al., 2019). However, these materials are typically orders of magnitude below the stiffness regime of native tendon and are therefore generally unsuitable for the mechanically demanding environment of a tendon injury site.

Fiber-reinforced hydrogel composites (FRHCs), incorporating both polymeric fibers and hydrogel-based materials, thus represent a promising approach to simultaneously providing the cellular and biomechanical features critical for tendon repair. By incorporating reinforcing fibers, such as collagen, silk, or synthetic materials into an injectable hydrogel matrix, the resulting composite can provide improved tensile strength, stiffness, and toughness compared to hydrogels alone while also providing a tenogenic microenvironment. Furthermore, incorporation of aligned fibers into these materials can mimic the aligned structure of native tendon tissue (Hiraki et al., 2021), expedite tendon progenitor cell (TPC) recruitment (Kent et al., 2022; Xie et al., 2022), and promote tenogenic differentiation (G. Yang et al., 2016).

In this review, we discuss recent advances in the development of fiber-reinforced hydrogel composites for tendon repair. We explore various scaffold compositions and resulting mechanical properties as well as the methods of fabrication and characterization of these composites. Additionally, we examine the *in vitro* and *in vivo* performance of these composites, including their ability to promote cell adhesion, proliferation, and differentiation, as well as their efficacy in enhancing tendon healing and regeneration. Finally, we discuss the challenges and future directions for the development of FRHCs for tendon repair, including challenges associated with clinical translation of these materials.

2.4 Fiber-reinforced hydrogel composite mechanics

The ideal biomaterial for tendon repair should satisfy two major design criterions: mechanical and biological. The first category involves the mechanical performance of the graft upon implantation, which has been the primary focus of early attempts at developing biomaterial scaffolds to augment load-bearing, connective tissue repair (Frazier and Clark, 1980; Glousman et al., 1988; Lieberman et al., 1988; Majima et al., 2007; Parsons et al., 1989; Richmond et al., 1992). Properties like compressive/tensile strength, fatigue strength, resistance to creep deformation, and frictionless gliding against adjacent tissues are important for early restoration of the load bearing function of the tissue, especially in light of the known clinical benefits of early weightbearing and controlled range of motion (Kauwe, 2017; Sorrenti, 2006). However, despite achieving improved functional restoration of Achilles tendon function in the short term, these implants result in long-term complications related to scaffold rupture and poor integration with the native tendon (Parsons et al., 1989; Ratcliffe et al., 2015). Problems with these fibrous scaffolds generally stemmed from neglecting biological design criteria, which limited the ability of the graft to integrate with the native tissue and encourage cell-mediated remodeling of the scaffold into functional tendon over time. Factors like the capacity for cell recruitment, biochemical cues engendering tenogenic differentiation of recruited cells, and degradability to allow for cell-mediated remodeling of the scaffold and matrix synthesis are essential to the long-term performance of implants and the resulting formation of new tendon that functions comparably to the native tissue.

FRHCs show great promise for achieving the biological goals of a tendon scaffold due to their highly tunable composition. For example, the bulk hydrogel component of an FRHC can be comprised of natural materials such as collagen, hyaluronic acid, or chitosan, favoring cell-mediated remodeling and integration with the native tendon (Malandain et al., 2023; Y. Wang et al., 2021b; Weitkamp et al., 2021). Conversely, synthetic materials like poly(ethylene glycol) (PEG) (Macdougall et al., 2018), polyvinyl alcohol (PVA) (No et al., 2020b), or functionalized dextran (Kent et al., 2022) require additional engineering to present appropriate microenvironmental cues to drive integration and remodeling (e.g., cell-degradable crosslinks and moieties enabling cell adhesion), but they allow for more precise tuning of these cues and pose the added benefit of improved scalability. The fibrous component can also be formed from a range of natural or synthetic materials, and many innovative fabrication approaches have been recently established to achieve precise control over fibrous architecture in 3D. Fibers as large as 300 μm in diameter (recapitulating the upper length-scale of tendon fascicles) have been fabricated by crosslinking a polymer solution in a Teflon mold (Patel et al., 2018), but diameters more akin to those of collagen fibrils that hierarchically assemble to form fascicles (20-500 nm) (Siadat et al., 2021) can be achieved through techniques like solution electrospinning (SES) (G. Yang et al., 2016; Younesi et al., 2014), melt electrowriting (MEW) (Castilho et al., 2018; Visser et al., 2015), or meltblowing (Jenkins et al., 2017) (**Figure 2.1**). Topographical features like fiber anisotropy and crimp of the fibrous component can also be achieved either during fiber fabrication (Davidson et al., 2020b; Orr et al., 2015; G. Yang et al., 2016) or during crosslinking of the composite material (Hiraki et al., 2021; No et al., 2020b; Szczesny et al., 2017). FRHCs enable myriad combinations of natural or synthetic bulk and fibrous components, providing an unprecedented level of tunability in these composite scaffolds toward engineering a tenogenic microenvironment.

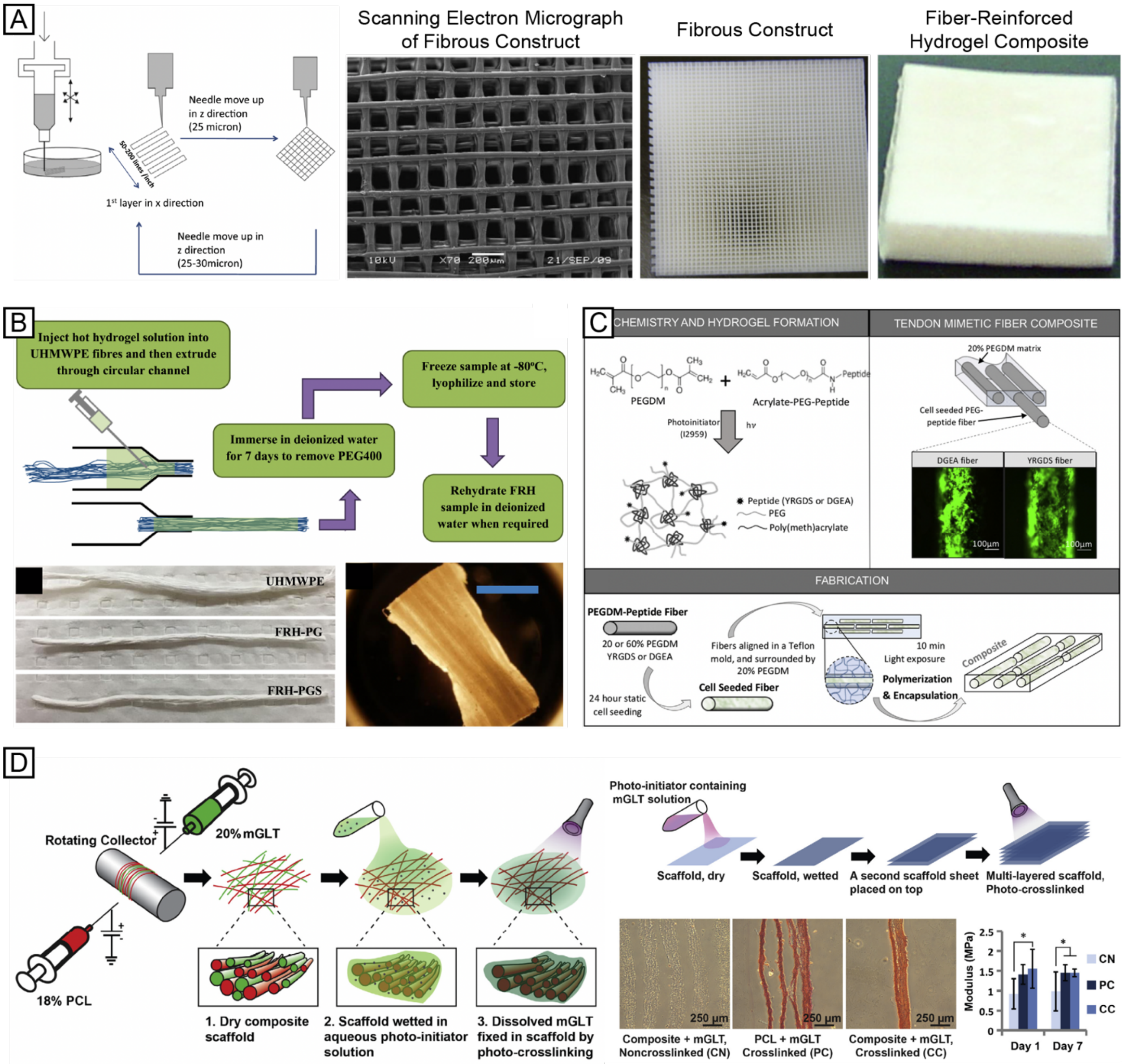
A
Needle move up
in z direction
(25 micron)
50-200 lines /inch
1st layer in x direction
Needle move up in
z direction
(25-30micron)
Scanning Electron Micrograph
of Fibrous Construct
10kV X70 200μm 21/SEP/09
Fibrous Construct
Fiber-Reinforced
Hydrogel Composite
B
Inject hot hydrogel solution into UHMWPE fibres and then extrude through circular channel
Immerse in deionized water for 7 days to remove PEG400
Freeze sample at -80ºC, lyophilize and store
Rehydrate FRH sample in deionized water when required
UHMWPE
FRH-PG
FRH-PGS
C
CHEMISTRY AND HYDROGEL FORMATION
PEGDM
Acrylate-PEG-Peptide
Photoinitiator
(I2959)
hν
Peptide (YRGDS or DGEA)
PEG
Poly(meth)acrylate
TENDON MIMETIC FIBER COMPOSITE
20% PEGDM matrix
Cell seeded PEG-
peptide fiber
DGEA fiber
YRGDS fiber
100μm
100μm
FABRICATION
PEGDM-Peptide Fiber
20 or 60% PEGDM
YRGDS or DGEA
24 hour static
cell seeding
Cell Seeded Fiber
Fibers aligned in a Teflon
mold, and surrounded by
20% PEGDM
10 min
Light exposure
Polymerization
& Encapsulation
Composite
D
Rotating Collector
20% mGLT
18% PCL
1. Dry composite
scaffold
2. Scaffold wetted in
aqueous photo-initiator
solution
3. Dissolved mGLT
fixed in scaffold by
photo-crosslinking
Photo-initiator containing
mGLT solution
Scaffold, dry
Scaffold, wetted
A second scaffold sheet
placed on top
Multi-layered scaffold,
Photo-crosslinked
250 μm
250 μm
250 μm
Composite + mGLT,
Noncrosslinked (CN)
PCL + mGLT
Crosslinked (PC)
Composite + mGLT,
Crosslinked (CC)
Modulus (MPa)
2.5
2
1.5
1
0.5
0
*
*
CN
PC
CC
Day 1
Day 7

Figure 2.1: FRHC fabrication technologies. A) Fabrication schematic, scanning electron micrograph, and photograph of a 3D fibrous scaffold made from a polyurethane blend; photograph of polyurethane scaffold impregnated with an epoxy-amine hydrogel to form an FRHC. **B**) Extrusion of an aligned, ultra-high molecular weight polyethylene (UHMWPE) fiber-reinforced hydrogel composite; fibers are extruded either in a PVA/gelatin hydrogel with (FRH-PGS) or without (FRH-PG) strontium hardystonite. **C**) Alignment of cell-laden PEG dimethacrylate (PEGDM) fibers in a Teflon mold enables patterned encapsulation in a PEGDM hydrogel. **D**) SES onto a rotating mandrel generates an aligned scaffold of polycaprolactone (PCL) and gelatin methacrylate (mGLT), then mGLT fibers are dissolved in a photo-initiator solution, and UV exposure yields an FRHC; multi-layer constructs exhibit tensile moduli on the order of 10^1 Mpa. A) Adapted with permission (Agrawal et al., 2013). Copyright 2013, Elsevier. B) Adapted with permission (No et al., 2020b). Copyright 2020, American Chemical Society. C) Adapted with

permission (Patel et al., 2018). Copyright 2018, Elsevier. D) Adapted with permission (G. Yang et al., 2016). Copyright 2016, Elsevier.

While fiber reinforcement does improve the stiffness and strength of a hydrogel (Bas et al., 2015; Beckett et al., 2020; Strange et al., 2014), the mechanical properties of FRHCs are generally inferior compared to native tendon. Most FRHCs developed for connective tissue repair applications have tensile moduli on the order of 10^0-10^1 Mpa (Agrawal et al., 2013; Castilho et al., 2018; Gunes et al., 2020; Gunes et al., 2022; Iannace et al., 1995; Patel et al., 2018; Qiao et al., 2021; Ravishankar et al., 2021; Weitkamp et al., 2021; G. Yang et al., 2016), which pales in comparison to the tensile modulus of native tendon (10^2-10^3 Mpa) (Wren et al., 2001; Zajac, 1989) (**Figure 2.2**). No et al. recently described a composite of a PVA/gelatin hydrogel with ultrahigh molecular weight polyethylene fibers possessing a tensile modulus of ~1.2 Gpa and yield strength of ~80 Mpa, comparable to that of native tendon (No et al., 2020b; Wren et al., 2001). Despite this initial strength, however, constructs explanted from injured rat patellar tendons at 8 weeks exhibited moduli and strengths of 10 Mpa and 750 kPa, respectively, at the scaffold-tendon interface, mirroring the failure mechanism seen in patients who received pure fibrous scaffolds (Parsons et al., 1989). All the above FRHCs were able to encourage cell infiltration, tenogenic differentiation, and aligned collagen deposition, underlining the biological efficacy of these constructs. Therefore, the clinical indication of FRHCs for tendon repair may need to be narrowed as an adjunct to suture repair, for example, to obviate the demand for mechanical performance immediately upon implantation.

A final tradeoff to consider from a material perspective is the strategy of implantation. While many of the proposed fabrication methods require that a whole construct be formed, implanted as a solid, and sutured to the adjacent tendon, a subset of FRHCs can be crosslinked *in* *situ* (Diba et al., 2018; Jordan et al., 2017; Kent et al., 2022). These constructs are formed by introducing a crosslinking molecule to a solution of bulk hydrogel backbone containing a suspension of cell-adhesive fibers (**Figure 2.2**). In addition to facilitating percutaneous delivery, *in situ* crosslinking allows the FRHC to conform and in some cases adhere to the irregular geometry of a ruptured tendon stub, theoretically expediting cell recruitment and tissue integration. Injectable FRHCs cannot achieve the level of control over 3D fibrous architecture achievable during *in vitro* fabrication performed prior to implantation, but topographical anisotropy of *in situ* polymerized FRHCs can still be tuned to a degree (**Figure 2.2**). For example, Hiraki et al. incorporated superparamagnetic nanoparticles within the fibrous component of an FRHC to achieve topographical anisotropy during *in situ* gelation under a 650 mT magnetic field (Hiraki et al., 2021). The fiber alignment attained through this method promoted spreading and co-alignment of embedded murine tendon progenitor cells *in vitro*, establishing promising evidence that magnetic alignment of fibers during *in situ* crosslinking may be adequate for driving the formation of organized and anisotropic cells and tissue during tendon healing.

	Fibrous Scaffolds	Hydrogels	Fiber-Reinforced Hydrogel Composites
	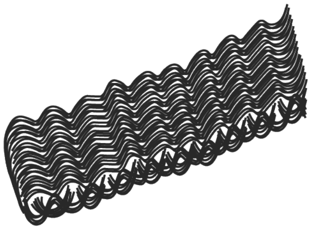 Pure fibrous scaffolds consist of woven, natural or synthetic fibers. Dense, aligned fibers provide uniaxial tensile strength and anisotropic cell-scale topography.	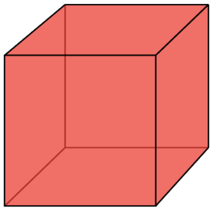 Hydrogels form when natural or synthetic polymers are crosslinked in aqueous solution. Biochemical cues can be delivered by the material itself or through fixation to the backbone.	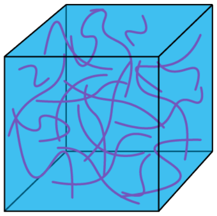 Fiber-reinforced hydrogel composites (FRHCs) are composed of a fiber suspension or scaffold embedded in a bulk hydrogel. Natural or synthetic materials can comprise either component.
Fabrication Methods	Solution electrospinning (SES), melt electrowriting (MEW), electrophoretic compaction, co-axial extrusion	Bulk croslinking with a bi-functionalized ion, organic molecule, or peptide	SES or MEW + Bulk crosslinking
Tensile Modulus	10^1-10^2 MPa	10^{-1}-10^0 MPa	10^1 MPa
Injectability	✗	✓	✓
Tunable Topography	✓	✗	✓
Alignability	✓	✗	✓

Figure 2.2: Comparison of fabrication methods and features of pure fibrous scaffolds, hydrogels, and fiber-reinforced hydrogel composites.

2.5 Engineered cues for effective tenogenesis and cell-mediated repair

The innate tendon healing response involves three key phases: (1) inflammation, (2) cell recruitment/proliferation, and (3) tenogenic differentiation of progenitors and extracellular matrix (ECM) remodeling (F. Wu et al., 2017a). A hematoma forms immediately following injury, then in the subsequent hours to days, neutrophils, monocytes, and macrophages invade the resulting fibrin clot to phagocytose necrotic material and release pro-inflammatory and chemotactic factors

(Sharma and Maffulli, 2006). The cell recruitment phase occurs over the first 2 weeks following injury, during which TPCs and other stromal progenitors migrate into the defect. Many putative tissue origins and lineages have been reported to contribute to this mesenchymal progenitor pool (Bi et al., 2007; Dyment et al., 2014; Harvey et al., 2019), with the tendon fascicles, epitenon, and paratenon (largely perivascular) all suspected to contain progenitor cells that can activate upon injury and participate in the repair process (Best and Loiselle, 2019; Bi et al., 2007; Dyment et al., 2013; Nichols et al., 2023). Recruited TPCs differentiate and synthesize a provisional matrix predominately composed of type III collagen (Sharma and Maffulli, 2006), then over the subsequent weeks to months, type I collagen is secreted and remodeled to form the neotendon (Sharma and Maffulli, 2006; F. Wu et al., 2017a). Unfortunately, this remodeling often leads to the formation of relatively isotropic, hypercellular, hypervascularized scar tissue that has been associated with chronic pain and increased risk of re-rupture (Józsa and Kannus, 1997). Indeed, the Achilles epitenon has been shown to house distinct populations of progenitors that are biased toward either a scleraxis (Scx)$^+$ tenogenic (pro-regenerative) or α-smooth muscle actin (αSMA)$^+$ myofibroblastic (pro-fibrotic) phenotype (Nichols et al., 2023) (**Figure 2.3**). The mechanobiological, topographical, soluble, and immunomodulatory cues presented by an FRHC would likely be critical in influencing this fate switch and the resulting composition, mechanical properties, and function of the regenerated tissue. To address aberrant scar tissue formation in the endogenous tendon repair process, the biological goals of a tendon FRHC are highlighted in the following sections.

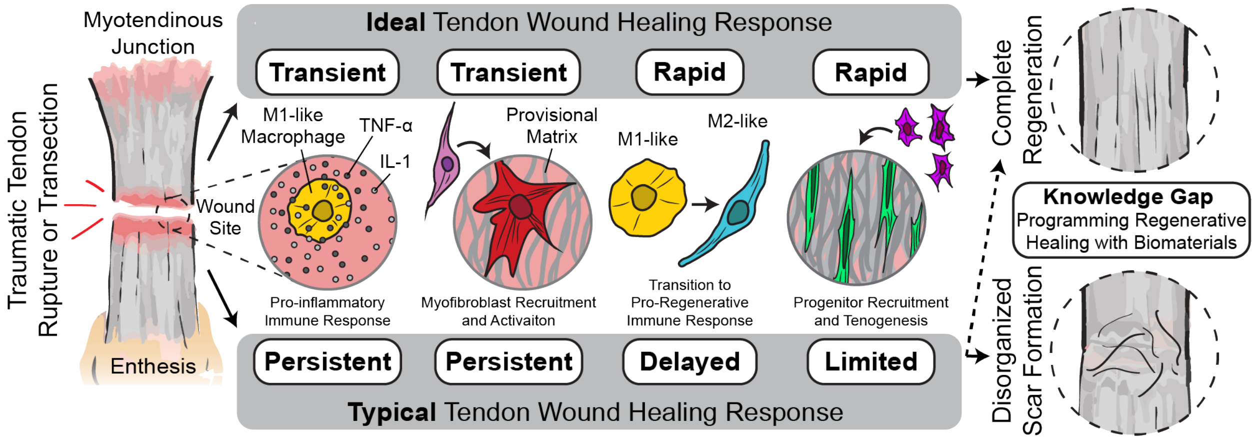
Myotendinous Junction
Traumatic Tendon Rupture or Transection
Wound Site
Enthesis
Ideal Tendon Wound Healing Response
Transient
Transient
Rapid
Rapid
M1-like Macrophage
TNF-α
IL-1
Provisional Matrix
M1-like
M2-like
Pro-inflammatory Immune Response
Myofibroblast Recruitment and Activaiton
Transition to Pro-Regenerative Immune Response
Progenitor Recruitment and Tenogenesis
Persistent
Persistent
Delayed
Limited
Typical Tendon Wound Healing Response
Complete Regeneration
Knowledge Gap
Programming Regenerative Healing with Biomaterials
Disorganized Scar Formation

Figure 2.3: Typical vs. ideal tendon wound healing response. Following injury, a persistent pro-inflammatory response occurs, whereby M1-like macrophages invade the wound site and secrete pro-inflammatory cytokines like tumor necrosis factor (TNF)-α and interleukin (IL)-1. Myofibroblastic differentiation of invading stromal progenitors results in scar tissue formation in lieu of functional tissue regeneration. Ideally, early polarization to an M2-like phenotype and tenogenic differentiation of stromal progenitors would lead to more complete tendon regeneration.

2.5.1 Tendon progenitor cell recruitment

A FRHC therapeutic for improving tendon healing must either deliver or efficiently recruit the TPCs needed for synthesizing, remodeling, and maintaining the regenerated tissue. Cell implantation may be a promising approach, with seminal work in this field showing that implanting a pre-contracted, MSC-laden collagen construct in a rabbit Achilles tendon defect results in improved biomechanical and structural properties of the regenerated tissue (Awad et al., 2003; Butler et al., 2007; Young et al., 1998). Moreover, *in vitro* pre-culture of tissue grafts affords opportunities for priming cells with tenogenic cues (e.g., growth factors or uniaxial cyclic stretch) (Garvin et al., 2003; Nirmalanandhan et al., 2008; Rinoldi et al., 2019a; Rinoldi et al., 2019b; Sakabe et al., 2018; Scott et al., 2011). In FRHCs, cells can be encapsulated stochastically (G. Yang et al., 2016) or patterned via pre-adhesion to the fibrous component (Patel et al., 2018; Weitkamp et al., 2021). Pre-cellularized scaffolds offer distinct advantages, especially in older patients where age-related changes result in diminished TPC abundance or differentiation potential and increased TPC senescence (Y. Li et al., 2019b). Additionally, the use of autologous cells in these patients is hindered by the rapid phenotypic drift that occurs during *in vitro* expansion of human tenocytes and TPCs, in addition to numerous regulatory hurdles and significantly higher costs inherent to cell-based therapies (Q. Tan et al., 2012; Yao et al., 2006). For younger patients with relatively potent TPC pools, and until ongoing progress in induced pluripotent stem cell technology establishes viable strategies to generating TPCs or tenocytes (Lui, 2015), biomaterial strategies that can effectively recruit (i.e., drive migration and proliferation of) endogenous TPCs to the injury site are needed.

FRHCs allow for modular inclusion of topographical and soluble cues to encourage TPC migration into the injury site. Inclusion of fibrous topography has been shown to drive TPC migration and proliferation into both natural and synthetic hydrogels (Kent et al., 2022; Xie et al., 2022), likely through contact guidance whereby cells sense and respond to the anisotropic mechanics of a fibrillar microenvironment (Thrivikraman et al., 2021) (**Figure 2.4**). For example, Xie et al. developed a collagen/poly(lactic acid) hybrid fibrous scaffold that improved proliferation of rat rotator cuff and Achilles tendon-derived cells via incorporation of a cell-adhesive collagen yarn (Xie et al., 2022). Additionally, our own studies examining FRHCs containing dextran vinyl sulfone fibers embedded in a bulk hydrogel formed from dextran vinyl sulfone and crosslinked with a protease-cleavable peptide show that contact guidance cues enhance TPC migration from the epitenon of mouse Achilles tendons (Kent et al., 2022) (**Figure 2.4**). The impact of this pro-migratory cue may be further improved with an aligned fibrous topography. While the relationship between fibrous anisotropy and cell recruitment has not been studied directly in FRHCs, ECM alignment is known to influence the organization of focal adhesions and cell polarity, thereby directing cell migration (Gigante et al., 2008; W. Y. Wang et al., 2018a). More specific to tendon, Matsumoto et al. observed improved cell recruitment following implantation of a lax (disorganized) vs. straightened (aligned) rat patellar tendon graft, suggesting that fiber alignment plays a role in TPC recruitment *in vivo* (Matsumoto et al., 1998).

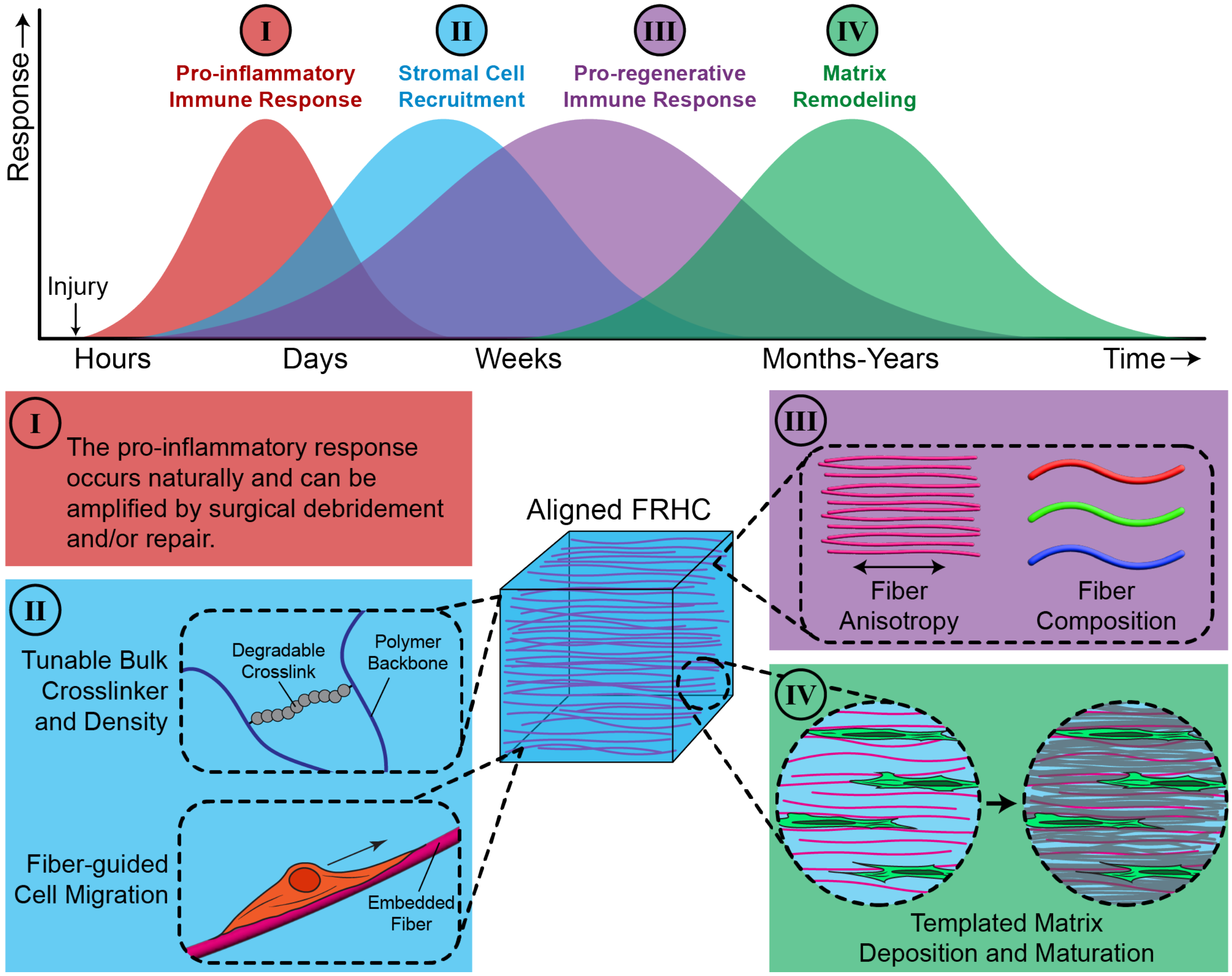
I
Pro-inflammatory Immune Response
II
Stromal Cell Recruitment
III
Pro-regenerative Immune Response
IV
Matrix Remodeling
Response
Injury
Hours
Days
Weeks
Months-Years
Time
I
The pro-inflammatory response occurs naturally and can be amplified by surgical debridement and/or repair.
II
Tunable Bulk Crosslinker and Density
Degradable Crosslink
Polymer Backbone
Fiber-guided Cell Migration
Embedded Fiber
Aligned FRHC
III
Fiber Anisotropy
Fiber Composition
IV
Templated Matrix Deposition and Maturation

Figure 2.4: Tunable physical microenvironmental features of an FRHC address key phases of tendon healing. Tunable crosslink density and degradability, in addition to fiber-guided cell migration, can be used to control recruitment of TPCs. Fiber composition and anisotropy can influence macrophage polarization. Finally, aligned fibrous topography templates deposition and maturation of aligned, *de novo* collagen fibrils.

Chemotactic and mitogenic cues can also be incorporated and delivered by FRHCs to recruit endogenous TPCs to the repair site. Previous work has shown that transforming growth factor (TGF)-β1 (Kaji et al., 2020; Yoon et al., 2018), platelet-derived growth factor (PDGF)-AB (Qu et al., 2017), PDGF-BB (Thomopoulos et al., 2007), connective tissue growth factor (CTGF) (X. Li et al., 2019a; Tarafder et al., 2019a), stromal-derived cell factor (SDF)-1 (Hocking, 2015), and periostin (Y. Wang et al., 2021b) can encourage migration and proliferation of TPCs or mesenchymal stromal cells (MSCs). In terms of biomaterial delivery applications, the most direct approach has been to mix soluble factors into a hydrogel solution prior to crosslinking (Moshiri et al., 2015; Yoon et al., 2018). While straightforward to implement, this strategy typically results in a rapid and transient release of chemotactic factors over the course of a few days. Recognizing the advantages of sustained delivery of chemotactic cues that promote TPC recruitment over the 2 weeks following injury, prior work has also explored incorporation of micro- and nano-scale delivery vehicles toward this end. Tarafder et al. used a double-emulsion technique to encapsulate CTGF in PLGA microspheres, which they 3D printed into polycaprolactone microfibers to form an implantable mesh. Gradual degradation of these microspheres following implantation yielded sustained delivery of CTGF to a rat rotator cuff defect, promoting TPC recruitment and resulting in a strong fibrocartilaginous interface at the enthesis (Tarafder et al., 2019a). Furthermore, Hettiaratchi et al. recently demonstrated the utility heparin-based delivery vehicles for sustained release of a wide range of heparin-binding soluble factors (Hettiaratchi et al., 2014; Hettiaratchi and Shoichet, 2019; Rinker et al., 2018; Subbiah et al., 2020; Zimmermann et al., 2017). Given the modular nature of FRHCs, chemokines or chemokine-laden delivery vehicles can be incorporated into the fibrous and/or bulk components of an FRHC to deliver these critical, early pro-migratory cues to the tendon injury site.

2.5.2 Driving tenogenic differentiation

To promote robust tendon regeneration, a key requirement of the engineered microenvironment within an FRHC is its ability to promote tenogenic differentiation of recruited cells. Despite the extremely high stiffness of native tendon at the macro-scale, TPCs and MSCs are sensitive to matrix elasticity and tend to favor tenogenic differentiation in softer microenvironments (Engler et al., 2006; Islam et al., 2017). Islam et al. seeded human MSCs onto compacted collagen sheets of varying stiffness, finding that 100 Mpa substrates resulted in upregulation of chondrogenic and osteogenic markers while softer (1 and 10 Mpa) substrates yielded upregulation of SCX and COL1A1 (Islam et al., 2017). Stiffer microenvironments have also been strongly associated with myofibroblastic differentiation, with previous work implicating more efficient activation of latent TGF-β1 (Wipff et al., 2007) and elevated Rho-associated kinase signaling (Akhmetshina et al., 2008; D. L. Matera et al., 2021). Together, these findings suggest that the bulk substance of an FRHC should ideally be limited to a magnitude of ~10^1 Mpa or less to effectively support tenogenic differentiation of recruited or delivered cells.

FRHCs can provide anisotropic, cell-scale physical cues that can be tuned independently of the bulk stiffness, allowing for uniaxial cell spreading and organization without the drawback of aberrant trans-differentiation common to stiffer, purely fibrous scaffolds (English et al., 2015). Fibrous topography is required to achieve an elongated morphology in recruited cells; a spindle morphology is characteristic of tenocytes in healthy tendon, and appears to be necessary for a mesenchymal progenitor cell to undergo tenogenic differentiation in post-developmental contexts (Kishore et al., 2012; Zhu et al., 2010). Topographical alignment of the matrix is thought to be another critical differentiation cue within a tendon FRHC. While there is no published data on the effect of alignment in an FRHC on tenogenic differentiation, many groups have provided evidence supporting a pro-tenogenic effect of topographical anisotropy on 2D substrates and in purely fibrous 3D settings (Baldwin et al., 2021; El Khatib et al., 2020; Islam et al., 2017; Kishore et al., 2012; G. Wu et al., 2018; S. Wu et al., 2017b; Z. Yin et al., 2010; Zhu et al., 2010). Prior studies have explored the application of aligned fibrous components in tendon FRHCs, and the presence of aligned topography in an FRHC appears to be compatible with robust tenogenesis (Deepthi et al., 2015; Nivedhitha Sundaram et al., 2019; No et al., 2020b; G. Yang et al., 2016). As such, from both a cell recruitment and a tenogenic differentiation perspective, alignment of the fibrous topography appears to be a fundamental requirement for a tendon FRHC.

Aside from static mechanical properties of the construct, uniaxial cyclic strain has been established as another important physical mediator of tenogenic differentiation. Some degree of loading on the tendon during healing appears to be critical for appropriate matrix remodeling that supports restoration of tensile strength of the repaired tissue (Kauwe, 2017; Killian et al., 2012). *In vitro* and *in vivo* models have also demonstrated the importance of externally applied load in upregulating tenogenic genes during healing (Garvin et al., 2003; Nirmalanandhan et al., 2008; Rinoldi et al., 2019a; Rinoldi et al., 2019b; Scott et al., 2011; Triantafillopoulos et al., 2004) and development (Kaji et al., 2021; Pan et al., 2018). For example, using a bioartificial tendon formed from murine MSCs cultured in a collagen hydrogel between two rigid posts, Scott et al. showed that subjecting these constructs to 10% cyclic strain at 0.1 Hz for two hours/day resulted in the upregulation of *Scx* and *Col1a1* (Scott et al., 2011). Successful mechanical integration of an FRHC with adjacent tendon stubs following implantation or in situ gelation is required for transmitting dynamic mechanical tensile cues to embedded or recruited cells during healing. Suture fixation is generally employed for solid scaffolds (Deepthi et al., 2015; No et al., 2020b), but other approaches have been explored for tendon tissue engineering. Freedman et al. developed an interpenetrating network of alginate, polyacrylamide, and chitosan that can adhere to wet tendon intraoperatively and interpenetrate the native ECM over time (Freedman et al., 2022). Our group employed a Michael-type addition chemistry that proceeds between a vinyl sulfonated dextran backbone and a dithiolated peptide crosslinker (Kent et al., 2022); as this chemistry is not selective to exogenous peptides, covalent bonds also form with thiol-containing proteins in the ECM of adjacent tissue. A completely different, innovative approach was demonstrated by Qu et al., who showed that PLGA microsphere-mediated release of collagenase resulted in better tissue-scaffold integration through early, partial degradation of the tendon stub (Qu et al., 2017).

Pro-tenogenic soluble cues can be delivered by FRHCs via the same approaches outlined above for chemokine release. Myriad growth factors including TGF-β1 (Kashiwagi et al., 2004; Rajpar and Barrett, 2019), 2 (Font Tellado et al., 2018; Sakabe et al., 2018), and 3 (Sakabe et al., 2018; Tarafder et al., 2019a); insulin growth factor 1 (Rajpar and Barrett, 2019); growth differentiation factor 5 (Font Tellado et al., 2018); PDGF-AA (Harvey et al., 2019); PDGF-BB (Chen et al., 2022; Javanshir et al., 2020); bone morphogenic protein 12 (Rajpar and Barrett, 2019); CTGF (Lee et al., 2015); and basic fibroblast growth factor (Rajpar and Barrett, 2019) have been shown to improve tenogenic differentiation of TPCs and MSCs in previous work. Inorganic, soluble tenogenic cues have also been investigated, with No et al. incorporating strontium-hardystonite (Sr-HT) nanoparticles into the bulk of a tendon FRHC (No et al., 2020b). Although Sr-HT delivery did not increase tenogenic expression, this work establishes a potential means of supplementing growth factors with inorganic soluble cues for more robust tenogenesis (**Figure 2.4**).

2.5.3 Templating aligned matrix deposition

Although FRHCs can achieve low stiffness regimes that are conducive to tenogenic differentiation, their inadequate mechanical properties relative to native tendon also necessitate the rapid deposition and organization of *de novo* collagen to achieve functional mechanical properties of the regenerated neotendon. Compared to native tendon, where fibrils exceeding 100 nm in diameter comprise ~50% of its dry mass, restoration of native fibrillar ultrastructure is limited following tendon injury such that fibers >100 nm in diameter are completely absent, even after 14 months of healing (Williams et al., 1985). Hence, physical cues that support production and maturation of collagen fibrils and template-guided collagen alignment are likely critical microenvironmental design parameters for effective tendon FRHCs (**Figure 2.4**).

The anisotropic topography of aligned FRHCs is crucial to the templating of aligned matrix deposition from implanted or recruited TPCs. Isotropic hydrogels have been shown to enhance deposition and organization of type I collagen (Breidenbach et al., 2015; Z. Yang et al., 2017), but subsequent alignment of this matrix is believed to be dependent upon externally applied loads (Nirmalanandhan et al., 2007). Cells in fibrous scaffolds and FRHCs, on the other hand, excel at generating aligned collagenous ECM independently of externally applied loads (Baker and Mauck, 2007; No et al., 2020b; G. Yang et al., 2016). For example, the fiber-reinforced PVA hydrogel designed by No. et al was infiltrated with densely aligned, mature collagen fibrils after 8 weeks of implantation in a rat patellar defect (No et al., 2020b). As an adjunct to the uniaxial strain imposed on an implanted construct *in vivo*, aligned topographical cues likely further enhance matrix production and remodeling. Fiber diameter may also influence cellular matrix remodeling behavior, but this relationship appears to be dependent on cell source. Two groups applied SES to generate aligned PLGA fibers of varying diameter and studied the resulting behavior of seeded cells; while El Khatib et al. observed higher expression of type I collagen and tenomodulin in ovine amniotic epithelial stem cells on 1.3 vs. 2.5 µm fibers (El Khatib et al., 2020), Erisken et al. saw the opposite in end-differentiated, human rotator cuff tenocytes on 0.7 vs 1.8 µm fibers (Erisken et al., 2013). Future work is needed to evaluate the interplay between fiber diameter, expression of matrix proteins and critical mediators of remodeling like tenomodulin, and maturation and organization of *de novo* collagenous matrices within FRHCs.

2.5.4 Immunomodulation

Crosstalk between stromal and immune cells, particularly macrophages, plays a key role in cell differentiation and matrix remodeling behavior during connective tissue repair (E. Chung and Son, 2014; Pajarinen et al., 2019; Sorkin et al., 2020; Y. Wang et al., 2014; Xiong et al., 2022). This topic, as it pertains to both tendinopathy and tendon healing, has been extensively reviewed elsewhere (Crosio and Huang, 2022; Sunwoo et al., 2020). Briefly, macrophages, which exist on a spectrum from M1 (pro-inflammatory) to M2 (pro-regenerative) phenotypes, can be usefully described as either "M1-like" or "M2-like" with regard to their expression of relevant signals guiding stromal cell behavior during tendon healing (Murray et al., 2014). Immediately following tendon injury in humans, M1-like macrophages invade the wound site to degrade ECM, phagocytose debris, and secrete pro-inflammatory cytokines. These cytokines cause tendon fibroblasts to secrete more pro-inflammatory cytokines, upregulate matrix metalloproteases, and downregulate genes associated with matrix production (Manning et al., 2015). At around 4 weeks following injury, M2-like macrophages begin to predominate, which secrete anti-inflammatory cytokines and promote stromal cell proliferation and matrix production (de la Durantaye et al., 2014; Sugg et al., 2014). However, at this point in the healing process, increased TGF-β1 production by M2-like macrophages is thought to drive scar tissue formation and heterotopic ossification (Sorkin et al., 2020; Wojciak and Crossan, 1993). Recently, Arvind et al. found that neonatal C57BL/6 mice, which exhibit more complete tendon regeneration compared to their adult counterparts, show increased secretion of pro-M2 cytokines at 3 days post-injury, with markedly elevated M2-like macrophages at the wound site by 14 days (Arvind et al., 2021). Collectively, these studies suggest that, while an early inflammatory response is necessary for robust tendon healing, the repair process may be improved by encouraging rapid polarization to an M2-like phenotype (**Figure 2.3**).

FRHCs can influence macrophage polarization through a range of microenvironmental cues. Although this interaction has not been studied directly in FRHCs, specific physical and biochemical features of hydrogels and pure fibrous scaffolds have been linked to M2 polarization. In hydrogel scaffolds, for example, softer materials tend to favor M2 polarization. Srindharan et al. cultured THP-1-derived macrophages in collagen-coated polyacrylamide gels of varying stiffness, showing that stiffer (323 kPa) and softer (< 88 kPa) substrates drove M1 and M2 polarization, respectively (Sridharan et al., 2019). Increased fibril density in collagen gels is also associated with M1 polarization of macrophages, although the relative contributions of increased fibril density and the coincident increase in substrate stiffness remains uncharacterized (Sapudom et al., 2020). Using electrospun poly(L-lactic acid) scaffolds, Cai et al. found that inclusion of silk fibroin in the fibers drove M2 polarization *in vitro* as well as improved biomechanical properties of rat Achilles tendons at 3 and 6 months post-injury (Cai et al., 2023) (**Figure 2.4**). Fiber anisotropy has not been shown to directly influence macrophage polarization, but it can desensitize tenocytes to pro-inflammatory cytokines secreted by M1-like macrophages, potentially posing an additional, pro-regenerative role of aligned topography in FRHCs (Schoenenberger et al., 2018)

(**Figure 2.4**). Additionally, it should be noted that many of the soluble factor delivery strategies outlined above can be applied to cytokine delivery for timed macrophage polarization. This application has not been studied for tendon regeneration, but Spiller et al. biotinylated decellularized bone scaffolds to achieve sequential delivery of M1- followed by M2-polarizing cytokines (Spiller et al., 2015). A similar, sequential polarization from an M1- to an M2-like macrophage phenotype may be applied to a tendon FRHC as well.

2.6 Conclusion and future outlook

FRHCs offer a promising strategy to positively influence the innate tendon healing response by effectively recruiting tendon progenitor cells, modulate the immune environment, drive tenogenic differentiation of recruited progenitors, and template aligned matrix deposition. The integration of mechanical, topographical, and soluble cues within FRHCs enhances their effectiveness in influencing cell behavior and tissue remodeling. Moreover, the potential for *in situ* crosslinking of FRHCs offers advantages in terms of percutaneous delivery and adaptation to the irregular geometry of ruptured tendon stubs.

However, it is crucial to acknowledge that there are translational hurdles barring clinical application of FRHCs for tendon regeneration. The mechanical properties of FRHCs, while advantageous with respect to the biological goals of tendon repair, remain mechanically inferior compared to native tendon. Balancing the trade-off between mechanical performance and biological effectiveness is therefore a key consideration in the continued development and clinical application of FRHCs. Mass transport poses another important hurdle. FRHCs have been validated *in vitro* and in small animal models, but the length scales of unrepaired human tendon defects would likely require the use of porogens or pre-vascularized constructs. These limitations may necessitate a more focused application (e.g., as an adjunct to suture repair or with limb immobilization), rather than a standalone solution for mechanically demanding scenarios.

The future of FRHCs for tendon repair holds promise in addressing the shortcomings of current treatment strategies. Ongoing research is needed to (1) further optimize cell recruitment; (2) identify and deliver physical and biochemical tenogenic cues; (3) incorporate timed soluble factory deliver vehicles for immunomodulation, stromal cell recruitment, and tenogenic differentiation; (4) improve integration with the native tendon; and (5) explore clinical translation. As these biomaterials continue to evolve, they may offer new avenues for improving outcomes of tendon injury. In a synthetic FRHC, the following thesis chapters focus on items 1-3 by co-opting fibrous topography and microgel-delivered chemokines to drive murine TPC invasion into the construct (Chapter 3), exploring the role of physical and topographical microenvironmental cues on TGF-β3-mediated tenogenic differentiation of murine TPCs and human tendon-derived cells (Chapter 4), and investigating the influence of fibrous topography on a tenogenic vs. fibrochondrogenic fate switch in murine TPCs (Chapter 5). Lastly, Chapter 6 will provide a summary of key findings from this thesis and outline future directions including improving mass transport, influencing immune polarization, and translational considerations.

Chapter 3: Physical and Soluble Cues Enhance Tendon Progenitor Cell Invasion into Injectable Synthetic Hydrogels

3.1 Authors

Robert N. Kent III, Mohamed Said, Megan E. Busch, Ethan R. Poupard, Ariane Tsai, Jingyi Xia, Daniel L. Matera, William Y. Wang, Samuel J. DePalma, Harrison L. Hiraki, Megan L. Killian, Adam C. Abraham, Jae-Won Shin, Alice H. Huang, Ariella Shikanov, Brendon M. Baker

3.2 Abstract

Synthetic hydrogels represent an exciting avenue in the field of regenerative biomaterials given their injectability, orthogonally tunable mechanical properties, and potential for modular inclusion of cellular cues. Separately, recent advances in soluble factor release technology have facilitated control over the soluble milieu in cell microenvironments via tunable microparticles. A composite hydrogel incorporating both of these components could robustly mediate tendon healing following a single injection. Here, a synthetic hydrogel system with encapsulated, electrospun fiber segments and a novel, microgel-based soluble factor delivery system achieves precise control over topographical and soluble features of an engineered microenvironment, respectively. We demonstrate that 3D migration of tendon progenitor cells can be enhanced via combined mechanical, topographical, and microparticle-delivered soluble cues in both a tendon progenitor cell spheroid model and an *ex vivo* murine Achilles tendon model. These results indicate that fiber

reinforced hydrogels can drive the recruitment of endogenous progenitor cells relevant to the regeneration of tendon and, likely, a broad range of connective tissues (**Figure 3.1**).

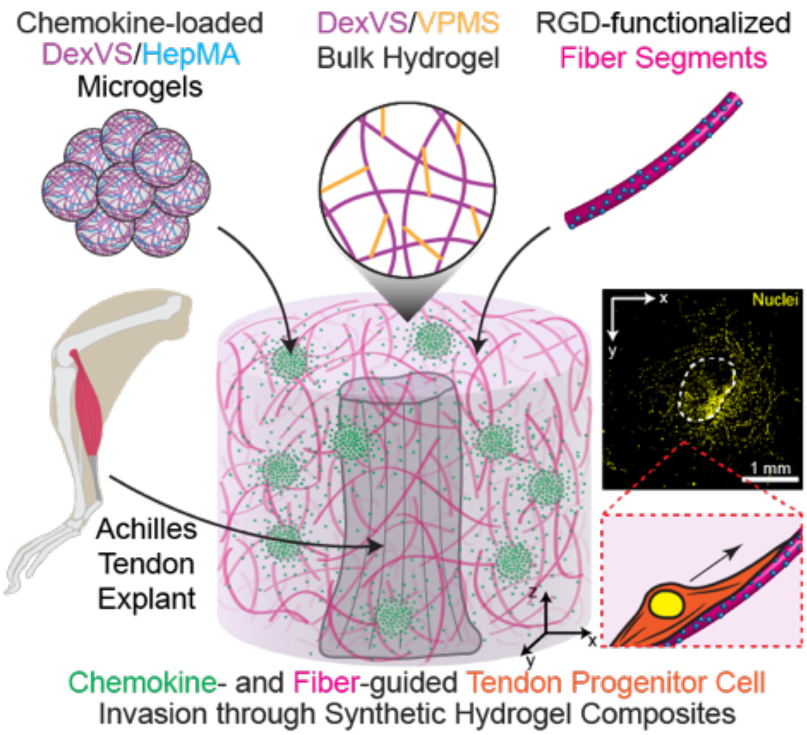
Chemokine-loaded DexVS/HepMA Microgels
DexVS/VPMS Bulk Hydrogel
RGD-functionalized Fiber Segments
Nuclei
x
y
1 mm
Achilles Tendon Explant
z
x
y
Chemokine- and Fiber-guided Tendon Progenitor Cell Invasion through Synthetic Hydrogel Composites

Figure 3.1: A composite hydrogel-based scaffold providing control over soluble and physical microenvironmental cues was designed to direct the 3D migration of tendon progenitor cells (TPCs). Microgel-mediated chemokine delivery, along with contact guidance afforded by RGD-functionalized fiber segments, promoted tendon progenitor cell invasion from *ex vivo* tendons into an injectable composite hydrogel. This material strategy offers a promising route toward augmenting tendon repair and, likely, that of a range of other connective tissues.

3.3 Introduction

In the United States, 124 million cases of musculoskeletal injury are reported annually, with an overall financial burden > 5% of the GDP (*United states bone and joint initiative: The burden of musculoskeletal disease in the united states, fourth edition*, 2016). Tendon and ligament injuries comprise an estimated 45% of these cases (Praemer et al., 1999). In particular, the Achilles tendon (AT) is one of the most commonly injured (~30,000 cases annually) given its enormous mechanical demands, especially during sports activity (Lemme et al., 2018). Current treatment options for AT rupture include surgical approximation of the tendon stubs or the conservative route of temporary immobilization and rehabilitation; unfortunately, both treatment options end in comparably poor patient outcomes with regard to functional restoration, return to pre-injury levels of activity, chronic pain, and heightened risk of reinjury (Lantto et al., 2016; Nilsson-Helander et al., 2010). These poor outcomes are largely attributed to the generation of disorganized, hypervascularized, hypercellular scar tissue lacking the architecture and mechanical properties necessary to meet the functional demands of the tendon (Józsa and Kannus, 1997; Killian et al., 2012). Thus, restoration of native tendon composition and architecture following AT rupture would dramatically improve patient outcomes and reduce the significant economic burden of these injuries (James et al., 2008).

Despite possessing a population of tendon progenitor cells (TPCs) in the epitenon, injured tendons fail to recruit or properly differentiate these progenitors (Best et al., 2021; Best and Loiselle, 2019; Harvey et al., 2019; Howell et al., 2017; Jones et al., 2003; Sharma and Maffulli, 2006; F. Wu et al., 2017a). Therefore, therapies that can influence the identity and quantity of repair cells recruited to the injury site are likely required for the regeneration of functional tendon in lieu of dysfunctional scar tissue. While injection and suture-based delivery of drugs and biologics such as growth factors, platelet-rich plasma, and stem cells have shown some promise, these approaches lack the spatiotemporal control required for regenerating the tendon's native architecture (de Vos et al., 2010; Efird et al., 2018; Font Tellado et al., 2015; Tarafder et al., 2019b; Tempfer et al., 2018). To address this problem, efforts have shifted toward tissue constructs engineered to recapitulate the biomechanical and topographical properties of tendon. However, even with aligned topography, materials whose tensile moduli approach that of native tendon can promote aberrant differentiation of progenitors towards chondrogenic or osteogenic lineages (English et al., 2015; Qu et al., 2017; Tarafder et al., 2019a; Y. Wang et al., 2021b; Yoon et al., 2018).

Synthetic hydrogels represent an exciting approach to tissue repair-mediating biomaterials that can be localized to an internal wound defect through minimally invasive administration. Typically composed of polymer chains crosslinked into a solid bulk by protease-cleavable peptides, these materials also benefit from tunable and modular inclusion of biochemical moieties in addition to tailorable mechanical properties (D.L. Matera et al., 2019). However, optimizing physical cues to permit cell infiltration while still maintaining the mechanical properties required for a musculoskeletal implant remains challenging (No et al., 2020a; Tatara and Mikos, 2016). Analogous to rebar-reinforced concrete, synthetic fibers can mechanically reinforce hydrogels by increasing their tensile strength with the added benefit of providing topographical cues that guide 3D cell migration and spreading (Baker and Mauck, 2007; D.L. Matera et al., 2019; No et al., 2020a). Separately, recent advances in soluble factor release technology have demonstrated heparin microparticle-mediated, sustained release of growth factors. Through affinity interactions that reversibly bind and stabilize growth factors and chemokines, heparin-based particles circumvent the issue of burst release associated with typical microparticle-based delivery systems (Hettiaratchi et al., 2014; Hettiaratchi and Shoichet, 2019; Rinker et al., 2018; Zimmermann et al., 2017). A composite hydrogel incorporating tunable fibrous topography and soluble factor delivery could mediate tendon regeneration with a single injection.

Here, we developed a synthetic mimic of the provisional matrix that forms shortly after AT rupture to assess whether the recruitment of tendon progenitor cells (TPCs) can be enhanced via combined mechanical, topographical, and microparticle-delivered soluble cues. We formed hydrogels from vinyl sulfonated dextran (DexVS) crosslinked with an MMP-labile peptide and imbued this microenvironment with topographical cues by incorporating electrospun DexVS fiber segments (D.L. Matera et al., 2019). This material approach facilitated orthogonal tuning of fibrous topography and bulk mechanics, both of which influences TPC invasion. Monodisperse populations of hybrid DexVS microgels with covalently incorporated heparin were then fabricated to release PDGF-BB, a chemokine that potently induces TPC migration. Using this material platform, we found that recruitment of murine TPCs into DexVS hydrogels was enhanced by fibrous topographical cues and microgel-delivered PDGF-BB. These cues translated effectively to an *ex vivo* model of TPC recruitment from the epitenon of explanted murine ATs.

3.4 Results and discussion

3.4.1 PDGF-BB drives TPC invasion into DexVS hydrogels

For efficient screening of microenvironmental conditions that promote TPC recruitment, we chose a spheroid model given its throughput and clear demarcation of initial cell positions relative to final positions following cellular outgrowth (Hiraki et al., 2021; Y. C. Huang and Liu, 2012; D. L. Matera et al., 2021; Vinci et al., 2015). Previous work has explored the role of various chemokines on the recruitment of TPCs during development and healing *in vivo* in addition to scratch and transwell migration assays *in vitro* (Kaji et al., 2020; Qu et al., 2017; Sugg et al., 2018). Using this prior work as a starting point, we tested a panel of known chemokines comprised of transforming growth factor (TGF)-β1, stromal cell-derived factor (SDF)-1α, and platelet-derived growth factor (PDGF)-BB for their ability to recruit TPCs into synthetic, cell-degradable DexVS/VPMS hydrogels (**Figure 3.2A**). A range of doses (media supplemented with 10-100 ng mL^{-1}) was tested for each chemokine. Independent of dose, PDGF-BB was the only soluble cue capable of driving 3D TPC invasion into synthetic hydrogel matrices, as evidenced by increased outgrowth area, number of migrating cells, and total migration distance (**Figure 3.2B-E**). This result was unexpected given the range of contexts in which TGF-β1 and SDF-1α have previously been shown to promote TPC recruitment (Kaji et al., 2020; Qu et al., 2017). Previous work has implicated increased matrix metalloproteinase (MMP) production, which facilitates extracellular matrix (ECM) degradation, in the mechanism of PDGF-induced cell migration (Lim et al., 2017). Therefore, our observation that solely PDGF-BB induces TPC migration into MMP-cleavable DexVS/VPMS hydrogels may stem from the nanoporosity of these materials (D.L. Matera et al., 2019), 3D migration through which necessitates enhanced protease activity and cytoskeletal remodeling (Mellstrom et al., 1988; Tidball and Spencer, 1993) compared to 2D and *in vivo* settings.

Since PDGF-BB has previously been demonstrated to act as both a chemokine and a mitogen (Bornfeldt et al., 1995; Cochran et al., 1983; Seppa et al., 1982), we next investigated the extent to which these two distinct cell functions contributed to TPC outgrowth from spheroids in synthetic hydrogels. A higher proportion of cells were positive for Ki67 immunostaining with PDGF-BB treatment compared to vehicle controls (**Figure 3.2F,G**), indicating that PDGF-BB-mediated proliferation may contribute to the increased number of invading cells. To confirm the role of proliferation in PDGF-BB-driven cell invasion, cell division was pharmacologically blocked by mitomycin C treatment prior to spheroid formation and encapsulation. Strikingly, inhibiting cell proliferation completely abrogated enhanced outgrowth in response to PDGF-BB (**Supplemental Figure 3.1**). Taken together, these results indicate that PDGF-BB-induced proliferation is a key component of TPC outgrowth into synthetic hydrogels, challenging the classical paradigm that cell migration and proliferation represent mutually exclusive cell functions (W. Y. Wang et al., 2020).

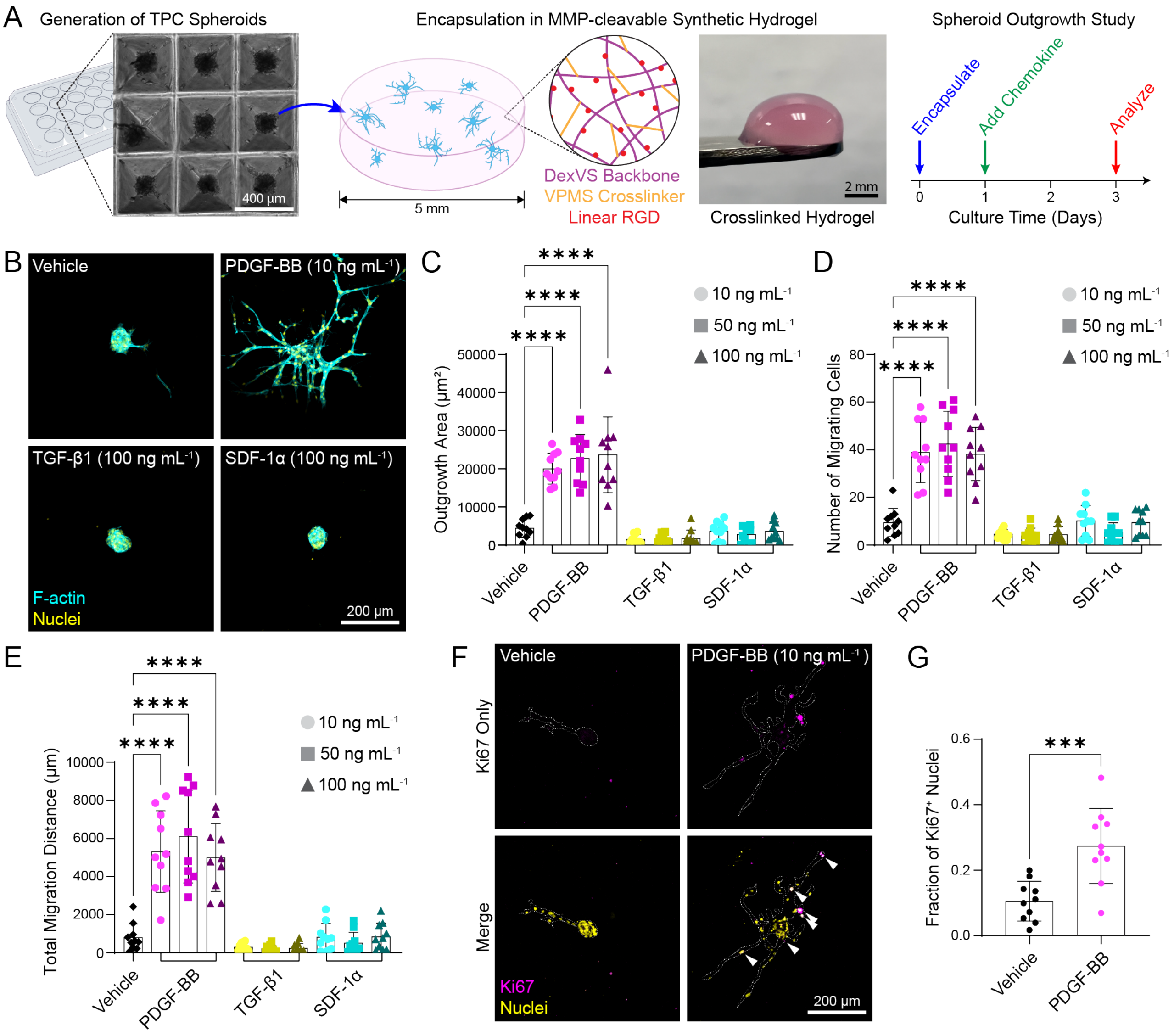

Figure 3.2: PDGF-BB enhances TPC invasion into synthetic hydrogels. A) Experimental schematic; TPC spheroids were encapsulated in a 0.5 kPa DexVS/VPMS hydrogel,(D. L. Matera et al., 2020) and outgrowth proceeded for three days before fixation, with chemokine supplementation on day 1. **B**) Confocal fluorescent images of spheroid outgrowth, varying chemokine identity and concentration. Quantification of (**C**) spheroid outgrowth area (μm^2), (**D**) number of migrating cells, and (**E**) total migration distance (μm) (n = 10 spheroids, N = 2). **F**) Confocal fluorescent images of spheroids stained for Ki67, with dotted white lines delineating cytoplasmic boundaries. White arrowheads indicate Ki67$^+$ nuclei in the merged panels. **G**) Quantification of the fraction of Ki67$^+$ nuclei (n = 10). All data are presented as mean ± standard

deviation. Asterisks indicate statistically significant comparisons, with ***p<0.001 and ****p<0.0001 by ordinary one-way ANOVA with Tukey's multiple comparisons test or Student's t-test.

3.4.2 Fibrous topography enhances PDGF-BB-driven TPC invasion

Nanoporous synthetic hydrogels can support cell migration and are ideal for minimally invasive therapeutic administration via injection. However, in contrast to native ECM, these amorphous materials lack cell-scale fibrous topography, which is known to impact cell spreading and migration (Baker et al., 2012; D.L. Matera et al., 2019; Trappmann et al., 2017). Therefore, we explored the effect of incorporating synthetic, cell-adhesive fibers on TPC spheroid outgrowth in a DexVS hydrogel. DexVS fiber segments were electrospun and functionalized with RGD to enable cell adhesion required for migration and contact guidance (**Figure 3.3A**). The surrounding DVS bulk hydrogel was functionalized with RGD as well to allow TPCs to adhere, spread, and migrate independently of additional fibrous guidance queues. In the presence of 10 ng mL^{-1} PDGF-BB, inclusion of cell-adhesive fibers led to marked increases in cell outgrowth compared to non-fibrous controls. This result is intuitive given the well-described role of contact guidance in cell spreading and migration, where cells sense and respond to the anisotropic mechanics and topography of cell-adhesive fibrillar ECM (Thrivikraman et al., 2021). Incorporating synthetic fiber segments provides anisotropic mechanical cues in an otherwise isotropic hydrogel, likely facilitating contact-guided, 3D cell migration into the construct (D. L. Matera et al., 2021).

To evaluate the effect of bulk crosslinking on fiber-guided TPC migration, hydrogels were crosslinked with 12.5 or 20.0 mM VPMS to achieve bulk stiffnesses of ~0.5 or 2.0 kPa, respectively (D. L. Matera et al., 2020). Importantly, and in contrast to those of natural hydrogels, topographical cues in this system can be tuned independently of bulk mechanical properties (D. L. Matera et al., 2020; D.L. Matera et al., 2019). While increasing crosslinking density led to a general attenuation in migration, outgrowth in more densely crosslinked (20 mM VPMS) gels was partially rescued at the highest fiber density tested (**Figure 3.3B-E**). These results suggest that a minimum threshold of fiber density may be required at a given bulk crosslinking density such that the contact guidance cues are readily accessible to encapsulated cells. In the interest of eventually pursuing *in vivo* applications of this biomaterial system in mechanically demanding tissue spaces (Tatara and Mikos, 2016; Trappmann et al., 2017), we screened TPC outgrowth as a function of VPMS concentration to find that 15 mM VPMS is the threshold above which migration is significantly limited in nonfibrous hydrogels (**Supplemental Figure 3.2**). Subsequent outgrowth studies were thus performed in bulk hydrogels formed at 15 mM VPMS.

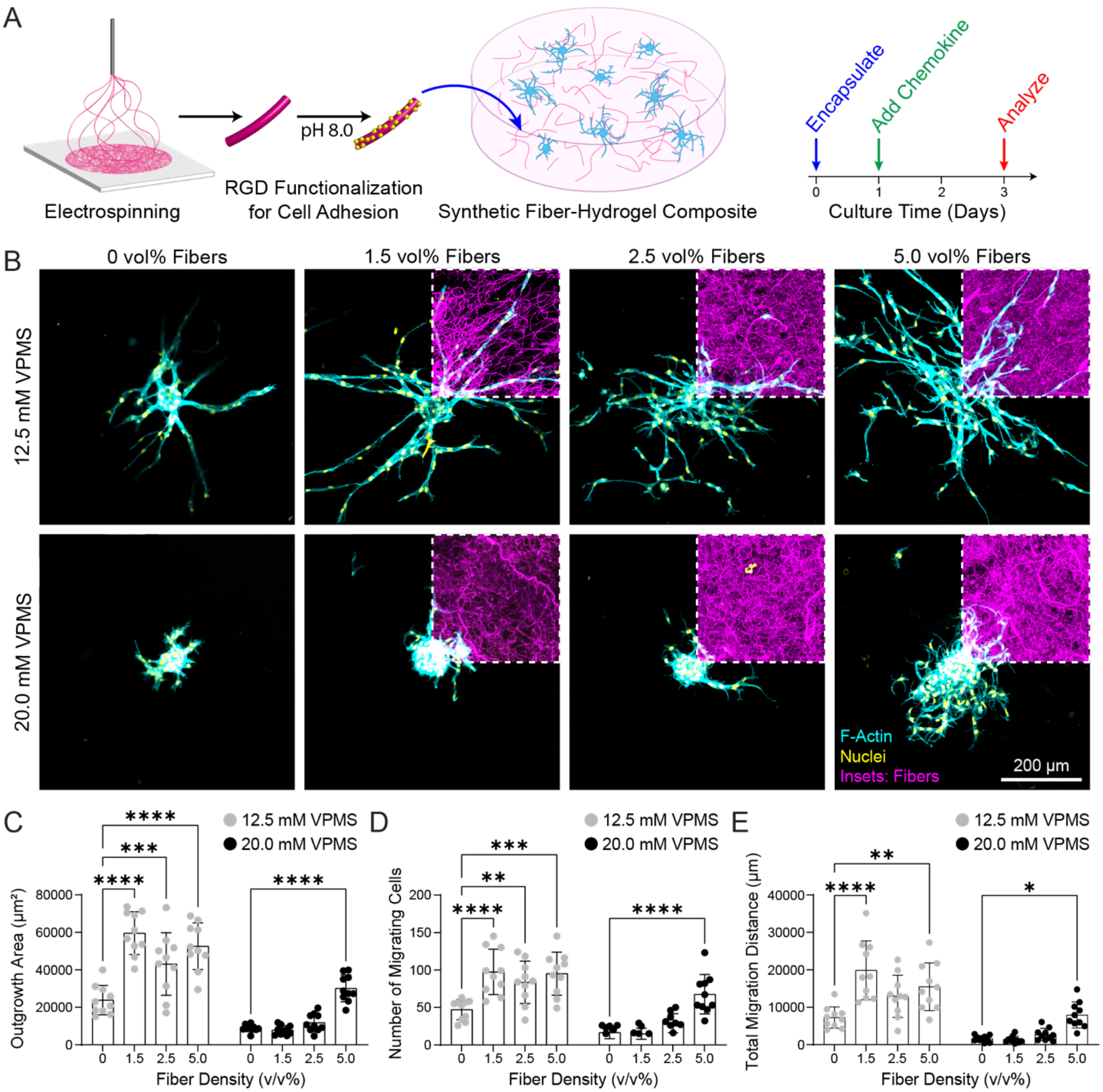

Figure 3.3: Fibrous topography enhances TPC invasion. A) Experimental schematic; DexVS fibers were electrospun, functionalized with cell-adhesive RGD, and co-encapsulated with TPC spheroids in a DexVS/VPMS hydrogel; following encapsulation, all samples were supplemented with PDGF-BB on day 1, and outgrowth proceeded until fixation on day 3. **B**) Confocal fluorescent images of TPC spheroid outgrowth, varying fiber density and bulk stiffness. Quantification of (**C**) TPC spheroid outgrowth area (μm^2), (**D**) number of migrating cells, and (**E**) total migration distance (μm) (n = 10, N = 2). All data are presented as mean ± standard deviation. Asterisks indicate statistically significant comparisons, with **p<0.01, ***p<0.001, and ****p<0.0001 by ordinary two-way ANOVA with Tukey's multiple comparisons test.

We hypothesized that removing RGD from the bulk hydrogel would maximize the capacity of topographical cues on guiding cell migration, as cells would only be able to form adhesions on the encapsulated fibers. However, by repeating spheroid outgrowth studies in fibrous DexVS hydrogels with the bulk hydrogel functionalized with a scrambled sequence (CRDGS, i.e., RDG), we found that the presence or absence of adhesive moieties in the bulk hydrogel had no impact on fiber-mediated outgrowth (**Supplemental Figure 3.3**). The finding that fibrous topography can promote 3D TPC migration suggests that aligned 3D topography may improve alignment of recruited TPCs (Hiraki et al., 2021) and, possibly, alignment of *de novo* ECM (Baker and Mauck, 2007; Y. Wang et al., 2021b). Thus, anticipating future work that will investigate the effects of aligned fibrous topography on cell and *de novo* ECM organization, we used the RDG-functionalized bulk hydrogel in all subsequent outgrowth studies.

3.4.3 Hybrid DexVS/HepMA microgels enable tunable release of TPC chemokines

Achieving gradual release of chemokines is paramount for eventual *in vivo* translation of this material system, which would ideally only involve a single transcutaneous or intraoperative administration. Having identified a chemokine that robustly mediates TPC proliferation and migration, we next incorporated PDGF-BB into microgels to mediate gradual release of this factor to drive TPC recruitment. Given that the rate of soluble factor release is theoretically dependent on microparticle geometry (Ritger and Peppas, 1987a, 1987b), high-throughput generation of spherical microgels with controlled and monodisperse diameters is critical. Therefore, we fabricated microfluidic droplet-generating devices possessing defined geometries to generate spherical microgels over a range of diameters (**Figure 3.4A-B**) (Hati et al., 2016; Mao et al., 2017; Utech et al., 2015).

Heparin-based delivery vehicles can prolong the release of heparin-binding soluble cues in cell microenvironments, preventing the burst release associated with traditional soluble factor delivery vehicles (Hettiaratchi et al., 2014; Hettiaratchi and Shoichet, 2019). To take advantage of heparin's known affinity for a wide range of chemokines and growth factors, including PDGF-BB (Hettiaratchi et al., 2014; Hettiaratchi and Shoichet, 2019; Rinker et al., 2018; Sakiyama-Elbert and Hubbell, 2000; Subbiah et al., 2020; Zimmermann et al., 2017), we fabricated hybrid microgels by covalently incorporating methacrylated heparin (HepMA) into DexVS microgels via photoinitiated crosslinking (**Figure 3.4C**) (Davidson et al., 2020a), Microgels (150-µm diameter) containing 1, 5, and 10 wt/v% HepMA were loaded at 250 ng mL^{-1} with PDGF-BB and assayed by ELISA for PDGF-BB release over the course of one week. HepMA incorporation led to a marked attenuation in PDGF-BB release rate (**Figure 3.4D**). Increasing DexVS weight percent above 10 wt/v%v resulted in a slower release rate, likely due to decreased pore size, but not nearly to the extent of HepMA inclusion (**Figure 3.4E**). Microgel size and chemokine loading duration showed no effect, whereas doubling the chemokine loading concentration resulted in equivalent release profiles in terms of the fraction of loaded PDGF-BB, enabling facile control over the absolute mass of delivered payload (**Supplemental Figure 3.4**). Together, these results demonstrate that affinity interactions between sulfate-rich heparin and positively charged PDGF-BB dictate the rate of release, rather than the steric hindrance traditionally associated with drug-delivering biomaterials (Datta et al., 2014; Ionescu et al., 2010; Mohanraj et al., 2019; Singh et al., 2010; Wong et al., 2018). Importantly, this delivery vehicle can be employed for a wide range of soluble factors to drive chemotaxis, differentiation, or immunomodulation so long as they carry a positive charge in physiologic conditions (Hettiaratchi et al., 2014; Hettiaratchi and Shoichet, 2019; Rinker et al., 2018; Sakiyama-Elbert and Hubbell, 2000; Subbiah et al., 2020; Zimmermann et al., 2017).

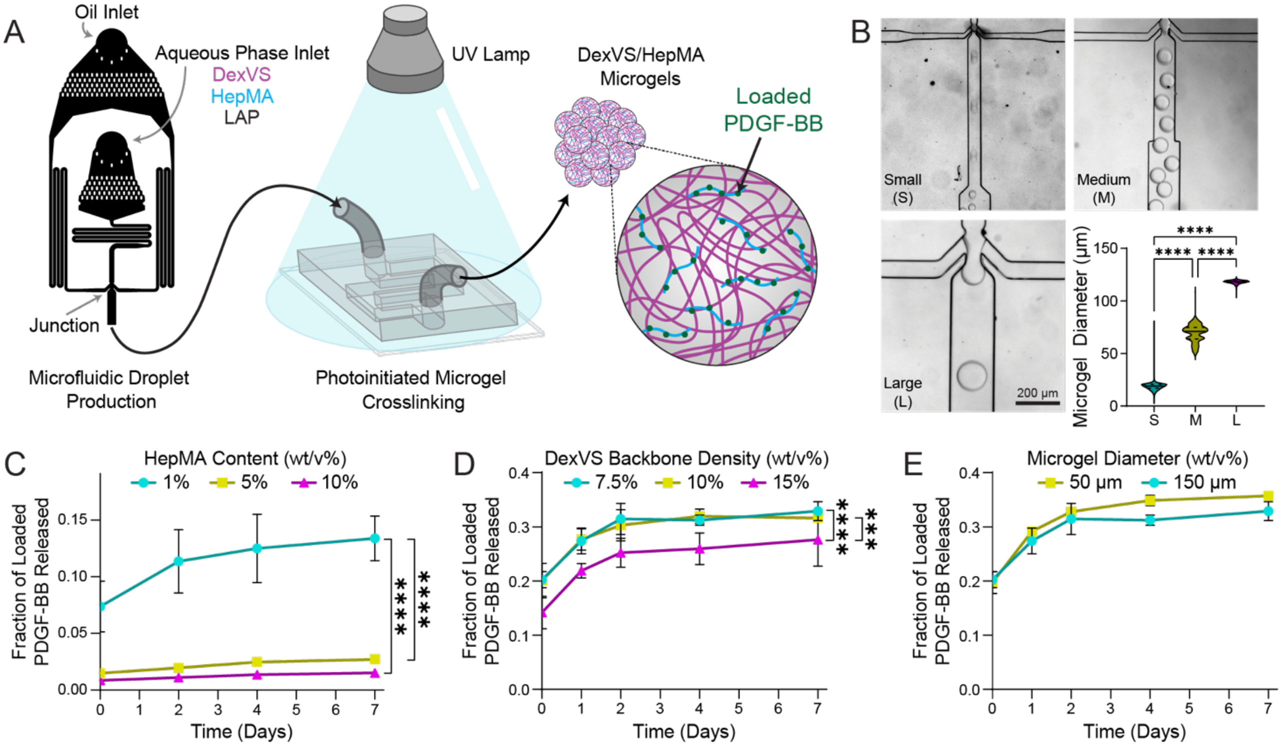

Figure 3.4: Heparin content dictates soluble factor release kinetics from hybrid microgels. A) AutoCAD rendering of a microfluidic device design for generating and photo-crosslinking monodisperse DexVS/HepMA microgels. **B**) Images of varying droplet diameter as a function of channel geometry and quantification of droplet diameters (Small n = 13,827, Medium n = 476, Large n = 1,748) (solid horizontal line denotes median; dashed lines denote Q1 and Q3). **C**) PDGF-BB released from hybrid microgels over time, varying HepMA wt/v%, (**D**) DexVS wt/v%, and (**E**) microgel diameter (all n = 2) (data presented as mean ± standard deviation). Asterisks indicate statistically significant comparisons, with ***$p<0.001$ and ****$p<0.0001$ by ordinary one-way ANOVA with Tukey's multiple comparisons test.

3.4.4 Computational modeling predicts microgel-mediated delivery of chemokines by hybrid microgels

To better understand chemokine release kinetics from hybrid microgels encapsulated in a bulk hydrogel, we developed a model in COMSOL representing a 10x field of view centered on a cell spheroid with surrounding microgels incorporated at a density of 2.5 v/v% (**Figure 3.5A**). Varying the fluid diffusion coefficient of microgels ($D_{\mu G}$) as a surrogate for HepMA content, with lower $D_{\mu G}$ values reflecting higher HepMA concentration, we first explored the effect of $D_{\mu G}$ and the diffusion coefficient of the bulk hydrogel (D_B) on the formation of chemokine concentration gradients adjacent to the cell spheroid. This screen suggests that varying HepMA concentration can impact chemokine gradients over three days, but only within a D_B range of 10^{-12} to 10^{-14} m^2 s^{-1} (**Figure 3.5B**). Previous work has measured the diffusion coefficient of DexVS/VPMS hydrogels 10^{-16} to 10^{-15} m^2 s^{-1}, but these values were determined by diffusion of fluorescent dextran (W. Y. Wang et al., 2021a). Given that PDGF-BB is a globular protein (and not a linear polysaccharide), we expect D_B here to be above this range. For all subsequent perturbations, we set D_B and $D_{\mu G}$ to 10^{-12} and 10^{-15} m^2 s^{-1}, respectively. Randomly re-arranging the microgels suggested that microgel distribution has no effect on chemokine gradients (**Figure 3.5C,D**), an important observation given the stochastic nature of microgel encapsulation within hydrogel composites. Finally, we varied microgel diameter, keeping the density of microgels constant at 2.5 v/v%. The model, contrasting our ELISA data (**Figure 3.4E**), indicates that 50-µm microgels produce a steeper gradient compared to 150-µm microgels (**Figure 3.5E,F**).

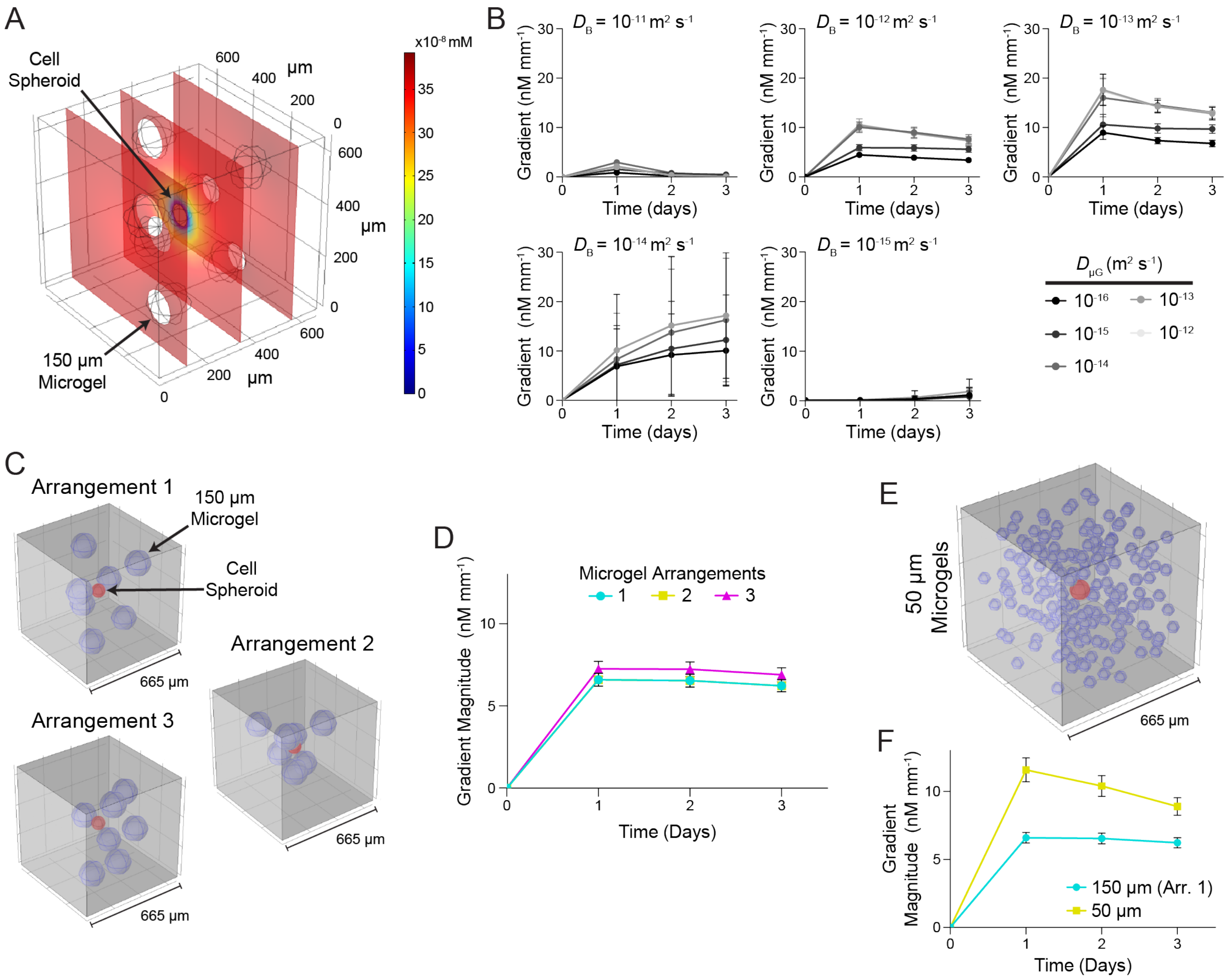

Figure 3.5: Computational model predicts release kinetics from hydrogel-encapsulated microgels. A) Rendering of spatial distribution of chemokine (150-µm microgels incorporated at 2.5 v/v%) on day 3, with bulk (D_B) and microgel ($D_{\mu G}$) diffusion coefficients set to 10^{-12} and 10^{-15} $m^2\ s^{-1}$. **B**) Gradient of chemokine concentration (nM mm^{-1}) over the first 20 microns adjacent to the TPC spheroid boundary across a range of D_B and $D_{\mu G}$ over a 3-day period. **C**) Renderings of model geometries with the microgel distribution in (A) and (B) (Arrangement 1) and two additional random arrangements, with cell spheroids shown in red and hybrid microgels shown in blue. **D**) Gradient quantification of arrangements in (C). **E**) Rendering of model geometry with 50-µm microgels incorporated at 2.5 v/v%. **F**) Gradient magnitude of the model in (**E**) compared to Arrangement 1 from (C). All data are presented as mean ± standard deviation. n = 6 radial directions for all gradient measurements.

3.4.5 Microgel-delivered PDGF-BB induces TPC invasion into composite hydrogels

Given our *in vitro* and *in silico* observations that HepMA incorporation critically governs the rate of soluble factor release from hybrid microgels, we explored the effect of HepMA content on TPC recruitment in a novel, composite hydrogel that facilitates simultaneous control over topographical and soluble features of the microenvironment. Hybrid microgels (150-µm diameter) containing varying amounts of HepMA were loaded with PDGF-BB at 500 ng mL^{-1} and incorporated into hydrogels at 2.5 v/v%. To evaluate the effect of microgel-mediated, sustained delivery of PDGF-BB on spheroid outgrowth, we included a condition lacking microgels where soluble PDGF-BB was instead added directly to the media (10 ng mL^{-1}) immediately following encapsulation and again on day 2. These studies demonstrated that microgels containing 5 wt/v% HepMA result in more outgrowth compared to both the vehicle and soluble PDGF-BB groups (**Figure 3.6A-E**). To visualize the microgels and determine to what extent migrating cells physically interact with them, microgels were fluorescently labeled with fluorescein. High magnification imaging revealed that invading cells recruited and migrated along fiber segments, traveling around rather than on or through the microgels (**Figure 3.6F**). This observation was not surprising given that photo-crosslinked DexVS is not proteolytically cleavable, and microgels were not functionalized with cell-adhesive ligands. Considering the possibility that sequestration of cell-secreted factors (Hettiaratchi et al., 2014) is responsible for enhanced TPC recruitment relative to that elicited by soluble PDGF-BB (**Figure 3.6B-E**), we performed an additional experiment with non-loaded microgels and found that heparin content alone has no effect on TPC invasion (**Supplemental Figure 3.5A-D**). These results, in conjunction with our finding that TPC outgrowth is insensitive to PDGF-BB concentration (**Figure 3.2B-E**), strongly indicate that microscale, spatial organization of soluble factor presentation (Pruett et al., 2021) is responsible for the observed enhancement in cell recruitment.

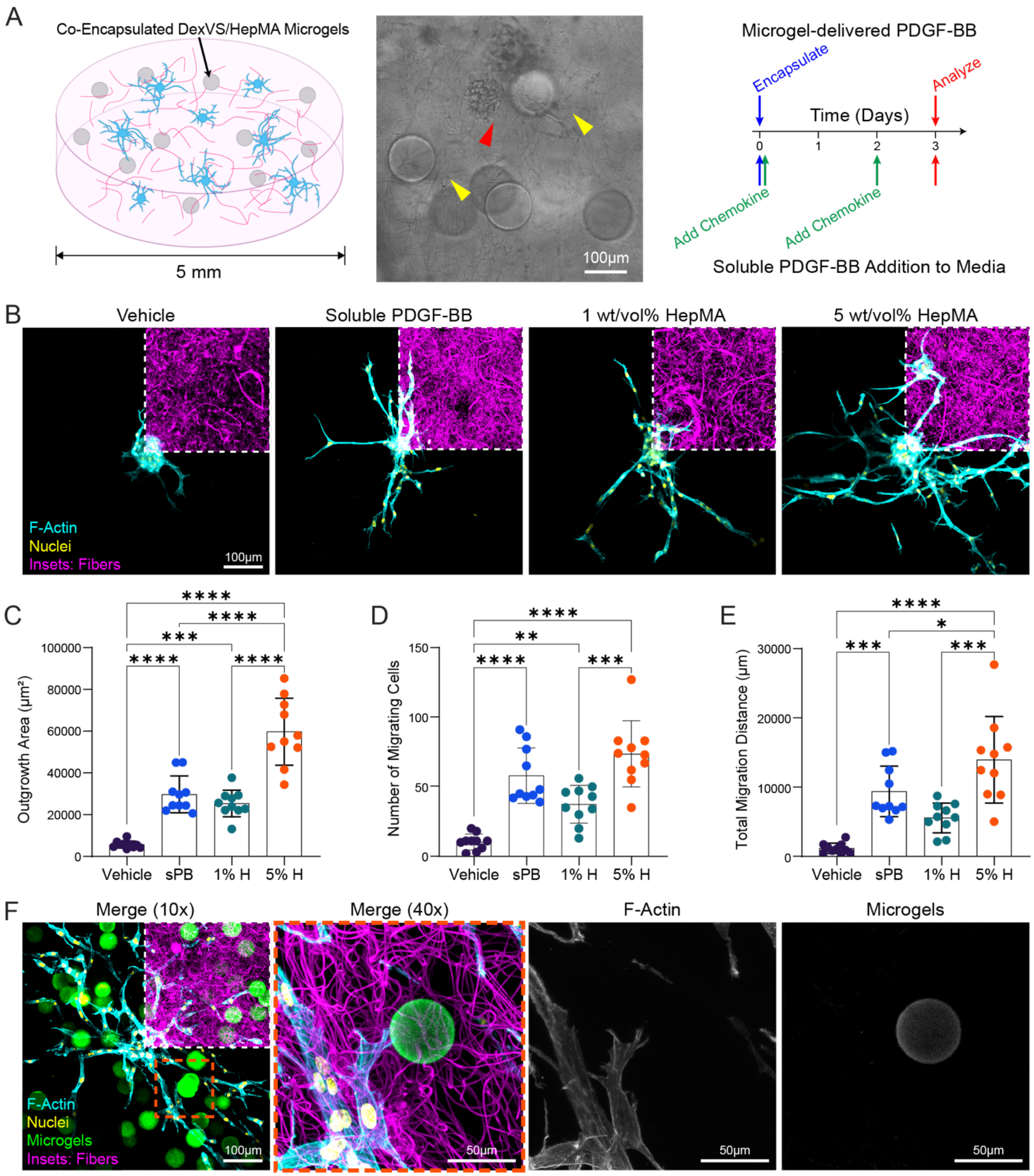

Figure 3.6: Microgel-delivered PDGF-BB drives 3D TPC invasion. A) Experimental schematic; brightfield image of spheroids (red arrowhead) and microgels (yellow arrowheads); timeline of cell encapsulation, chemokine addition for the soluble PDGF-BB condition, and fixation. **B**) Confocal fluorescent images of TPC outgrowth in response to basal media (Vehicle), soluble PDGF-BB (sPB), and PDGF-BB released from microgels containing 1 (1% H) or 5 (5% H) wt/v% HepMA. Quantification of (**C**) TPC outgrowth area (µm^2), (**D**) number of migrating

cells, and (**E**) total migration distance (μm) (n = 10, N = 2). (**F**) TPC outgrowth in response to PDGF-BB released from fluorescein-labeled microgels (5 wt/v% HepMA); orange dotted line in the 10x merge (650-μm z-range) denotes region displayed in the 40x images (100-μm z-range). All data are presented as mean ± standard deviation. Asterisks indicate statistically significant comparisons, with $^*p<0.05$, $^{**}p<0.01$, $^{***}p<0.001$, and $^{****}p<0.0001$ by ordinary one-way ANOVA with Tukey's multiple comparisons test.

Future pre-clinical studies in rodents aiming to repair tendon injuries will require small volumes (~3-5 μL) of hydrogel solution crosslinked *in situ*. The inclusion of smaller microgels would improve homogeneity of the injected material, with a more consistent number of microgels delivered upon injection. The ELISA and computational data differed on the effect of microgel size on soluble factor release profile (**Figure 3.4E, 3.5F**), and so we evaluated the effect of microgel size on spheroid outgrowth by incorporating 50- or 150-μm, PDGF-BB-laden microgels at 2.5 v/v%. Contrasting the computational model (**Figure 3.5**), we observed minimal differences in TPC invasion as a function of microgel size (**Supplemental Figure 3.5E-H**). A likely explanation for this disparity may be that the two microgel diameters result in unequal but sufficient PDGF-BB delivery to augment TPC outgrowth, especially given that this outgrowth is stimulated over a range of non-zero concentrations when added directly to the media (**Figure 3.2B-E**).

A key benefit of this material system is its injectability. At minimum, as an adjunct to open surgical repair of an injured tendon, injectability (as compared to a pre-formed hydrogel graft) would allow the material to completely fill the intricate geometry of a tendon defect, maximizing the interface between the hydrogel and adjacent tissues to facilitate TPC recruitment and regeneration. For non-operative management following tendon rupture (Soroceanu et al., 2012), this material could be a delivered through a minimally invasive, transcutaneous injection at the site of the defect. Ultrasound guidance may be required in this case, but ultrasound-guided injections are already a clinical standard in the treatment of Achilles tendinopathy (Drakonaki et al., 2016). Despite the low viscosity of our material system prior to crosslinking, the inclusion of suspended fiber segments and microgels may complicate its injectability. Therefore, to demonstrate injectability of the composite system, we delivered a DexVS/VPMS gel mixture containing 2.5 v/v% each of fiber segments and 50-µm microgels through a 25-gauge needle into a mold with complex geometry, where it crosslinked to form a hydrogel (**Supplemental Figure 3.6**). Of note, confocal imaging of molded hydrogels showed no evidence of damage to either microgels or fibers nor alterations to their random distribution following injection.

3.4.6 Microgel-delivered PDGF-BB drives TPC recruitment from the Achilles tendon

The physical and soluble cues studied above showed robust migratory responses in a TPC spheroid model, which was ideal for screening a wide parameter space given its high throughput and ease of assessment. However, utility of these cues requires validation in a more relevant model of cell recruitment from native tendon. Since previous studies have demonstrated a population of TPCs residing in the epitenon with tenogenic potential (Harvey et al., 2019), we immunostained axial sections of adult (8-12 week) mouse AT and confirmed the presence of stem cell antigen (Sca)-1-positive progenitor cells in the epitenon (**Figure 3.7A**). We then established an *ex vivo* model of TPC recruitment from ATs explanted from adult Scleraxis (Scx)-GFP reporter mice. These genetically engineered mice were used to assess whether biomaterial-recruited TPCs possess tenogenic potential, as Scx is a well-established early tenogenic transcription factor (Best and Loiselle, 2019; Howell et al., 2017; A. H. Huang et al., 2015; Sakabe et al., 2018). Mouse ATs were halved at the midsubstance and encapsulated in fibrous (2.5 v/v% fiber density) hydrogel composites to study the effect of PDGF-BB delivered by 50-μm microgels containing 5 wt/v% HepMA (**Figure 3.7B,C**).

Progenitor cell recruitment during tendon healing *in vivo* is known to occur over the first 1-2 weeks following injury (Sharma and Maffulli, 2006; F. Wu et al., 2017a). To examine whether a different cell/tissue geometry influences microgel-generated PDGF-BB release over a relevant timeframe, we modified the COMSOL model to represent a 10x field of view adjacent to the surface of a mouse Achilles tendon explant and simulated release over a 10-day period. In contrast to the spheroid model, which produced a steady chemokine gradient over three days, the gradient in the tendon explant model demonstrated exponential decay over the 10-day period (**Figure 3.7D,E**), likely stemming from a higher magnitude of flux into the tendon explant compared to that of the smaller cell spheroid. To isolate the effect of the microgels themselves, we evaluated a model containing no microgels but with the initial condition of a uniform distribution of PDGF-BB throughout the hydrogel. Even though the initial concentration of PDGF-BB was equal to the average initial concentration taken across the volume of the microgel model (12.5 ng mL^{-1}), microgel-mediated delivery yielded a >3-fold higher PDGF-BB gradient at all timepoints (**Figure 3.7E**).

Our findings *in silico* motivated four experimental conditions for the *ex vivo* model: (1) a vehicle control, (2) soluble PDGF-BB replenished in the media every 48 hours (10 ng mL^{-1}), (3) PDGF-BB mixed into the hydrogel bulk prior to gelation at 12.5 ng mL^{-1} (same total input mass of PDGF-BB as in group 4), and (4) microgel-delivered PDGF-BB (loaded at 500 ng mL^{-1}, and incorporated at 2.5 v/v%). During healing, the majority of TPCs are likely recruited from the region of epitenon adjacent to the wound site (Best et al., 2021; Best and Loiselle, 2019; Sharma and Maffulli, 2006; F. Wu et al., 2017a), and so only the first 500 μm of tissue adjacent to the transection site was considered. This focused analysis also sought to maintain equivalence of proximal and distal segments. Over the course of 10 days, TPC invasion from explanted murine ATs was strongly encouraged by microgel-delivered PDGF-BB, on par with a condition where soluble PDGF-BB was replenished at 48-hour intervals (**Figure 3.7F-H; Supplemental Figure 3.7**). In agreement with the computational model, an initial, uniform distribution of PDGF-BB resulted in minimal TPC outgrowth, similar to the vehicle control. However, in contrast to the 3-day spheroid outgrowth model, TPC recruitment in response to microgel-delivered PDGF-BB did not exceed that of the soluble PDGF-BB condition, implying that depletion of microgel payload over the 10-day period negated any beneficial effects garnered from spatially organized delivery (Pruett et al., 2021).

For invading TPCs to contribute productively to the repair process following tendon injury, at minimum, it is critical that they have the capacity to differentiate toward a tenogenic lineage (Howell et al., 2017). Use of AT explants from ScxGFP reporter mice (Pryce et al., 2007) allowed us to evaluate whether tendon cells recruited into composite hydrogels maintained tenogenic potential. Staining for Sca-1 indicated that the majority of recruited cells were indeed multipotent progenitors, likely originating from the epitenon (**Figure 3.7A,I**). Moreover, a majority of these TPCs showed evidence of a pro-tenogenic phenotype as evidenced by ScxGFP expression (**Figure 3.7I,J**). While future work will focus on determining the salient microenvironmental features conducive to tenogenic differentiation, we suspect that the fibrous topography plays a major role by governing the spread state of TPCs. For example, *in vitro* chondrogenesis is favored in microenvironments that present minimal adhesive cues (e.g., alginate) such that the cells maintain a rounded morphology (Mo et al., 2009). Indeed, cell shape is known to regulate lineage commitment in stem cells (McBeath et al., 2004), with previous work suggesting that a spindle morphology may bias stem cells toward a tenogenic lineage (Kishore et al., 2012).

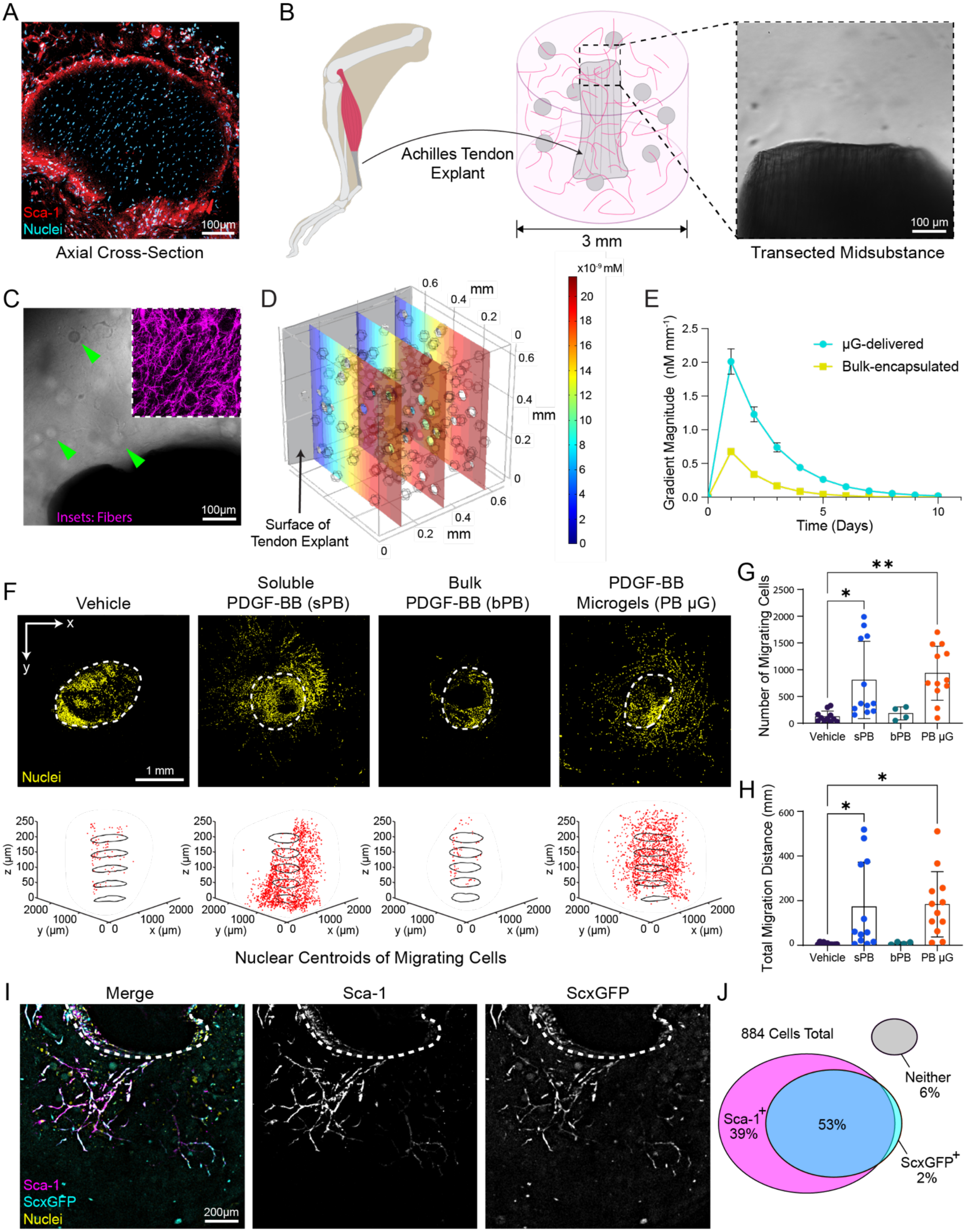
A
Sca-1
Nuclei
100μm
Axial Cross-Section
B
Achilles Tendon
Explant
3 mm
100 μm
Transected Midsubstance
C
Insets: Fibers
100μm
D
Surface of
Tendon Explant
mm
0.6
0.4
0.2
0
x10⁻⁹ mM
20
18
16
14
12
10
8
6
4
2
0
E
Gradient Magnitude (nM mm⁻¹)
2.5
2.0
1.5
1.0
0.5
0.0
Time (Days)
0
5
10
μG-delivered
Bulk-encapsulated
F
Vehicle
Soluble
PDGF-BB (sPB)
Bulk
PDGF-BB (bPB)
PDGF-BB
Microgels (PB μG)
x
y
Nuclei
1 mm
250
200
150
100
50
0
z (μm)
2000
1000
y (μm)
x (μm)
Nuclear Centroids of Migrating Cells
G
Number of Migrating Cells
2500
2000
1500
1000
500
0
*
**
Vehicle
sPB
bPB
PB μG
H
Total Migration Distance (mm)
600
400
200
0
*
*
Vehicle
sPB
bPB
PB μG
I
Merge
Sca-1
ScxGFP
Sca-1
ScxGFP
Nuclei
200μm
J
884 Cells Total
Neither
6%
Sca-1⁺
39%
53%
ScxGFP⁺
2%

Figure 3.7: Microgel-delivered PDGF-BB recruits Scx$^+$ TPCs from explanted murine Achilles tendon. **A**) Confocal fluorescent image of an axial cross-section of a mouse AT demonstrating Sca-1$^+$ progenitors residing in the epitenon. **B**) Experimental schematic; brightfield image of the transected tendon midsubstance encapsulated in a DexVS hydrogel. **C**) Brightfield image of an encapsulated tendon in a fibrous (inset) DexVS hydrogel containing hybrid microgels (green arrows). **D**) COMSOL model rendering of spatial distribution of PDGF-BB released from 50-μm microgels in the tendon explant model on day 10. **E**) Gradient of PDGF-BB concentration (nM mm^{-1}) over the first 20 microns adjacent to the tendon explant boundary for microgel-delivered vs. bulk-encapsulated (12 ng mL^{-1}) PDGF-BB (n = 5 radial directions). **F**) Confocal fluorescent images (axial view) of cell nuclei within and migrating from the tendon, orthogonally projected over a 500-micron stack of images, where white dotted lines mark the tissue boundary; 3D plots of nuclear centroids (red dots) outside the tissue boundary (black contours) showing the first 250 μm of tissue adjacent to the transection site for simplicity. Quantification of (**G**) number of migrating cells and (**H**) total migration distance (μm) within 500 μm of the transection site (n = 12, N = 3 [n = 4 in bPB group]). **I,** Representative confocal fluorescent image of migrating ScxGFP reporter cells, stained for Sca-1 (n = 5, N = 2). **J,** Quantification of Sca-1 and ScxGFP positivity among migrating cells. All data are presented as mean ± standard deviation. Asterisks indicate statistically significant comparisons, with $^*p<0.05$ and $^{**}p<0.01$ by ordinary one-way ANOVA with Tukey's multiple comparisons test.

3.5 Conclusion

Here we developed a composite hydrogel system capable of delivering tunable mechanical, soluble, and topographical microenvironmental cues to recruit tendon progenitor cells across multiple *in vitro* settings. This system revealed that microgel-delivered PDGF-BB and fibrous topography potently drive TPC invasion into synthetic hydrogel matrices in both a TPC spheroid and *ex vivo* Achilles tendon model. Overall, this work suggests that modular, fiber-reinforced DexVS hydrogels offer a promising route toward a regenerative tendon scaffold given their: (1) mechanical durability evidenced by the range of bulk moduli permissive to fiber-mediated migration, and (2) programmed regulation of the soluble milieu following a single administration. Furthermore, given that this injectable, acellular material can be administered via a minimally invasive procedure and does not require patient or donor cell isolation (Ni et al., 2013), it would face fewer regulatory hurdles and have lower associated costs. Finally, our evidence of tenogenic potential in invading TPCs motivates future work where we will leverage fibrous topographical alignment and timed growth factor delivery to orchestrate the spread state and organization of invading TPCs, tenogenic differentiation, alignment of *de novo* ECM, and ultimately, functional tissue regeneration.

3.6 Materials and methods

3.6.1 Reagents

All reagents were purchased from Sigma-Aldrich and used as received, unless otherwise stated.

3.6.2 Cell isolation and culture

For all animal procedures, the Institutional Animal Care and Use Committee (IACUC) guidelines for survival surgery in rodents and the IACUC Policy on Analgesic Use in Animals Undergoing Surgery were followed (Protocol #PRO00009868). All cells used in this work were harvested from 6 to 9-week-old C57BL/6J mice (Jackson Laboratory, Bar Harbour, ME). Tail tendons were removed from euthanized mice and then encapsulated in 2 mg mL^{-1} type I collagen. Encapsulated tissues were cultured in an incubator set to 37°C and 5% CO_2 in DMEM containing L-glutamine (Thermo Fisher, Waltham, MA), 1 v/v% penicillin/streptomycin/fungizone, and 10 v/v% fetal bovine serum (basal media) for 10 days to allow tendon progenitor cells (TPCs) to migrate into the collagen gel (Shimada et al., 2014). Following isolation and expansion of TPCs, collagen gels were digested in 0.25 mg mL^{-1} collagenase from *C. histolyticum* with 0.025 w/v % trypsin-EDTA. The resulting slurry was filtered through a cell strainer and then plated. Adherent TPCs were cultured in basal media, and cells at passage 1 were used for all experiments. For studies where cell proliferation was inhibited, TPC cultures were treated with 40 μg mL^{-1} mitomycin C for two hours, washed with basal media, then incubated for at least one hour prior to trypsinization for use in outgrowth studies.

3.6.3 Polymer synthesis

Dextran functionalized with vinyl sulfone groups (DexVS) was synthesized as previously described (Yu and Chau, 2012). Briefly, 5 g of 86 kDa dextran (MP Biomedicals, Irvine, CA) was dissolved in a 250 mL solution of 100 mM sodium hydroxide in Milli-Q water. On a stir plate set to 700 rpm, divinyl sulfone (Alfa Aesar, Haverhill, MA) was added to the solution, and the reaction proceeded for 3.5 minutes before termination by addition of 2.5 mL of 12 M hydrochloric acid. To achieve vinyl sulfone / dextran repeat unit ratios appropriate for hydrogel formation (16%) and fiber fabrication (65%), 3.88 mL and 12.5 mL of divinyl sulfone were added to substitution reactions, respectively. After vinyl sulfone addition, the product was dialyzed against Milli-Q water for 72 hours with twice daily changes and then lyophilized for 72 hours to yield a dry product. All reaction products were characterized via ^{1}H NMR.

Heparin methacrylate (HepMA) was synthesized as previously described (Davidson et al., 2020a; DePalma et al., 2021). Briefly, 0.5 g of 13.5-15 kDa heparin from porcine intestinal mucosa was dissolved in 50 mL of sterile PBS, and sodium hydroxide was added dropwise to bring the pH to 9. The solution was placed on a stir plate in a 4 °C refrigerator, then while stirring at 500 rpm, 99.3 μL of methacrylic anhydride was added. Sodium hydroxide was added intermittently over the next 24 hours to maintain a pH of ~8. The product was then dialyzed against Milli-Q water and lyophilized as described above.

3.6.4 Fiber segment fabrication and functionalization

An electrospinning solution was prepared by dissolving DexVS (65% vinyl sulfone functionalization) in a 1:1 solution of dimethyl formamide and Milli-Q water with 0.015 wt/v% 2-Hydroxy-4′-(2-hydroxyethoxy)-2-methylpropiophenone (Irgacure 2959) photoinitiator. For fluorescent visualization of fibers, methacrylated rhodamine (Polysciences, Inc., Warrington, PA) was added at 0.5 mM. In a humidity-controlled glovebox (21°C, 30-35% humidity), DexVS fibers were electrospun onto a slowly rotating (linear velocity 3.14 cm s^{-1}), grounded mandrel using a gap distance of 7 cm, voltage of -7.5 kV, and flow rate of 0.2 mL hr^{-1}. An ultraviolet lamp was directed at the opposite side of the mandrel; every 15 minutes, the lamp was turned on for 5 minutes to expose deposited fibers to 100 mW cm^{-2} UV light. Continuous UV exposure over the course of layer-by-layer fiber deposition ensured that fibers were adequately and uniformly photo-crosslinked.

The crosslinked fiber mat was removed from the mandrel and transferred to Milli-Q water. Two rounds of pipetting, vortexing, centrifugation, and resuspension were performed to break up the fiber mat into individual fiber segments and remove any clumps and residual crosslinking reagents. Purified fibers were resuspended at 10 v/v% in PBS and stored in a light-protected box at 4°C. Prior to use in hydrogel constructs, fiber segments were functionalized by resuspension in 50 mM 4-(2-hydroxyethyl)-1-piperazineethanesulfonic acid (HEPES) buffer at 10 v/v% along with cell-adhesive CGRGDS (RGD) (2.0 mM) and 5 mM sodium hydroxide. Functionalization proceeded via Michael-type addition at 37°C for 15 minutes, then fibers were washed with PBS and resuspended in HEPES buffer.

3.6.5 Fabrication of composite hydrogels

DexVS hydrogels were formed using previously described methods.(D.L. Matera et al., 2019) Briefly, DexVS was dissolved in PBS containing 50 mM HEPES buffer. Either cell-adhesive RGD or scrambled CGRDGS (RDG) was incorporated at 2.0 mM. Additionally, to control the number of VS groups available for crosslinking, cysteine was added at 9.1 mM. After this pre-reaction proceeded on ice for 20 minutes, other components (functionalized fiber segments, microgels, spheroids, etc.) were added to the mixture followed by the addition of an MMP-cleavable, dithiolated GCRDVPMSMRGGDRCG (VPMS) crosslinking peptide. Gelation via Michael-type addition was initiated by addition of sodium hydroxide (33 mM) and carried out at 37°C for 35 minutes before hydration in basal media. Bulk stiffnesses of ~0.5 and 2.0 kPa were achieved by crosslinking DexVS hydrogels with 12.5 and 15.0 mM VPMS, respectively; DexVS concentrations of 3.3 and 3.4 wt/v% were used to ensure that the ratio of free vinyl sulfone groups to VPMS molecules was consistent between the two conditions.(D.L. Matera et al., 2019) To demonstrate injectability of the composite hydrogel, plain (only DexVS and VPMS) and composite (containing fibers and DexVS/HepMA microgels) hydrogel mixtures were loaded into a syringe and injected through a 25-gauge needle into polylactic acid molds with irregular geometries. Following crosslinking of the hydrogels, molds were dissolved in PBS overnight.

3.6.6 TPC spheroid formation and encapsulation

TPC spheroids were formed by seeding 0.2 million cells on 400 µm Aggrewell plates (Stemcell Technologies, Vancouver, BC, Canada) coated with Pluronic F-127 followed by centrifugation at 400 g and overnight incubation. This seeding density yielded ~165 cells per spheroid. Polydimethylsiloxane (PDMS) (Dow, Midland, MI) was prepared at a 1:10

crosslinker:base ratio and cast to form circular molds (5 mm diameter, 1.8 mm height). Molds were plasma etched, bonded to 18 mm glass coverslips, coated with a solution of 2 mg mL^{-1} porcine skin gelatin and dried in an 80°C oven to subsequently release hydrogels from circular molds. Spheroids were collected from Aggrewell plates via repeated pipetting in basal media. The resulting suspension was centrifuged at 150 g for 30 seconds, and the supernatant was replaced with 50 mM HEPES buffer before addition to the hydrogel mixture at 750 spheroids mL^{-1}. 35 µL of spheroid/hydrogel suspension was added to each mold, yielding ~25 spheroids per hydrogel (**Figures 3.2-3.3, 3.5**). After hydrating in basal media and incubating overnight, gels were released from the molds and cultured free-floating.

3.6.7 Hybrid microgel synthesis and chemokine loading

Hybrid microgels composed of DexVS and HepMA were generated on a custom-designed microfluidic droplet generating device. Devices were designed in AutoCAD, and a master mold was fabricated using a SU-8 negative photoresist (Kayaku, Westborough, MA). PDMS (1:10 crosslinker:base ratio) devices were replica cast from SU-8 masters, cleaned, and bonded to glass as described above (see *TPC spheroid formation and encapsulation*). An aqueous phase was prepared by dissolving DexVS (16% functionalization) and HepMA in PBS with 50mM HEPES buffer, 0.5 mg mL^{-1} lithium phenyl-2,4,6-trimethylbenzoylphosphinate photoinitiator, and 2 v/v% N-vinylpyrrolidone. DexVS and HepMA concentrations were varied to study their effect on soluble factor release profiles.

An oil phase was prepared by adding 1.0 wt/v% perfluoropolyethylene (Ran Biotechnologies, Beverly, MA) to HFE-7500 (3M, St. Paul, MN), a perfluorinated mineral oil. A syringe pump was used to flow the aqueous and oil phases through the microfluidic droplet generating device at 0.5 and 1.0 mL/hr, respectively, to generate water-in-oil droplets with a high degree of monodispersity (Fig. 3). The resulting emulsion traveled through Tygon tubing to a second PDMS microfluidic device consisting of a series of 200 μm-wide channels in a 1x1 cm array. This array was exposed under a UV lamp at 100 mW cm^{-2} throughout the droplet generation process, with each microgel receiving ~20 seconds of exposure at the flow rate stated above.

The emulsion was collected and then broken by the addition of PBS and 20 v/v% perfluorooctanol (PFO) (Alfa Aesar, Haverhill, MA). Oil and PFO were removed from collected microgels via centrifugation for 5 minutes at 1000 g, and washed microgels were stored in PBS containing 4 v/v% penicillin/streptomycin/fungizone. To measure microgel diameter, a suspension of microgels was flowed in a monolayer across a polystyrene surface. A video of this flow was recorded on a brightfield microscope, with frames collected every 5 seconds, and custom MATLAB code (MathWorks, Portola Valley, CA) identified and measured diameters of microgels in each frame. Recombinant murine PDGF-BB (Peprotech, Cranbury, NJ) was then added to a suspension of microgels in 0.1 wt/v% bovine serum albumin (250 ng mL^{-1} and 500 ng mL^{-1} for release profile characterization and cell-based studies, respectively). This suspension was incubated for two days at 4°C, then microgels were washed twice with PBS containing 50 mM HEPES buffer before incorporation into hydrogels at 2.5 v/v%.

3.6.8 Chemokine release characterization

Hybrid microgels were fabricated with varying amounts of DexVS and HepMA using droplet generator devices that yielded spherical microgels with 50- or 150-μm diameters. After loading with PDGF-BB at 250 ng mL^{-1} and washing, 50 μL of microgels was resuspended in 150 μL of PBS containing 0.1 wt/v% bovine serum albumin in a microcentrifuge tube. At each timepoint, tubes were shaken and centrifuged, then 35 μL of supernatant was removed, replaced with fresh supernatant, and stored at -80°C for the remainder of the study. PDGF-BB concentration in each sample was measured via ELISA (DuoSet, R&D Systems, Minneapolis, MN) to calculate the fraction of theoretically loaded PDGF-BB that was released at each timepoint throughout the assay.

3.6.9 Computational modeling of microgel-mediated chemokine delivery

COMSOL Multiphysics (COMSOL AB, Stockholm, Sweden) was used to quantify and visualize spatial distributions of PDGF-BB undergoing Fickian diffusion in a 665x665x665-μm volume of a DexVS hydrogel. Spheres representing hybrid microgels loaded with 500 ng mL^{-1} were distributed at 2.5 v/v% around a 100-μm sphere representing a cell spheroid. The fluid diffusion coefficient of the microgels was varied to simulate HepMA incorporation, and the effect of this parameter was explored over a range of bulk diffusion coefficients. Flux was permitted at all boundaries, and equations representing the boundary conditions assumed that flux into one face of the model would match flux out of the opposite face. Any PDGF that diffused into the spheroid was eliminated from the model to simulate cell receptor binding. The model was sampled at 24 h intervals for 3 days by measuring the PDGF-BB concentration along lines drawn in the positive and negative x, y, and z directions (n = 6) and then calculating the slope of this concentration with respect to distance from the spheroid boundary over the first 20 μm.

A similar model was developed to simulate the *ex vivo* model, wherein the analyzed volume was the 665x665x665-μm region adjacent a 1 mm diameter cylinder representing a mouse Achilles tendon. Similar to the cell spheroid, any PDGF-BB that diffused into the tendon was eliminated from the model. The model was sampled at 24h intervals for 10 days in the form of PDGF-BB concentration along lines drawn normal to the tendon surface and ±25° in two orthogonal directions (n=5). The slope of this concentration with respect to distance from the line's origin was then calculated over the first 20 μm.

3.6.10 *Ex vivo* Achilles tendon outgrowth model

Circular PDMS molds (4 mm diameter) were fabricated as above (section 2.5), and a 0.5 mm-thick PDMS ring with a 1.25 mm hole at the center was bonded at the base of each mold. Molds were coated with gelatin as above (section 2.5). ATs were harvested from 9-12 week old C57BL/6 ScxGFP reporter mice (Pryce et al., 2007). Following euthanasia, hindlimbs were transected at the knee, skinned, and placed in a dish of Leibovitz's L-15 media (Thermo Fisher, Waltham, MA) containing 4 v/v% penicillin/streptomycin/ fungizone and 10 v/v% fetal bovine serum. The AT was retrieved by making cuts at the myotendinous junction and calcaneal enthesis. Remaining fat and muscle tissue was then removed, and the tendon was transected at the midsubstance.

Tendons were washed in 25 μL of a DexVS hydrogel solution before being placed vertically in PDMS molds with the enthesis or myotendinous junction anchored by the ring at the base and the midsubstance facing upward. 25 μL of fibrous DexVS hydrogel solution was then transferred into each mold to encapsulate the tendons, and gels were hydrated with basal media after incubating for 35 minutes at 37°C. After incubating overnight, gels were released from molds and cultured free-floating.

3.6.11 Microscopy and image analysis

Fluorescent images were captured on a Zeiss LSM800 confocal microscope. To quantify TPC spheroid outgrowth, samples were stained with phalloidin (Invitrogen, Waltham, MA) and Hoechst 33342, and z-stacks were collected at 10x magnification and 5-µm intervals to encompass the volume of cell outgrowth for a given spheroid. Custom MATLAB code was developed to quantify outgrowth area as defined by F-actin-positive regions outside of the spheroid body in a max-projection of the imaged volume. This code also identified the 3D coordinates of centroid of nuclei outside the spheroid body, calculated their distance from the center of the spheroid body, and counted the number of migrating cells in addition to their total migration distance. For proliferation studies, cells were also stained with Ki67 (Ki67 rabbit anti-mouse, Invitrogen, Waltham, MA), and the number of Ki67$^+$ nuclei was counted manually.

Encapsulated ATs treated with soluble PDGF-BB or PDGF-BB-laden microgels were stained with Hoechst 33342 and an antibody against stem cell antigen (Sca)-1 (Sca-1 [Ly-6A/E] rat anti-mouse, Invitrogen, Waltham, MA). At 10x magnification, Z-stacks of nuclei, immunostained Sca-1, and ScxGFP expression were collected at 5-µm intervals, spanning the first 500 µm of tendon adjacent to the transection site (midsubstance). Gaussian filters were applied to all images to remove noise and background. A custom MATLAB code demarcated the boundary of the tendon tissue at 50-µm intervals, identified the 3D coordinates of migrating nuclei, and quantified the intensity of the Sca-1 and ScxGFP channels in pixels contained in a 5x5x5-µm cube centered at each nuclear centroid. Coordinates of nuclear centroids were also used to count the number of migrating cells and calculate their total migration distance from the nearest tissue boundary. For further visualization of cell recruitment, 3D renderings of TPC nuclei were generated in AVIA (AVIA Health, Chicago, IL).

3.6.12 Statistics

Pre-processing of all data involved exclusion of extreme outliers (i.e., greater than 3 interquartile ranges removed from the median). ELISA data from PDGF-BB release studies was also normalized to the theoretically loaded mass of PDGF-BB. All data are presented as mean ± standard deviation unless stated otherwise in the corresponding figure legend. Sample size is indicated within corresponding figure legends, with n technical replicates and N biological replicates (N = 1 unless stated otherwise). For *ex vivo* studies, each mouse yielded 4 samples, and so a total of 10 mice were used across three experiments (N = 1 for bulk PDGF-BB group). Statistical significance was determined by ordinary one- or two-way analysis of variance (ANOVA) with Tukey's multiple comparisons test or two-sided Student's t-test where appropriate ($\alpha = 0.05$). All statistical analyses were performed in Prism (GraphPad Software, San Diego, CA).

3.7 Supplemental figures

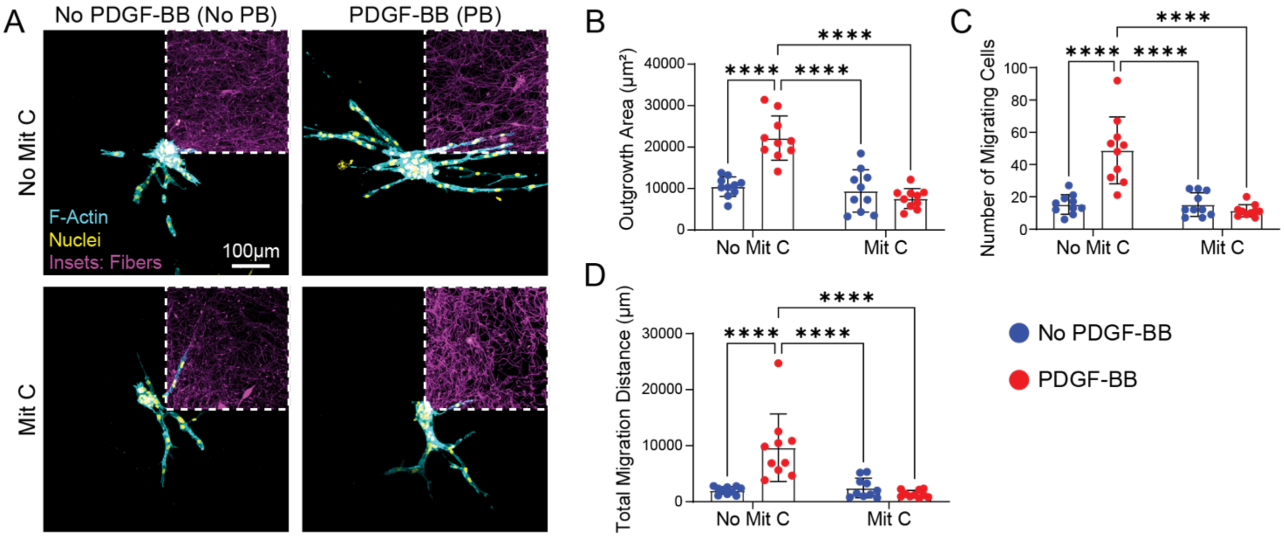

Supplemental Figure 3.1: Blocking cell proliferation abrogates the migratory response to PDGF-BB. A) Confocal fluorescent images of TPC spheroid outgrowth into fibrous (2.5 v/v%) DexVS hydrogels (15 mM VPMS) after three days of culture, varying mitomycin C pre-treatment and PDGF-BB supplementation. Quantification of (**B**) TPC spheroid outgrowth area, (**C**) number of migrating cells, and (**D**) total migration distance. Asterisks indicate statistically significant comparisons, with ****p<0.0001 by ordinary two-way ANOVA with Tukey's multiple comparisons test.

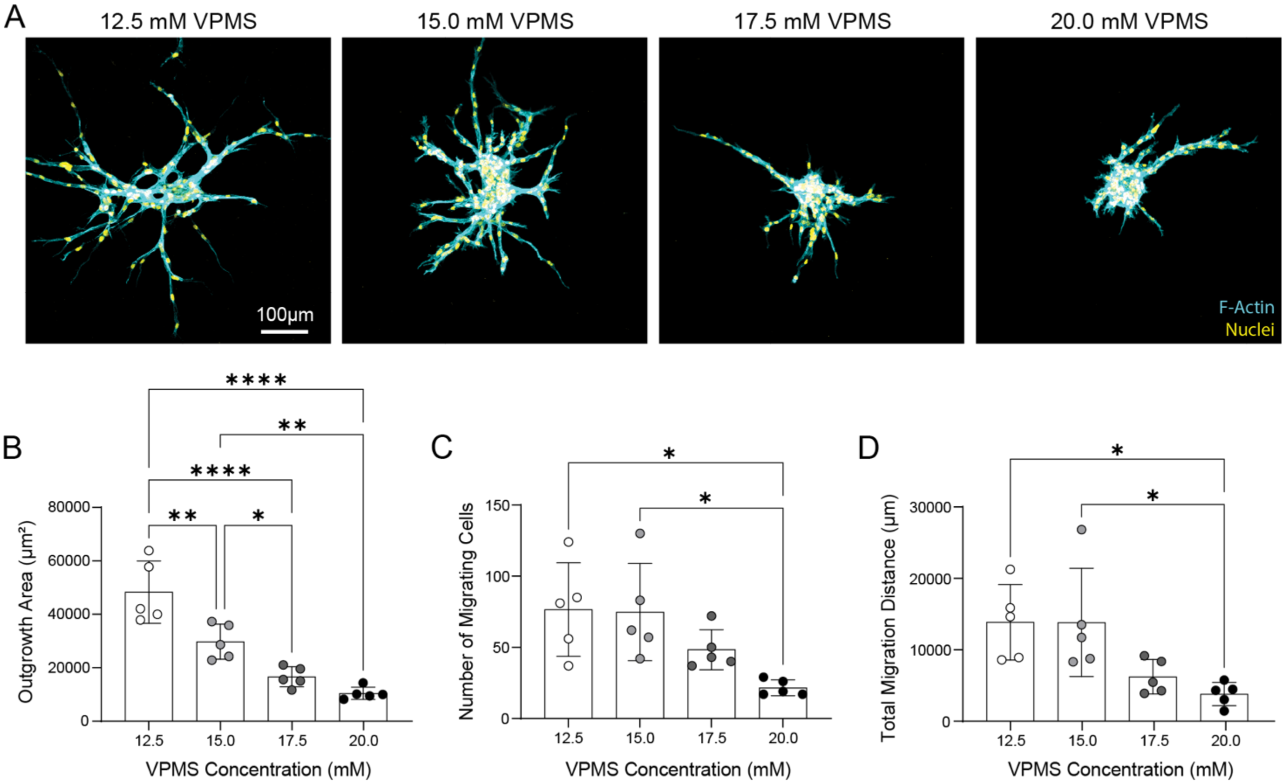

Supplemental Figure 3.2: Bulk stiffness screen. **A**) Confocal fluorescent images of TPC spheroid outgrowth into nonfibrous DexVS hydrogels after three days of culture, varying VPMS crosslinker concentration. Quantification of (**B**) TPC spheroid outgrowth area, (**C**) number of migrating cells, and (**D**) total migration distance. Asterisks indicate statistically significant comparisons, with *p<0.05, **p<0.01, and ****p<0.0001 by ordinary one-way ANOVA with Tukey's multiple comparisons test.

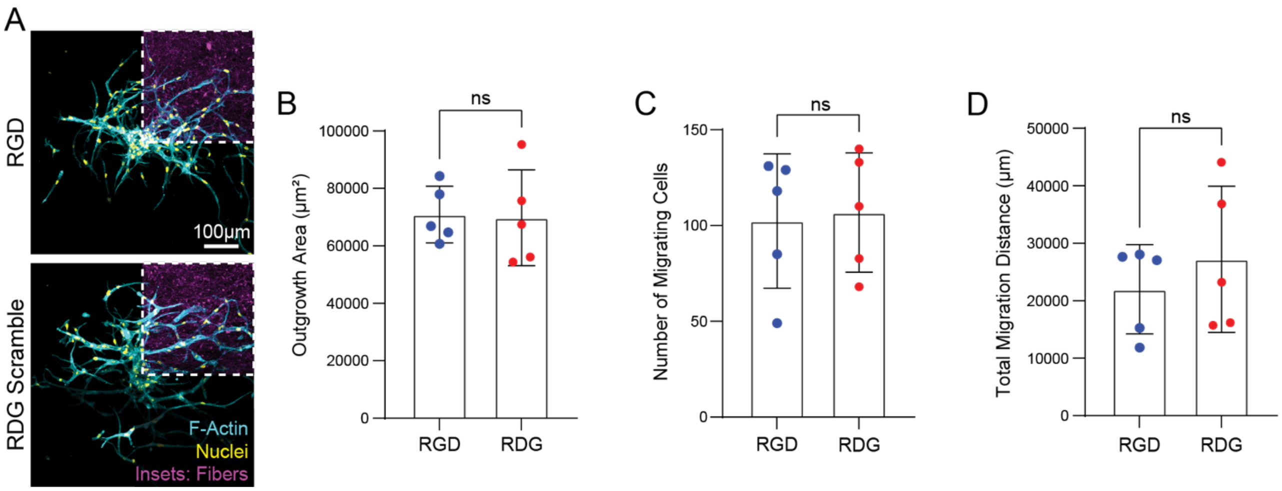

Supplemental Figure 3.3: Effect of bulk functionalization with cell-adhesive ligand in fibrous hydrogels. **A**) Confocal fluorescent images of TPC spheroid outgrowth into fibrous (2.5 v/v%) DexVS hydrogels (15 mM VPMS) after three days of culture, with hydrogel bulk functionalization consisting of either cell-adhesive RGD or scrambled RDG peptides. Quantification of (**B**) TPC spheroid outgrowth area, (**C**) number of migrating cells, and (**D**) total migration distance. Statistical comparisons were made via Student's t-tests (α = 0.05).

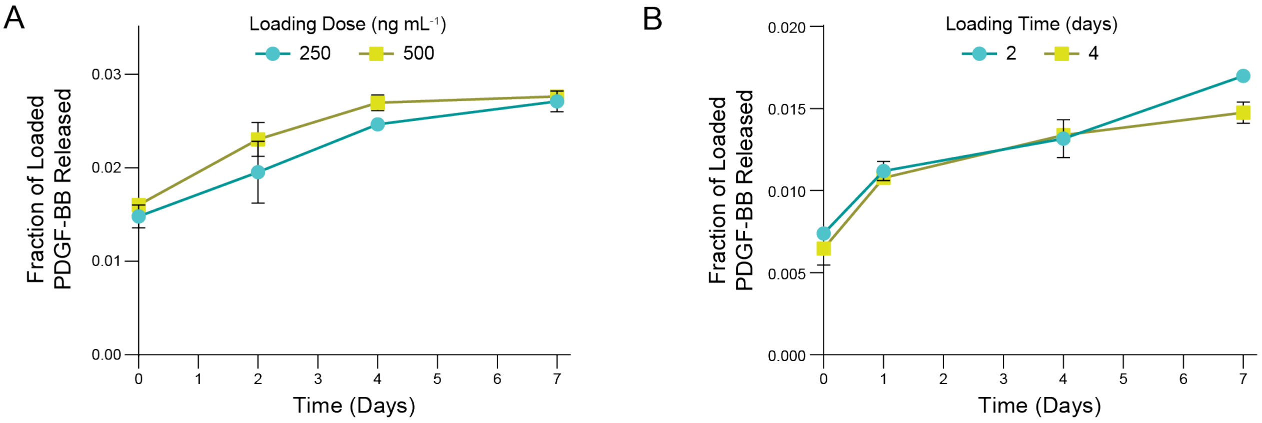

Supplemental Figure 3.4: Soluble factor release profiles as a function of PDGF-BB loading dose and loading time. **A**) Fraction of loaded PDGF-BB released from DexVS microgels (5 wt/v% HepMA) with varying loading dose. **B**) Fraction of loaded PDGF-BB released from DexVS microgels (10 wt/v% HepMA) loaded at 250 ng mL^{-1}, with varying loading time. Statistical comparisons were made via ordinary one-way ANOVA with Tukey's multiple comparisons test (α = 0.05).

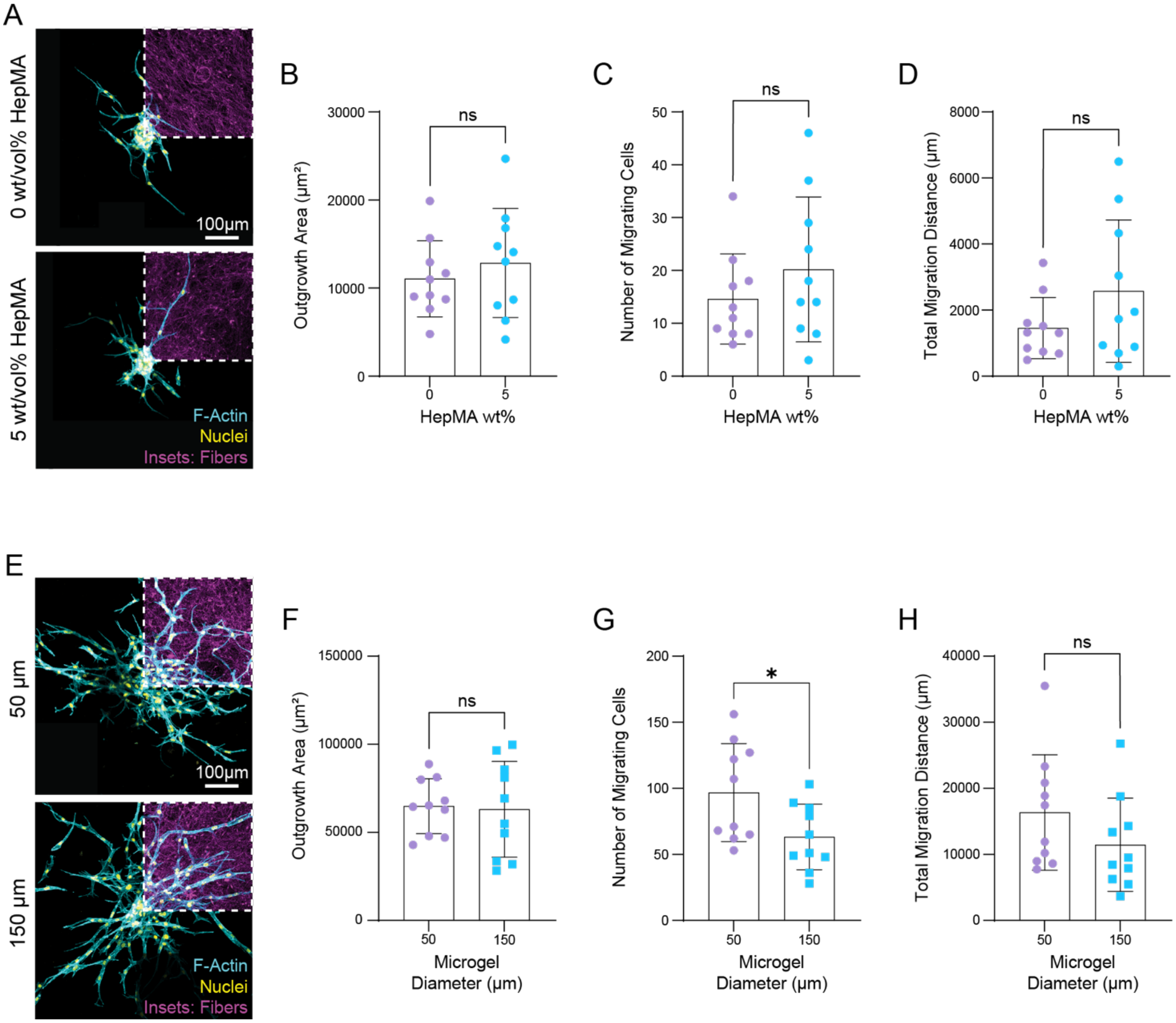

Supplemental Figure 3.5: Isolated effects of HepMA content and microgel size on TPC invasion. A) Confocal fluorescent images of 3 days of TPC spheroid outgrowth into fibrous (2.5 v/v%) DexVS hydrogels (15 mM VPMS), with non-loaded microgels containing either 0 or 5 wt/v% HepMA. Quantification of (**B**) TPC spheroid outgrowth area, (**C**) number of migrating cells, and (**D**) total migration distance. **E**) TPC spheroid outgrowth with PDGF-BB delivered from 50- or 150-µm diameter microgels (encapsulated at a density of 2.5 v/v%; PDGF-BB loaded at 500 ng mL^{-1}). Quantification of (**F**) TPC spheroid outgrowth area, (**G**) number of migrating cells, and (**H**) total migration distance. Asterisks indicate statistically significant comparisons, with *p<0.05 by Student's t-test.

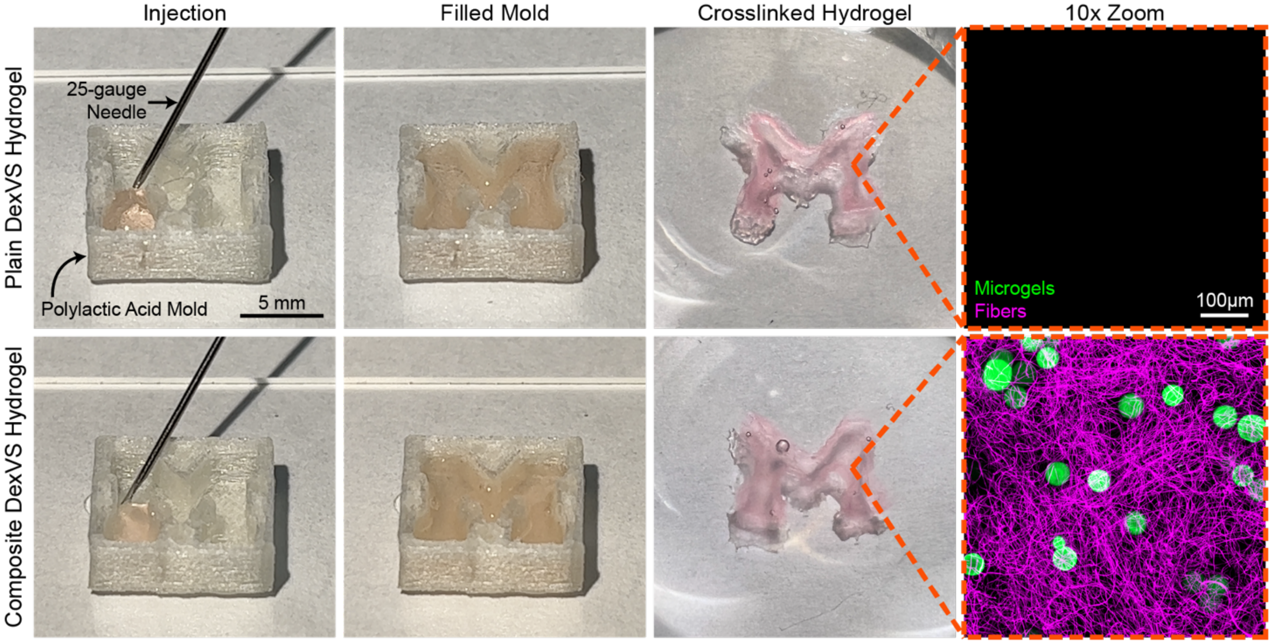
Injection
Filled Mold
Crosslinked Hydrogel
10x Zoom
Plain DexVS Hydrogel
Composite DexVS Hydrogel
25-gauge Needle
Polylactic Acid Mold
5 mm
Microgels
Fibers
100μm

Supplemental Figure 3.6: Demonstration of injectability of composite hydrogel. Plain and composite (containing DexVS fibers and DexVS/HepMA microgels) DexVS hydrogel solutions are injected into a mold with irregular geometry through a 25-gauge needle. Confocal fluorescent images of the resulting hydrogels, orthogonally projecting over a 30-micron stack of images.

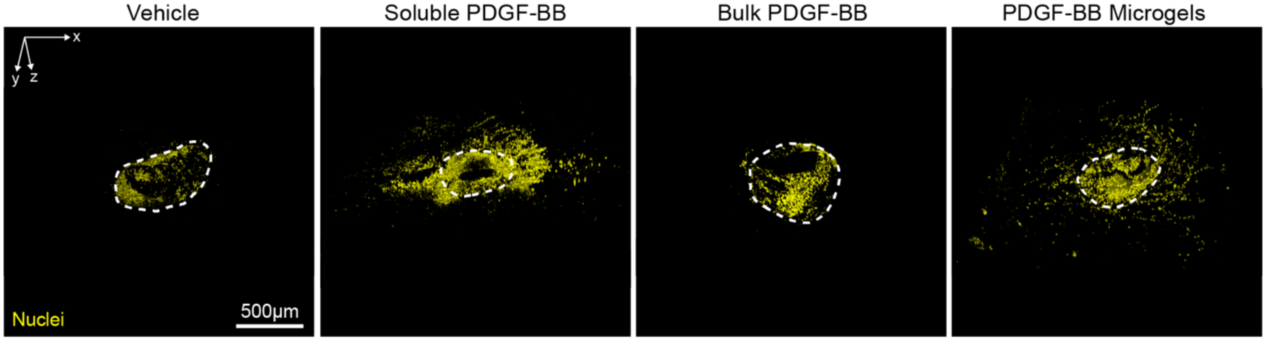
Vehicle
Soluble PDGF-BB
Bulk PDGF-BB
PDGF-BB Microgels
x
y
z
Nuclei
500μm

Supplemental Figure 3.7: Three-dimensional renderings of TPC outgrowth from a murine Achilles tendon. 3D renderings from confocal fluorescent images of cell nuclei migrating into composite DexVS hydrogels. Dotted white lines denote tissue boundaries. These renderings were generated from the same four images shown in Figure 3.7.

Chapter 4: Engineered Microenvironmental Cues from Fiber-reinforced Hydrogel Composites Drive Tenogenesis and Aligned Collagen Deposition

Note: this chapter contains unpublished work currently in peer review

4.1 Authors

Robert N. Kent III, Maggie E. Jewett, Trevor P. Buck, Mohamed Said, LeeAnn A. Hold, Eileen A. Crawford, MD, Megan L. Killian, PhD, Adam C. Abraham, PhD, Alice H. Huang, PhD, Brendon M. Baker, PhD

4.2 Abstract

Effective tendon regeneration following injury is contingent on appropriate differentiation of recruited cells and deposition of mature, aligned, collagenous extracellular matrix that can withstand the extreme mechanical demands placed on the tissue. As such, myriad biomaterial approaches have been explored to provide biochemical and physical cues that encourage tenogenesis and template aligned matrix deposition in lieu of dysfunctional scar tissue formation. Fiber-reinforced hydrogels present an ideal biomaterial system toward this end given their transdermal injectability, tunable stiffness over a range amenable to tenogenic differentiation of progenitors, and capacity for modular inclusion of biochemical cues. Here, tunable and modular, fiber-reinforced, synthetic hydrogels are employed to elucidate salient microenvironmental

determinants of tenogenesis and aligned collagen deposition by tendon progenitor cells. Transforming growth factor β3 drives a cell fate switch toward pro-regenerative or pro-fibrotic phenotypes, which can be biased toward the former by culture in softer microenvironments or inhibition of the RhoA/ROCK activity. Furthermore, studies demonstrate that topographical anisotropy in fiber-reinforced hydrogels critically mediates the alignment of *de novo* collagen fibrils, reflecting native tendon architecture. These findings inform the design of cell-free, injectable, synthetic hydrogels for tendon tissue regeneration and, likely, that of a range of load-bearing connective tissues (**Figure 4.1**).

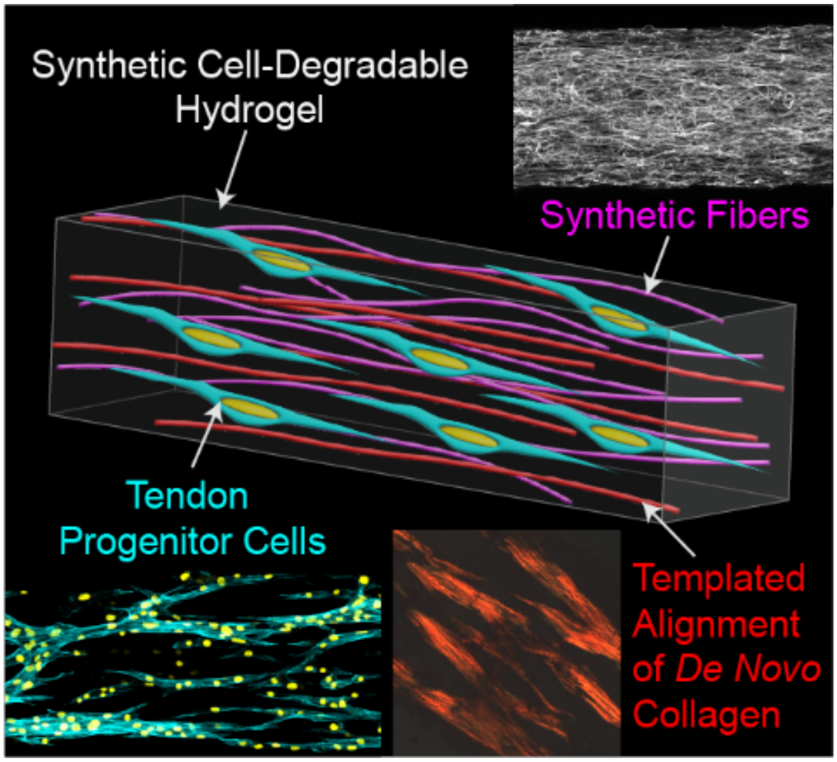
Synthetic Cell-Degradable Hydrogel
Synthetic Fibers
Tendon Progenitor Cells
Templated Alignment of *De Novo* Collagen

Figure 4.1: Fiber-reinforced hydrogel composites were employed to elucidate salient microenvironmental determinants of tenogenesis and aligned collagen deposition by tendon progenitor cells. Culture in these soft, 3D microenvironments potentiated transforming growth factor β3-mediated tenogenic differentiation of tendon progenitor cells, and fibrous topographical anisotropy templated alignment of *de novo* collagen fibrils. These findings inform the design of cell-free, injectable hydrogels for tendon tissue regeneration.

4.3 Introduction

Tendon and ligament injuries comprise ~45% of the 124 million cases of musculoskeletal injury reported annually in the United States (Lemme et al., 2018; Praemer et al., 1999; United states bone and joint initiative: The burden of musculoskeletal disease in the united states, fourth edition, 2016**)**. Particularly in adults, Achilles tendons are unable to fully regenerate following injury, resulting in comparably poor outcomes regardless of surgical or conservative management (Lantto et al., 2016; Nilsson-Helander et al., 2010). Poor clinical outcomes following tendon rupture are largely attributed to the generation of disorganized, hypercellular scar tissue that causes chronic pain, fails to meet the mechanical demands of the tendon, and heightens the risk of reinjury (Killian et al., 2012; Sharma and Maffulli, 2006; F. Wu et al., 2017a). Better approaches for treating tendon injuries are therefore desperately needed, which could be informed by contexts where regenerative tendon healing occurs naturally.

Robust tendon healing requires the recruitment, organization, and differentiation of appropriate cell types. Models of Achilles tendon injury in neonatal C57BL/6 and adult MRL/MpJ mice demonstrate recruitment of tendon progenitor cells (TPCs), which undergo tenogenic differentiation and regenerate functional tissue (Arvind et al., 2021; Best and Loiselle, 2019; George et al., 2021; Howell et al., 2017; Kaji et al., 2020; Kallenbach et al., 2022; Sakabe et al., 2018). Although tendon progenitor cells exist in the adult C57BL/6 mouse and human epitenon (Howell et al., 2017; Nichols et al., 2023; Walia and Huang, 2019), they contribute to both tenogenic and fibrogenic cell populations; the latter is thought to drive formation of disorganized, dysfunctional scar tissue, which is mechanically inferior and prone to reinjury (Howell et al., 2017; Killian et al., 2012; Nichols et al., 2023). New therapies that can drive tenogenic (and prevent fibrogenic) differentiation of recruited progenitors and provide a template for aligned matrix deposition could therefore result in improved functional regeneration of tendon and greatly reduce the economic burden of these injuries.

Toward this end, prior strategies have focused on the delivery of tenogenic drugs and biologics via injection or suture-based delivery (de Vos et al., 2010; Efird et al., 2018; Tarafder et al., 2019b; Tempfer et al., 2018). While demonstrating promising biological responses, these approaches failed to template organized collagen deposition within the healing tissue (Baker and Mauck, 2007; Baker et al., 2012; Font Tellado et al., 2015). Aligned, fibrous scaffolds can provide such a template and even approach the mechanical properties of native tendon upon implantation, but they exhibit poor tissue integration and drive aberrant cell differentiation, adversely impacting tissue regeneration (Cai et al., 2023; English et al., 2015; Islam et al., 2017; Koh et al., 2002; No et al., 2020a). Synthetic hydrogels therefore represent an exciting avenue in the field of regenerative biomaterials given their transdermal injectability, tunable mechanical properties, and potential for modular inclusion of physical and soluble microenvironmental cues to drive regenerative biology (Purcell et al., 2014; Testa et al., 2017; Y. Wang et al., 2021b). Moreover, fiber-reinforced hydrogel composites (FRHCs) allow for orthogonal tuning of bulk mechanical properties and fibrous topography, simultaneously providing (1) a soft microenvironment amenable to tenogenesis and inhibitory to myofibroblastic differentiation, and (2) organized fibrous topography to template *de novo* matrix deposition (Hiraki et al., 2021; D.L. Matera et al., 2019). Previous work from our lab has shown that fiber-reinforced, synthetic hydrogels are amenable to the recruitment of TPCs from the epitenon of adult murine Achilles tendons (Kent et al., 2022). This injectable composite demonstrated synergistic, pro-migratory effects of fibrous topography and microgel-delivered platelet-derived growth factor BB on TPCs, with a majority of recruited cells expressing *Scleraxis* (*Scx*), an early and critical tenogenic transcription factor (Best and Loiselle, 2019; A. H. Huang et al., 2015; Liu et al., 2021; Sakabe et al., 2018; Schweitzer et al., 2001).

Building on this work, here we systematically developed 2D then 3D engineered culture platforms to identify salient topographical, adhesive, and soluble cues that drive tenogenic differentiation of TPCs in addition to aligned, collagenous matrix production reflecting the matrix architecture of native tendon. To delineate biological processes central to tendon regeneration in 3D, we designed cell-degradable FRHCs imbued with topographical cues by incorporating cell-adhesive fiber segments (Kent et al., 2022; D.L. Matera et al., 2019). We confirmed observations from previous studies that TGF-β is tenogenic (Kaji et al., 2020; Kallenbach et al., 2022; Sakabe et al., 2018; G. K. Tan et al., 2020), but also elucidated microenvironmental determinants of a fate switch between myofibroblastic vs. tenogenic differentiation. Finally, we applied FRHC design features optimized with murine TPCs and found that human tendon-derived cell (TDC) tenogenesis and matrix production appears to be highly contingent on the extent and chronicity of tendinopathy in the tissue from which cells are derived. Collectively, these findings provide fundamental insights into the microenvironmental cues that promote tenogenesis and define key material design parameters of injectable, fibrous hydrogel composites for improved tendon regeneration.

4.4 Results and discussion

4.4.1 TGF-β2 and -β3 induce ScxGFP expression in TPCs

Murine TPCs were harvested from C57BL/6 *ScxGFP* reporter mice using previously described methods (**Figure 4.2A**) (Bi et al., 2007; Shimada et al., 2014). This mouse, developed by Pryce et al., was created by injecting into fertilized eggs a transgene construct inserted into the first exon of *Scx* (Pryce et al., 2007). While this mouse cannot report accessibility and expression of the native *Scx* locus, it can serve as a screening tool for identifying microenvironmental cues that promote *Scx* expression and support tenogenesis. For the sake of throughput in screening potential tenogenic growth factors (GFs) at concentrations identified previously in the literature (Harvey et al., 2019; Kashiwagi et al., 2004; Lee et al., 2015; Rajpar and Barrett, 2019; Tarafder et al., 2019a), initial studies were performed with *ScxGFP* reporter TPCs cultured on fibronectin-coated glass coverslips. As evidenced by elevated *ScxGFP* expression, TGF-β most potently drove tenogenic differentiation among the GFs investigated, with TGF-β3 being the most tenogenic of the three TGF-β isoforms (**Figure 4.2B-C, F**). While TGF-β-induced tenogenesis was further substantiated by increased expression of *Scx*, t*enascin C* (*Tnc*), and *collagen 1a2* (*Col1a2*) via qPCR, other canonical genes associated with tenogenesis including *tenomodulin* (*Tnmd*), *mohawk* (*Mkx*), *fibromodulin* (*Fmod*), *biglycan* (*Bgn*), *decorin* (*Dcn*), *collagen 1a1* (*Col1a1*), and *collagen 3a1* (*Col3a1*) were downregulated or showed no change (**Figure 4.2D**) (Walia and Huang, 2019). Live imaging of the *ScxGFP* reporter suggested that TGF-β-induced, early tenogenesis requires ~6 days to occur (**Figure 4.2E-F**), and therefore all subsequent differentiation studies were performed over one week.

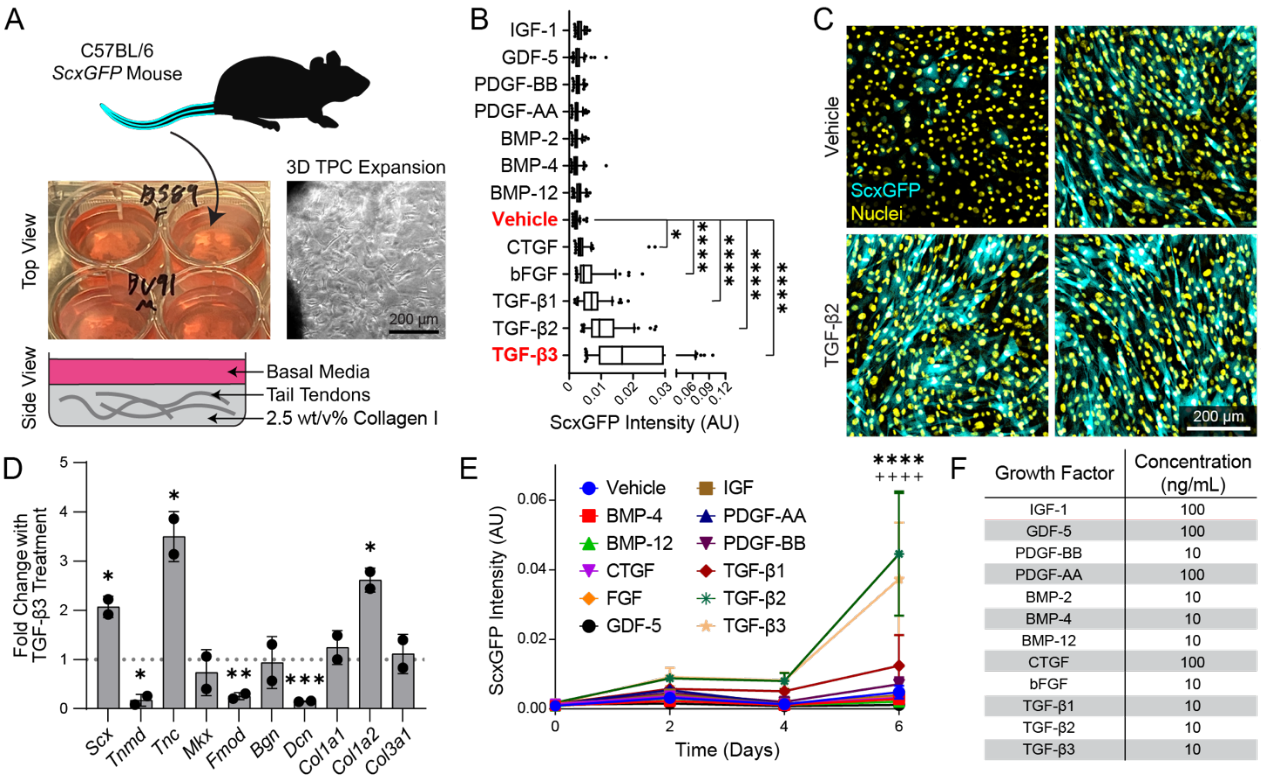

Growth Factor	Concentration (ng/mL)
IGF-1	100
GDF-5	100
PDGF-BB	10
PDGF-AA	100
BMP-2	10
BMP-4	10
BMP-12	10
CTGF	100
bFGF	10
TGF-β1	10
TGF-β2	10
TGF-β3	10

Figure 4.2: TGF-β2 and -β3 induce *ScxGFP* expression in murine TPCs. A) Protocol schematic for isolating TPCs from *ScxGFP* mouse tail tendons; tendons were harvested and encapsulated in a type I collagen hydrogel, expanded in 3D for 10 days, then plated on polystyrene dishes for standard cell culture. **B**) ScxGFP intensity (AU) in TPCs cultured on fibronectin-coated glass for 7 days in media supplemented with a panel of putative tenogenic growth factors (n = 300-400 cells, N = 2). Boxes denote medians and span interquartile ranges; whiskers span 95% confidence intervals. **C**) Representative fluorescent images of TPC monolayers treated with basal media or supplemented with various TGF-β isoforms. **D**) Fold change in expression of canonical tenogenic genes with TGF-β3 treatment of TPC monolayers for 7 days (n = 2, N = 3). A fold change of 1 is denoted with a black, dotted line. **E**) Time-lapse imaging of ScxGFP intensity (AU) over the course of a 6-day TPC culture in media supplemented with a panel of growth factors (n = 6 fields of view [FOVs]). Statistical indicators represent comparisons between the vehicle control and TGF-β2 (*) or TGF- β3 (+). **F**) Table of growth factors and respective concentrations supplemented to culture media in (B-E). Unless stated otherwise, all data are reported as mean ± standard deviation. Asterisks indicate statistically significant comparisons, with $^{*}p<0.05$, $^{**}p<0.01$, $^{***}p<0.001$, and $^{****}p<0.0001$ by ordinary one-way ANOVA with Tukey's multiple comparisons test or Student's t-test.

4.4.2 Organization of fibrous topography influences tenogenic differentiation of TPCs in 2D

Having confirmed a soluble, biochemical driver of TPC tenogenesis, we began to interrogate the role of physical microenvironmental cues in supporting or attenuating this differentiation program. Previous work has demonstrated the potential of topographical anisotropy for promoting a tenogenic phenotype *in vitro* in TPCs and mesenchymal stem cells, which is intuitive given the highly aligned ECM of native tendon (Islam et al., 2017; Kishore et al., 2012; Z. Yin et al., 2010; Zhu et al., 2010). To investigate the role of topographical alignment in TGF-β3-induced tenogenesis of TPCs, we electrospun non-aligned or aligned dextran vinyl sulfone (DexVS) fibers onto glass substrates, functionalized fibers with cell-adhesive CGRDGS (RGD) peptide, then seeded and cultured TPCs with exogenous TGF-β3 (**Figure 4.3A**). These fibers have been shown to have similar diameter to collagen fibers *in vivo*, with both having a diameter of ~1 μm (D. L. Matera et al., 2020). To our surprise, we found that *ScxGFP* expression did not vary as a function of topographical alignment in this context (**Figure 4.3B**), contrasting findings from previous work (Islam et al., 2017; Kishore et al., 2012; Z. Yin et al., 2010; Zhu et al., 2010). Even when seeded at a low density (13,500 cells cm^{-2}), TPCs rapidly achieved confluency on these substrates over the course of one week, likely due to the known mitogenic effects of TGF-β on mesenchymal cells (Y. Li et al., 2022). Confluent TPCs achieved a spindle, uniaxial morphology with evident co-alignment to neighboring cells, independent of fiber alignment (**Figure 4.3B, D; Supplemental Figure 4.1D**) (Park et al., 2020).

To better maintain TPC morphology reflecting the topographical alignment of underlying matrix fibers, TPCs were pre-treated with mitomycin C to prevent cell proliferation over the course of the study (**Supplemental Figure 4.1A**). Now-individualized TPCs demonstrated a spindle morphology on aligned substrates, coincident with increased *ScxGFP* expression compared to TPCs cultured on non-aligned fibers (**Figure 4.3C, E**). Fiber alignment showed minimal effects on nuclear morphology, with TPCs exhibiting similar nuclear areas and eccentricities independent of mitomycin C treatment and substrate alignment (**Supplemental Figure 4.1B-C**) (Stoll et al., 2010). Together, these results support prior findings that a spindle, uniaxial morphology, which can be encouraged by but does not necessarily require alignment of cell-adhesive fibers, is a critical determinant of TPC tenogenesis.

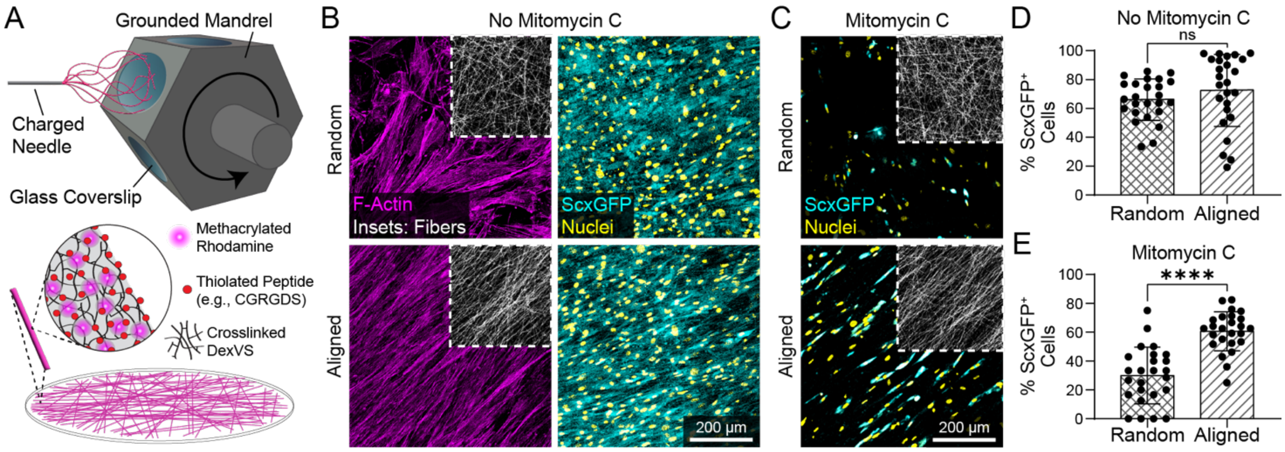

Figure 4.3: Adhesive anisotropy influences TPC tenogenesis in 2D only when cell proliferation is limited. A) Schematic of DexVS fiber-coated coverslip fabrication. A solution of DexVS and methacrylated rhodamine was electrospun onto coverslips mounted to a grounded, rotating mandrel, with mandrel rotation speed dictating the resulting alignment of deposited fibers; fibers were crosslinked then functionalized with cell-adhesive CGRGDS. **B**) Fluorescent images of TPCs seeded on random or aligned substrates and cultured with TGF-β3 for one week (n = 25 FOVs, N = 3). **C**) Fluorescent images of mitomycin C pre-treated TPCs in the same culture conditions as in (B) (n = 25 FOVs, N = 2). Quantification of % of TPCs expressing *ScxGFP* (**D**) without mitomycin C pre-treatment and (**E**) with mitomycin C pre-treatment. All data are reported as mean ± standard deviation. Asterisks indicate statistically significant comparisons, with ****$p<0.0001$ by Student's t-test (ns denotes a non-significant comparison).

4.4.3 TGF-β isoforms differentially regulate tenogenic vs. myofibroblastic differentiation

Our work and others' have demonstrated the tenogenic potential of TGF-β ligands (Sakabe et al., 2018; G. K. Tan et al., 2020); however, TGF-β signaling is known to induce myofibroblastic differentiation in a range of mesenchymal cell types, including TPCs (Manning et al., 2011; Voleti et al., 2012; Wipff et al., 2007). Having observed differential promotion of *ScxGFP* expression as a function of TGF-β isoform (**Figure 4.2**), we next explored the capacity of TGF-β1, -β2, and -β3 to induce tenogenic vs. myofibroblastic differentiation of TPCs. Screening these isoforms again, with TPCs adhering to aligned fibers, we found that TGF-β1 uniquely promoted robust F-actin stress fiber formation (**Figure 4.4A-B**), suggesting heightened cytoskeletal contractility previously associated with myofibroblastic differentiation (Sandbo and Dulin, 2011). While all three isoforms resulted in increased *αSMA* expression relative to vehicle controls, this increase was most attenuated with TGF-β3 treatment as compared to the other isoforms (**Figure 4.4C, E**). As in the initial screen performed on glass (which lacked topography) (**Figure 4.2**), all three isoforms resulted in heightened *ScxGFP* expression compared to the vehicle control (**Figure 4.4D**). This implied fate switch highlights the potential for TGF-β3 in promoting a regenerative phenotype following tendon injury, where tenogenic differentiation and resulting tissue regeneration may be favored over myofibroblastic differentiation and disorganized scar formation (Howell et al., 2017). However, despite its demonstrated efficacy *in vitro,* TGF-β3 alone has been shown to drive fibrosis in lieu of functional tendon regeneration *in vivo* (Manning et al., 2011), and so we went on to explore additional microenvironmental cues and their interaction with TGF-β3-mediated tenogenesis vs. myofibroblastic differentiation.

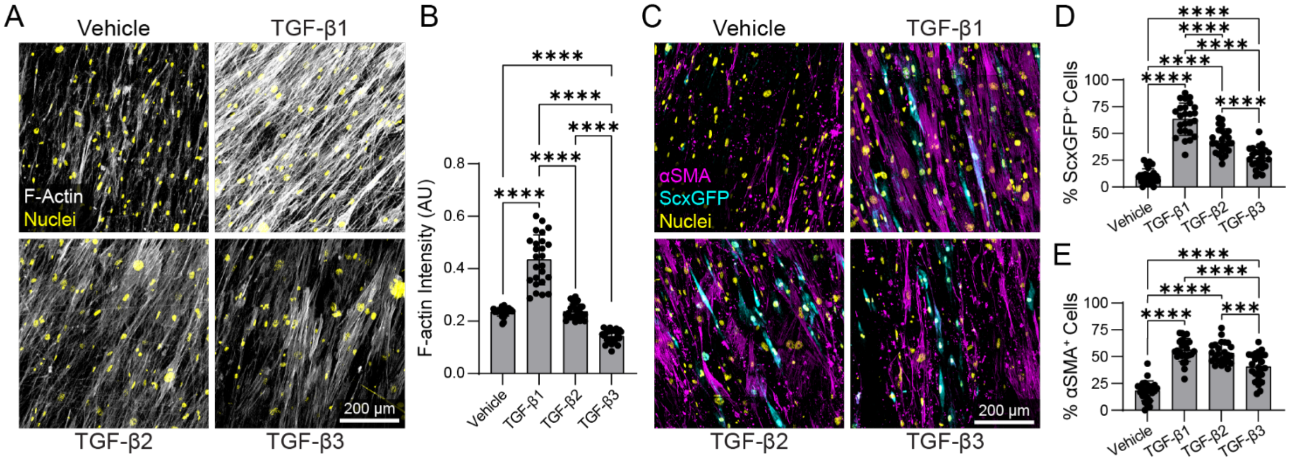

Figure 4.4: TGF-β isoforms differentially regulate a tenogenic vs. myofibroblastic fate switch. TPCs were cultured for 7 days on aligned fiber-coated coverslips in basal media or supplemented with various isoforms of TGF-β. **A**) Fluorescent images of TPCs stained for F-actin. **B**) Quantification of F-actin intensity (AU) (n = 25 FOVs, N = 2). **C**) Fluorescent images of *ScxGFP* reporter TPCs stained for αSMA. Quantification of % of TPCs expressing (**D**) *ScxGFP* and (**E**) *αSMA* (n = 25 FOVs, N = 2). All data are reported as mean ± standard deviation. Asterisks indicate statistically significant comparisons, with ***p<0.001 and ****p<0.0001 by ordinary one-way ANOVA with Tukey's multiple comparisons test or Student's t-test.

4.4.4 TGF-β3-induced tenogenesis is a mechanosensitive process dependent on actomyosin contractility

To determine whether the contractile state of TPCs impacts tenogenic vs. myofibroblastic differentiation in response to TGF-β, we next interrogated direct regulators of actin organization and dynamics to elucidate cytoskeletal mediators of this fate switch (D. L. Matera et al., 2021). Over the course of 7 days, TPCs on aligned fibrous substrates were supplemented every 48 hours with a small molecule agonist of Rho/Rho-kinase (ROCK) (lysophosphatidic acid [LPA]) or inhibitors of Rho/ROCK (Y27632 or H1152), Rac1 (NSC23766), Cdc42 (ML141), or myosin activity (blebbistatin) (**Figure 4.5A**). Rho/ROCK agonism and Rac1 inhibition both resulted in decreased *ScxGFP* expression in TGF-β3-treated TPCs, while Rho/ROCK, Cdc42, and myosin inhibition all resulted in increased *ScxGFP* expression (**Figure 4.5B-C**). Rho/ROCK inhibition resulted in the largest increase in *ScxGFP* expression, but treatment with H1152 limited cell proliferation more than Y27632 treatment (**Supplemental Figure 4.2**), so the latter was used in subsequent 2D studies.

To assess the effect of ROCK inhibition on the contractile state of the cell during tenogenic differentiation, identical samples were fixed at day 0, 2, 4 and 6. Rho/ROCK inhibition via Y27632 enhanced *ScxGFP* expression over the course of the study, led to diminished F-actin stress fiber intensity, and almost completely abrogated αSMA expression observed in TPCs treated with TGF-β3 only (**Figure 4.5D-E**). Actin stress fibers terminate at cell-ECM adhesions (i.e., focal adhesions) (Abercrombie et al., 1971; Burridge et al., 1988); focal adhesions are typically visualized by the protein vinculin, which is recruited to focal adhesions in a force-dependent manner (Carisey et al., 2013; Grashoff et al., 2010). Supporting the above observations, the diminished contractile state induced by Rho/ROCK inhibition was substantiated by a reduction in vinculin intensity within focal adhesions despite a consistent number of focal adhesions per cell (**Figure 4.5F-H; Supplemental Figure 4.3**). Taken together, these data indicate that TGF-β3 exerts pleiotropic effects on TPCs, inducing proliferation and promoting tenogenesis, but also enhancing contractility, which appears to predispose the cell toward myofibroblastic as opposed to tenogenic differentiation. While there appears to be some tenogenic advantage to using TGF-β3 instead of isoforms 1 or 2 (**Figure 4.4)**, Rho/ROCK inhibition further potentiates and hinders TGF-β3's tenogenic and pro-myofibroblastic effects, respectively.

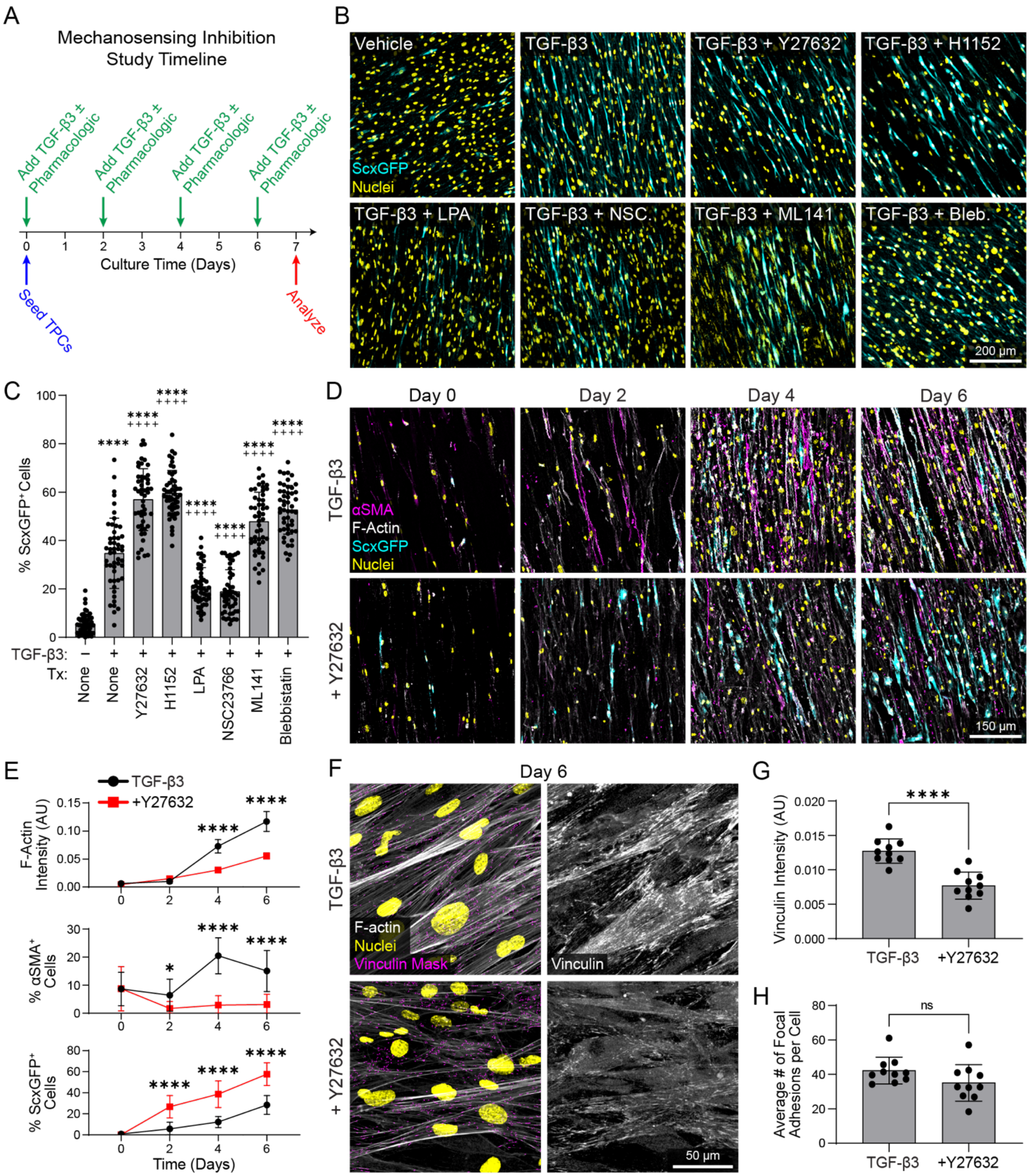

Figure 4.5: Rho/ROCK inhibition promotes TGF-β-mediated tenogenesis. A) *ScxGFP* reporter TPCs were cultured for 7 days on aligned fiber-coated coverslips in basal media containing TGF-β3 and supplemented with various pharmacologics targeting Rho GTPase regulators of actin cytoskeleton dynamics or myosin. **B**) Fluorescent images of *ScxGFP* reporter TPCs. **C**) Quantification of % of TPCs expressing *ScxGFP* (n = 50 FOVs, N = 3). Statistical indicators represent comparisons to basal media (*) and media supplemented with TGF-β3 only

(+). **D**) Fluorescent images of identical TPC cultures supplemented with TGF-β3 or TGF-β3 and Y27632 (+Y27632), fixed on days 0, 2, 4, and 6; samples were stained for F-actin and αSMA for quantitative analysis. **E**) Quantification of F-actin intensity (AU), % of TPCs expressing *ScxGFP*, and % of TPCs expressing αSMA (n = 25 FOVs, N = 2). **F**) Fluorescent images of TPC cultures fixed on day 6 and stained for vinculin. The binarized vinculin mask denotes focal adhesions and regions within which vinculin intensity was quantified. Quantification of (**G**) vinculin intensity (AU) and (**H**) average number of focal adhesions per cell (n = 10 FOVs). All data are reported as mean ± standard deviation. Asterisks indicate statistically significant comparisons, with ****$p<0.0001$ by ordinary one- or two-way ANOVA with Tukey's multiple comparisons test or Student's t-test (ns denotes a non-significant comparison).

4.4.5 3D fiber density and alignment influence spreading and alignment of TPCs but not early tenogenesis

Apart from pharmacologic disruption of actomyosin contractility, myofibroblastic differentiation can also be inhibited by culturing cells on or in soft hydrogel substrates, which is well-known to decrease cell contractility (X. Huang et al., 2012). In previous work, we showed that a DexVS hydrogel crosslinked with an MMP-labile peptide (VPMS) and reinforced with RGD-functionalized DexVS fibers promotes TPC recruitment from a mouse epitenon (Kent et al., 2022). Compared to fibronectin- and DexVS fiber-coated glass coverslips (on the order of multiple GPa) (Ford and Rajagopalan, 2018), FRHCs possess far lower bulk moduli on the order of 0.5-6 kPa (D. L. Matera et al., 2020; D.L. Matera et al., 2019). Anticipating a potential shift in the pleotropic effects of TGF-β in this softer, 3D microenvironment, we re-tested the three TGF-β isoforms for their ability to induce *ScxGFP* expression in TPCs encapsulated in FRHCs with the same crosslinking density as in our previous work (15.0 mM VPMS) (Kent et al., 2022). Consistent with our prior work, the inclusion of randomly oriented, cell-adhesive (RGD-functionalized) fiber segments in FRHCs enabled contact guidance of encapsulated TPCs, resulting in cells attaining a spindle morphology (**Figure 4.6**) (Kent et al., 2022; Thrivikraman et al., 2021). Similar to our findings on 2D fibrous substrates (**Figure 4.4**), exogenous addition of TGF-β3 was associated with the greatest increase in *ScxGFP* expression and the smallest increase in *αSMA* expression compared to the vehicle control (**Figure 4.6A-B**). We also observed a marked decrease in the proportion of *αSMA*$^+$ TPCs in soft, 3D hydrogels as compared to stiff, 2D settings, likely due to the influence of decreased matrix stiffness and dimensionality on cell adhesion and actomyosin contractility, both of which generally are required for myofibroblastic differentiation (**Figures 4.4E, 4.6B**) (X. Huang et al., 2012; D. L. Matera et al., 2020). TGF-β1 signaling is known to exhibit different downstream transcriptional effects in regenerative (MRL-MpJ) vs. fibrotic (adult C57BL/6) tendon healing environments, where C57BL/6 tendons show positively-enriched inflammatory and fibrotic pathways (Kallenbach et al., 2022). Future work should therefore assess the broader transcriptional profiles of TPCs as a function of exposure to different isoforms of TGF-β.

To study the role of fibrous topographical alignment in tenogenesis in 3D, we developed a microfluidic chip capable of flow-aligning fiber segments, resulting in FRHCs with distinct domains possessing non-aligned or aligned fibers. Independent of fiber alignment, TPCs consistently contact-guided along embedded fibers to achieve uniaxial, spindle morphologies, but at a population level, adopted an orientation reflecting global fiber alignment (**Figure 4.6C**). Surprisingly, neither fiber density nor alignment influenced *ScxGFP* expression of encapsulated TPCs (**Figure 4.6D-E**). A potential explanation for the disparate influences of fiber alignment in 2D vs. 3D may lie in the difference between how TPCs engage adhesive fibers across these two settings. While TPCs on 2D fibrous substrates engage multiple fibers simultaneously, thereby disrupting their spindle morphology on randomly oriented substrates, TPCs in 3D FHRCs typically engaged only a single fiber, regardless of overall fiber alignment. As such, TPC in FHRCs consistently achieved a spindle morphology whether encapsulated fibers were collectively aligned or disorganized. These observations further support the notion that a spindle morphology is a pro-tenogenic cytoskeletal state for TPCs, but they also suggest that tenogenesis is not influenced by the collective organization of TPCs.

MMP-labile crosslink density influences hydrogel stiffness but also modulates cell spreading kinetics in 3D (Long et al., 2022; Trappmann et al., 2017), and so we additionally screened crosslinking density for its effect on TPC morphology and *ScxGFP* expression. We noted a TGF-β3-mediated increase in nuclear ScxGFP intensity in FHRCs crosslinked with 17.5 mM compared to 12.5 mM VPMS; however, heightened crosslinking also resulted in diminished spreading of the TPCs, motivating the use of a crosslinker concentration of 15.0 mM for all subsequent 3D studies (**Supplemental Figure 4.4**). With heterogeneous spreading noted across the crosslinking densities tested in this study, readouts of cytosolic ScxGFP intensity were likely confounded, and so this design decision was based primarily on nuclear ScxGFP intensity.

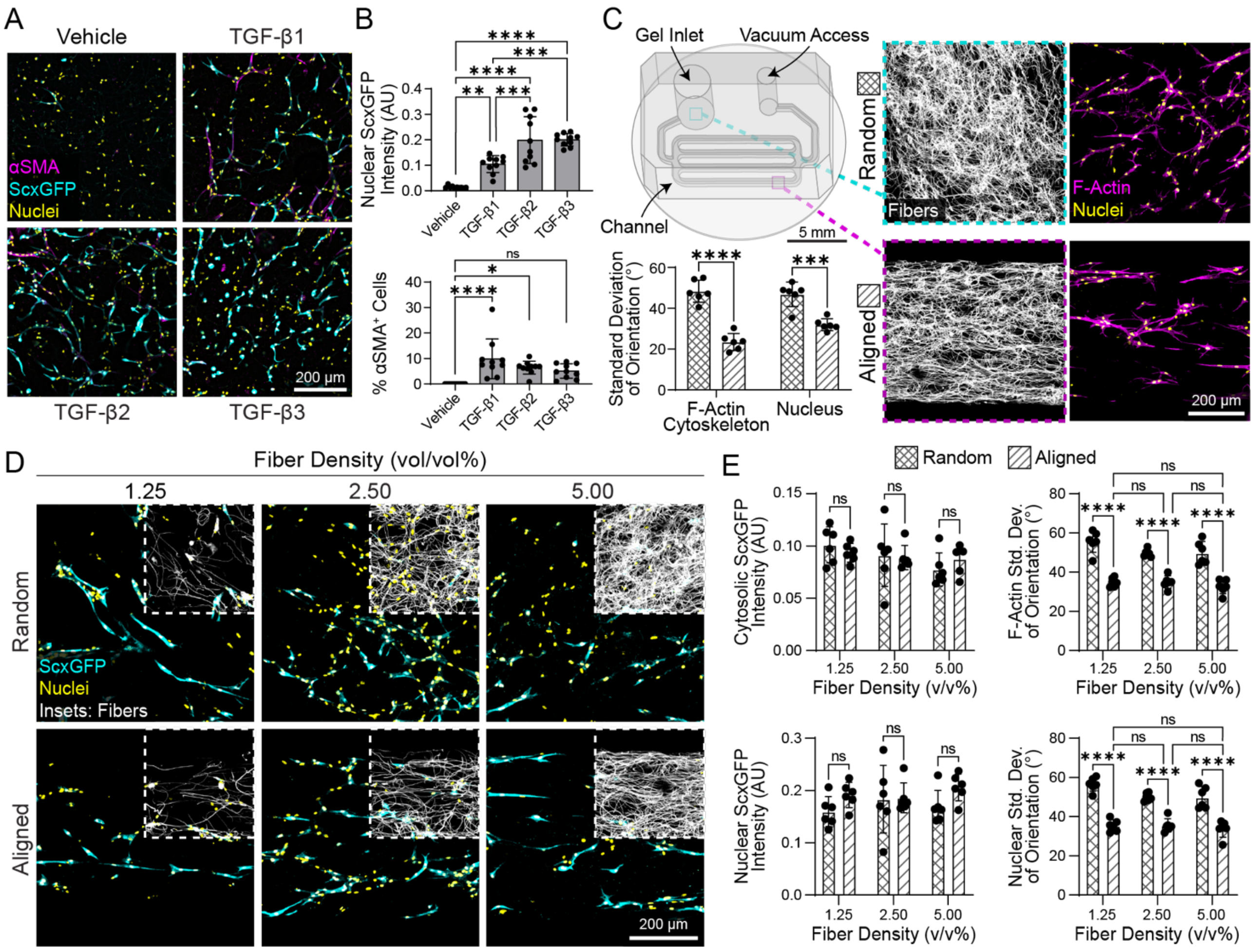

Figure 4.6: TPC spreading and tenogenesis in fiber-reinforced hydrogel composites (FRHCs) with tunable topographical anisotropy. **A**) Fluorescent images of *ScxGFP* reporter TPCs encapsulated in DexVS FRHCs and cultured for 7 days in basal media or supplemented with various isoforms of TGF-β. **B**) Quantification of nuclear ScxGFP intensity (AU) and % of cells expressing αSMA (n = 10 FOVs). **C**) Schematic of microfluidic flow-alignment device used to generate FRHCs with anisotropic fibrous topography. Fluorescent images of fibers and TPCs fixed after 7 days of culture in random and flow-aligned regions of the device. Quantification of standard deviation of orientation (°) of TPC cytoskeletons and nuclei (n = 6 FOVs). **D**) Fluorescent images of TPCs cultured for 7 days with TGF-β3 in DexVS FRHCs with varying fiber density and alignment. **E**) Quantification of nuclear and cytosolic ScxGFP intensity (AU) in addition to the standard deviation of orientation (°) of TPC cytoskeletons and nuclei (n = 6 FOVs, N = 3). All data are reported as mean ± standard deviation. Asterisks indicate statistically significant comparisons, with *$p<0.05$, **$p<0.01$, ***$p<0.001$, and ****$p<0.0001$ by ordinary one- or two-way ANOVA with Tukey's multiple comparisons test (ns denotes a non-significant comparison).

4.4.6 Inhibition of cell contractility potentiates tenogenesis in 3D microenvironments

To confirm the pro-tenogenic influence of Rho/ROCK inhibition identified in our earlier 2D studies (**Figure 4.5B-C**) on *ScxGFP* expression in 3D, TPCs in aligned FHRCs were treated with TGF-β3, Y27632, or both over the course of one week. Y27632 dosing was screened again in 3D, and 10 μM was found to yield a more consistent increase in *ScxGFP* expression compared to the 30 μM dose employed in 2D studies (**Figure 4.7A-B; Supplemental Figure 4.5**). While *ScxGFP* expression was primarily driven by TGF-β3, Rho/ROCK inhibition via Y27632 resulted in an additional, albeit marginal increase in *ScxGFP* expression that was most prominent intranuclearly, suggesting a possible relationship between the contractile state of TPCs and nuclear localization of Scleraxis (**Figure 4.7A-B**). We speculate that there may be biological significance to this apparent nuclear localization given the role of Scleraxis as a transcription factor, but future work is needed to delineate the roles of nuclear vs. cytoplasmic Scleraxis as it pertains to tenogenic differentiation. Screening the same panel of canonical tenogenic genes as in 2D studies (**Figure 4.2**), we found that exogenous TGF-β3 addition to Rho/ROCK-inhibited TPCs resulted in marked upregulation of *Scx*, *Tnc*, *Mkx*, *Fmod*, *Bgn*, *Dcn*, and *Col1a2*, indicating more robust tenogenesis of TPCs in FRHCs as compared culture on 2D substrates (**Figure 4.7C**). We hypothesize that the combined influences of a softer microenvironment and Rho/ROCK inhibition better promote tenogenesis over myofibroblastic differentiation. Dimensionality may also play a role in this fate switch because, in contrast to 2D cultures, 'substrate stiffness' in 3D cultures is related to crosslinking density, which is at the same time inhibitory to cell spreading and myofibroblastic differentiation (D. L. Matera et al., 2020).

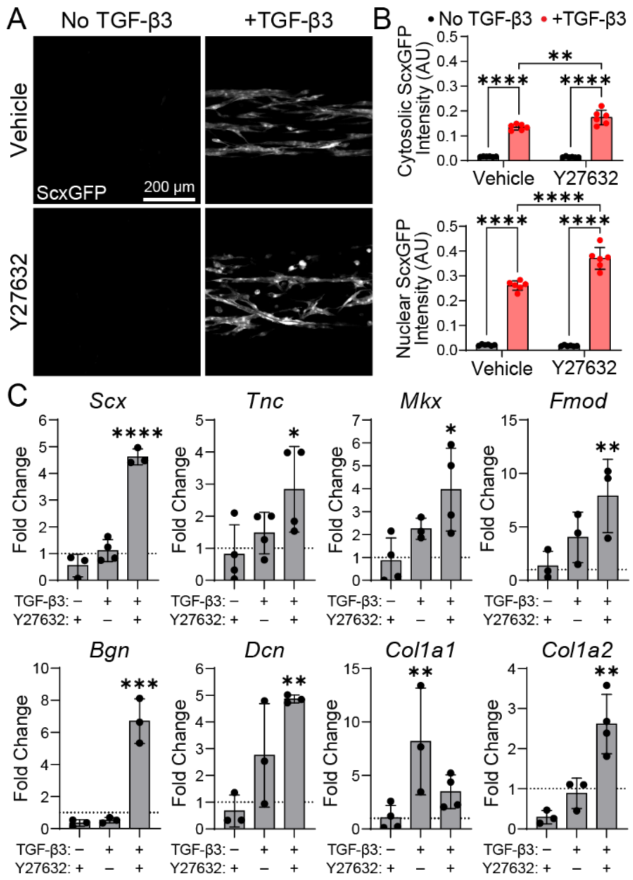

Figure 4.7: Rho/ROCK inhibition potentiates TGF-β-mediated tenogenesis in 3D. A) Fluorescent images of *ScxGFP* reporter TPCs encapsulated in flow-aligned FRHCs and cultured for 7 days in basal media or supplemented with Y27632, TGF-β3, or both. **B**) Quantification of cytosolic and nuclear ScxGFP intensity (AU) (n = 6 FOVs, N = 2). **C**) Fold change in expression of canonical tenogenic genes by TPCs encapsulated in FRHCs and treated with Y27632, TGF-β3, or a combination for 7 days (n = 3, N = 2). A fold change of 1 is denoted with a black, dotted line. All data are reported as mean ± standard deviation. Asterisks indicate statistically significant comparisons, with $*p<0.05$, $**p<0.01$, $***p<0.001$, and $****p<0.0001$ by ordinary one- (soluble condition) or two-way (TGF-β3 treatment, Y27632 treatment) ANOVA with Tukey's multiple comparisons test.

4.4.7 Topographical alignment templates de novo matrix production

While fiber orientation in 3D did not impact tenogenesis over short-term, 1 week-long studies (**Figure 4.6**), we hypothesized that topographical anisotropy may yet influence long-term maintenance of the tenogenic phenotype and the organization of *de novo* collagen synthesized by differentiated TPCs. Therefore, we performed 4-week studies examining the effect of TGF-β3 treatment as a function of fiber alignment on TPC tenogenesis and matrix deposition in FHRCs. Similar to observations at 1 week, heightened *ScxGFP* expression was driven only by TGF-β3 treatment and remained insensitive to fiber alignment (**Figure 4.8A-D**).

A critical outcome of robust tenogenesis in the context of tendon healing is the deposition of aligned collagen fibrils capable of bearing the tensile loads required of tendons. Matrix organization is particularly important, as this is a major delineator between functional tendon and scar tissue, both of which are predominantly composed of type I collagen (Kastelic et al., 1978; Sharma and Maffulli, 2006; Thomopoulos et al., 2015; F. Wu et al., 2017a). Moreover, with *Dcn*, *Tnc*, and *Col1a1* all being heavily implicated in fibrosis in other organs (Baghy et al., 2012; Bhattacharyya et al., 2022), maturity and organization of *de novo* collagen fibrils represents a critical feature of tendon healing. To assess these more salient outcomes, cryosections from FHRCs cultured for 4 weeks were stained with Picrosirius Red to visualize fibrillar collagens, providing a measure of collagen content, but also a measure of the maturity and alignment of the collagen fibrils via birefringence imaged under polarized light (Rittie, 2017). Picrosirius Red staining showed that topographical alignment had no effect on the amount of collagen deposited but drastically improved the maturity (i.e., fibril size and intra-fibrillar crosslinking) and alignment of *de novo* collagen fibrils, as measured by birefringence under polarized light (**Figure 4.8E-H**). Collagen content showed a dose-dependent relationship with fiber density, with composites containing 2.5 v/v% fibers achieving ~60% collagen by weight (**Figure 4.8I-K**); this is notable given that native tendon is 60-85% collagen by weight (Duscher and Schiffman, 2019; Kastelic et al., 1978). *De novo* collagen fibrils showed increased maturity and alignment with increasing fiber density, but this relationship reversed above 2.5 v/v% (**Figure 4.8L**). This diminishing return in *de novo* collagen maturity and organization with respect to synthetic fiber density could be attributed to TPC engagement to multiple fibers, which may confound cell alignment as compared to engagement to fewer fibers (Baker et al., 2015; Thrivikraman et al., 2021). This phenomenon may be akin to our observations in 2D, where engagement to abundant, randomly oriented fibers disrupted TPCs' ability to achieve a spindle morphology (**Figure 4.3C**).

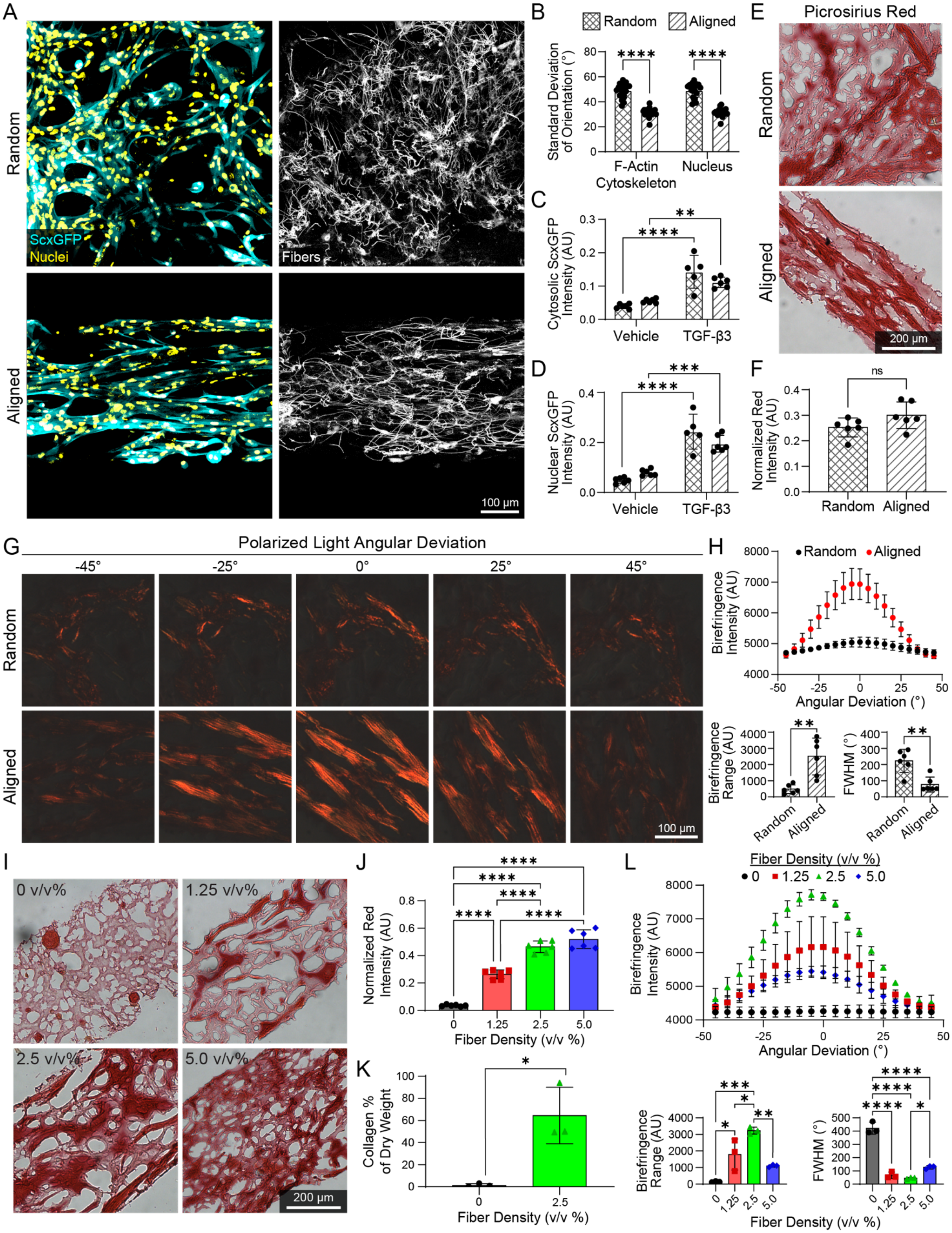
A
Random
Aligned
ScxGFP
Nuclei
Fibers
100 μm
B
Random
Aligned
Standard Deviation of Orientation (°)
80
60
40
20
0
****
****
F-Actin Cytoskeleton
Nucleus
C
Cytosolic ScxGFP Intensity (AU)
0.3
0.2
0.1
0.0
**
****
Vehicle
TGF-β3
D
Nuclear ScxGFP Intensity (AU)
0.4
0.2
0.0
***
****
Vehicle
TGF-β3
E
Picrosirius Red
Random
Aligned
200 μm
F
Normalized Red Intensity (AU)
ns
0.4
0.3
0.2
0.1
0.0
Random
Aligned
G
Polarized Light Angular Deviation
-45°
-25°
0°
25°
45°
Random
Aligned
100 μm
H
Random
Aligned
Birefringence Intensity (AU)
8000
7000
6000
5000
4000
-50
-25
0
25
50
Angular Deviation (°)
Birefringence Range (AU)
4000
3000
2000
1000
0
**
Random
Aligned
FWHM (°)
400
300
200
100
0
**
Random
Aligned
I
0 v/v%
1.25 v/v%
2.5 v/v%
5.0 v/v%
200 μm
J
Normalized Red Intensity (AU)
0.8
0.6
0.4
0.2
0.0
****
****
****
****
****
0
1.25
2.5
5.0
Fiber Density (v/v %)
K
Collagen % of Dry Weight
100
80
60
40
20
0
*
0
2.5
Fiber Density (v/v %)
L
Fiber Density (v/v %)
0
1.25
2.5
5.0
Birefringence Intensity (AU)
8000
7000
6000
5000
4000
-50
-25
0
25
50
Angular Deviation (°)
Birefringence Range (AU)
4000
3000
2000
1000
0
***
*
*
**
0
1.25
2.5
5.0
FWHM (°)
500
400
300
200
100
0
****
****
****
*
0
1.25
2.5
5.0
Fiber Density (v/v %)

Figure 4.8: 3D aligned fibrous topography templates *de novo* collagen deposition in FHRCs. **A**) Fluorescent images of *ScxGFP* reporter TPCs encapsulated in FRHCs with varying fiber alignment and cultured for 4 weeks with TGF-β3. Quantification of (**B**) standard deviation of orientation (°) of TPC cytoskeletons and nuclei, (**C**) cytosolic ScxGFP intensity, and (**D**) nuclear ScxGFP intensity (n = 6 FOVs, N = 2). **E**) Brightfield images of Picrosirius Red-stained frozen sections of 4-week TPC cultures in random and aligned FRHCs. **F**) Quantification of normalized red intensity (AU) (n = 6, N = 2). **G**) Polarized light images of random and aligned 4-week FRHC cultures over a range of angular deviation. **H**) Quantification of birefringence intensity (AU) as a function of angular deviation (°), birefringence range (AU), and full width at half maximum (°) (n = 6 FOVs, N = 2). **I**) Brightfield images of Picrosirius Red-stained sections of 4-week TPC cultures in flow-aligned FRHCs with varying fiber density. Quantification of (**J**) normalized red intensity (AU) (n = 6 FOVs), (**K**) collagen % dry weight (n = 3 hydrogels), and (**L**) birefringence intensity (AU) as a function of angular deviation (°), birefringence range (AU), and full width at half maximum (FWHM) (°) (n = 3 FOVs). All data are reported as mean ± standard deviation. Asterisks indicate statistically significant comparisons, with *$p<0.5$, **$p<0.01$, ***$p<0.001$, and ****$p<0.0001$ by ordinary one- or two-way ANOVA with Tukey's multiple comparisons test or Student's t-test (ns denotes a non-significant comparison).

4.4.8 Tenogenesis of human tendon-derived cells in FRHCs is donor-dependent

To assess the translatability of our material design parameters derived from murine TPCs, we isolated tendinopathic TDCs from human donors and cultured them in the conditions optimized above. The average age of these patients was 57 ± 6.6 years (range: 50-63 years; all female), which is within the typical age range of patients presenting with insertional Achilles tendinitis or biceps tendinopathy associated with rotator cuff disease (**Figure 4.9A**) (Murthi et al., 2000; van der Vlist et al., 2019). For Donors 1 and 2 (Achilles), portions of the tissue sample were sectioned and stained with Hematoxylin and Eosin to obtain Bonar tendinopathy scores of 4 and 9, respectively, suggesting that TDCs from Donor 2 originated from a more tendinopathic environment than those from Donor 1 (**Supplemental Figure 4.7**). A tendinopathy score for Donor 3's tissue was not obtained (**Figure 4.9A**), but this patient had a diagnosis of chronic biceps tendinopathy that was confirmed intraoperatively.

To assess the effects of TGF-β3 and cytoskeletal contractility on early tenogenesis of human TDCs in FRHCs, TDCs from each donor were cultured in fibrous (2.5 v/v%) DexVS hydrogels for 1 week, supplemented either with TGF-β3 or a combination of TGF-β3 and Y27632. With combined TGF-β3 treatment and Rho/ROCK inhibition, while TDCs from Donor 1 showed positive fold changes in MKX, TNC, TNMD, and COL1A1, Donor 2 generally showed no change in expression of these genes, and Donor 3 exhibited significant downregulation of TNC, TNMD, and COL3A1 (**Figure 4.9B**). Overall, none of the three TDC populations upregulated canonical tenogenic genes to the same extent as murine TPCs (**Figure 4.7C, 4.9B**).

To evaluate deposition and organization of *de novo* collagen, samples were cultured in flow-aligned FRHCs (2.5 v/v% fibers) for 2-4 weeks with or without TGF-β3 supplementation. 3D cultures from Donors 1 and 2 began to contract away from the underlying glass substrate at 2 weeks, and so they were fixed in paraformaldehyde at that timepoint while Donor 3's culture was able to proceed to 4 weeks without issue. At their endpoints, frozen sections of FRHCs were stained with Picrosirius Red (**Figure 4.9C**). Intuitively, TGF-β3 treatment resulted in increased collagen deposition by TDCs from Donors 1 and 2. However, Donor 3's culture did not respond with increased collagen deposition with TGF-β3 treatment compared to vehicle controls (**Figure 4.9C-D**). The maturity and organization of *de novo* collagen was reflected via birefringence under polarized light in cultures from Donors 1 and 2, which showed greater birefringence intensity and dependence on sample orientation compared to that of Donor 3 (**Figure 4.9E-F**). TDCs also exhibited heightened αSMA and F-actin intensities via immunofluorescence in response to TGF-β3, implying myofibroblastic differentiation in all three donor cultures. A shift toward this myofibroblastic phenotype was most prominent in cultures from Donor 3 (**Supplemental Figure 4.8**). Taken together, these results demonstrate that the regenerative capacity of human TDCs varies as a function of donor source (i.e., patient, disease progression, and anatomical location). Epitenon-derived progenitor populations are known to contribute to both fibrotic and regenerative healing in humans, where the former population is characterized by enrichment of pro-fibrotic and pro-inflammatory genes (Nichols et al., 2023). With increasing severity of chronic inflammation, this progenitor pool may become depleted or biased toward a pro-fibrotic phenotype, precluding tenogenesis and limiting deposition of mature, aligned collagen fibrils during healing.

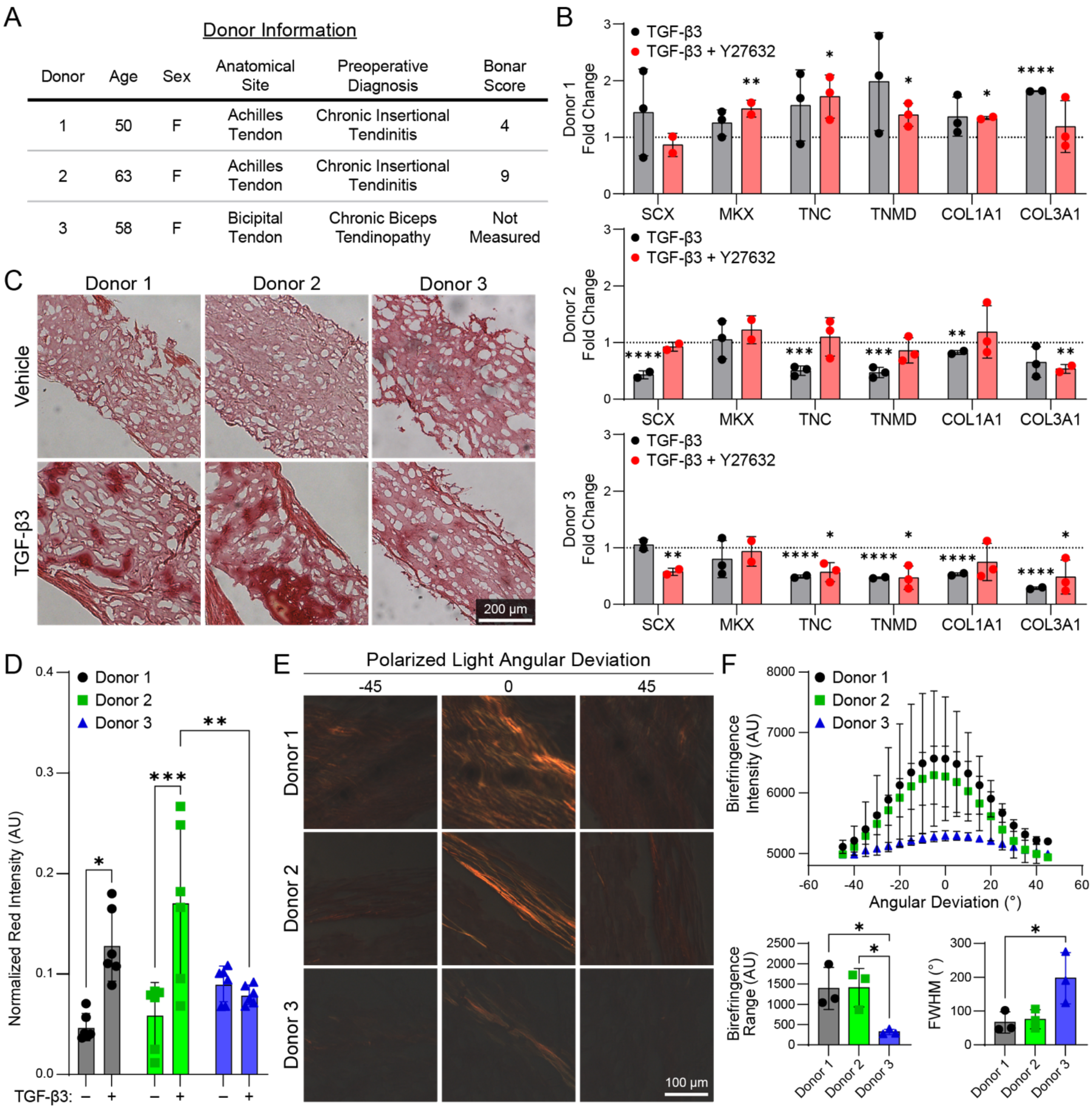

Donor	Age	Sex	Anatomical Site	Preoperative Diagnosis	Bonar Score
1	50	F	Achilles Tendon	Chronic Insertional Tendinitis	4
2	63	F	Achilles Tendon	Chronic Insertional Tendinitis	9
3	58	F	Bicipital Tendon	Chronic Biceps Tendinopathy	Not Measured

Figure 4.9: Human TDCs exhibit variable capacity for tenogenesis and organized collagen deposition. A) Demographic information and Bonar tendinopathy scores for 3 tendon tissue donors from whom human TDCs were isolated. **B**) Fold change in expression of canonical tenogenic genes by TDCs encapsulated in FRHCs and treated with TGF-β3 or a combination of TGF-β3 and Y27632 for 7 days (n = 3 hydrogels). A fold change of 1 is denoted with a black, dotted line. **C**) Brightfield images of Picrosirius Red-stained frozen sections of 2- (Donors 1 and 2) and 4-week (Donor 3) TDC cultures in flow-aligned FRHCs. **D**) Quantification of normalized red intensity (AU) (n = 6 FOVs). **E**) Polarized light images of aligned 2-4-week FRHC cultures with TGF-β3 over a range of angular deviation. **F**) Quantification of birefringence intensity (AU) as a function of angular deviation (°), birefringence range (AU), and full width at half maximum

(FWHM) (°) (n = 3 FOVs). All data are reported as mean ± standard deviation. Asterisks indicate statistically significant comparisons, with *p<0.05, **p<0.01, ***p<0.001, and ****p<0.0001 by ordinary one- or two-way ANOVA with Tukey's multiple comparisons test.

4.5 Conclusion

Here, we applied a combination of 2D and 3D engineered culture platforms to identify the salient physical and biochemical cues driving tenogenic differentiation and organized matrix deposition by murine TPCs and human TDCs. This work highlights a tenogenic vs. myofibroblastic fate switch as a function of TGF-β isoform, where TGF-β3 treatment, softer substrates, and actin cytoskeletal dysregulation by Rho/ROCK inhibition led to more complete tenogenic differentiation. While an aligned, fibrous topography drove tenogenesis of individualized TPCs in 2D, the impact of fiber alignment in 3D FRHCs was limited to the organization of *de novo* collagenous matrix, delineating the roles of cell spreading morphology and cellular organization in tenogenic differentiation and matrix remodeling, respectively. These findings inform design parameters of cell-free, injectable, synthetic hydrogels for tendon tissue regeneration. Finally, we showed that human TDCs exhibit heterogeneity with respect to their tenogenesis and matrix synthesis in response to TGF-β3. Cell-free therapies that depend on recruitment of endogenous progenitors will therefore require a better understanding of the pathways regulating a pro-fibrotic vs. pro-regenerative phenotype in these cell populations to uncover novel therapeutic targets. For example, next-generation FRHCs could modulate the soluble milieu to prime the immune response toward an M2-like phenotype, which is known to yield a more pro-regenerative tendon healing response (Arvind et al., 2021; E. Chung and Son, 2014; Schoenenberger et al., 2018; Spiller et al., 2015). Future work will therefore explore the effects of FRHC injection on TPC and immune cell recruitment, immune phenotype polarization, tenogenic differentiation of TPCs, and functional tendon regeneration in a murine Achilles tendon injury model.

4.6 Materials and methods

4.6.1 Reagents

All reagents were purchased from Sigma-Aldrich or Fisher Scientific and used as received, unless otherwise stated.

4.6.2 Cell isolation and culture

For all animal procedures, the Institutional Animal Care and Use Committee (IACUC) guidelines for survival surgery in rodents and the IACUC Policy on Analgesic Use in Animals Undergoing Surgery were followed (Protocol #PRO00009868). Murine cells used in this work were harvested from 12 6-9 week-old C57BL/6 mice (6 female, 6 male). A ScxGFP mouse colony was maintained by breeding ScxGFP$^{+/-}$ heterozygotes modified from a C57BL/6 background with WT C57BL/6J mice, and progeny were genotyped (ScxGFP$^{+/-}$ vs. ScxGFP$^{-/-}$) using a Dual Fluorescent Protein Flashlight (Model DFP-1, Nightsea, Lexington, MA). Tail tendons were removed from euthanized mice and then encapsulated in a 2 mg mL^{-1} type I collagen hydrogel. Encapsulated tissues were cultured in an incubator (37°C and 5% CO_2) in DMEM containing L-glutamine (ThermoFisher, Waltham, MA), 1 v/v% penicillin/streptomycin/fungizone, and 10 v/v% fetal bovine serum (termed ‘basal media’) for 10 days to allow tendon progenitor cells (TPCs) to migrate from tendons into the collagen gel (Shimada et al., 2014). Following isolation and expansion of TPCs, collagen gels were digested in 0.25 mg mL^{-1} collagenase from *C. histolyticum* with 0.025 w/v % trypsin-EDTA. The resulting slurry was filtered through a cell strainer and then plated. Adherent TPCs were cultured in basal media, and cells at passage 1 were used for all experiments. For studies where cell proliferation was inhibited, TPC cultures were treated with 40 μg mL^{-1} mitomycin C for two hours, washed with basal media, then incubated for at least one hour prior to trypsinization for use in studies.

Human tendon-derived cells (TDCs) were isolated from multiple sources in accordance with Institutional Review Board guidelines. One cell population was isolated from a chronically tendinopathic, proximal bicipital tendon that was harvested by a board-certified sports medicine surgeon (E.A.C.) during a biceps tenodesis (Protocol #HUM00226997). Two other populations were isolated from Achilles tendon tissue acquired during insertional debridement and repair procedures by a board-certified foot and ankle surgeon (P.G.T.) (Protocol #HUM00196928). All human TDCs were isolated from their respective tissues using previously described methods (Bi et al., 2007; Shimada et al., 2014).

4.6.3 Polymer synthesis

Dextran functionalized with vinyl sulfone groups (DexVS) was synthesized as previously described (Yu and Chau, 2012). Briefly, 5 g of 86 kDa dextran (MP Biomedicals, Irvine, CA) was dissolved in a 250 mL solution of 100 mM sodium hydroxide in Milli-Q water. On a stir plate set to 700 rpm, divinyl sulfone (Alfa Aesar, Haverhill, MA) was added to the solution, and the reaction proceeded for 3.5 minutes before termination by addition of 2.5 mL of 12 M hydrochloric acid. To achieve vinyl sulfone / dextran repeat unit ratios appropriate for hydrogel formation (16%) and fiber fabrication (65%), 3.88 mL and 12.5 mL of divinyl sulfone were added to the reactions, respectively. After vinyl sulfone addition, the product was dialyzed against Milli-Q water for 72 hours with twice-daily changes and then lyophilized for 72 hours to yield a dry product. All reaction products were characterized via ^{1}H NMR.

4.6.4 2D cell culture

For initial 2D studies screening tenogenic growth factors, glass coverslips were UV/ozone treated for 5 minutes prior to being incubated at 37°C in phosphate-buffered saline (PBS) containing 50 µg mL^{-1} fibronectin (Corning, Corning, NY) for 15 minutes. Fibronectin-functionalized coverslips were washed twice with PBS and then seeded with a suspension of TPCs in basal media (13,500 cells cm^{-2}).

To generate fiber-coated coverslips, an electrospinning solution was prepared containing 0.7 g mL^{-1} DexVS (65% vinyl sulfone functionalization) in 1:1 dimethyl formamide and Milli-Q water with 0.6 wt/v% lithium phenyl-2,4,6-trimethylbenzoylphosphinate (LAP; Colorado Photopolymer Solutions, Boulder, CO) photoinitiator, and (1) 2.5 v/v% methacrylated rhodamine (25 mM; Polysciences, Inc., Warrington, PA) for fluorescent visualization or (2) 5.0 v/v% glycidyl methacrylate when fluorescent labeling was not required. In a humidity-controlled glovebox (21°C, 30-35% humidity), DexVS fibers (1 µm diameter) (D. L. Matera et al., 2020) were electrospun onto 18 mm glass coverslips mounted to a grounded mandrel with a gap distance of 7 cm, voltage of -5.5 kV, and a flow rate of 0.2 mL hr^{-1}. The mandrel was rotated at 100 rpm (0.92 m s^{-1} surface speed) or 2100 rpm (19.3 m s^{-1} surface speed) to respectively yield random and aligned fiber orientations. Fibers were primarily photocrosslinked dry (100 mW cm^{-2} UV light) for 2 minutes and then secondarily crosslinked in a solution of 1 mg mL^{-1} LAP for 20 seconds. Coverslips were then washed twice with PBS and then incubated at 37°C for 15 minutes in a 1.0 mM solution of cell-adhesive CGRGDS (RGD) in 50 mM 4-(2-hydroxyethyl)-1-

piperazineethanesulfonic acid (HEPES) buffer containing 10 μg mL^{-1} phenol red and buffered to a pH of 8.0 with sodium hydroxide. RGD-functionalized fiber-coated coverslips were then washed twice with PBS prior to seeding with a suspension of TPCs in basal media (13,500 cells cm^{-2}).

4.6.5 Fiber segment fabrication and functionalization for FHRCs

An electrospinning solution was prepared by dissolving DexVS (65% vinyl sulfone functionalization) at 0.7 g mL^{-1} in a 1:1 solution of dimethyl formamide and Milli-Q water with 0.015 wt/v% 2-Hydroxy-4′-(2-hydroxyethoxy)-2-methylpropiophenone (Irgacure 2959) photoinitiator. For fluorescent visualization of fibers, methacrylated rhodamine (Polysciences, Inc., Warrington, PA) was added at 0.5 mM. In the same humidity-controlled glovebox described above, DexVS fibers were electrospun onto a slowly rotating (linear velocity 3.14 cm s^{-1}), grounded mandrel using a gap distance of 7 cm, voltage of -5.5 kV, and flow rate of 0.2 mL hr^{-1}. A UV lamp was directed at the opposite side of the mandrel; every 15 minutes, the lamp was turned on for 5 minutes to expose deposited fibers to 100 mW cm^{-2} UV light. Intermittent UV exposure over the course of layer-by-layer fiber deposition ensured that fibers were adequately and uniformly photocrosslinked. The resulting fiber segments had the same diameter as those spun onto glass coverslips for 2D studies (1 μm diameter) (D. L. Matera et al., 2020).

The crosslinked fiber mat was removed from the mandrel and transferred to Milli-Q water. Two rounds of pipetting, vortexing, centrifugation, and resuspension were performed to break up the fiber mat into individual fiber segments and remove clumps and residual crosslinking reagents. Purified fibers were resuspended at 10 v/v% in PBS and stored in a light-protected box at 4°C. Prior to incorporation in hydrogel constructs, fiber segments were functionalized by resuspension at 10 v/v% in 50 mM HEPES buffer along with cell-adhesive CGRGDS (RGD) (2.0 mM) and 5 mM sodium hydroxide. Functionalization proceeded via Michael-type addition at 37°C for 15 minutes, then fibers were washed with PBS and resuspended in HEPES buffer.

4.6.6 Fabrication of FRHCs

DexVS hydrogels were formed using previously described methods (D.L. Matera et al., 2019). Briefly, DexVS was dissolved in PBS containing 50 mM HEPES buffer. Either cell-adhesive RGD or scrambled CGRDGS (RDG) was incorporated at 2.0 mM. Additionally, to neutralize residual VS groups and prevent unintended crosslinking, cysteine was added at 9.1 mM. After this pre-reaction proceeded on ice for 20 minutes, cells and functionalized fiber segments were added to the mixture followed by the addition of an MMP-cleavable, dithiolated GCRDVPMSMRGGDRCG (VPMS) crosslinking peptide. Bulk stiffnesses ranging from 0.5-6 kPa were achieved by crosslinking DexVS hydrogels with 12.5-27.5 mM VPMS, respectively; DexVS concentrations of 3.30-4.13 wt/v% were used to ensure that the ratio of free vinyl sulfone groups to VPMS molecules were consistent across crosslinking densities (D. L. Matera et al., 2020). Gelation via Michael-type addition was initiated by addition of sodium hydroxide (33 mM).

Hydrogel composites were cast in circular molds to generate gels with isotropic fibrous topography. Polydimethylsiloxane (PDMS) (Dow, Midland, MI) was prepared at a 1:10 crosslinker:base ratio, casted, and biopsy-punched to form circular molds (5 mm diameter, 1.8mm height). Molds were plasma etched, bonded to 18 mm glass coverslips, coated with a solution of 2 mg mL^{-1} porcine skin gelatin (to enable eventual de-adhesion from the hydrogel), and dried in an 80°C oven for 20 minutes. 35 µL of FHRC precursor suspension was added to each mold, and crosslinking proceeded at 37°C for 45 minutes. A rotisserie rotated the sample at 5 rpm to prevent cells and fibers from settling under gravity prior to gelation. After crosslinking, FHRCs were hydrated in basal media and released from the molds the following morning.

A 4-channel microfluidic chip was designed to flow-align fibers within FHRCs. The device was designed in SolidWorks (Dassault Systèmes, Vélizy-Villacoublay, France), and a master mold was 3D printed via a Formlabs Form 3 stereolithography printer with v4 resin (Formlabs, Somerville, MA). Printed molds were treated with trichloro(1H,1H,2H,2H-perfluorooctyl)silane to facilitate release of PDMS replica casts (1:25 crosslinker:base ratio). The softer PDMS was used in this instance to allow for an airtight seal to be formed with a glass coverslip without the need for plasma etching so that the molds could be easily removed after hydrogel crosslinking. 3 mm and 1.5 mm holes were punched in the inlet and vacuum ports of the device (**Figure 4.6C**), respectively, then devices were washed with isopropanol followed by ethanol. The device's 500x500 μm channels were coated with 2 mg mL^{-1} porcine skin gelatin and dried in an 80°C oven for 20 minutes to facilitate eventual de-molding of the FHRC. An 18 mm glass coverslip was plasma etched for 2 minutes and then functionalized with 3-mercaptopropyl triethoxysilane via overnight gas deposition so that the FHRC could covalently adhere to the coverslip via Michael-type addition. Molds were adhered noncovalently to thiolated coverslips, 30 μL hydrogel mixtures were added to the inlet ports, and gels were flowed into the devices using a syringe pump withdrawing 250 μL s^{-1}. Some gel was allowed to remain in the loading port so that there was a matched, isotropic region of the hydrogel to compare to the anisotropic regions within channels (**Figure 4.6C**). Crosslinking then proceeded in a 37°C rotisserie oven for 20 minutes, then devices were transferred to a 12-well plate in 1 mL of basal media and incubated at 37°C for an additional 25 minutes. Finally, PDMS molds were peeled from the coverslips, leaving the crosslinked FHRC (containing isotropic and anisotropic regions) covalently adhered to the glass.

4.6.7 Real-time quantitative PCR

Total RNA was isolated using Trizol reagent followed by phenol-chloroform separation. RNA yield was quantified using a Nanodrop spectrometer (ND-1000, Nanodrop Technologies, Wilmington, DE) in addition to A260/A280 to confirm a value between 1.6 and 2.1 for each isolate. cDNA was synthesized at 40-50 ng μL^{-1} using the SuperScript First Strand Synthesis kit (Invitrogen, Life Technologies, Carlsbad, CA), and cDNA samples were diluted to 0.2-0.8 ng μL^{-1} in amplification reactions solutions. Amplification was carried out using an Eppendorf Nexus GX2 thermocycler (Eppendorf, Hamburg, DE), with intron-spanning primers and Fast SYBR Green Reaction Mix (Applied Biosystems, Foster City, CA). Expression of genes of interest were determined and normalized to the housekeeping genes 40S ribosomal protein S29 (*S29*) or glyceraldehyde-3-phosphate dehydrogenase (GAPDH) for mouse and human samples, respectively, using the comparative Ct method.

For 3D cultures in DexVS hydrogel composites, single-cell suspensions were isolated prior to lysis in Trizol. A digestion solution was prepared in Accutase (Gibco, Billings, MT) containing 3 v/v% dextranase (Cellendes, Kusterdingen, Germany), 2 v/v% liberase, 0.5 mg mL^{-1} collagenase from *C. histolyticum*, and 2 mM ethylene glycol-bis(β-aminoethyl ether)-N,N,N′,N′-tetraacetic acid. Hydrogel composites were washed at 37°C in DMEM for 30 minutes to remove serum proteins and then transferred to the digestion solution (1 mL of digestion solution for every 105 µL of hydrogel). Digestion proceeded in a bacteria shaker set to 37°C and 300 rpm for 20-25 minutes. Digests were diluted in 5 mL of basal media, strained through a 70 µm filter, centrifuged at 500 g for 4 minutes, and resuspended in Trizol. RT-qPCR analysis was then performed as above.

4.6.8 Orthohydroxyproline assay

Hydrogel composites were flash-frozen at -80°C, lyophilized, then weighed to determine dry weights. Samples were then digested in papain(Mauck et al., 2006), and collagen content was determined via an orthohydroxyproline assay using previously described methods (Stegemann and Stalder, 1967). Briefly, papain digests were hydrolyzed in 6N HCl at 110°C in sealed ampoules for 16 hours. The hydrolyzed product was then dried in a vacuum over NaOH for 8 hours and then resuspended in a buffer containing citric acid monohydrate (5 wt/v%), acetic acid (1.2 v/v%), and sodium acetate trihydrate (12 wt/v%). 150 μL of samples and standards, serially diluted in buffer, were added to a 96-well plate, 75 μL of chloramine T solution was added to each well, then the plate was incubated at room temperature for 20 minutes. 75 μL of p-dimethylaminobenzaldehyde solution was then added, the plate was incubated in a 70°C water bath for 20 minutes, then the plate was cooled in an ice bath prior to reading absorbance at 540 nm. Hydroxyproline content was converted to collagen using a factor of 7.14 (Neuman and Logan, 1950). This conversion factor is an estimate and is therefore susceptible to slight bias based on the prevailing collagen type present.

4.6.9 Histology

Paraformaldehyde-fixed composite hydrogels were incubated in 30 wt/v% sucrose in PBS at 4°C overnight and then embedded in optimal cutting temperature (OCT) compound (SCIgen, Sunnyvale, CA) containing 30 wt/v% sucrose. After freezing on a bed of crushed dry ice, glass coverslips were removed from the embedded construct. Samples were then embedded in a larger block of OCT and then sectioned at 12 μm thickness (CM3050 Cryotome, Leica Microsystems, Wetzlar, Germany). Picrosirius Red staining was performed on sectioned samples to visualize fibrillar collagen content.

Portions of the two human Achilles tendon samples were separated prior to TDC isolation for tendinopathy scoring. These sample portions were fixed in 4% paraformaldehyde at 4°C, and paraffin-embedded sections (6 µm thickness) were stained with Hematoxylin and Eosin. Bonar scores were calculated based on cell morphology, collagen arrangement, cellularity, vascularity, and the presence of ground substance (Fearon et al., 2014). QuPath software was used to quantify cellularity and evaluate for presence of ground substance (Bankhead et al., 2017).

4.6.10 Microscopy and image analysis

Fluorescent images were captured on a Zeiss LSM800 confocal microscope. Samples were fixed in 4% paraformaldehyde, permeabilized in Triton X, and stained with phalloidin (Invitrogen, Waltham, MA) and Hoechst 33342 to visualize F-actin and nuclei, respectively. For studies assessing the extent of myofibroblastic differentiation, samples were stained with an antibody against α-smooth muscle actin (αSMA [1A4] mouse anti-mouse, ab7817, Abcam, Cambridge, UK). For studies examining focal adhesions, samples were simultaneously fixed and permeabilized at 37°C for 10 minutes; samples were then stained with an antibody against vinculin (vinculin [hVIN-1], mouse anti-mouse, V9264, Sigma Aldrich, St. Louis, MO). All FOVs acquired were mutually exclusive. To quantify fluorescent intensity in TPC monolayers, custom MATLAB code (MathWorks, Portola Valley, CA) was developed to quantify intensity within nuclei and in the cytosolic region immediately surrounding each nucleus. To quantify fluorescent intensity in 3D, Gaussian filters were applied to all images to remove noise and background. A custom MATLAB code demarcated nuclear and cytosolic regions (via Hoechst and F-actin stains) and quantified fluorescent intensity in voxels comprising each nucleus and cytosol. In general, nuclear

ScxGFP was brighter than cytosolic ScxGFP, potentially implying an intact nuclear localization sequence in the transgene construct that allows for active nuclear transport of ScxGFP (**Figure 4.**).

Brightfield (10x) and polarized light (40x) images of Picrosirius Red-stained hydrogel sections were acquired on a Zeiss Axioplan 2 upright microscope. A rotating stage was used to acquire images from -45° to 45° of deviation at 5° intervals, where deviation denotes orientation the long axis of the flow channel relative to the polarizer in aligned regions. For non-aligned (random) regions, a deviation of 0° was defined as the orientation showing the brightest birefringence. All FOVs acquired were mutually exclusive. Custom MATLAB code identified hydrogel regions in each image and quantified red intensity as the ratio of red to the sum of red, green, and blue intensity of each pixel. Another script identified a circular region of interest (100 μm radius) at the center of each polarized light image and quantified birefringent intensity as the average luminance within this region at each interval of angular deviation.

4.6.11 Statistics

Statistical significance was determined by one- or two-way analysis of variance (ANOVA) with Tukey's multiple comparisons test or two-sided student's t-test where appropriate ($\alpha = 0.05$). Datapoints were defined as outliers if they were >1.5 interquartile ranges from the median and excluded prior to statistical comparison. Sample size is indicated within corresponding figure legends, and all data are presented as mean ± standard deviation.

4.7 Supplemental figures

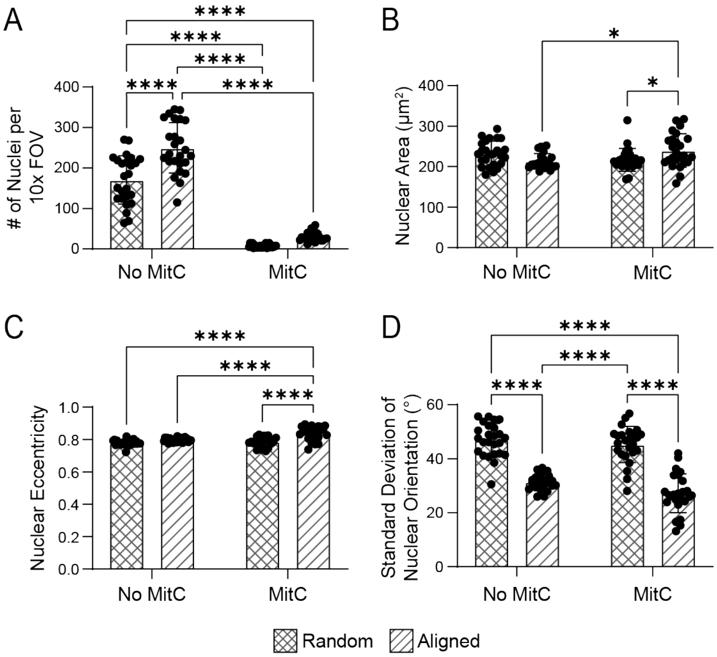

Supplemental Figure 4.1: Blocking cell proliferation minimally affects nuclear morphology or collective orientation. Quantifications of nuclear counts and morphology in TPCs cultured with TGF-β3 for 7 days on random and aligned, fiber-coated coverslips, with and without mitomycin C (MitC) pre-treatment. **A**) Number of nuclei per 10X FOV. **B**) Nuclear area (µm^2). **C**) Nuclear eccentricity. **D**) Standard deviation of orientation (°) of TPC nuclei. All data are reported as mean ± standard deviation, and n = 25 FOVs. Asterisks indicate statistically significant comparisons, with *p<0.05 and ****p<0.0001 by ordinary two-way ANOVA with Tukey's multiple comparisons test.

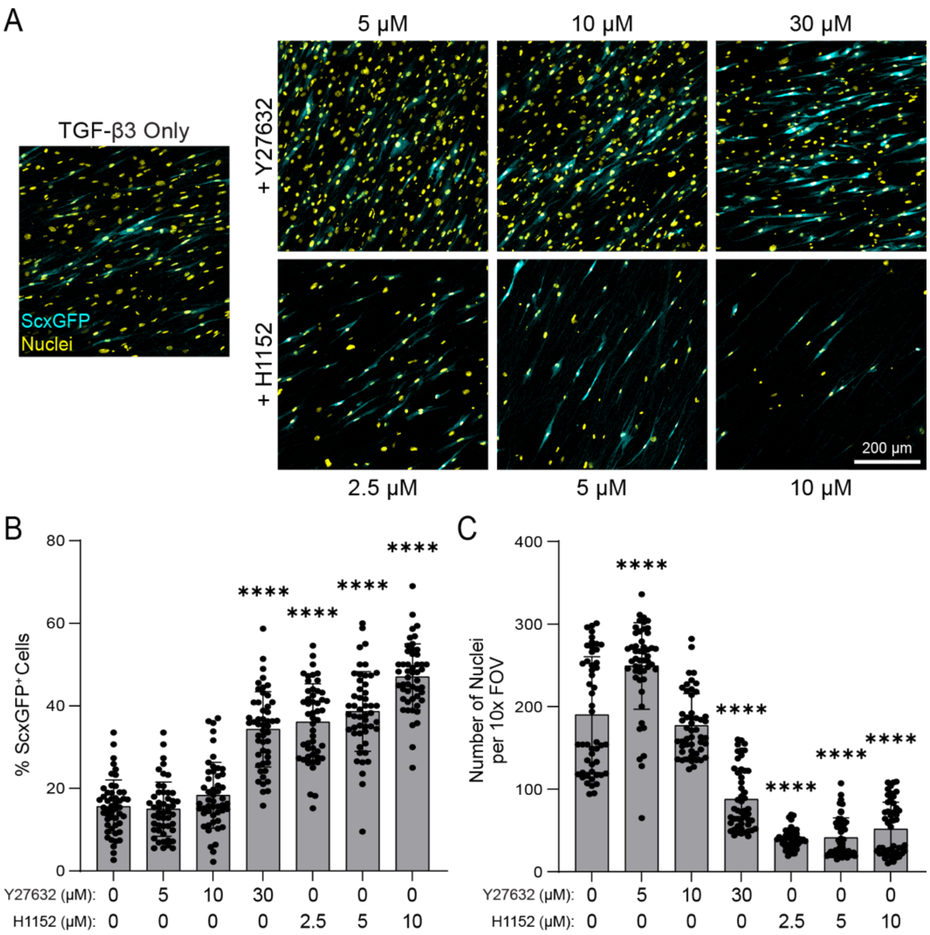

Supplemental Figure 4.2: Dose screens for Rho/ROCK inhibitors Y27632 and H1152. A) Fluorescent images of *ScxGFP* reporter TPCs cultured on aligned, fiber-coated coverslips for 7 days with TGF-β3, TGF-β3 and Y27632 (+Y27632), or TGF-β3 and H1152 (+H1152); inhibitors were tested at a range of doses. Quantification of (**B**) % of TPCs expressing *ScxGFP* and (**C**) number of nuclei per 10x FOV (n = 50 FOVs). All data are reported as mean ± standard deviation. Asterisks indicate statistically significant comparisons, with ****$p<0.0001$ by ordinary one-way ANOVA with Tukey's multiple comparisons test.

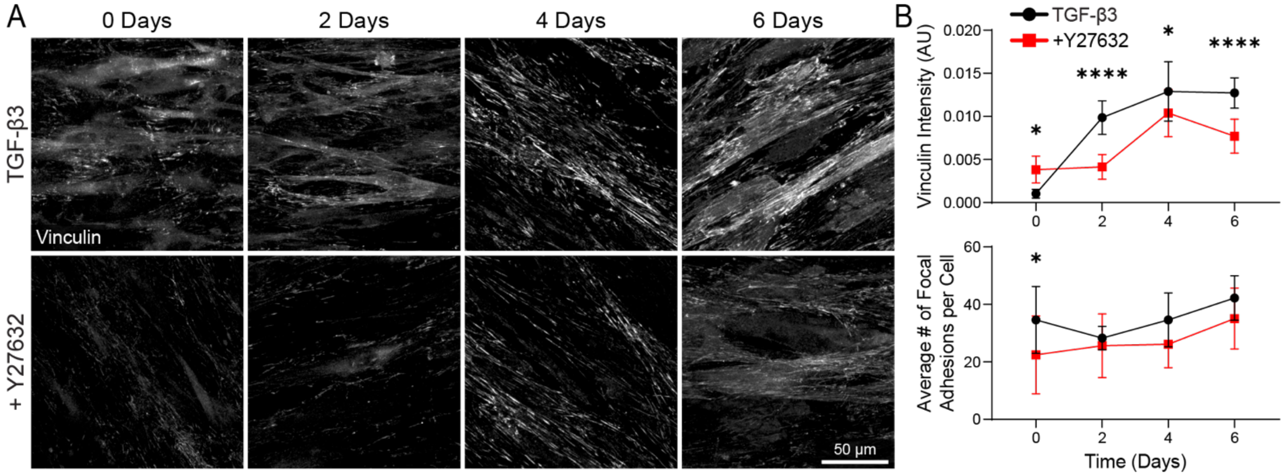
A
0 Days
2 Days
4 Days
6 Days
TGF-β3
+ Y27632
Vinculin
50 µm
B
TGF-β3
+Y27632
Vinculin Intensity (AU)
0.020
0.015
0.010
0.005
0.000
*
****
*
****
Average # of Focal Adhesions per Cell
60
40
20
0
*
0
2
4
6
Time (Days)

Supplemental Figure 4.3: Vinculin aggregation at focal adhesions during TPC tenogenesis. **A**) Fluorescent images of TPC cultures on aligned, fiber-coated coverslips with TGF-β3 or TGF-β3 and Y27632 (+Y27632); identical samples were fixed on days 0, 2, 4, and 6. **B**) Quantification of vinculin intensity (AU) and average number of focal adhesions (FA's) per cell (n = 10 FOVs). All data are reported as mean ± standard deviation. Asterisks indicate statistically significant comparisons, with *p<0.05 and ****p<0.0001 by Student's t-test.

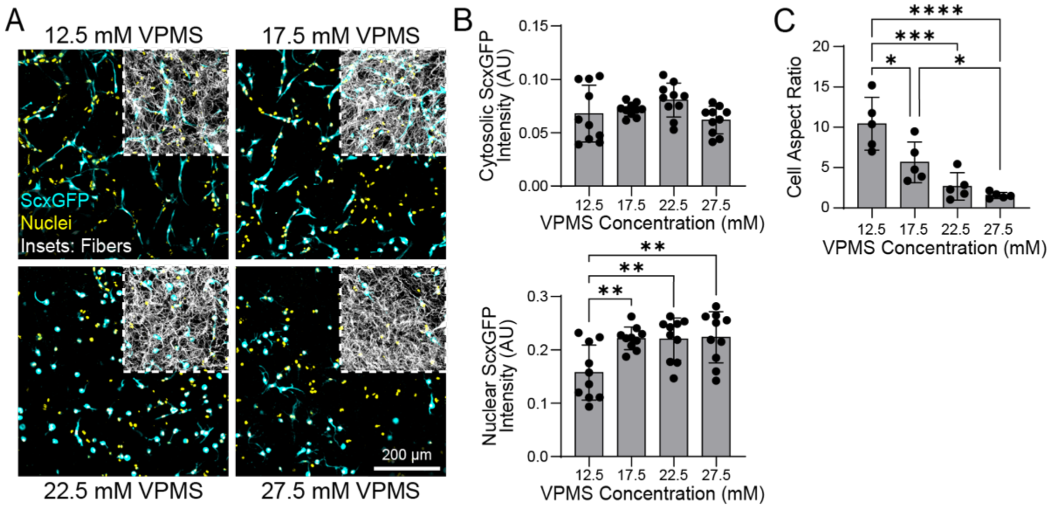

Supplemental Figure 4.4: Screen of bulk crosslink density in FRHCs. **A**) Fluorescent images of *ScxGFP* reporter TPC cultures with TGF-β3 in FRHCs (2.5 v/v% fibers) with varying crosslink densities. Quantification of (**B**) cytosolic and nuclear ScxGFP intensity (AU) and (**C**) cell aspect ratio (n = 10 FOVs). All data are reported as mean ± standard deviation. Asterisks indicate statistically significant comparisons, with *p<0.05, **p<0.01, ***p<0.001, and ****p<0.0001 by ordinary one-way ANOVA with Tukey's multiple comparisons test.

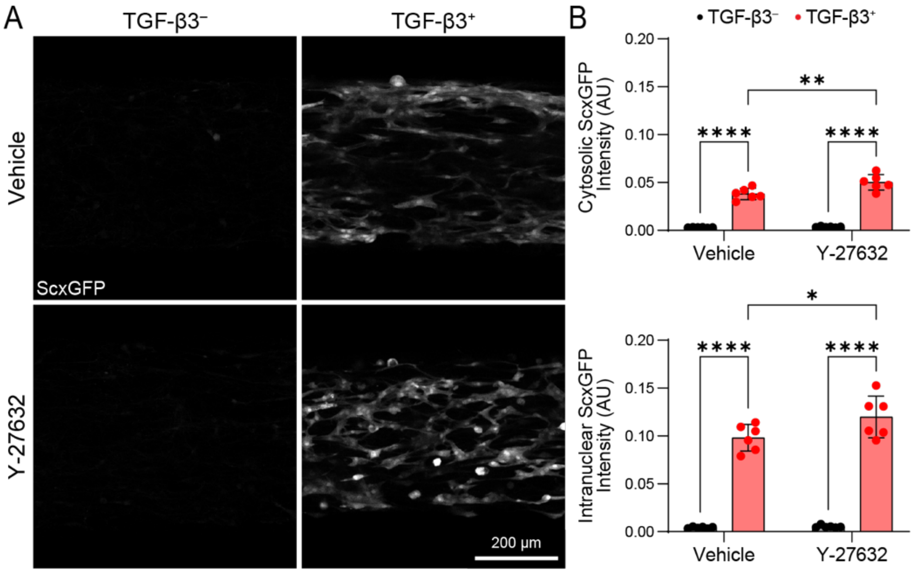
A
TGF-β3$^-$
TGF-β3$^+$
Vehicle
Y-27632
ScxGFP
200 µm
B
• TGF-β3$^-$ • TGF-β3$^+$
Cytosolic ScxGFP Intensity (AU)
0.20
0.15
0.10
0.05
0.00
**
****
****
Vehicle
Y-27632
Intranuclear ScxGFP Intensity (AU)
0.20
0.15
0.10
0.05
0.00
*
****
****
Vehicle
Y-27632

Supplemental Figure 4.5: Rho/ROCK inhibition of TPCs in FRHCs with 30μM Y27632. A) Fluorescent images of *ScxGFP* reporter TPC cultures in flow-aligned FRHCs (2.5 v/v% fibers) with basal media or supplemented with Y27632 (30μM), TGF-β3, or both. Quantification of (**B**) cytosolic and nuclear ScxGFP intensity (AU) (n = 6 FOVs). All data are reported as mean ± standard deviation. Asterisks indicate statistically significant comparisons, with $*p<0.05$, $**p<0.01$, and $****p<0.0001$ by ordinary two-way ANOVA with Tukey's multiple comparisons test.

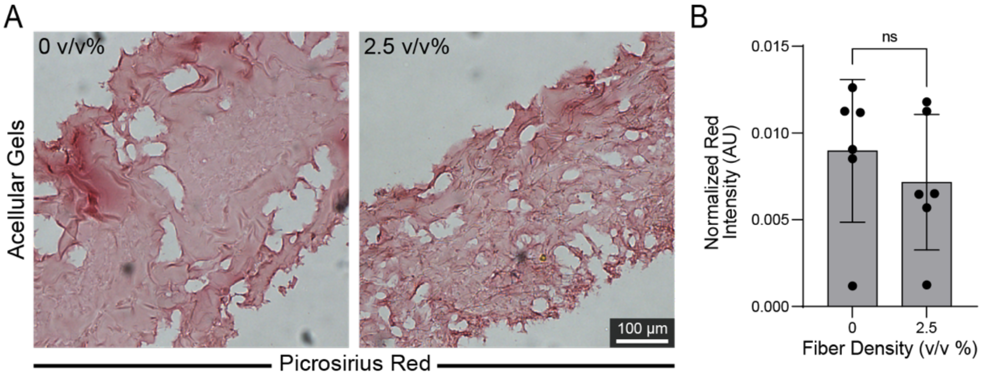
A
0 v/v%
2.5 v/v%
Acellular Gels
100 µm
Picrosirius Red
B
ns
Normalized Red Intensity (AU)
0.015
0.010
0.005
0.000
0
2.5
Fiber Density (v/v %)

Supplemental Figure 4.6: Fiber density does not impact Picrosirius Red staining in acellular FRHCs. A) Brightfield images of Picrosirius Red-stained frozen sections of random and aligned, acellular FRHCs. **B**) Quantification of normalized red intensity (AU) (n = 6 FOVs). All data are reported as mean ± standard deviation. ns denotes a non-significant comparison by Student's t-test.

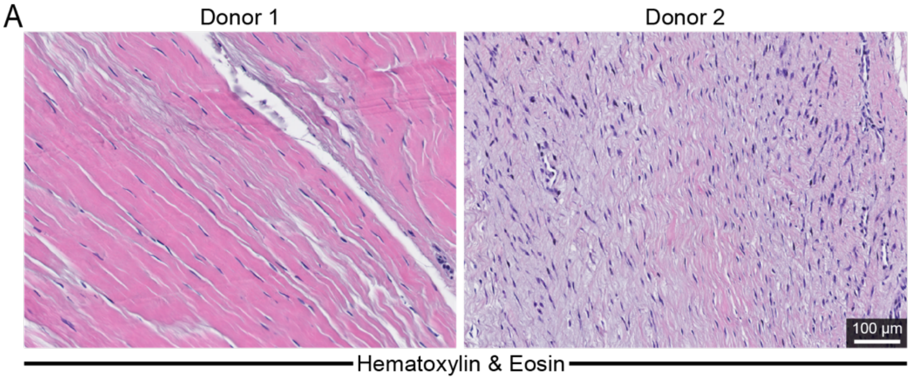

B

Bonar Scoring

	Donor 1	Donor 2
Cell Morphology	Grade 0	Grade 3
Collagen Arrangement	Grade 1	Grade 3
Cellularity	Grade 1	Grade 2
Vascularity	Grade 2	Grade 1
Ground Substance	Grade 0	Grade 0

Supplemental Figure 4.7: Bonar tendinopathy scoring for human TDC donors. A) Brightfield images of hematoxylin and eosin-stained paraffin-embedded sections of donor Achilles tendon tissues. **B**) Bonar tendinopathy scoring, where each criteria receives a grade between 0 (least tendinopathic) and 3 (most tendinopathic).

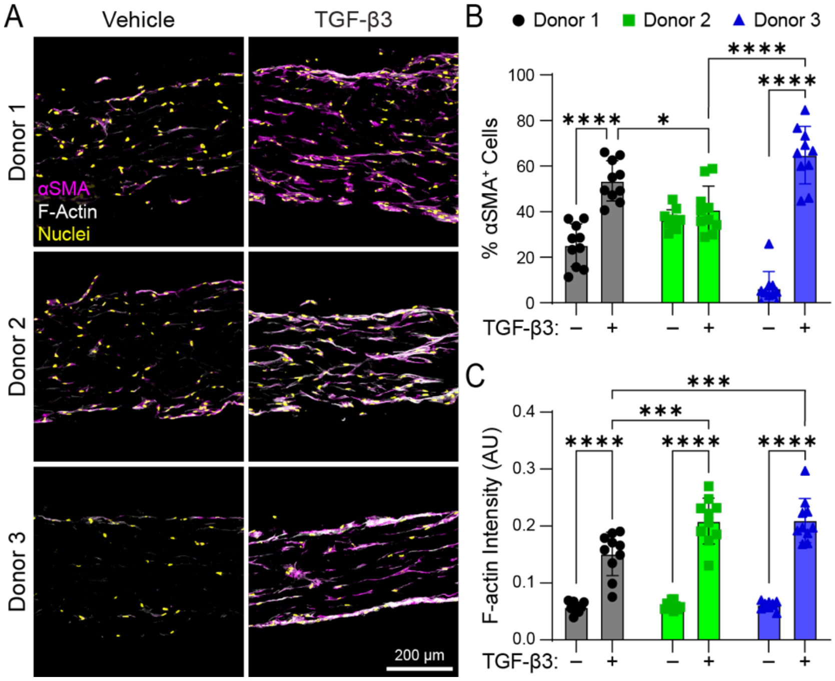

Supplemental Figure 4.8: Myofibroblastic differentiation of human TDCs in FRHCs. A) Fluorescent images of frozen sections of human TDC cultures in flow-aligned FRHCs (2.5 v/v% fibers) with basal media or supplemented TGF-β3. Quantification (**B**) % of TPCs expressing *αSMA* and (**C**) F-actin intensity (AU) (n = 10 FOVs). All data are reported as mean ± standard deviation. Asterisks indicate statistically significant comparisons, with *p<0.05, ***p<0.001, and ****p<0.0001 by ordinary two-way ANOVA with Tukey's multiple comparisons test.

Chapter 5: Fibrous Topographical Cues Govern a Tenogenic vs. Fibrochondrogenic Fate Switch

Note: this chapter contains unpublished work in preparation for submission

5.1 Authors

Robert N. Kent III, Maggie E. Jewett, Trevor P. Buck, Ariella Shikanov, Alice H. Huang, Brendon M. Baker

5.2 Abstract

Fiber-reinforced hydrogel composites are a promising approach to augmenting tendon healing, which is often disrupted in part by aberrant differentiation of recruited progenitor cells. Transforming growth factor β3 is an established soluble cue for encouraging tenogenic differentiation, but it is also known to induce chondrogenic differentiation in microenvironments with minimal cell-adhesive cues. Here, we used a synthetic, fiber-reinforced hydrogel composite to interrogate the impact of cell-adhesive fibrous topography on a tenogenic vs. fibrochondrogenic fate switch in transforming growth factor β3-treated tendon progenitor cells. We demonstrate that tendon progenitor cells in non-fibrous hydrogels adopt a rounded morphology and a fibrochondrogenic phenotype, with tendon progenitor cells in fibrous hydrogels exhibiting spindle morphologies and a cleaner tenogenic phenotype. Furthermore, we find that Rac1 inhibition and cyclic stretch increase fibrochondrogenic differentiation. Finally, we show that fibrous topography

primarily drives tendon progenitor cell recruitment from the tendon stubs in a mouse model of Achilles tendon rupture and minimally impacts fibrochondrogenic differentiation. Overall, this work contributes to understanding microenvironmental cues influencing progenitor cell fate during tendon repair, information critical for developing effective tissue regeneration therapies.

5.3 Introduction

Tendon healing in typically results in the formation of disorganized scar tissue, preventing the tissue from fully regaining its prior mechanical function and predisposing the patient to reinjury (Sharma and Maffulli, 2006; F. Wu et al., 2017a). Understanding that aberrant differentiation of recruited progenitors during healing contributes to these adverse outcomes, biomaterial strategies for augmenting tendon regeneration have focused on engineering a pro-tenogenic cell microenvironment through a combination of physical and soluble cues (No et al., 2020a).

Many prior studies have found that TGF-β3 drives tenogenic differentiation of tendon progenitor cells (TPCs), mesenchymal stem cells, and other stem cells, highlighting this pleiotropic growth factor as a possible therapeutic tool for orchestrating the tenogenic differentiation of recruited mesenchymal progenitor cells following tendon injury (Barsby et al., 2014; Sakabe et al., 2018; Tarafder et al., 2019a; Wee et al., 2022). Unfortunately, TGF-β3 is also well-known to induce chondrogenesis under the certain physical microenvironmental conditions, in particular those with minimal cell-adhesive cues (e.g., alginate and agarose) (C. Chung and Burdick, 2009; Dahlin et al., 2014; Du et al., 2023; A. H. Huang et al., 2009; D. Li et al., 2020). Cell shape has been heavily implicated in regulating lineage commitment of stem cells, with previous work suggesting that a spindle morphology may bias stem cells toward a tenogenic lineage (Kishore et al., 2012; Zhu et al., 2010) as compared to a rounded morphology, which has been associated with chondrogenesis (Mo et al., 2009).

Therefore, we co-opted a tunable, synthetic, fiber-reinforced hydrogel composite to study the role of cell-adhesive fibrous topography on tenogenic differentiation of murine TPCs. We formed fiber-reinforced hydrogel composites (FRHCs) from vinyl sulfonated dextran (DexVS) crosslinked with an MMP-labile peptide and imbued the material with cell-adhesive topographical cues by incorporating electrospun DexVS fibers functionalized with RGD peptides (D. L. Matera et al., 2020). Using this system, we found that TGF-β3 drove a fibrochondrogenic phenotype in TPCs encapsulated in non-fibrous hydrogels, and that this phenotype was more purely tenogenic in fibrous conditions. Application of cyclic strain of FRHCs also promoted fibrochondrogenic differentiation, possibly through down-regulation of Rac1. Finally, in a murine model of Achilles tendon ruptures, we show that fibrous topography drives TPC recruitment into the wound site, with recruited cells trending toward lower Sox9 expression in fibrous conditions. Together, this work offers insight into the interplay between fibrous topographical cues provided by FRHCs and tenogenic differentiation recruited cells.

5.4 Results and discussion

5.4.1 TGF-β3-mediated scleraxis production is attenuated by aligned 3D cell-adhesive fibers in FRHCs

To study the isolated effect of cell-adhesive fibrous topography on TPC tenogenesis, we used a PDMS microfluidic chip to encapsulate scleraxis (Scx)GFP reporter TPCs in flow-aligned DexVS FRHCs (**Figure 5.1A**). Although there are a range of canonical genes associated with tenogenesis, Scx is a key and early tenogenic transcription factor, making ScxGFP reporter lines attractive for screening pro-tenogenic microenvironmental cues (Pryce et al., 2007; Sakabe et al., 2018). FRHCs were comprised of (1) a bulk of DexVS functionalized with a non-cell-adhesive RDG scramble peptide and crosslinked with an MMP-labile peptide (VPMS) and (2) electrospun DexVS fiber segments (0 or 2.5 v/v%) functionalized with cell-adhesive RGD (D. L. Matera et al., 2020). To induce tenogenic differentiation, media was supplemented with transforming growth factor (TGF)-β3 at 10 ng mL^{-1} (Sakabe et al., 2018; Tarafder et al., 2019a). After one week of culture, inclusion of fibrous topography caused TPCs to adopt a collectively aligned, spindle morphology and yielded alignment of encapsulated cells that reflected the alignment of embedded fibers (**Supplemental Figure 5.1**). In contrast, TPCs in hydrogels lacking fibers possessed a rounded morphology and, in some cases, formed spherical clusters of 2-4 cells (**Figure 5.1B**).

Given the established relationship of aligned fibrous topography and tenogenic differentiation in 3D constructs (Baldwin et al., 2021; El Khatib et al., 2020; Islam et al., 2017), we hypothesized that the presence of fibrous topography would further promote tenogenic differentiation as evidenced by increased ScxGFP production. Instead, we observed that TGF-β3-mediated ScxGFP production is attenuated by the presence of cell-adhesive fibrous topography (**Figure 5.1B,C**). This result was surprising, especially given the well-characterized relationship between a spindle morphology and tenogenic differentiation (Zhu et al., 2010). However, previous work has identified a Scx^{+}, fibrocartilaginous progenitor population that contributes to enthesis formation during development and injury (Blitz et al., 2013; Fukuma et al., 2023; Ideo et al., 2020; Sugimoto et al., 2013). Therefore, we sought to further characterize the TPC phenotypes generated in non-fibrous and fibrous composites.

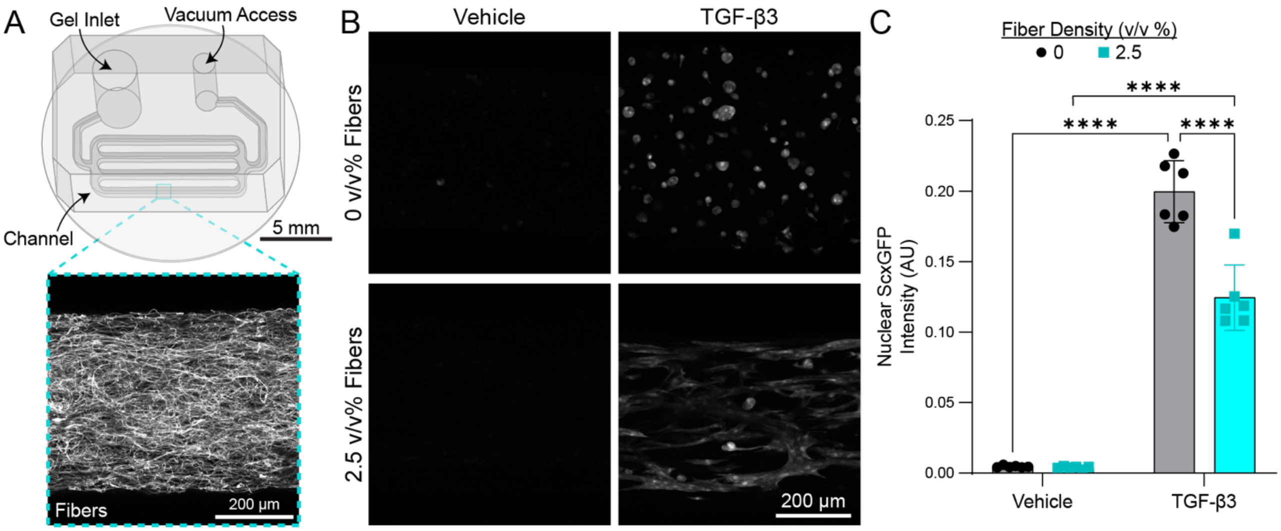

Figure 5.1: ScxGFP expression by TPCs is attenuated by 3D fibrous topography. A) A 4-channel microfluidic chip flow-aligned DexVS FRHCs on glass coverslips. **B**) GFP-channel fluorescent images of ScxGFP reporter TPCs cultured for one week in flow-aligned DexVS hydrogels with 0 or 2.5 v/v% fibers in basal media with or without TGF-β3. **C**) Quantification of nuclear ScxGFP intensity (AU) (n = 6 FOVs, N = 2). All data are reported as mean ± standard deviation. Asterisks indicate statistically significant comparisons, with ****p<0.0001 by ordinary two-way ANOVA with Tukey's multiple comparisons test.

5.4.2 TPCs in afibrous, non-cell-adhesive hydrogels exhibit a fibrochondrogenic phenotype

Fibrocartilaginous progenitor populations are characterized by co-expression of Scx and SRY-box transcription factor (Sox) 9 (Sugimoto et al., 2013). Moreover, these Scx^{+}/Sox9^{+} cells are known to generate type I and type II collagen (Blitz et al., 2013). To further characterize TPC phenotype as a function of fibrous topography, and to allow time for production of fibrillar collagens, ScxGFP reporter TPCs were cultured in FRHCs with TGF-β3 supplementation for four weeks. Similarly to one-week cultures, nuclear ScxGFP intensity was decreased by the inclusion of cell-adhesive fibrous topography (**Figure 5.2A,B**); however, the magnitude of this decrease was highly variable across the four biological replicates tested (**Supplemental Figure 5.2A**). Bi-weekly live imaging also demonstrated that, regardless of fibrous topography, ScxGFP intensity peaked at 1.5 weeks and then gradually attenuated for the remainder of the study (**Supplemental Figure 5.2E**). Immunofluorescent staining for Sox9 also revealed a decrease in nuclear Sox9 intensity with fibrous inclusion (**Figure 5.2A,E; Supplemental Figure 5.2D**). Viewed in light of a fibrochondrogenic phenotype, the coincident increase in ScxGFP and Sox9 in non-fibrous hydrogels at 4 weeks is intuitive because Scx is known to regulate Sox9-dependent transcription in fibrocartilage progenitors (Furumatsu et al., 2010).

Immunofluorescent staining revealed that fiber inclusion does not impact cytosolic type I collagen intensity, but it does decrease cytosolic type II collagen intensities (**Figure 5.2A,C-D**). Type I collagen is produced by both tenocytes and fibrochondrocytes (Bernard-Beaubois et al., 1997; Blitz et al., 2013), with fibrochondrocytes typically producing more type II collagen (Blitz et al., 2013), and so these results were consistent with increased fibrochondrogenic differentiation in non-fibrous microenvironments. Although these findings were maintained in a paired analysis of the four biological replicates (**Supplemental Figure 5.2B-C**), they may have been confounded by fiber-driven matrix production (**Chapter IV, Figure 4.8I,J**). Ongoing work will therefore quantify overall type I and type II collagen intensities over the entire field of view to provide an additional measure of *de novo* matrix production. ELISA studies will also provide a more direct measure of type I and type II collagen content.

We then measured expression of a panel of canonical tenogenic and fibrochondrogenic genes in TPCs cultured in non-fibrous and fibrous conditions at 1 and 4 weeks. At 1 week of culture, TPCs showed increased expression of *Scx* and trended toward decreased expression of tenascin C (*Tnc*), mohawk (*Mkx*), fibromodulin (*Fmod*), decorin (*Dcn*), type I collagen α1 (*Col1a1*), aggrecan (*Acan*), cartilage oligomeric matrix protein (*COMP*), type II collagen α1 (*Col2a1*), type X collagen α1 (*Col10a1*), and versican (*Vcan*) (**Supplemental Figure 5.3A**). At 4 weeks of culture, while every gene with the exception of *Col2a1* trended toward a positive fold change in fibrous compared to non-fibrous conditions, none were statistically significant (**Supplemental Figure 5.3B**). Ongoing work will repeat multiple biological replicates of these studies at a higher level of replication (n = 4) to clarify these results.

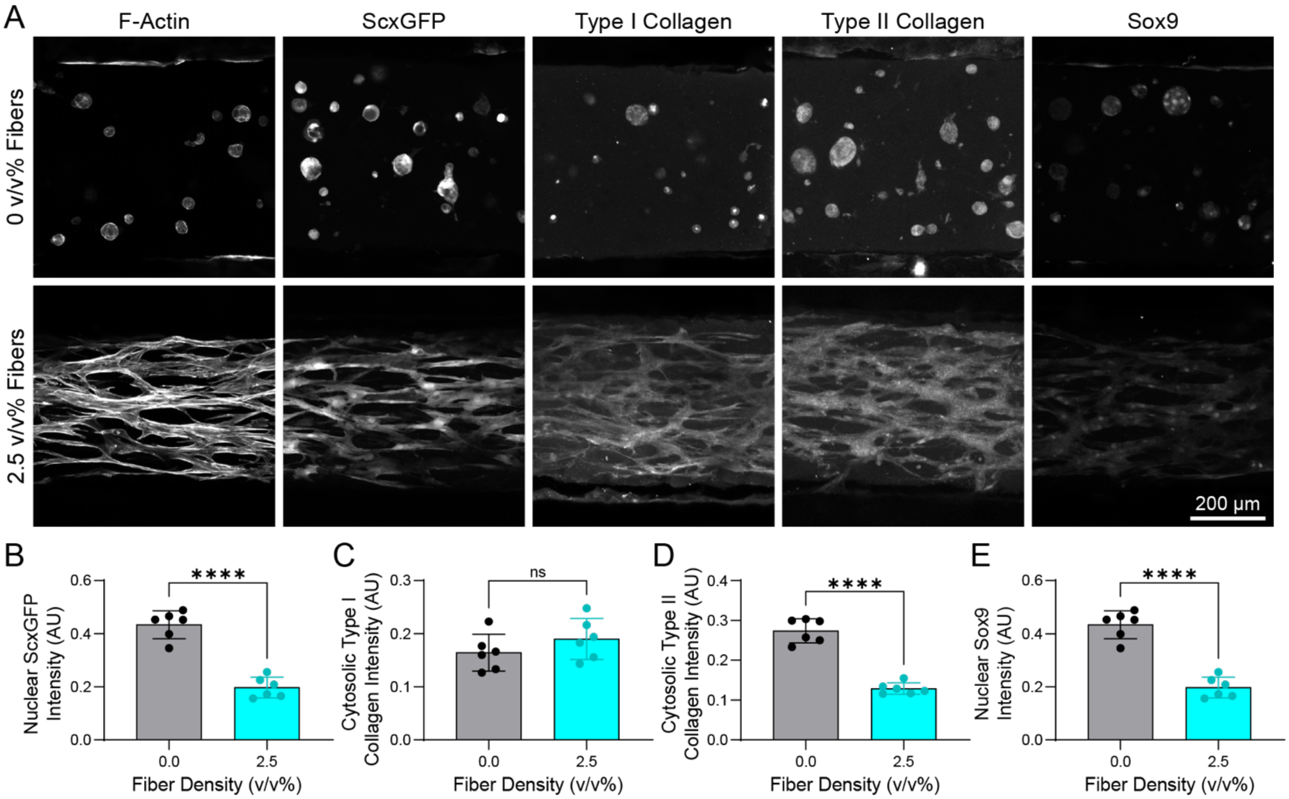

Figure 5.2: Fibrous topography limits fibrochondrogenic differentiation over four weeks of culture. A) Fluorescent images of ScxGFP reporter TPCs cultured for four weeks in flow-aligned DexVS hydrogels with 0 or 2.5 v/v% fibers with TGF-β3 supplementation. Quantification of (**B**) nuclear ScxGFP intensity, (**C**) cytosolic type I collagen intensity, (**D**) cytosolic type II collagen intensity, and (**E**) nuclear Sox9 intensity (AU) (n = 6 FOVs, N = 4). All data are reported as mean ± standard deviation. Asterisks indicate statistically significant comparisons, with ****p<0.0001 by Student's t-test (ns denotes a non-significant comparison).

5.4.3 hMSC chondrogenic medium and non-fibrous conditions synergistically drive fibrochondrogenic differentiation

Having observed a potential tenogenic vs. fibrochondrogenic fate switch as a function of cell-adhesive fibrous topography in FRHCs, we sought to determine the relative contributions of a non-fibrous microenvironment and chondrogenic soluble factors to fibrochondrogenic differentiation. Toward this end, TPCs in DexVS hydrogels (0 or 2.5 v/v% fibers) were cultured either in basal media with TGF-β3 or in a commercially available hMSC chondrogenic differentiation medium (Lonza). Both media include ascorbate and TGF-β3, but the latter is an ITS-based, chemically defined medium supplemented with the chondrogenic factor dexamethasone (Johnstone et al., 1998).

Staining again for type I collagen, type II collagen, and Sox9, we found that culture in chondrogenic media biases TPCs toward a fibrochondrogenic phenotype in non-fibrous and fibrous microenvironments. This study redemonstrated increased nuclear ScxGFP and Sox9 intensities in non-fibrous compared to fibrous conditions, but culture in chondrogenic media further intensified nuclear ScxGFP and Sox9 in both fiber conditions (**Figure 5.3A-B**). Cytosolic type I and type II collagen intensities showed similar trends (**Figure 5.3A,B**), supporting the notion that chondrogenic soluble conditions and a non-fibrous microenvironment synergistically drive fibrochondrogenic differentiation. However, the magnitude of these changes were likely attenuated in 2-week compared to 4-week studies (**Figure 5.2; Figure 5.3**).

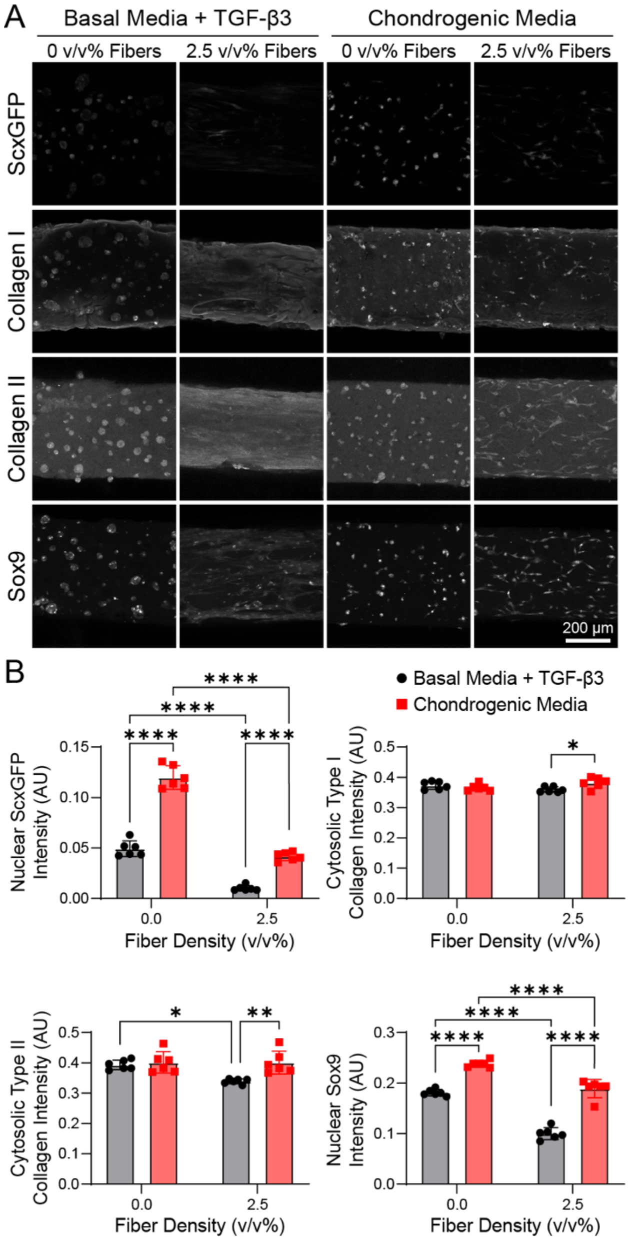

Figure 5.3: hMSC chondrogenic medium further boosts TPC chondrogenesis in non-fibrous hydrogels. A) Fluorescent images of ScxGFP reporter TPCs cultured for two weeks in flow-aligned DexVS hydrogels with 0 or 2.5 v/v% fibers in basal media or hMSC chondrogenic medium (both with TGF-β3 supplementation). **B**) Quantification of nuclear ScxGFP intensity, cytosolic type I collagen intensity, cytosolic type II collagen intensity, and nuclear Sox9 intensity (AU) (n = 6 FOVs). All data are reported as mean ± standard deviation. Asterisks indicate statistically significant comparisons, with *p<0.05, **p<0.01, and ****p<0.0001 by ordinary two-way ANOVA with Tukey's multiple comparisons test.

5.4.4 Rac1 inhibition favors fibrochondrogenic differentiation

To begin to investigate the mechanism by which fibrous topography limits fibrochondrogenic differentiation of encapsulated TPCs, we treated samples with chemical inhibitors of RhoA/Rho kinase (ROCK) (Y27632) and Rac1 (NSC23766). RhoA/ROCK and Rac1 are critical regulators of actin cytoskeletal dynamics, primarily promoting cell contractility and spreading, respectively (del Pozo et al., 2000; D. L. Matera et al., 2021; Price et al., 1998). We therefore hypothesized that these two cell functions would be involved in the contact-guided spreading that occurs when a TPC engages an anisotropic, cell-adhesive fiber (Thrivikraman et al., 2021), such that their inhibition would increase fibrochondrogenic differentiation. After two weeks of culture, RhoA/ROCK inhibition yielded mixed results, increasing ScxGFP intensity and attenuating Sox9 intensity in non-fibrous conditions and decreasing both markers in fibrous conditions (**Figure 5.4A,B**). Y27632 showed some evidence of cytotoxicity after only 1 week of exposure in our previous work (**Supplemental Figure 4.2**), complicating interpretation of these findings. In contrast, inhibition of cell spreading with Rac1 generally resulted in increased fibrochondrogenic differentiation in fibrous and non-fibrous conditions (**Figure 5.4A,B**). Ongoing work will measure morphometric features of TPCs to quantify spreading, but Rac1 inhibition qualitatively appeared to blunt cell spreading, potentially hindering the anti-fibrochondrogenic effects of fibrous topography.

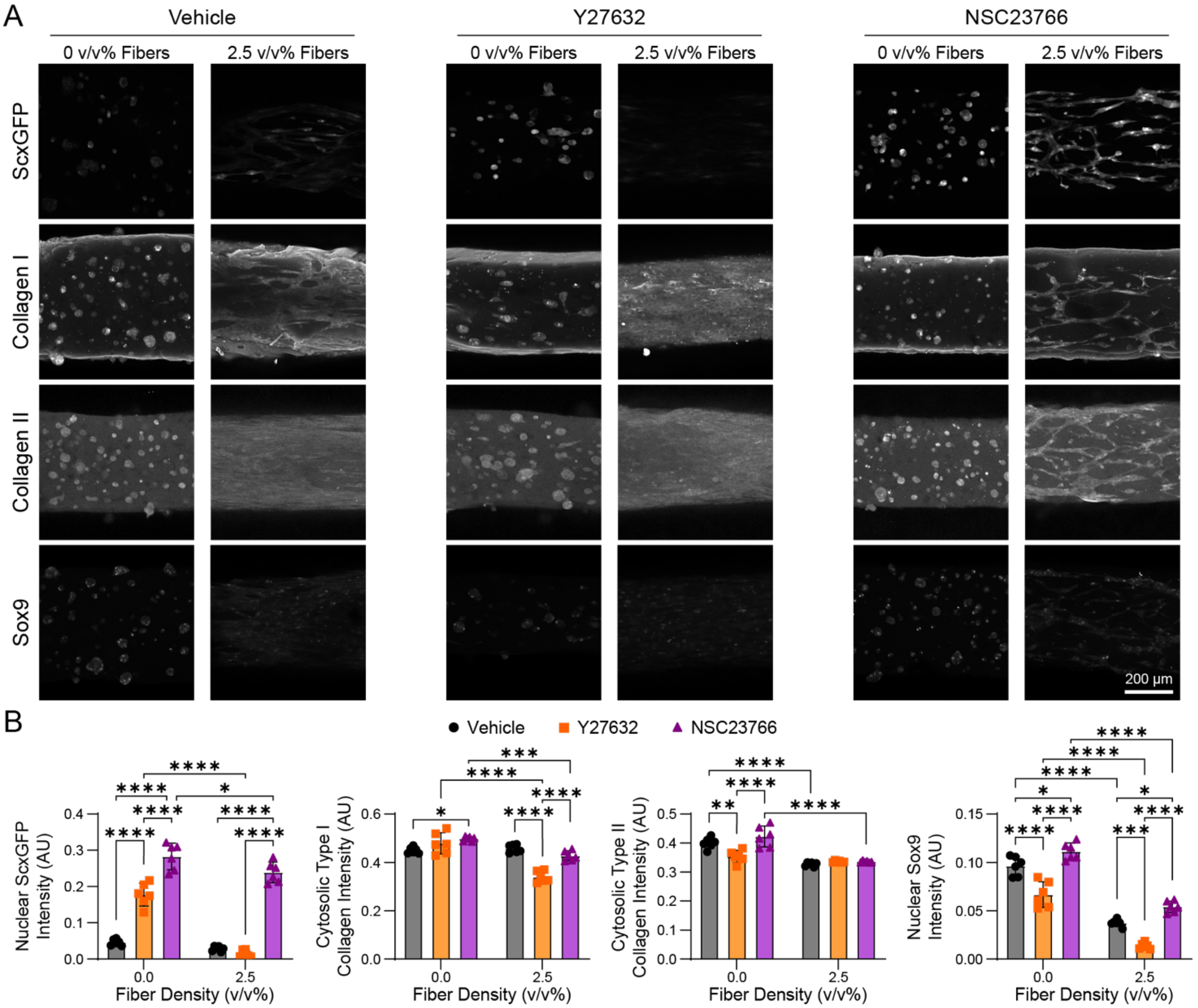

Figure 5.4: Rac1 inhibition favors TPC fibrochondrogenic differentiation. A) Fluorescent images of ScxGFP reporter TPCs cultured for two weeks in flow-aligned DexVS hydrogels with 0 or 2.5 v/v% fibers in basal media with TGF-β3; cultures were additionally supplemented with DMSO, Y27632, or NSC23766. **B**) Quantification of nuclear ScxGFP intensity, cytosolic type I collagen intensity, cytosolic type II collagen intensity, and nuclear Sox9 intensity (AU) (n = 6 FOVs). All data are reported as mean ± standard deviation. Asterisks indicate statistically significant comparisons, with *$p<0.05$, **$p<0.01$, ***$p<0.001$, and ****$p<0.0001$ by ordinary two-way ANOVA with Tukey's multiple comparisons test.

Externally applied, cyclic strain is an established tenogenic cue (Garvin et al., 2003; Nirmalanandhan et al., 2008; Rinoldi et al., 2019a; Rinoldi et al., 2019b; Scott et al., 2011; Triantafillopoulos et al., 2004), but fibrochondrogenic markers in response to this cue have not been studied in the setting of tendon repair. Separately, Katsumi et al. showed that rat vascular smooth muscle cells down-regulate Rac1 in response to externally applied load in a strain-dependent manner (Katsumi et al., 2002), suggesting that dynamic strain of TPCs could also be pro-fibrochondrogenic. To evaluate this hypothesis, we flow-aligned FRHCs (2.5 v/v% fibers) on the floor of a stretchable PDMS well and mounted it to a motorized assembly with rigid boundary conditions to apply uniform strain along the axis of flow alignment (**Figure 5.5A; Supplemental Figure 5.4**). FRHCs were supplemented with TGF-β3 and cultured either (1) in static conditions or (2) dynamic conditions with application of 10% strain at 0.5Hz (with 10 seconds of rest after each cycle) for two hours, followed by 6 hours of rest (Scott et al., 2011). At one week of culture, dynamically strained TPCs showed increased expression of *Scx*, *TnC*, *Fmod*, and *Dcn*, consistent with previous work (Garvin et al., 2003; Scott et al., 2011). However, genes specific to fibrochondrogenic differentiation, including *Acan*, *Comp*, *Col2a1*, *Col10a1*, and *Vcan*, were also upregulated (**Figure 5.5B**).

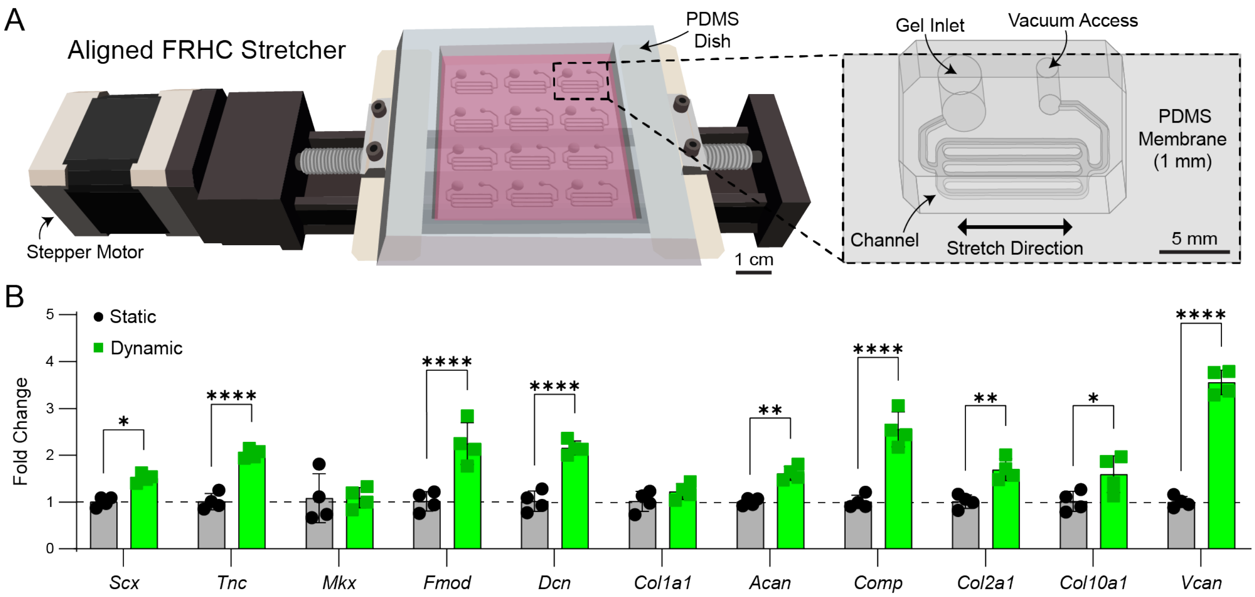

Figure 5.5: Cyclic stretch drives fibrochondrogenic gene expression by TPCs. A) Schematic of aligned FRHC stretcher; a PDMS well is mounted to a motorized assembly, FRHCs are flow-aligned on the base of the well, and actuation results in strain parallel to the direction of flow alignment. **B**) Fold change in expression of canonical tenogenic and fibrochondrogenic genes by TPCs encapsulated in FRHCs and cultured in static or dynamic stretch conditions with TGF-β3. All data are reported as mean ± standard deviation. Asterisks indicate statistically significant comparisons, with *$p<0.05$, **$p<0.01$, and ****$p<0.0001$ by ordinary two-way ANOVA with Tukey's multiple comparisons test.

5.4.5 Fibrous topography drives ScxGFP$^+$ TPC recruitment *in vivo* but minimally impacts fibrochondrogenic differentiation

To study the impact of fibrous topography on fibrochondrogenic differentiation during tendon healing *in vivo*, we performed bilateral Achilles tenotomies on ScxGFP C57BL/6 mice and crosslinked DexVS hydrogels *in situ* (**Figure 5.6A-B**). Implants delivered to left and right hindlimbs contained 0 and 2.5 v/v% fibers, respectively, and hindlimbs were immobilized in full plantarflexion to minimize widening of the tendon gap. At two weeks post-injury, inclusion of fibrous topography resulted in increased recruitment of ScxGFP$^+$ TPCs from the tendon stubs but no significant reduction in nuclear Sox9 intensity (**Figure 5.6C-F**). While Sox9 intensity trended downward in the fibrous condition, the difference in recruitment likely confounded the comparison through a difference in the cell lineages present in the wound site.

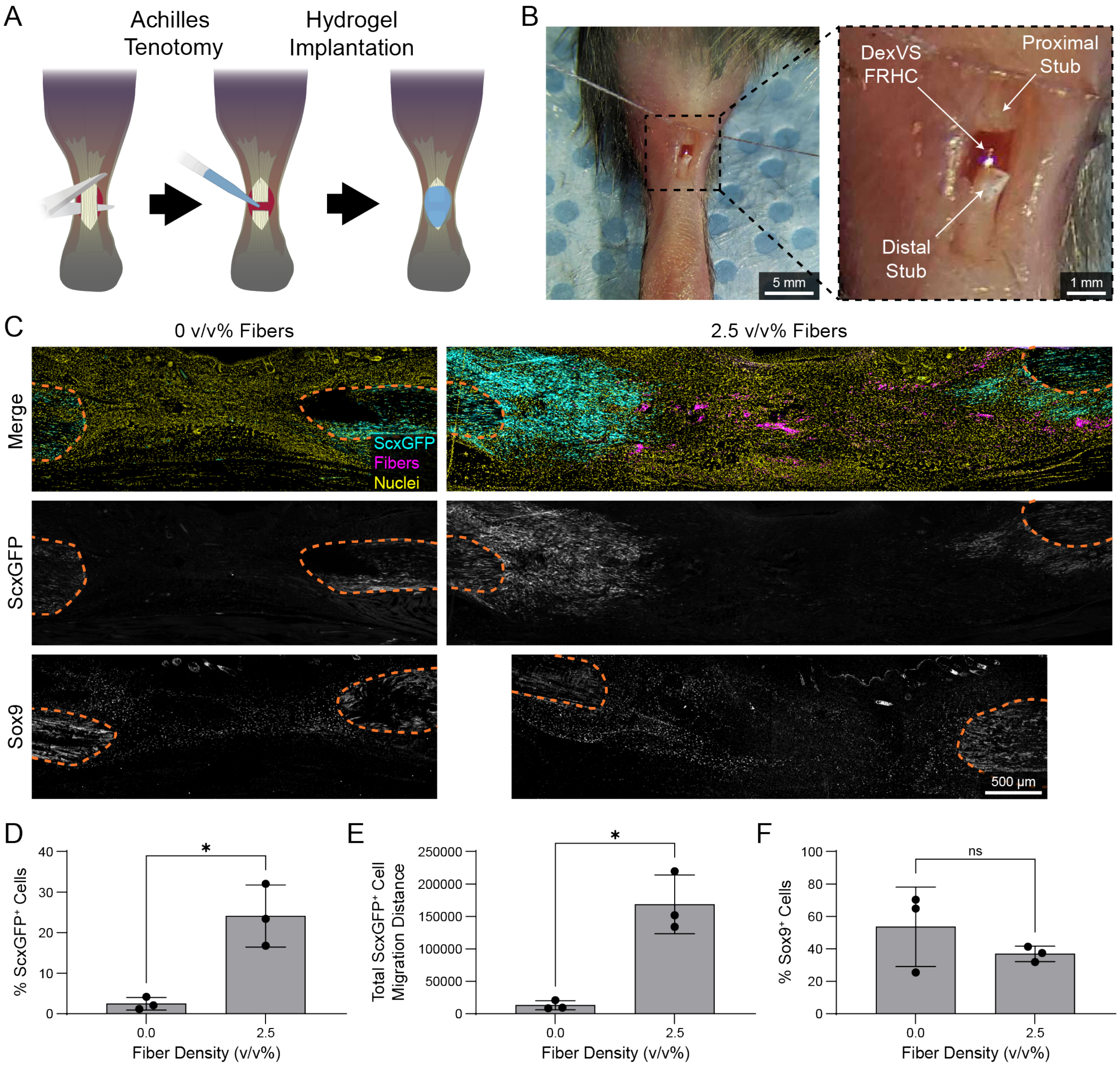
A
Achilles Tenotomy
Hydrogel Implantation
B
DexVS FRHC
Proximal Stub
Distal Stub
5 mm
1 mm
C
0 v/v% Fibers
2.5 v/v% Fibers
Merge
ScxGFP
Fibers
Nuclei
ScxGFP
Sox9
500 µm
D
% ScxGFP⁺ Cells
0
10
20
30
40
*
0.0
2.5
Fiber Density (v/v%)
E
Total ScxGFP⁺ Cell Migration Distance
0
50000
100000
150000
200000
250000
*
0.0
2.5
Fiber Density (v/v%)
F
% Sox9⁺ Cells
0
20
40
60
80
100
ns
0.0
2.5
Fiber Density (v/v%)

Figure 5.6: Fibrous topography drives ScxGFP$^+$ TPC recruitment to the site of injury. A) Diagram of a ScxGFP reporter mouse Achilles tenotomy followed by injection and *in situ* crosslinking of an FRHC. **B**) Intraoperative photograph of the transected Achilles during FRHC *in situ* crosslinking. **C**) Fluorescent images sectioned hindlimbs two weeks following implantation of DexVS hydrogels with 0 or 2.5 v/v% fibers. Quantification of (**D**) % ScxGFP$^+$ nuclei between the tendon stubs, (**E**) total migration distance of ScxGFP$^+$ cells from the tendon stub, and (**F**) % Sox9$^+$ nuclei between the tendon stubs (N = 3). All data are reported as mean ±

standard deviation. Asterisks indicate statistically significant comparisons, with $^{**}p<0.01$ by paired Student's t-test (ns denotes a non-significant comparison).

5.5 Conclusion

We investigated the influence of cell-adhesive fibrous topography on tenogenic and fibrochondrogenic differentiation of TPCs encapsulated in flow-aligned DexVS FRHCs. Despite our initial hypothesis, the presence of cell-adhesive fibrous topography attenuated TGF-β3-mediated scleraxis (Scx) production by TPCs due to the nuanced interplay between *Scx* expression and tenogenic differentiation. Additionally, TPCs in non-fibrous hydrogels exhibited a fibrochondrogenic phenotype characterized by the co-expression of Scx and Sox9 in addition to increased production of type II collagen. Furthermore, our exploration of potential mechanisms of this fate switch revealed that Rac1 inhibition favored fibrochondrogenic differentiation, suggesting a key mediator of cytoskeletal dynamics in response to fibrous topography. Potentially through Rac1 down-regulation, cyclic stretch, a known tenogenic cue, induced fibrochondrogenic gene expression in TPCs. Finally, in a murine tendon healing model, fibrous topography drove the recruitment of ScxGFP^{+} TPCs but had minimal impact on nuclear Sox9 intensity, highlighting the role of fibrous topography in cell recruitment to FRHCs. Overall, our findings contribute to a deeper understanding of the interplay between fibrous topography, mechanical cues, and TPC fate determination during tendon repair. These data help to elucidate salient microenvironmental cues that drive pro-regenerative vs. maladaptive differentiation of progenitor cells during connective tissue repair, information critical to the development of effective tissue regeneration therapies.

5.6 Materials and methods

5.6.1 Reagents

All reagents were purchased from Sigma-Aldrich or Fisher Scientific and used as received, unless otherwise stated.

5.6.2 Cell isolation and culture

For all animal procedures, the Institutional Animal Care and Use Committee (IACUC) guidelines for survival surgery in rodents and the IACUC Policy on Analgesic Use in Animals Undergoing Surgery were followed (Protocol #PRO00009868). Murine cells used in this work were harvested from 6-9 week-old C57BL/6 mice. A ScxGFP mouse colony was maintained by breeding ScxGFP$^{+/-}$ heterozygotes modified from a C57BL/6 background with WT C57BL/6J mice, and progeny were genotyped (ScxGFP$^{+/-}$ vs. ScxGFP$^{-/-}$) using a Dual Fluorescent Protein Flashlight (Model DFP-1, Nightsea, Lexington, MA). Tail tendons were removed from euthanized mice and then encapsulated in a 2 mg mL^{-1} type I collagen hydrogel. Encapsulated tissues were cultured in an incubator (37°C and 5% CO_2) in DMEM containing L-glutamine (ThermoFisher, Waltham, MA), 1 v/v% penicillin/streptomycin/fungizone, 50 µg mL^{-1} ascorbate-2-phosphate, and 10 v/v% fetal bovine serum (termed 'basal media') for 10 days to allow tendon progenitor cells (TPCs) to migrate from tendons into the collagen gel (Shimada et al., 2014). Following isolation and expansion of TPCs, collagen gels were digested in 0.25 mg mL^{-1} collagenase from *C. histolyticum* with 0.025 w/v % trypsin-EDTA. The resulting slurry was filtered through a cell strainer and then plated. Adherent TPCs were cultured in basal media, and cells at passage 1 were used for all experiments. Human mesenchymal stem cell chondrogenic differentiation medium (Lonza, Basel, Switzerland) was used in chondrogenic media studies. This ITS-based, chemically defined medium contains dexamethasone, ascorbate, sodium pyruvate, L-glutamine, proline, and gentamicin sulfate-amphotericin. For Rho/ROCK and Rac1 inhibition studies, Y27632 (sc-281642A, Santa Cruz Biotechnology, Dallas, TX) and NSC23766 (sc-281642A, Santa Cruz Biotechnology, Dallas, TX) were added to the media, respectively, at 10 ng mL^{-1}.

5.6.3 Polymer synthesis

Dextran functionalized with vinyl sulfone groups (DexVS) was synthesized as previously described (Yu and Chau, 2012). Briefly, 5 g of 86 kDa dextran (MP Biomedicals, Irvine, CA) was dissolved in a 250 mL solution of 100 mM sodium hydroxide in Milli-Q water. On a stir plate set to 700 rpm, divinyl sulfone (Alfa Aesar, Haverhill, MA) was added to the solution, and the reaction proceeded for 3.5 minutes before termination by addition of 2.5 mL of 12 M hydrochloric acid. To achieve vinyl sulfone / dextran repeat unit ratios appropriate for hydrogel formation (16%) and fiber fabrication (65%), 3.88 mL and 12.5 mL of divinyl sulfone were added to the reactions, respectively. After vinyl sulfone addition, the product was dialyzed against Milli-Q water for 72 hours with twice-daily changes and then lyophilized for 72 hours to yield a dry product. All reaction products were characterized via ^{1}H NMR.

5.6.4 Fiber segment fabrication and functionalization

An electrospinning solution was prepared by dissolving DexVS (65% vinyl sulfone functionalization) at 0.7 g mL^{-1} in a 1:1 solution of dimethyl formamide and Milli-Q water with 0.015 wt/v% 2-Hydroxy-4′-(2-hydroxyethoxy)-2-methylpropiophenone (Irgacure 2959) photoinitiator. For fluorescent visualization of fibers, methacrylated rhodamine (Polysciences, Inc., Warrington, PA) was added at 0.5 mM. In the same humidity-controlled glovebox described above, DexVS fibers were electrospun onto a slowly rotating (linear velocity 3.14 cm s^{-1}), grounded mandrel using a gap distance of 7 cm, voltage of -5.5 kV, and flow rate of 0.2 mL hr^{-1}. A UV lamp was directed at the opposite side of the mandrel; every 15 minutes, the lamp was turned on for 5 minutes to expose deposited fibers to 100 mW cm^{-2} UV light. Intermittent UV exposure over the course of layer-by-layer fiber deposition ensured that fibers were adequately and uniformly photocrosslinked. The resulting fiber segments have a similar diameter to collagen fibrils observed *in vivo* (1 µm diameter) (D. L. Matera et al., 2020).

The crosslinked fiber mat was removed from the mandrel and transferred to Milli-Q water. Two rounds of pipetting, vortexing, centrifugation, and resuspension were performed to break up the fiber mat into individual fiber segments and remove clumps and residual crosslinking reagents. Purified fibers were resuspended at 10 v/v% in PBS and stored in a light-protected box at 4°C. Prior to incorporation in hydrogel constructs, fiber segments were functionalized by resuspension at 10 v/v% in 50 mM HEPES buffer along with cell-adhesive CGRGDS (RGD) (2.0 mM) and 5 mM sodium hydroxide. Functionalization proceeded via Michael-type addition at 37°C for 15 minutes, then fibers were washed with PBS and resuspended in HEPES buffer.

5.6.5 Fabrication of FRHCs

DexVS hydrogels were formed using previously described methods (D.L. Matera et al., 2019). Briefly, DexVS was dissolved in PBS containing 50 mM HEPES buffer. Scrambled CGRDGS (RDG) was incorporated at 2.0 mM. Additionally, to neutralize residual VS groups and prevent unintended crosslinking, cysteine was added at 9.1 mM. After this pre-reaction proceeded on ice for 20 minutes, cells and functionalized fiber segments were added to the mixture followed by the addition of an MMP-cleavable, dithiolated GCRDVPMSMRGGDRCG (VPMS) crosslinking peptide. Bulk stiffnesses ranging from 0.5-6 kPa were achieved by crosslinking DexVS hydrogels with 12.5-27.5 mM VPMS, respectively; DexVS concentrations of 3.30-4.13 wt/v% were used to ensure that the ratio of free vinyl sulfone groups to VPMS molecules were consistent across crosslinking densities.(D. L. Matera et al., 2020) Gelation via Michael-type addition was initiated by addition of sodium hydroxide (33 mM).

A 4-channel microfluidic chip was designed to flow-align fibers within FHRCs. The device was designed in SolidWorks (Dassault Systèmes, Vélizy-Villacoublay, France), and a master mold was 3D printed via a Formlabs Form 3 stereolithography printer with v4 resin (Formlabs, Somerville, MA). Printed molds were treated with trichloro(1H,1H,2H,2H-perfluorooctyl)silane to facilitate release of PDMS replica casts (1:25 crosslinker:base ratio). The softer PDMS was used in this instance to allow for an airtight seal to be formed with a glass coverslip or PDMS membrane without the need for plasma etching so that the molds could be easily removed after hydrogel crosslinking. 3 mm and 1.5 mm holes were punched in the inlet and vacuum ports of the device (Figure 5.1A), respectively, then devices were washed with isopropanol followed by ethanol. The device's 500x500 μm channels were coated with 2 mg mL^{-1} porcine skin gelatin and dried in an 80°C oven for 20 minutes to facilitate eventual de-molding of the FHRC. An 18 mm glass coverslip was plasma etched for 2 minutes and then functionalized with (3-mercaptopropyl)trimethoxysilane via overnight gas deposition so that the FHRC could covalently adhere to the coverslip via Michael-type addition. Molds were adhered noncovalently to thiolated coverslips, 30 μL hydrogel mixtures were added to the inlet ports, and gels were flowed into the devices using a syringe pump withdrawing 250 μL s^{-1}. Crosslinking then proceeded in a 37°C rotisserie oven for 20 minutes, then devices were transferred to a 12-well plate in 1 mL of basal media and incubated at 37°C for an additional 25 minutes. Finally, PDMS molds were peeled from the coverslips, leaving the crosslinked FHRC (containing isotropic and anisotropic regions) covalently adhered to the glass.

To flow-align FRHCs intended for qPCR analysis, where a higher number of cells is required compared to immunofluorescence analysis, 115 µL FRHCs were seeded with TPCs (5 M mL^{-1}) and flow-aligned in a spiral device on a 25 mm glass coverslip. Similar to the 4-channel device, the spiral device produced a 500x500 µm channel. Spiral FRHCs were crosslinked, adhered to glass substrates, de-molded, and cultured as described above.

5.6.6 Application of dynamic strain to FRHCs

To fabricate a PDMS well (6x7x1 cm) for applying strain to an FRHC *in* vitro, a well mold was 3D-printed (High Temp Resin, Formlabs, Somerville, MA) and pre-treated with trichloro(1H,1H,2H,2H-perfluorooctyl)silane to allow for de-molding. PDMS (1:15 crosslinker:base ratio) was casted, and the top of the cast settled under gravity to form a uniform, 1 mm membrane at the floor of the well. Well casts were pre-cured at 40°C overnight, de-molded, then fully cured at 80°C overnight. PDMS wells were then cleaned with isopropanol followed by ethanol, then then they were functionalized with (3-mercaptopropyl) trimethoxysilane to allow for covalent adhesion to DexVS FRHCs. The same 4-channel PDMS molds described above were adhered non-covalently to the 1 mm PDMS membrane at the bottom of the well, and then flow alignment, crosslinking, and de-molding of the FRHCs proceeded as normal (Figure 5.5A).

For static conditions, FRHC-loaded PDMS wells were placed in a 150 mm petri dish. To apply dynamic strain, a motorized assembly (XSlide, Velmex, Bloomfield, NY) was fitted with custom, 3D-printed adaptors (Durable Resin, Formlabs, Somerville, MA) to enable mounting of the PDMS well with rigid boundary conditions (Figure 5.5A). A lid was 3D-printed from poly(lactic acid) via fused deposition modeling (Ultimaker S5, Utrecht, Netherlands) and spray-coated with polyurethane (Varathane Oil Based, Home Depot, Ann Arbor, MI) to limit permeability to water vapor; the lid rested on the frame of the motorized assembly, leaving 1 mm of clearance between the lid and the walls of the PDMS well for gas exchange and to prevent wear between moving parts. The motorized stage applied 12.17 ± 0.007% strain to the PDMS well and adhered FRHCs (Supplemental Figure 5.4B,C) at 0.5 Hz with 10 seconds of rest between each cycle; FRHCs were dynamically loaded for 2 hours at a time followed by 6 hours of continuous rest for the duration of a study (Scott et al., 2011). 15 mL of media were refreshed in the static and dynamic PDMS wells every 48 hours.

5.6.7 Real-time quantitative PCR

Single-cell suspensions were isolated from FRHCs prior to lysis in Trizol. A digestion solution was prepared in Accutase (Gibco, Billings, MT) containing 3 v/v% dextranase (Cellendes, Kusterdingen, Germany), 2 v/v% liberase, 0.5 mg mL^{-1} collagenase from *C. histolyticum*, and 2 mM ethylene glycol-bis(β-aminoethyl ether)-N,N,N′,N′-tetraacetic acid. Hydrogel composites were washed at 37°C in DMEM for 30 minutes to remove serum proteins and then transferred to the digestion solution (1 mL of digestion solution for every 105 μL of hydrogel). Digestion proceeded in a bacteria shaker set to 37°C and 300 rpm for 20-25 minutes. Digests were diluted in 5 mL of basal media, strained through a 70 μm filter, centrifuged at 500 g for 4 minutes, and resuspended in Trizol. RT-qPCR analysis was then performed as above.

Total RNA was isolated using Trizol reagent followed by phenol-chloroform separation. RNA yield was quantified using a Nanodrop spectrometer (ND-1000, Nanodrop Technologies, Wilmington, DE) in addition to A260/A280 to confirm a value between 1.6 and 2.1 for each isolate.

cDNA was synthesized at 40-50 ng μL^{-1} using the SuperScript First Strand Synthesis kit (Invitrogen, Life Technologies, Carlsbad, CA), and cDNA samples were diluted to 0.2-0.8 ng μL^{-1} in amplification reactions solutions. Amplification was carried out using an Eppendorf Nexus GX2 thermocycler (Eppendorf, Hamburg, DE), with intron-spanning primers and Fast SYBR Green Reaction Mix (Applied Biosystems, Foster City, CA). Expression of genes of interest were determined and normalized to the housekeeping genes 40S ribosomal protein S29 (*S29*) using the comparative Ct method.

5.6.8 Mouse Achilles tenotomy and FRHC implantation

For all animal procedures, the Institutional Animal Care and Use Committee (IACUC) guidelines for survival surgery in rodents and the IACUC Policy on Analgesic Use in Animals Undergoing Surgery were followed (Protocol #PRO00009868). ScxGFP$^{+/-}$ C57BL/6 mice, aged 12-20 weeks, were anesthetized via inhalation of 2.5 v/v% isoflurane, then carprofen (Rimadyl, Zoetis, Parsippany-Troy Hills, NJ) was injected subcutaneously at 5 mg/kg bodyweight for preemptive analgesia. Eyes were covered in ophthalmic ointment (Puralube, Dechra Pharmaceuticals, Northwich, United Kingdom), and then hair was removed from the posterior and medial surfaces of both hindlimbs using powered hair clippers followed by 30 seconds in a potassium thioglycolate and calcium hydroxide-based hair removal product (Nair, Church & Dwight, Ewing, NJ). Hindlimbs were then washed thrice with betadine and sterile saline, then the mouse was positioned prone on the heated stage (37°C) of a Leica M60 dissection microscope (Leica Microsystems, Wetzlar, Germany) and secured with tape.

After confirming an absent pedal reflex, a posterior, 2mm, vertical incision was created with microscissors over the midsubstance of the Achilles tendon, then the skin was bluntly dissected away from the underlying fascia medial and lateral to the Achilles. A pointed forceps tip was then used to bluntly tunnel laterally, deep to the Achilles and superficial to the plantaris and posterior tibial artery. With the forcep tip in place to protect deeper structures, microscissors were used to perform an Achilles tenotomy. Hemostasis was achieved at this time if necessary, then a 7-0 PGA suture was placed across the proximal margin of the wound and left untied to elevate the skin from the edges of the wound, creating a trough around the transected Achilles.

VPMS crosslinker and NaOH were then added to a DexVS FRHC precursor solution with 0 or 2.5 v/v% DexVS fibers. This precursor solution was identical to the formulation described above for *in vitro* studies, although 50% of the typical amount of cystine quencher was used to account for the highly proteolytic environment of an acutely injured tendon (Sharma and Maffulli, 2006; F. Wu et al., 2017a), and PDGF-BB was included at 20 ng mL^{-1} to promote TPC recruitment (Kent et al., 2022). Once mixed, 2-3 uL of FRHC suspension were injected into the wound site and wiped away with gauze to help prevent dilution of the final implant. After repeating this process twice, the wound site was filled completely with the FRHC suspension (5-6 uL), then crosslinking was allowed to proceed for 5 minutes. The suture placed at the proximal wound margin was then anchored and run distally to close the wound over the FRHC. The closed incision was cleaned with sterile saline, then gel superglue (Loctite, Henkel Adhesives, Düsseldorf, Germany) was applied to the remaining hair on the lateral ankle before the hindlimb was wrapped in a cord tie (Velcro, Manchester, NH) to immobilize the ankle in full plantarflexion. Additional superglue was applied to the posterior hip of the mouse to secure the cast proximally. Mice were then transferred to a warmed (37°C) recovery cage and allowed to emerge from anesthesia on room air, and mice were monitored daily for the first 7 days postoperatively.

5.6.9 Histology

Retrotibial soft tissue was removed from paraformaldehyde-fixed hindlimbs, incubated in 30 wt/v% sucrose in PBS at 4°C overnight, and then embedded in optimal cutting temperature (OCT) compound (SCIgen, Sunnyvale, CA) containing 30 wt/v% sucrose. Hindlimbs were then sectioned at 12 μm thickness in the sagittal plane (CM3050 Cryotome, Leica Microsystems, Wetzlar, Germany).

5.6.10 Microscopy and image analysis

Fluorescent images were captured on a Zeiss LSM800 confocal microscope. Samples were fixed in 4% paraformaldehyde, permeabilized in Triton X, and stained with phalloidin (Invitrogen, Waltham, MA) and Hoechst 33342 to visualize F-actin and nuclei, respectively. For studies assessing the extent of tenogenic vs. fibrochondrogenic differentiation, samples were stained with an antibodies against type I collagen (Col1a1 rabbit-anti-mouse, AB765P, Sigma-Aldrich), type II collagen (Col2a1 mouse-anti-moue, II-II6B3, Hybridoma Bank, Iowa City, IA), and Sox9 (Sox9 rabbit-anti-mouse, AB5535, Sigma-Aldrich). All FOVs acquired were mutually exclusive. To quantify fluorescent intensity in 3D, Gaussian filters were applied to all images to remove noise and background. A custom MATLAB code demarcated nuclear and cytosolic regions (via Hoechst and F-actin stains) and quantified fluorescent intensity in voxels comprising each nucleus and cytosol. For tissue stains, the image was analyzed only within a rectangular ROI spanning but not including the tendon stubs.

5.6.11 Statistics

Statistical significance was determined by one- or two-way analysis of variance (ANOVA) with Tukey's multiple comparisons test or two-sided Student's t-test where appropriate ($\alpha = 0.05$). Datapoints were defined as outliers if they were >1.5 interquartile ranges from the median and excluded prior to statistical comparison. Sample size is indicated within corresponding figure legends, and all data are presented as mean ± standard deviation.

5.7 Supplemental figures

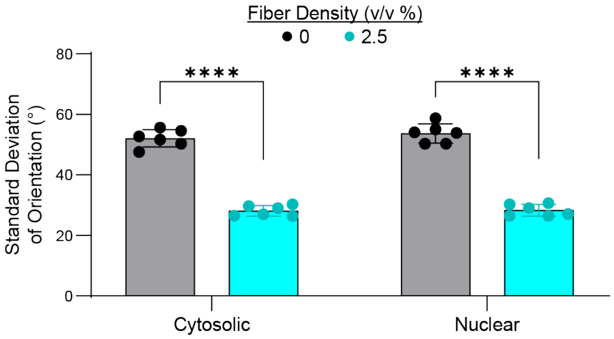

Supplemental Figure 5.1: Aligned fibrous topography is mirrored by cell orientation. Quantification of standard deviation of orientation (°) of TPC cytosols and nuclei after 1 week of culture in DexVS hydrogels with 0 or 2.5 v/v% fibers with TGF-β3 supplementation (n = 6 FOVs, N = 2). All data are reported as mean ± standard deviation. Asterisks indicate statistically significant comparisons, with ****$p<0.0001$ by ordinary two-way ANOVA with Tukey's multiple comparisons test.

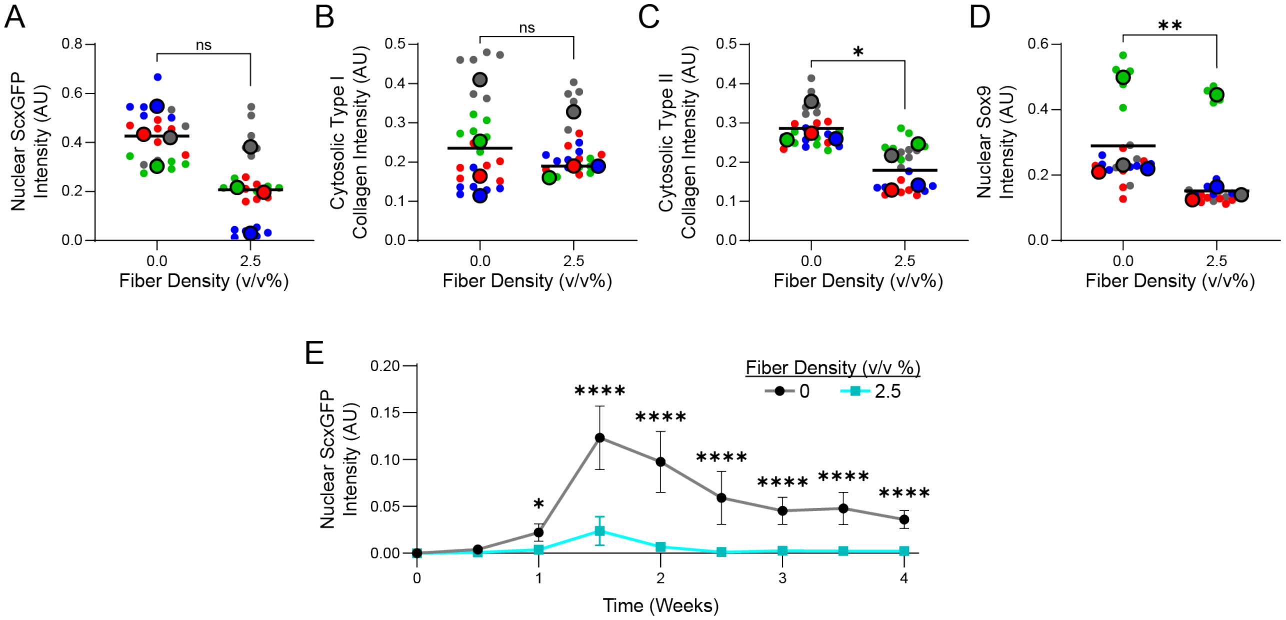

Supplemental Figure 5.2: Biological replicates and live imaging of nuclear ScxGFP. In TPCs cultured in DexVS hydrogels (0 or 2.5 v/v% fibers) for 4 weeks, quantification of (**A**) nuclear ScxGFP intensity, (**B**) cytosolic type I collagen intensity, (**C**) cytosolic type II collagen intensity, and (**D**) nuclear Sox9 intensity (AU) (n = 6 FOVs, N = 4). **E**) Quantification of nuclear ScxGFP intensity (AU) in live-imaged samples at half-week intervals over four weeks (n = 6 FOVs). All data are reported as mean ± standard deviation. Asterisks indicate statistically significant comparisons, with *p<0.05, **p<0.01, and ****p<0.0001 by ordinary two-way ANOVA with Tukey's multiple comparisons test or paired Student's t-test (ns denotes a non-significant comparison).

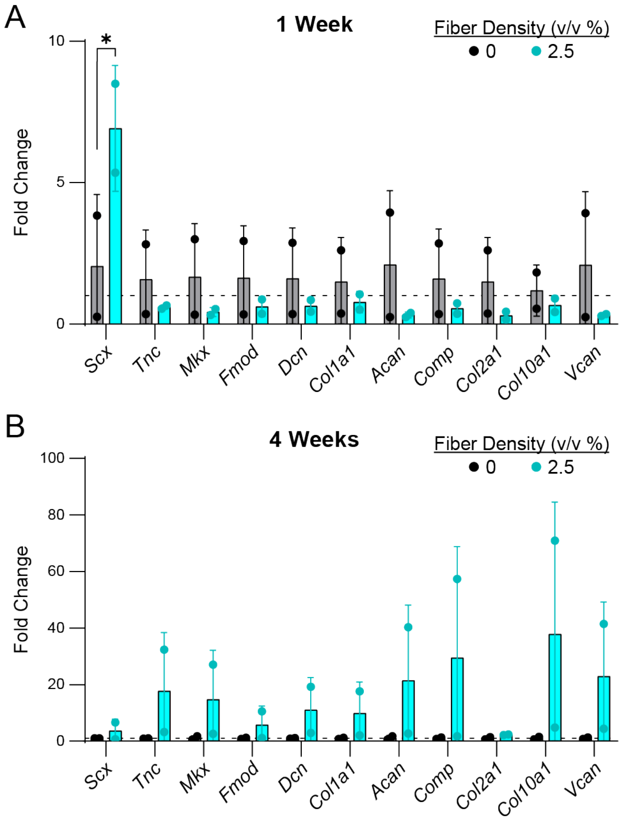

Supplemental Figure 5.3: TPC gene expression as a function of fibrous topography. Fold change in expression of canonical tenogenic and fibrochondrogenic genes by TPCs encapsulated in DexVS hydrogels (0 or 2.5 v/v% fibers) at (**A**) 1 week and (**B**) 4 weeks of culture (n = 2 hydrogels). All data are reported as mean ± standard deviation. Asterisks indicate statistically significant comparisons, with *p<0.05 by ordinary two-way ANOVA with Tukey's multiple comparisons test.

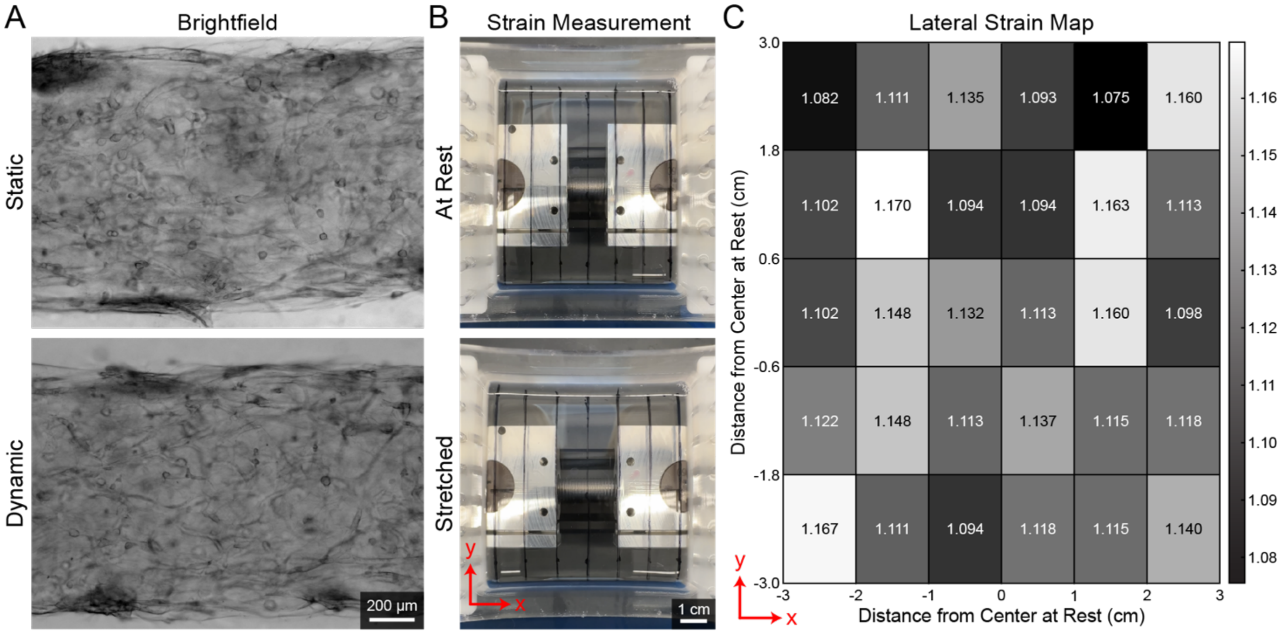

Supplemental Figure 5.4: Validation of FRHC stretch assembly. A) Brightfield images of FRHCs after one week of culture in static and dynamic strain conditions. **B**) Photographs of a resting and stretched PDMS well, with black vertical lines spaced 1 cm apart at rest. **C**) Quantification of lateral strain (in the x direction) across the base of the PDMS well.

Chapter 6: Conclusions and Future Directions

6.1 Summary of findings

Fiber-reinforced hydrogel composites (FRHCs) pose a promising strategy for engineering biomaterial therapies to improve tissue regeneration following tendon injury. Chapter 2 described the evolution of biomaterial strategies for tendon repair, wherein initial approaches focusing on mechanics and topography shifted toward a more holistic set of scaffold design criteria that address specific biological phases of tendon healing. Through tunable, modular incorporation of biochemical cues, fibrous topography, and soluble factor delivery vehicles, synthetic FRHCs excel at encouraging cell recruitment, polarizing the immune phenotype, driving tenogenic differentiation, and templating aligned deposition of *de novo* ECM. A pressing need in the continued development of tendon FRHCs, however, is successful integration of these features in an injectable composite capable of conforming to the wound margins and crosslinking *in situ*. Therefore, this thesis focused on integrating tunable, synthetic biomaterials and novel soluble factor delivery systems to create a modular, injectable hydrogel with spatiotemporal control over two key phases of tendon healing: 1) progenitor cell recruitment to the injury site and 2) tenogenic differentiation contributing to aligned matrix deposition and functional tissue regeneration.

This thesis employed a combination of microfluidically generated, heparin affinity-based soluble factor delivery vehicles; 2D and 3D synthetic fibrous substrates with fine control over topographical density and alignment; mechanically actuated 3D cell culture; and a range of *in* *vitro*, *in silico*, *ex vivo*, and *in vivo* models. Using these systems, this thesis interrogated the role of specific microenvironmental cues delivered by a synthetic, dextran vinyl sulfone (DexVS) FRHC in promoting tendon progenitor cell (TPC) recruitment and tenogenesis thereof. Chapter 3 examined the synergistic impact of microgel-delivered PDGF-BB and fibrous topography on TPC recruitment (Kent et al., 2022). Chapter 4 studied the combined role of growth factor supplementation and fibrous topography on tenogenic differentiation in addition to alignment and maturation of collagenous matrix. Chapter 5 built on the previous chapter, examining the influence of cell-adhesive fibrous topography on tenogenic and fibrochondrogenic differentiation of TPCs. Overall, 1) development of an injectable FRHC that regulates multiple temporal phases of tendon healing and 2) an improved understanding of the microenvironmental cues driving functional tendon regeneration will provide new information critical to the advancement of biomaterial therapeutics geared toward connective tissue regeneration.

6.2 Future directions

6.2.1 Delayed delivery of soluble tenogenic cues

Fine control over multi-staged release of soluble factors is needed for addressing multiple stages of tendon healing (Sharma and Maffulli, 2006; F. Wu et al., 2017a). Early release of chemokines driving stromal cell recruitment and pro-regenerative immune polarization should be followed by delayed release of pro-tenogenic cues like transforming growth factor (TGF)-β3. In Chapter 3, this thesis applied hybrid microgels comprised of methacrylated heparin and DexVS to achieve sustained release of platelet-derived growth factor (PDGF)-BB and induce TPC recruitment from an Achilles tendon stub *ex vivo* (Kent et al., 2022). However, even with maximized heparin concentrations, these microgels expend their payload within the first 2 weeks following implantation, making them inviable for delivering pro-tenogenic cues following stromal cell recruitment. Thus, strategies are needed for delayed, ideally cell-mediated release of tenogenic soluble cues are needed to achieve robust tendon regeneration with a single therapeutic intervention.

Recent work in bone tissue engineering has demonstrated the use of composite biomaterial scaffolds for multi-staged release of soluble cues. Subbiah et al. embedded heparin nanoparticles in an alginate scaffold, leveraging their difference in negative charge magnitude to orchestrate early delivery of vascular endothelial growth factor followed by bone morphogenetic protein 2 (Subbiah et al., 2020). Another approach physically adsorbed interferon γ to a decellularized bone scaffold and also attached interleukin (IL)-4 via a biotin-streptavidin interaction to achieve sequential delivery of M1- and M2-polarizing cytokines (Spiller et al., 2015). While disparate release rates can temporally shift the peak concentrations achieved at the site of implantation, no approach based on non-covalent interactions has been able to demonstrate true delayed release. Therefore, alternate release mechanisms are needed that will not activate merely by the passage of time.

Covalent linkage via a cell-degradable peptide, for example, would theoretically delay payload release until recruited cells locally secrete MMPs. In the case of TGF-β3, this scheme offers the added benefit of matrix-bound TGF-β presentation (Wipff et al., 2007), which would also act locally on recruited cells. Conjugation of recombinant TGF-β3 to a DBCO molecule would facilitate a click reaction to an azide-modified, cell-degradable peptide. Alternatively, a peptide fragment of TGF-β3 containing the TGFBR2 binding site could be synthesized with an azide-modified peptide in its primary sequence, allowing it to click on to a DBCO-modified, cleavable peptide. Finally, building on the microfluidic droplet generation technique described in Chapter 3, self-assembled nanofilm coatings or double-emulsion droplet generation could physically sequester tenogenic soluble cues until slow degradation of the outer shell occurs (Bian et al., 2011; Mohanraj et al., 2019). A major next step in improving tendon FRHCs may be adapting similar technologies to these highly modular scaffolds for robust tenogenic differentiation.

6.2.2 Immunomodulation

The immune system plays an important role throughout the tendon healing process. While an early, pro-inflammatory response is needed to initiate healing, a delayed transition to a pro-regenerative immune phenotype poses a potential driver of incomplete regeneration and scar tissue formation (Arvind et al., 2021). During tendon repair, macrophages are known to engage in crosstalk with stromal progenitor cells, influencing behavior of the latter as a function of polarization state (E. Chung and Son, 2014; Pajarinen et al., 2019). Moreover, previous tendon tissue engineering work has demonstrated polarization of macrophages to a pro-regenerative, M2-like phenotype via presentation of specific physical and soluble cues (Cai et al., 2023; Spiller et al., 2015; Sridharan et al., 2019). In Chapters 3 and 4 of this thesis, we respectively investigate strategies for sustained soluble factor delivery and physical, pro-tenogenic cues within an FRHC. However, there remains a need for integrated delivery of M2-polarizing and pro-tenogenic microenvironmental cues in addition to characterization of their potential interaction.

Release of M2-polarizing cytokines like IL-4, -10, and -13 represents a useful application of the heparin-based soluble factor delivery technology outlined in Chapter 3 (Kent et al., 2022). These microgels function through charge-based affinity between negatively-charged sulfate groups decorating heparin and positively charged soluble proteins. Although proteins exhibit widely varying affinity for heparin (Martino et al., 2014), heparin-based delivery vehicles have demonstrated efficacy over a wide range of soluble factors (Hettiaratchi et al., 2014; Hettiaratchi and Shoichet, 2019; Rinker et al., 2018; Subbiah et al., 2020; Zimmermann et al., 2017). Thus, future work should explore applications of hybrid heparin/DexVS microgels for immunomodulation. Moreover, in the interest of integrated orchestration of multiple phases of tendon healing, interactions between these cues must be characterized through co-culture *in vitro* models and *in vivo* models of tendon injuries.

6.2.3 Translational considerations

For eventual translation of an injectable, synthetic FRHCs for tendon repair, several technical and logistical hurdles must be addressed. These include *in situ* alignment of fibrous topography, off-target effects of growth factors, consideration of length scale and requisite mass transport, and integration with surgical repair. Toward this end, collaborative efforts across multidisciplinary teams, involving biomaterial scientists, biomedical engineers, clinicians, and veterinarians are needed.

Alignment of fibers during *in situ* crosslinking of an injectable FRHC is an important translational challenge. While magnetic alignment has been demonstrated *in vitro* (Hiraki et al., 2021), future work is needed to adapt this approach to rodent models. Eventual clinical translation poses additional logistical and safety concerns given the magnetic field strength required to align fibers with this approach. Intraoperative magnetic alignment would likely be impractical, and so early rodent models should explore other delivery options like ultrasound-guided, transdermal injection in the early postoperative period.

Another critical translational hurdle lies in mitigating the off-site effects of growth factors. Chapter 3 showed that heparin-based delivery vehicles can drastically reduce the implanted mass of growth factor required to achieve a local cell invasion response (Kent et al., 2022). However, future work in rodent and large animal models is needed to characterize soluble factor concentrations in off-target volume compartments. PDGF-BB, for example, is known to stimulate cell survival and proliferation in numerous tumor types (Bartoschek and Pietras, 2018). Confirmation of targeted delivery of soluble cues is therefore required as an early translational step.

The translation of fiber-reinforced hydrogels to clinical applications also necessitates an investigation of length scale and mass transport considerations. Efficient transfer of nutrients, oxygen, and signaling molecules within the hydrogel matrix is critical for supporting cell viability and promoting effective tendon regeneration (No et al., 2020a). This issue is further complicated when translating these biomaterials from the mm length scales of tissue regenerated in rodent models compared to the cm length scales required in humans. Previous work has employed sacrificial fibers to generate microscale porosity in a poly(ε-caprolactone) tendon scaffold (Z. Wang et al., 2018b). Incorporation of sacrificial porogens in a tendon FRHC would reduce the already low tensile moduli of FRHCs for tendon repair applications. However, future work could explore combinations of sacrificial porogens and more robust crosslinking of the surrounding bulk hydrogel material, which could potentially yield more efficient mass transport without affecting bulk mechanical properties.

Finally, a critical challenge lies in reconciling the mechanical properties of pro-tenogenic FRHCs with the increasing dynamic forces experienced by tendons over the course of healing and rehabilitation. Given the poor tensile mechanics of FRHCs relative to native tendon (No et al., 2020b; Wren et al., 2001), future work should investigate the utility of FRHC implantation as an adjunct to suture repair. Large animal models would be ideal for this work, as injecting an FRHC into the space between interdigitated, frayed collagen fibers following suture repair would be most akin an eventual clinical application.

Appendix

MATLAB Scripts

A1 Threshold check

```
%Threshold Check
%Bobby Kent
%7/31/2020
%
%Script that asks for an image and then repeated user inputs for a
%grayscale range and then reflects it in the image.
%
%Input scale as a 1x2 vector or 'done' if done or 'ROI' if you want to
%change the zoomed ROI.
%
%Type 'Done' when you're done.
%
%Available settings
%1) Show a full image with a choosable 1024/1024 ROI. Asked for an initial
%ROI, then can input 'ROI' as a string for the scale at any time to update.
%
%Email bobbykent14@gmail.com with questions.

clear
clc
close all
warning off

%% Settings
%ROI
% ROI_switch = 1; %on
% ROI_switch = 0; %off
ROI_switch = 2; %Single frame

%File format
% fmt = 1; %.tif
% fmt = 2; chan = 1; %.mat (specify chan)
fmt = 3; chan = 1; scn = 1; %.mat with multiple scenes (specify chan and
scene)
```

```
%% Iterate Image

%Select image
if fmt == 1
    filename = uigetfile('*.tif');
    image_raw = imread(filename);
else
    filename = uigetfile('*.mat');
    load(filename);
    if fmt == 2
        image_raw = data{1}{chan,1};
    elseif fmt == 3
        image_raw = data{scn,1}{chan,1};
    end
end


%Initialize figure and show raw image
h_fig = figure(1);
set(h_fig,'Units','Normalized','Outerposition',[0.1 0 0.8 1]);
% image_raw = imgout;
image = mat2gray(image_raw);
imshow(image);

if ROI_switch ~= 2
    if ROI_switch == 1

        %Get coordinates
        [coord(1), coord(2)] = getpts;

        for i = 1:2 %Iterate through coordinates

            coord(i) = floor(coord(i));

            if coord(i) < 512
                coord_rng(i,:) = [1 1024];
            elseif coord(i) > 9728
                coord_rng(i,:) = [9216 10240];
            else
                coord_rng(i,:) = coord(i) + 512.*[-1 1];
            end
        end

        %Define ROI
        image_ROI =
image(coord_rng(2,1):coord_rng(2,2),coord_rng(1,1):coord_rng(1,2));

        %Update figure
        set(h_fig,'Units','Normalized','Outerposition',[0 0 1 1]);
        subplot(1,2,1); hold on
        imshow(image);

        plot([coord_rng(1,1) coord_rng(1,2) coord_rng(1,2) coord_rng(1,1)
coord_rng(1,1)],...
            [coord_rng(2,1) coord_rng(2,1) coord_rng(2,2) coord_rng(2,2)
coord_rng(2,1)],...
            '-r','LineWidth',2);

        pos = get(gca,'Position');
        set(gca,'Position',[pos(1) - 0.1 pos(2) - 0.2 pos(3) + 0.2 pos(4) +
0.3]);

        subplot(1,2,2);
        imshow(image_ROI);
    end
else
    image_ROI = image;
end

%Iterate until user likes scaling
done = 0;
scale = [1000 2000];
scale_prev = [1 65535];

while done == 0

    %Scale image and convert to grayscale
    scale = input('Input scale vector (min and max values out of 65,536): ');

    if strcmp(scale,'ROI')

        subplot(1,2,1); hold on
        imshow(image);

        pos = get(gca,'Position');
        set(gca,'Position',[pos(1) - 0.1 pos(2) - 0.2 pos(3) + 0.2 pos(4) +
0.3]);

        %Get coordinates
        [coord(1), coord(2)] = getpts;

        for i = 1:2 %Iterate through coordinates

            coord(i) = floor(coord(i));

            if coord(i) < 512
                coord_rng(i,:) = [1 1024];
            elseif coord(i) > 9728
```

```
                coord_rng(i,:) = [9216 10240];
            else
                coord_rng(i,:) = coord(i) + 512.*[-1 1];
            end
        end

        plot([coord_rng(1,1) coord_rng(1,2) coord_rng(1,2) coord_rng(1,1)
coord_rng(1,1)],...
            [coord_rng(2,1) coord_rng(2,1) coord_rng(2,2) coord_rng(2,2)
coord_rng(2,1)],...
            '-r','LineWidth',2);

        %Define ROI
        image_ROI =
image(coord_rng(2,1):coord_rng(2,2),coord_rng(1,1):coord_rng(1,2));
        subplot(1,2,2);
        imshow(image_ROI);
    elseif strcmp(scale,'Done')
        done = 1;
    elseif size(scale) == [1 2]
        scale_prev = scale;
        image = mat2gray(image_raw,scale);
        subplot(1,2,1); hold on
        imshow(image);
        if ROI_switch ~= 2
            plot([coord_rng(1,1) coord_rng(1,2) coord_rng(1,2) coord_rng(1,1)
coord_rng(1,1)],...
                [coord_rng(2,1) coord_rng(2,1) coord_rng(2,2) coord_rng(2,2)
coord_rng(2,1)],...
                '-r','LineWidth',2);
        end
        pos = get(gca,'Position');
        set(gca,'Position',[pos(1) - 0.1 pos(2) - 0.2 pos(3) + 0.2 pos(4) +
0.3]);

        if ROI_switch ~= 2
            image_ROI =
image(coord_rng(2,1):coord_rng(2,2),coord_rng(1,1):coord_rng(1,2));
        else
            image_ROI = image;
        end
        image_ROI_rgb = cat(3,image_ROI,image_ROI,image_ROI);

        subplot(1,2,2);
        if ~isempty(find(image_ROI == 1))
            [x, y] = find(image_ROI == 1);

            for i = 1:length(x)
                image_ROI_rgb(x(i),y(i),:) = [1 0 0];
            end
            imshow(image_ROI_rgb);
        else
            imshow(image_ROI_rgb);
        end
    else
        disp('Invalid Input');
    end
end

close all

disp(' ');
disp('=========================');
disp(['Scale = [' num2str(scale_prev(1)) ' ' num2str(scale_prev(2)) ']']);
disp('=========================');
```

A2 Color merge

```
%Color Merge
%Bobby Kent
%11/24/22
%
%Script that generates merged images from multiple channels. Each channel
%can be optionally Gaussian filtered.
%
%Select a single channel for each image you'd like to process. You'll need
%files in the same directory with an identical filename except for the
%channel (i.e., c1, c2, etc.) for every channel included in the user inputs
%for each image selected.
%
%Use threshold_check.m and batch_thresh_img.m to produce thresholded .tifs
%(from original data) before using this script.
%
%Email bobbykent14@gmail.com with questions.

clear
clc
close all

%% USER INPUTS
%Desired channels
chan_i = [1];

%Colors (normalized to 1) in order of channel 1, 2, 3, etc. (include a
%color for channels you aren't including too)
colors = [1 1 1;
    0 1 1;
    1 1 0];

%Amplifiers
amp = [2.5 1.5 2 3]; %Include a value for each channel (even ones you aren't
processing) (1 => unchanged)

%Lower threshold on 0-1 scale (one for every channel, even if not
%processing) (0 => unchanged)1
l_thresh = [0.15 0.1 0.1];

%Gaussian filter settings
%In order of channel 1, 2, 3, etc., include a 0 (no filter) or 1 (filter).
%Include a value even for channels you're not processing so that the index
%of the value matches the number of the channel it represents:
filt_chan = [1 0 0];

%[signal size, back size] with rows in order of filtered channels (use
gauss.m to find good values)
%For 10x TPCs (12/7/22):
```

```
%-Cytosolic [NS BS] = [4 70];
%-Nuclear [NS BS] = [3 30];
%-Vinculin (40x) [NS BS] = [2 100];

sig_back_size = [2 70; %Define in a [channel x NS/BS] matrix
    2 70;
    2 70;
    3 30];



%% FILTER AND MERGE IMAGES
%Select image
filenames_pre = uigetfile('*.tif','MultiSelect','On');
if ~iscell(filenames_pre) %Make an array even if n = 1
    filenames{1} = filenames_pre;
else
    filenames = filenames_pre;
end


%Iterate through selected files
for f = 1:length(filenames)

    %Get index of channel number for current filename
    c_i = strfind(filenames{f},'_ORG')-1;
    filt_i = find(filt_chan);

    %Iterate through all channels
    for c = chan_i

        %Load current image
        fname_curr = [filenames{f}(1:c_i-1) num2str(c)
filenames{f}(c_i+1:end)];
        img_raw = imread(fname_curr);
        img_raw = img_raw(:,:,1);

        %Initialize merged image
        if c == chan_i(1)
            sz = size(img_raw);
            merge = zeros(sz(1),sz(2),3);
        end

        %Filter ===========================================================
        filt_ii = find(filt_i==c);

        if ~isempty(filt_ii)

            %Calculate H parameters
            signalH = 
fspecial('gaussian',sig_back_size(filt_ii,1),sig_back_size(filt_ii,1)/3);
            backH = 
fspecial('gaussian',sig_back_size(filt_ii,2),sig_back_size(filt_ii,2)/3);

            %Apply lower threshold
            img_raw(img_raw<l_thresh(c)*65535) = 0;

            %Calculate background
            background = imfilter(img_raw,backH,'symmetric');

            %Subtract background and rescale
            img = img_raw - background;

            %Set anything that became negative to 0
            img(img<0) = 0;
            img = mat2gray(img);

            %Filter noise
            img = imfilter(img,signalH,'symmetric');
        else
            img = mat2gray(img_raw);
            img(img<l_thresh(c)) = 0; %Apply lower threshold
        end

        %Merge ============================================================
        for rgb_i = 1:3
            merge(:,:,rgb_i) = merge(:,:,rgb_i) + 
amp(c)*colors(c,rgb_i).*img;
        end
    end

    %Save merged image
    imwrite(merge,[filenames{f}(1:c_i-2) 'c' num2str(chan_i) '_MERGE.tif']);
end
```

A3 Nucleus counter 3D

```
%Nuc Counter 3D
%Bobby Kent
%4/22/21
%
%Function that takes a z-stack of nuclear channels and identifies 3D
%clusters. Returns 3D coordinates of all nuclei and optionally generates a
%video as a sanity check.
%
%Input xy zoom as the second argument (number between 0 and 1) so that the
%function can interpret nuclear volumes.
%
%The third argument is the nuclear volume limits, which must be a 1x2
%vector.
%
%***If you're not sure about your nuclear volume limits, check a histogram
%of nuclear volumes from a test sample and use that to define reasonable
%limits.
%
%Input the variable argument 'video' after the nuclear volume limits to
%store a sanity check.
%
%Email bobbykent14@gmail.com with questions.

function [centroid,nucVol,cent_map] =
nuccounter3D(nucmat,zoom,nucvol_limits,varargin)

if isempty(varargin)
    vid = 0;
else
    vid = 1;
end

%Get size of z-stack
xy_size = size(nucmat(:,:,1));
z_size = size(nucmat,3);

%Threshold image
[~, nucTVal_1] = imthresh_rnk(nucmat(:,:,1),'Z Bot');
[~, nucTVal_mid] = imthresh_rnk(nucmat(:,:,floor(z_size/2)),'Z
Middle',nucTVal_1);
[~, nucTVal_end] = imthresh_rnk(nucmat(:,:,z_size),'Z Top',nucTVal_mid);
slope_low = (nucTVal_mid-nucTVal_1)/(z_size/2);
slope_high = (nucTVal_end-nucTVal_mid)/(z_size/2);

maskmat = zeros(xy_size(1),xy_size(2),z_size); %Initialize 3D mask
for z = 1:z_size

    if z < z_size/2
```

```
        nucTVal = nucTVal_1 + slope_low*(z-1);
    else
        nucTVal = nucTVal_1 + slope_high*(z-floor(z_size/2)); %Extrapolate
threshold value in far half of the stack
    end

    %Get nuc image
    nuc = nucmat(:,:,z);

    %Binarize, close holes, and remove spurs
    nuc_temp = im2bw(nuc,nucTVal);
    nuc_temp = bwmorph(nuc_temp, 'close');
    nucMask = bwmorph(nuc_temp, 'spur');

    %Update 3D mask
    maskmat(:,:,z) = nucMask;
end

%Identify 3D clusters
CC = bwconncomp(maskmat,26);
allStats = regionprops3(CC,'Volume','Centroid');

nucCount = 0;
cent_map = zeros(xy_size);
%Iterate through clusters, volume exclude, and store
dot_size = 1;
z_v = [];
R_ct = 0;
for k=1:CC.NumObjects
    if allStats.Volume(k)/(zoom^2) >= nucvol_limits(1) &&
allStats.Volume(k)/(zoom^2) <= nucvol_limits(2)
        nucCount = nucCount + 1;
        centroid(nucCount,:) = allStats.Centroid(k,:); % if thfey're the
right size, record their centroid and increment nucCount
        nucVol(nucCount) = allStats.Volume(k)/zoom^2;

        %Build centroid map if storing
        if vid == 1
            if round(centroid(nucCount,1)) <= dot_size
                cent_map(round(centroid(nucCount,2))-
dot_size:round(centroid(nucCount,2))+dot_size,...

round(centroid(nucCount,1)):round(centroid(nucCount,1))+dot_size,round(centro
id(nucCount,3)))...
                        = ones(1+2*dot_size,1+dot_size);
            elseif round(centroid(nucCount,2)) <= dot_size

cent_map(round(centroid(nucCount,2)):round(centroid(nucCount,2))+dot_size,...
                        round(centroid(nucCount,1))-
dot_size:round(centroid(nucCount,1))+dot_size,round(centroid(nucCount,3)))...
```

```
                    = ones(1+dot_size,1+2*dot_size);
            elseif round(centroid(nucCount,1)) > xy_size(2)-dot_size
                cent_map(round(centroid(nucCount,2))-
dot_size:round(centroid(nucCount,2))+dot_size,...
                    round(centroid(nucCount,1))-
dot_size:round(centroid(nucCount,1)),round(centroid(nucCount,3)))...
                    = ones(1+dot_size,1+2*dot_size);
            elseif round(centroid(nucCount,2)) > xy_size(1)-dot_size
                cent_map(round(centroid(nucCount,2))-
dot_size:round(centroid(nucCount,2)),...
                    round(centroid(nucCount,1))-
dot_size:round(centroid(nucCount,1))+dot_size,round(centroid(nucCount,3)))...
                    = ones(1+dot_size,1+2*dot_size);
            else
                cent_map(round(centroid(nucCount,2))-
dot_size:round(centroid(nucCount,2))+dot_size,...
                    round(centroid(nucCount,1))-
dot_size:round(centroid(nucCount,1))+dot_size,round(centroid(nucCount,3)))...
                    = ones(1+2*dot_size,1+2*dot_size);
            end
        end

        z_v = [z_v round(centroid(nucCount,3))];
    end
end

%Assign an empty centroid matrix if nuc count = 0
if nucCount == 0
    centroid = [];
    nucVol = [];
end

%Fill out centroid map matix if any empty z
if vid == 1
    for z = setdiff(z_v,1:z_size)
        cent_map(:,:,z) = zeros(xy_size);
    end

    %Generate and save video for sanity check
    cd ..
    if exist('video_check') ~= 7
        mkdir('video_check');
    end
    cd video_check
    v = VideoWriter(varargin{1});
    open(v)

    cent_map_ortho = sum(cent_map,3);
    cent_map_ortho(cent_map_ortho > 1) = 1;
    for z = 1:z_size
```

```
        for k = 1:3 %RGB
            frame_overlay(:,:,k) = maskmat(:,:,z).*1;

            if k == 1
                frame_overlay(:,:,k) = frame_overlay(:,:,k) + cent_map_ortho;
            else
                frame_overlay(:,:,k) = frame_overlay(:,:,k) - cent_map_ortho;
            end

            ftemp = frame_overlay(:,:,k);
            ftemp(frame_overlay(:,:,k) > 1) = 1;
            ftemp(frame_overlay(:,:,k) < 0) = 0;
            frame_overlay(:,:,k) = ftemp;
        end

        writeVideo(v,frame_overlay);
    end
    close(v)
    cd ..
    cd mat_files
end
end
```

A4 Donut quant

```
%Donut Quant
%Bobby Kent
%6/1/2021
%
%Fucntion that takes a filename root and channel number for one or more
%channels of interest, then quantifies the mean cytosolic (donut) and
%nuclear intensities on a per-cell basis.
%
%Email bobbykent14@gmail.com with questions.

function [nucInt, cytoInt, cell_count] = donutquant(fnameStem, chanScale,
root, chans, chans_n, refNum_curr, msk_folder_n, tf_mt)

%Set radii to iterate through
radius_n = {'r15'}; %10x, 0.5 zoom
% radius_n = {'r30'}; %10x
% radius_n = {'r120'};

%Display progress
disp(['Processing ' root ' ...']);

%Load and threshold all channel images a single time
chanImg = cell(1,length(chans)); %Pre-allocate channel image cells

for ch = 1:length(chans)
    if tf_mt == 1
        chanFilename = strcat(fnameStem,chans{ch},'_ORG.tif');
        chanImg{ch} = mat2gray(imread(chanFilename),chanScale(ch,:));
    else
        chanFilename = strcat(fnameStem,'.mat');
        load(chanFilename);
        chanNum_curr = str2num(chans{ch}(end));
%         chanImg{ch} = mat2gray(data{str2num(refNum_curr)}{chanNum_curr,1});
%1024x1024 only
        chanImg{ch} = mat2gray(data{(str2num(refNum_curr)-
1)*2+1}{chanNum_curr,1}); %1024 and 512
    end
end
disp('Channel Images Loaded and Thresholded');

%Iterate through tiles
cell_i = 1; %Initialize cell counter

%Load mask file for present tile (variable is maskmat)
cd([msk_folder_n '\' root '_masks']);
load(['mask-' refNum_curr '.mat']);
cd ..
cd ..
```

```
%Save current cell index; will reset to this for each new channel
cell_tile_start = 1; %Artifact from tile version

%Iterate through channels
if numel(fieldnames(maskmat)) > 1
    for ch = 1:length(chans)

        %Get subimage of current channel and tile
        chan_subImg = chanImg{ch}; %Artifact from tile version

        for c = 1:length(maskmat.nuc)

            %Nuclear intensity
            nucMask = zeros(maskmat.imgsize);
            nucMask(maskmat.nuc{c}) = 1;
            nucInt.(chans_n{ch})(cell_i) = sum(sum(chan_subImg .*
nucMask))/length(maskmat.nuc{c});

            for r = 1:length(radius_n)

                %Cyto intensity
                cytoMask = zeros(maskmat.imgsize);
                cytoMask(maskmat.cyto.(radius_n{r}){c}) = 1;
                cytoInt.(chans_n{ch}).(radius_n{r})(cell_i) =
sum(sum(chan_subImg .* cytoMask))/length(maskmat.cyto.(radius_n{r}){c});
            end

            %Update cell count
            cell_i = cell_i + 1;
        end

        %Reset cell index for next channel
        if ch < length(chans)
            cell_i = cell_tile_start;
        end
    end
end

%Store cell count for the tile
cell_count = cell_i;

%Clear maskmat (not sure if this will automatically overwrite)
clear maskmat

disp(' ');

end
```

A5 Donut mask

```
%Donutmask
%Bobby Kent
%6/1/2021
%
%Function that takes a nuclear mask, draws a donut around each nucleus,
%and then stores nuclear and cyto masks in a folder.
%
%Email bobbykent14@gmail.com with questions.

function donutmask(nucMask, centroid, clusters, sz, root, refNum_list,
msk_folder_n)

%Set radii to iterate through
% radius = [30 40 50];
% radius_n = {'r30' 'r40' 'r50'};

%10x
% radius = 30;
% radius_n = {'r30'};

%10x, 0.5 zoom
radius = 15;
radius_n = {'r15'};

% %40x
% radius = 120;
% radius_n = {'r120'};

%% GET CENTROIDS AND CREATE MASKS
%Establish directory for masks
if exist(msk_folder_n) ~= 7
    mkdir(msk_folder_n);
end
cd(msk_folder_n);

%Iterate through roots
for rt = 1:length(root)

    %Display progress
    disp(['Processing ' root{rt} ' ...']);

    %Get into directory for present root
    mkdir([root{rt} '_masks']);
    cd([root{rt} '_masks']);

    %Get current nucMask, centroid, and clusters
    curr_nucMask = nucMask{rt};
    curr_centroid = centroid{rt};
    curr_clusters = clusters{rt};

    %Get subset of nucMask
    nuc_subMask = curr_nucMask; %(variable renamed in tile version)

    %Store image size for later reference
    maskmat.imgsize = sz;

    %Initialize cell counter
    cell_i = 1;

    for c = 1:size(curr_centroid,1)

        %Nuclear mask for current cell
        nucMask_r = zeros(sz,sz);
        nucMask_r(curr_clusters == c) = 1;

        %Store nuclear mask indices
        maskmat.nuc{cell_i} = find(nucMask_r == 1);

        for r = 1:length(radius)
            %Draw circular mask around current centroid
            circMask = drawCircMask(curr_centroid(c,:),radius(r),sz.*[1 1]);

            %Subtract ALL nuclei from current cyto mask image
            cytoMask_r = circMask - nuc_subMask;
            cytoMask_r(cytoMask_r == -1) = 0; %Make -1 -> 0

            %Store cyto mask indices for current radius
            maskmat.cyto.(radius_n{r}){cell_i} = find(cytoMask_r == 1);
        end

        %Update cell count
        cell_i = cell_i + 1;
    end

    %Save mask for current tile for later use / correlations
    save(['mask-' refNum_list{rt} '.mat'],'maskmat');
    clear maskmat


    %Back out to donut_mask directory
    cd ..
    disp(' ');
end

%Back out to image data directory
cd ..
```

A6 Focal adhesion quant

```
%Adhesion Quant
%Bobby Kent
%1/20/22
%
%Fucntion that takes a filename root and channel number for one or more
%channels of interest, then quantifies the mean focal adhesion intensity on
%a per-FOV basis.
%
%Also quantifies morphometrics for each focal adhesion.
%
%Email bobbykent14@gmail.com with questions.

function [adInt, adStats] = adhesionquant(fnameStem, chanScale, root, chans,
chans_n, refNum_curr, msk_folder_n,tf_mt)

%Set up strings for stat labeling
stat_n = {'Count',
'Area','Eccentricity','Orientation','MajorAxisLength','MinorAxisLength'};

%Display progress
disp(['Processing ' root '-' refNum_curr ' ...']);

if tf_mt == 1
%Load and threshold all channel images a single time
chanImg = cell(1,length(chans)); %Pre-allocate channel image cells
for ch = 1:length(chans)
    chanFilename = strcat(fnameStem,chans{ch},'_ORG.tif');
    chanImg{ch} = mat2gray(imread(chanFilename),chanScale(ch,:));
end
elseif tf_mt == 2
    %Wrote for 1 channel for now
    data = load([fnameStem '.mat']);
    chanImg_raw = data.data{str2num(refNum_curr)}{1,1};
    chanImg{1} = mat2gray(chanImg_raw,chanScale(1,:));
end
disp('Channel Images Loaded and Thresholded');

%Load mask file for present tile (variable is maskmat)
cd([msk_folder_n '\' root '_masks']);
load(['mask-' refNum_curr '.mat']);
cd ..
cd ..

%% Calculate FA intensity in channel(s) of interest
%Iterate through channels
for ch = 1:length(chans)

    %Get image of current channel
    chanImg_curr = chanImg{ch};

    %FA intensity
    adInt.(chans_n{ch}) = sum(sum(chanImg_curr .*
maskmat))/length(maskmat)^2;
end
if length(chans) == 0
    adInt = NaN;
end

%% FA morphometrics (from CDD's faquant2)
%Initialize adhesion counter
FA_ct = 0;

%Find and label clusters
maxVincArea = 10000;
[adh, adhCount] = bwlabel(maskmat,8);
adhStats =
regionprops(adh,'Area','Eccentricity','Orientation','MajorAxisLength','MinorA
xisLength');
for i=1:adhCount
    if adhStats(i,1).Area > maxVincArea
        adh(adhStats(i,1).PixelIdxList)=0;
    else
        for sn = 2:length(stat_n)
            rawAdh2D(i,sn) = adhStats(i,1).(stat_n{sn});
        end

        FA_ct = FA_ct + 1;
    end
end

%Store means per FOV
adStats.(stat_n{1}) = FA_ct;
for sn = 2:length(stat_n)
    if FA_ct > 0
        adStats.(stat_n{sn}).mean = mean(rawAdh2D(:,sn));
        adStats.(stat_n{sn}).stdev = std(rawAdh2D(:,sn));
    else
        adStats.(stat_n{sn}).mean = 0;
        adStats.(stat_n{sn}).stdev = 0;
    end
end

%Clear maskmat (not sure if this will automatically overwrite)
clear maskmat

disp(' ');

end
```

A7 Cell spheroid outgrowth quant

```
%Outgrowth Quant Script (+3D nuclear distance)
clear
clc
close all

%% Add your .mat directory
% cd X:\Data\DVSOPT\VP_FD_screens\screen2_4_14_21\mat_files

%% EDIT OUTPUT XLS
outputXlsName = 'outgrowth_quant_temp.xls';

%Store video?
% vid = 1; %Yes
vid = 0; %No

%% Set nuclear volume limits
% nucvol_limits = [100 4000];
% nucvol_limits = 1; %Unknown limits
nucvol_limits = 2; interval = 2500; %Bins
top_limit = 5*10^4;

%% Set up strings
chan_label = {'actin','nuc'};

%% Outgrowth Quant
fname_select_temp = uigetfile('*.mat','Choose Ortho Projections
Only','MultiSelect','On');
if ~iscell(fname_select_temp)
    fname_select{1} = fname_select_temp;
else
    fname_select = fname_select_temp;
end

for i = 1:length(fname_select)

    %Get current filename
    fname = fname_select{i};
    fname_label = fname(1:strfind(fname,'-MAX')-1);

    %Check zoom
    zoom_i = strfind(fname,'zoom');
    if ~isempty(zoom_i)
        zoom = str2num(fname(zoom_i - [3:-1:1]));
    else
        zoom = 1;
    end

    %Load image data
    ortho_struct = load(fname);
    zstack_struct = load([fname_label '.mat']);

    %Check if fiber image taken
    n_chan = size(ortho_struct.data{1},1); %Number of channels
    if n_chan == 3
        c = [2 3]; %Fibers are c1
    else
        c = [1 2]; %No fiber image
    end

    %Read in actin and nuclear projection images and threshold
    for c_i = 1:2
        orthoImgData.(chan_label{c_i}) = ortho_struct.data{1}{c(c_i),1};
    end
    [orthoMask.actin,~] = imthresh_rnk(orthoImgData.actin,'Ortho Mask',0.01);

    %Display actin/nucleus image and draw circular ROI based on spheroid
center
    for k = 1:3
        actin_nuc_merge(:,:,k) = mat2gray(orthoImgData.actin);
        if k == 2
            actin_nuc_merge(:,:,k) = mat2gray(orthoImgData.actin) +
mat2gray(orthoImgData.nuc);
        end
    end
    circFig = figure('visible','off','units','normalized','outerposition',[0
0 0.67 1]);
    imagesc(actin_nuc_merge); axis square
    set(gca,'visible','off');
    title('Click center of spheroid');
    center = ginput(1);
    circle = drawcircle('Center',center,'Radius',9,'Color',[1 0 0]);


    %Determine variance of mask pixel intensity in the circle as a function
of radius
    center_thresh = 0.25; %Number of pixels tolerated between body mask
center and centroid of overlap with actin mask
    center_diff = center_thresh + 1; %Initialize center diff
    count = 0;
    while center_diff > center_thresh

        r_v = 10:150; r = 0;
        var = 0;
        while var == 0
            r = r + 1;
            set(circle,'Radius',r_v(r)); %Update radius (10 pixels is the
first one checked)
            circ_mask = createMask(circle); %Make a mask from circular ROI
            mask_sum = orthoMask.actin + circ_mask.*2; %Double and add to
threshActinImage
            var = std(mask_sum(mask_sum > 1) - 2)^2; %Calculate variance at
this radius
        end

        rad = r_v(r) * 1.5;

        %Get centroid of mask overlap and adjust center
        set(circle,'Radius',rad);
        circ_mask = createMask(circle);
        overlap = orthoMask.actin.*circ_mask;
        overlapStat = regionprops(overlap,'Centroid');
        center_diff = sqrt((center(1) - overlapStat.Centroid(1))^2 +
(center(2) - overlapStat.Centroid(2))^2);

        %Reset center
        center = overlapStat.Centroid;
        set(circle,'Center',center);
    end

    r_v = 10:150;
    for r = 1:length(r_v)
        set(circle,'Radius',r_v(r)); %Update radius (10 pixels is the first
one checked)
        circ_mask = createMask(circle); %Make a mask from circular ROI
        mask_sum = orthoMask.actin + circ_mask.*2; %Double and add to
threshActinImage
        var(r) = std(mask_sum(mask_sum > 1) - 2)^2; %Calculate variance at
this radius
    end

    %Refine radius
    [~,max_dy_i] = max(diff(var)./diff(r_v)); %Inflection point
    r_norm = (r_v(1:max_dy_i) - min(r_v(1:max_dy_i)))./(max(r_v(1:max_dy_i))-
min(r_v(1:max_dy_i)));
    var_norm = (var(1:max_dy_i) -
min(var(1:max_dy_i)))./(max(var(1:max_dy_i))-min(var(1:max_dy_i)));
    var_d = var_norm-r_norm;
    [~,inflect_i] = min(var_d);
    rad = r_v(inflect_i);

    %Set final radius and confirm
    set(circle,'Radius',rad);
    button = 1;
    while isempty(button) ~= 1
        [x,y,button] = ginput(1);

        % arrow keys to adjust threshold value
        if button == 30 % up arrow
```

```
            rad = rad + 5;
        end
        if button == 31 % down arrow
            rad = rad - 5;
            if rad <= 0
                rad = 1;
            end
        end
        if button == 28 % left arrow
            rad = rad - 1;
            if rad <= 0
                rad = 1;
            end
        end
        if button == 29 % right arrow
            rad = rad + 1;
        end

        center = get(circle,'Center');
        set(circle,'Radius',rad,'Center',center);
    end

    %Update final circle
    center = get(circle,'Center');
    rad = get(circle,'Radius');
    circle = drawcircle('Center',center,'Radius',rad,'Color',[0 0 1]);

    %Draw polygon to remove single cells and adjacent spheroids
    poly = drawpolygon('Color',[0 1 1]);
    poly_mask = createMask(poly);
    orthoMask.actin = orthoMask.actin.*poly_mask;

    %Create a mask with the drawn ellipse to separate body from outgrowth
    body = createMask(circle);
    bodyMask = orthoMask.actin.*body;
    close

    %Generate a masked z-stack of nuclear channel image
    %Create actin z-stack matrix too for finding spheroid height
    z_size = size(zstack_struct.data{1},1)/c(2);
    nucmat = zeros([size(orthoMask.actin),z_size]);
    for z = 1:z_size
        actinmat = mat2gray(zstack_struct.data{1}{(z-1)*c(2)+c(1),1});
        nucmat(:,:,z) = mat2gray(zstack_struct.data{1}{(z-
1)*c(2)+c(2),1}).*(poly_mask-body);

        actinmat_sphere_sum = actinmat + body*2;
        sphere_sum(z) = sum(sum(actinmat(actinmat_sphere_sum>1)));
    end
    %Determine z-height of spheroid
    [~,z_i] = max(sphere_sum);
    z_i = z_i + floor(rad*0.624/zoom/5/2); %Set center as 1/2 spheroid radius
past the peak intensity sum

    %Find centroids of nuclei
    centroid = []; nucVol = [];
    if nucvol_limits == 1
        [centroid,nucVol] = nuccounter3D(nucmat,zoom,[1 10^4]);
        cd ..
        if exist('nucVol_histograms') ~= 7
            mkdir('nucVol_histograms');
        end
        cd nucVol_histograms
        h_hist = histogram(nucVol,50);
        title(fname_label,'FontSize',15,'Interpreter','none');
        set(gca,'YLim',[0 20]);
        saveas(h_hist,[fname_label '.fig']);
        cd ..
        cd mat_files
        keyboard
    elseif nucvol_limits == 2
        if vid == 1
            [centroid_raw,nucVol] = nuccounter3D(nucmat,zoom,[200
top_limit],fname_label);
        else
            [centroid_raw,nucVol] = nuccounter3D(nucmat,zoom,[200
top_limit]);
        end
        for n = 1:length(nucVol)
            mult = floor(nucVol(n)/interval);
            if mult > 1
                for d = 2:mult
                    centroid_raw = [centroid_raw; centroid_raw(n,:)];
                end
            end
        end
    else
        [centroid_raw,nucVol] = nuccounter3D(nucmat,zoom,nucvol_limits);
    end

    %Sum total pixel area of outgrowths
    outgrowth_mask = orthoMask.actin - bodyMask;
    outgrowth_sum = sum(sum(outgrowth_mask));
    body_sum = sum(sum(bodyMask));

    %Convert area to square microns
    outgrowth_sum = outgrowth_sum*0.38028/(zoom^2);
    body_sum = body_sum*0.38028/(zoom^2);
    %Convert spheroid coordinates to microns with the origin at the center
    %of the spheroid
    for d = 1:2
        centroid(:,d) = (centroid_raw(:,d) - center(d))*0.624/zoom; %XY zoom
scaling
    end
    centroid(:,3) = (centroid_raw(:,3) - z_i)*5; %Z interval scaling

    %Compute nuclear outcome measures
    nuc_count = size(centroid,1);
    nuc_dist = sqrt(centroid(:,1).^2 + centroid(:,2).^2 + centroid(:,3).^2);
    total_mig = sum(nuc_dist);
    mean_mug = total_mig/nuc_count;

    %Number of cells migrating >100 microns
    n_over100 = length(nuc_dist(nuc_dist > 100));

    %Add to matrix to export to xls
    if i == 1
        xls_mat = {'Filename','Outgrowth Area','Body Area','Nuc Count','Total
Mig Dist','Average Mig Dist','Count >100um'};
    end

    xls_mat(i+1,:) =
{fname_label,outgrowth_sum,body_sum,nuc_count,total_mig,mean_mug,n_over100};

    %Store centroids
    cd ..
    if exist('centroids') ~= 7
        mkdir('centroids');
    end
    cd centroids
    save([fname_label '.mat'],'centroid');
    cd ..
    cd mat_files

end

cd ..
if exist(outputXlsName)
    u_ans = input('Are you sure you want to overwrite? (Y/N) ');
    if u_ans == 'Y'
        xlswrite(outputXlsName,xls_mat);
    else
        disp('Aborted');
    end
else
    xlswrite(outputXlsName,xls_mat);
end
```

A8 Achilles ex vivo outgrowth quant

```
%Outgrowth Quant Script (+3D nuclear distance) for Achilles Tendon Tissue
clear
clc
close all

%% Add your .mat directory
cd X:\Data\TENCAP\uG_pilot_5_29_21\mat_files

%% EDIT OUTPUT XLS
outputXlsName = 'outgrowth_quant_temp.xls';

%Store video?
% vid = 1; %Yes
vid = 0; %No

%% Set nuclear volume limits
% nucvol_limits = [100 4000];
% nucvol_limits = 1; %Unknown limits
nucvol_limits = 2; interval = 2500; %Bins
top_limit = 5*10^4;

%% Set up strings
chan_label = {'nuc'};

%% Outgrowth Quant
fname_select_temp = uigetfile('*.mat','Choose Ortho Projections
Only','MultiSelect','On');

if ~iscell(fname_select_temp)
    fname_select{1} = fname_select_temp;
else
    fname_select = fname_select_temp;
end

for i = 1:length(fname_select)

    %Get current filename
    fname = fname_select{i};
    fname_label = fname(1:strfind(fname,'_MAX')-1);

    %Check zoom
    zoom_i = strfind(fname,'zoom');
    if ~isempty(zoom_i)
        zoom = str2num(fname(zoom_i - [3:-1:1]));
    else
        zoom = 1;
    end
    %Load image data
    ortho_struct = load(fname);
    zstack_struct = load([fname_label '.mat']);

    %Read in nuclear projection image
    orthoImgData = ortho_struct.data{1}{1,1};
%     [orthoMask.actin,~] = imthresh_rnk(orthoImgData.actin,'Ortho
Mask',0.01);

    %Check to see if the mask data exist for this file root already
    cd ..
    if exist('mask_data') ~= 7
        mkdir('mask_data');
    end
    cd mask_data

    if exist([fname_label '.mat']) ~= 2

        %Display ortho projection and draw tissue boundary
        maxFig =
figure('visible','off','units','normalized','outerposition',[0 0 0.67 1]);
        imagesc(orthoImgData); axis square
        set(gca,'visible','off');
        title('Outline Tissue Boundary');
        tissue_boundary = drawpolygon('Color',[1 0 1]);
        tissue_mask = createMask(tissue_boundary);

        %Draw polygon to define midsubstance and its outgrowth
        title('Define Midsubstance');
        midsub_poly = drawpolygon('Color',[1 1 0]);
        midsub_mask = createMask(midsub_poly);

        %Draw polygon to remove BS
        title('Cut out BS');
        poly = drawpolygon('Color',[0 1 1]);
        poly_mask = createMask(poly);

        save([fname_label
'.mat'],'tissue_mask','tissue_boundary','poly_mask','midsub_poly');
        close all
    end

    load([fname_label '.mat']);

    cd ..
    cd mat_files

    %Generate a masked z-stack of nuclear channel image
    %Create actin z-stack matrix too for finding spheroid height
    z_size = size(zstack_struct.data{1},1);
    nucmat = zeros([size(orthoImgData),z_size]);
    for z = 1:z_size
        nucmat(:,:,z) = mat2gray(zstack_struct.data{1}{z,1}).*(poly_mask-
tissue_mask);
    end

    %Find centroids of nuclei
    centroid = []; nucVol = [];
    if nucvol_limits == 1
        [centroid,nucVol] = nuccounter3D(nucmat,zoom,[1 10^4]);
        cd ..
        if exist('nucVol_histograms') ~= 7
            mkdir('nucVol_histograms');
        end
        cd nucVol_histograms
        h_hist = histogram(nucVol,50);
        title(fname_label,'FontSize',15,'Interpreter','none');
        set(gca,'YLim',[0 20]);
        saveas(h_hist,[fname_label '.fig']);
        cd ..
        cd mat_files
        keyboard
    elseif nucvol_limits == 2
        if vid == 1
            [centroid_raw,nucVol] = nuccounter3D(nucmat,zoom,[200
top_limit],fname_label);
        else
            [centroid_raw,nucVol] = nuccounter3D(nucmat,zoom,[200
top_limit]);
        end
        for n = 1:length(nucVol)
            mult = floor(nucVol(n)/interval);
            if mult > 1
                for d = 2:mult
                    centroid_raw = [centroid_raw; centroid_raw(n,:)];
                end
            end
        end
    else
        [centroid_raw,nucVol] = nuccounter3D(nucmat,zoom,nucvol_limits);
    end

    %Sum total pixel area of tissue
    tissue_sum_mid = sum(sum(tissue_mask.*midsub_mask));
    tissue_area_mid = tissue_sum_mid*0.38028/(zoom^2);
    tissue_sum_oth = sum(sum(tissue_mask.*(1-midsub_mask)));
    tissue_area_oth = tissue_sum_oth*0.38028/(zoom^2);

    %Get subset of centroids within the midsubstance region
    midsub_i =
inpolygon(centroid_raw(:,1),centroid_raw(:,2),midsub_poly.Position(:,1),midsu
b_poly.Position(:,2));

    %Get min nuclear distances from boundary
    d_min_midsub =
p_poly_dist(centroid_raw(midsub_i,1),centroid_raw(midsub_i,2),tissue_boundary
.Position(:,1),tissue_boundary.Position(:,2));
    d_min_oth =
p_poly_dist(centroid_raw(setdiff(1:end,midsub_i),1),centroid_raw(setdiff(1:en
d,midsub_i),2),tissue_boundary.Position(:,1),tissue_boundary.Position(:,2));

    %Convert centroid coordinates to microns
    centroid.midsub(:,[1 2]) = centroid_raw(midsub_i,[1 2]).*0.624/zoom;
    centroid.midsub(:,3) = centroid_raw(midsub_i,3)*5;
    centroid.other(:,[1 2]) = centroid_raw(setdiff(1:end,midsub_i),[1
2]).*0.624/zoom;
    centroid.other(:,3) = centroid_raw(setdiff(1:end,midsub_i),3)*5;

    %Compute nuclear outcome measures
    nuc_dist_mid = d_min_midsub.*0.624/zoom;
    nuc_count_mid = size(centroid.midsub,1);
    total_mig_mid = sum(nuc_dist_mid);
    mean_mug_mid = total_mig_mid/nuc_count_mid;

    nuc_dist_oth = d_min_oth.*0.624/zoom;
    nuc_count_oth = size(centroid.other,1);
    total_mig_oth = sum(nuc_dist_oth);
    mean_mug_oth = total_mig_oth/nuc_count_oth;

    %Number of cells migrating >100 microns
    n_over100_mid = length(nuc_dist_mid(nuc_dist_mid > 100));
    n_over100_oth = length(nuc_dist_oth(nuc_dist_oth > 100));

    %Add to matrix to export to xls
    if i == 1
        xls_mat_mid = {'Filename','Tissue Area','Nuc Count','Total Mig
Dist','Average Mig Dist','Count >100um'};
        xls_mat_oth = {'Filename','Tissue Area','Nuc Count','Total Mig
Dist','Average Mig Dist','Count >100um'};
    end

    xls_mat_mid(i+1,:) =
{fname_label,tissue_area_mid,nuc_count_mid,total_mig_mid,mean_mug_mid,n_over1
00_mid};
    xls_mat_oth(i+1,:) =
{fname_label,tissue_area_oth,nuc_count_oth,total_mig_oth,mean_mug_oth,n_over1
00_oth};

    %Store centroids
    cd ..
    if exist('centroids') ~= 7
        mkdir('centroids');
    end
    cd centroids
    save([fname_label '.mat'],'centroid');
    cd ..
    cd mat_files

end

cd ..
if exist(outputXlsName)
    u_ans = input('Are you sure you want to overwrite? (Y/N) ');
    if u_ans == 'Y'
        xlswrite(outputXlsName,xls_mat_mid,'Midsubstance');
        xlswrite(outputXlsName,xls_mat_oth,'Enthesis/MTJ');
    else
        disp('Aborted');
    end
else
    xlswrite(outputXlsName,xls_mat_mid,'Midsubstance');
    xlswrite(outputXlsName,xls_mat_oth,'Enthesis_MTJ');
end
```

A9 Microgel fluorescence quant

```
%Microgel Quant
%Bobby Kent
%3/1/22
%
%Function that takes an image of microgels and returns their intensity in
%addition to background intensity.
%
%Email bobbykent14@gmail.com with questions.

function [uG_int, back_int] = uGquant(uGimg)

    %Find circles
    rng = [90 110];
    [centers,radii] =
imfindcircles(uGimg,rng,'ObjectPolarity','Bright','Sensitivity',0.90);

    %Show image
    h_fig = figure(1);
    set(h_fig,'Units','Normalized','Outerposition',[0 0.3 0.6 0.6]);
    imshow(uGimg);

    %Plot circles
    viscircles(centers,radii,'LineWidth',2);

    %% Create mask
    uG_mask = zeros(size(uGimg));

    %Iterate through centers
    for c = 1:size(centers,1)

        %Make mask of current circle
        [x,y] = meshgrid(1:size(uGimg,1),1:size(uGimg,2));
        distance = (x-centers(c,1))^2+(y-centers(c,2))^2;
        mask_curr = distance < radii(c);

        %Add to running uG mask
        uG_mask = uG_mask + mask_curr;
    end

    keyboard
    %Initialize background mask
    back_mask = 1-uG_mask;

    %Cut out partial circles
    button = 1;
    while isempty(button) ~= 1 %Stay in loop until user hits enter

        [~,~,button] = ginput(1);
        if button == 29 %Right arrow
            poly = drawpolygon('Color',[0 1 1]);
            p_mask = createMask(poly);

            %Update background mask
            back_mask = back_mask - p_mask;
        end
    end

%     close all

    keyboard
    %Calculate mean microgel and background intensities
%     uG_int = uGimg*uG_mask
end
```

A10 Perinuclear expression quant

```
%Takoyaki Expression Quant Wrap
%Bobby Kent
%1/25/22
%
%Script that calls nuccounter3D to determine expression of a marker of
%interest for each cell.
%
%Email bobbykent14@gmail.com with questions.

clear
clc

%% Settings
z_interval = 5; %5 um slices
bot_limit = 300; %Lower limit for nuclear vol
interval = 2500; %Bin version of nuclear volume
top_limit = 5*10^4; %Upper limit of nuclear cluster volume
d_min_array = {};
rad = 5;
mpp = 0.624; %10x -> 0.624 microns/pixel
%***Also set n_bins in tako_outline.mat***

%Experiment title
experiment_title = 'GFSCX3D_BV92TPC_VP15_FD50';

%Cut out tissue?
% t_c = 1; %Yes
t_c = 0; %No

%Output individual cells or FOV means?
out_fmt = 1; %Per cell
% out_fmt = 2; %FOV

%Number of scenes?
n_s = 10;

%Name intensity data .mat
mat_name = 'intensity_data';

cd ..
if exist([mat_name '.mat']) == 2
    load([mat_name '.mat']);
end
cd('mat_files');

%Gaussian filter settings (determine using gauss.m)
nucNS = 3;
nucBS = 30;
```

```
cellNS = 4;
cellBS = 70;
%3 and 30 good for TPCs at 10x and 0.5 zoom

%Thresholds for channels of interest
chans = [1 2]; %Set channel of interest number(s)
chans_n = {'aSMA' 'ScxGFP'};
n_c = 3; %Set nuclear channel number
num_chan = 3; %Set number of channels

%Set thresholds for each channel (determine using threshold_check.m)
%***TEST THESE ON A GAUSSIAN-FILTERED IMAGE***
chanScale = [2000 45000;... %aSMA
    4000 40000]; %ScxGFP

%***Merged ortho image for outlining tissue is always shown in RGB. Edit
%"Load ortho projection and maker merged image" to change this.

%%

%Select file(s): z-stack, not ortho projection
fname_select_temp = uigetfile('*.mat','Choose Z-stacks
Only','MultiSelect','On');

if ~iscell(fname_select_temp)
    fname_select{1} = fname_select_temp;
else
    fname_select = fname_select_temp;
end

%Set up filter inputs
noiseHnuc = fspecial('gaussian',nucNS,nucNS/3);
backHnuc = fspecial('gaussian',nucBS,nucBS/3);
noiseHcell = fspecial('gaussian',nucNS,cellNS/3);
backHcell = fspecial('gaussian',nucBS,cellBS/3);

%% Iterate through selected files
for i = 1:length(fname_select)

    %Get current filename
    fname = fname_select{i};
    fname_label = fname(1:strfind(fname,'.mat')-1);
    root{i} = fname(length(experiment_title)+2:...

strfind(fname(length(experiment_title)+2:end),'10x')+length(experiment_title)
-1);

    %Check zoom
    zoom_i = strfind(fname,'zoom');
    if ~isempty(zoom_i)
```

```
        zoom = str2num(fname(zoom_i - [3:-1:1]));
    else
        zoom = 1;
    end

    %Display progress
    disp(['Processing image file: ' fname '...']);

    %Iterate through scenes
    for s = 1:n_s

        %Scene name
        scene_n = ['scene' num2str(s)];

        %Display progress
        disp(['Processing scene ' num2str(s) '...']);

        %Load image stack
        zstack_struct = load(fname);

        %Load ortho projection and make merged image
        ortho_data = load([fname(1:end-4) '_MAX.mat']);
        ortho_img = zeros([size(ortho_data.data{1}{1,1}),3]);
        for clr = 1:num_chan
            ortho_img(:,:,clr) = mat2gray(ortho_data.data{s,1}{clr,1});
        end

        %Draw masks
        if t_c == 1
            %Draw polygon to exclude tissue region
            circFig =
figure('visible','off','units','normalized','outerposition',[0 0 0.67 1]);
            imagesc(ortho_img); axis square
            set(gca,'visible','off');
            title('Draw Polygon to Exclude Tissue (Full Projection)');
            poly_tiss = drawpolygon('Color',[0 1 1]);
            gel_mask = createMask(poly_tiss);

            %Draw polygon to exclude periphery
            title('Draw Polygon to Exclude Periphery (Full Projection)');
            poly_periph = drawpolygon('Color',[1 0 1]);
            periph_mask = createMask(poly_periph);
            close all
        end

        %Initilize nuclear matrix
        z_size = size(zstack_struct.data{2*(s-1)+1,1},1)/num_chan;
        nucmat = zeros([size(zstack_struct.data{2*(s-
1)+1,1}{1,1}(:,:,1)),z_size]);
```

```
        %Generate a masked z-stack of nuclear channel images
        for z_i = 1:z_size

            %Matrix of nuclear images
            nuc_raw = mat2gray(zstack_struct.data{2*(s-1)+1,1}{(z_i-
1)*num_chan+n_c,1});
            if t_c == 1
                nuc_raw = nuc_raw.*(1-gel_mask).*periph_mask;
            end

            %Run the nuclear images through a gaussian filter
            background = imfilter(nuc_raw,backHnuc,'symmetric'); %Calculate
background
            nuc_noback = nuc_raw - background; %Subtract background
            nuc_noback(nuc_noback<0) = 0; %Set anything that became negative
to 0
            nuc_noback = mat2gray(nuc_noback); %Rescale
            nucmat(:,:,z_i) = imfilter(nuc_noback,noiseHnuc,'symmetric');
%Filter noise

            %Generate masked z-stack of other channel images
            for ch = 1:length(chans)

                %Matrix of channel images
                chan_raw = mat2gray(zstack_struct.data{2*(s-1)+1,1}{(z_i-
1)*num_chan+ch,1});
                if t_c == 1
                    chan_raw = chan_raw.*(1-gel_mask).*periph_mask;
                end

                %Run the nuclear images through a gaussian filter
                background = imfilter(chan_raw,backHcell,'symmetric');
%Calculate background
                chan_noback = chan_raw - background; %Subtract background
                chan_noback(chan_noback<0) = 0; %Set anything that became
negative to 0
                chan_noback = mat2gray(chan_noback); %Rescale
                chan_gauss = imfilter(chan_noback,noiseHcell,'symmetric');
%Filter noise

                %Threshold gaussian-filtered image
                chanmat{ch}(:,:,z_i) =
mat2gray(chan_gauss,chanScale(ch,:)./60000);
            end
        end

        %Threshold image (bottom, middle, and top bins)
        if s == 1 %Only do this once per file (same thresh for all scenes)
            bmt_i = [1 floor(z_size/2) z_size];
            z_labels = {'Z Bot' 'Z Middle' 'Z Top'};
```

```
      for t_i = 1:3
        if t_i == 1
          [~, thresh_bound(t_i)] =
imthresh_rnk(nucmat(:,:,bmt_i(t_i)),z_labels{t_i});
        else
          [~, thresh_bound(t_i)] =
imthresh_rnk(nucmat(:,:,bmt_i(t_i)),z_labels{t_i},thresh_bound(t_i-1));
        end
      end

      %Interpolate between 3 points for each z-plane
      slope_low = (thresh_bound(2) - thresh_bound(1))/floor(z_size/2);
      slope_high = (thresh_bound(3) - thresh_bound(2))/floor(z_size/2);

      thresh(1:floor(z_size/2)) = [0:floor(z_size/2)-1].*slope_low +
thresh_bound(1);
      thresh(floor(z_size/2)+1:z_size) = [0:ceil(z_size/2)-
1].*slope_high + thresh_bound(2);
    end

    %Map centroids of nuclei for the entire z-stack
    [centroid_raw,nucVol] =
nuccounter3D_tako_singlebin(nucmat,zoom,[bot_limit top_limit],thresh);

    %     %Duplicate data points for multinuclear clusters
    %     for n = 1:length(nucVol)
    %         mult = floor(nucVol(n)/interval);
    %         if mult > 1
    %             for d = 2:mult
    %                 centroid_raw = [centroid_raw; centroid_raw(n,:)];
    %             end
    %         end
    %     end

    %Iterate through centroids
    for c = 1:size(centroid_raw,1)

      %Get range of indices inside a cube surrounding the centroid
      for dim = 1:2
        D(Siadat et al.) = round(centroid_raw(c,dim)) +
round(rad/mpp*zoom.*[-1 1].*1.1);
      end

      D{3} = round(centroid_raw(c,3)) + round(rad/5.*[-1 1].*1.1); %5
microns/slice

      %Truncate if it exceeds the size of the image
      for dim = 1:3
        if D(Siadat et al.)(1) < 1
          D(Siadat et al.)(1) = 1;
```

```
                elseif D(Siadat et al.)(2) > size(nucmat,dim)
                    D(Siadat et al.)(2) = size(nucmat,dim);
                end
            end

            %         %Generate meshgrid and find indices inside a sphere of
desired
            %         %radius around the current centroid
            %         [Dx,Dy,Dz] =
ndgrid(D{1}(1):D{1}(2),D{2}(1):D{2}(2),D{3}(1):D{3}(2));
            %         I = find(sqrt((Dx-centroid_raw(c,1)).^2 + (Dy-
centroid_raw(c,2)).^2 + (Dz-centroid_raw(c,3)).^2) < rad/mpp*zoom);
            %
            %Iterate through channels of interest
            for ch = 1:length(chans)
                chan_ROI =
chanmat{ch}(D{2}(1):D{2}(2),D{1}(1):D{1}(2),D{3}(1):D{3}(2));

intensity_data.(root{i}).intensities.(chans_n{ch}).(scene_n){c} = chan_ROI;
                int_out.(root{i}).(chans_n{ch}).(scene_n)(c) =
max(mean(mean(chan_ROI)));
            end

            %Store meshgrid range
            intensity_data.(root{i}).mesh_range.(scene_n){c} = D;
        end


        %Duplicate data points for multinuclear clusters
        for n = 1:length(nucVol)
            mult = floor(nucVol(n)/interval);
            if mult > 1
                for d = 2:mult
                    for ch = 1:length(chans)
                        int_out.(root{i}).(chans_n{ch}).(scene_n) =
[int_out.(root{i}).(chans_n{ch}).(scene_n)...
                            int_out.(root{i}).(chans_n{ch}).(scene_n)(n)];

intensity_data.(root{i}).intensities.(chans_n{ch}).(scene_n) =
[intensity_data.(root{i}).intensities.(chans_n{ch}).(scene_n)...

intensity_data.(root{i}).intensities.(chans_n{ch}).(scene_n){n}];
                    end
                end
            end
        end

        %Convert centroid coordinates to microns
        centroid = [centroid_raw(:,1).*mpp/zoom centroid_raw(:,2).*mpp/zoom
centroid_raw(:,3).*5];
```

```
        %Average FOV data
        for ch = 1:length(chans)
            int_out.(root{i}).(chans_n{ch}).FOV(s) =
nanmean(int_out.(root{i}).(chans_n{ch}).(scene_n));
        end

        %Store centroids
        cd ..
        if exist('centroids') ~= 7
            mkdir('centroids');
        end
        cd centroids
        save([fname_label '_centroids.mat'],'centroid');
        cd ..

        cd mat_files
    end


disp('=====================================================================')
    disp(' ');
end

%Store intensity and spatial data
cd ..
save(mat_name,'intensity_data','int_out');
```

A11 3D cell expression and morphology quant

```
%Cell Expression and Morphology 3D
%Bobby Kent
%5/2/22
%
%Function that takes z-stacks in .mat form (see czi2mat) and performs 3D
%clustering to identify individual cells. Outputs intensity of a channel of
%interest within 3D cytosolic and nuclear regions in addition to cell
%morphometrics based on the cytosolic mask.
%
%Inputs handled via cell_express_morph_3D_wrap.
%
%Email bobbykent14@gmail.com with questions.

function [data_out] =
cell_EM_3D(img_data,ortho_data,f_label,chan_i,n_chans,COI_n,scale_vals,vol_li
mits,zoom,ph,dfmt)

%GM switch
gm = 1; %On
% gm = 0; %Off

%Gauss switch
% gs = 1; %On
gs = 0; %Off

%Cut and clean up cyto masks?
% cut = 1; %On
cut = 0; %Off

%Auto thresh?
a_t = 1; %Manual
% a_t = 2; thresh = [0.15 0.2]; %Auto [cyto nuc]

%Filter based on cyto vol and PAL?
fltr = 1; min_max_filt_thresh = [30000 110]; %On ([vol PAR_SD] minima
foranalysis)
% fltr = 0; %Off

if gm == 1
    load('gm_dat.mat');
end

%Set gauss parameters
if gs == 1
    %************EDIT THESE AS NEEDED******************
    signalSize = 5;
    backSize = 100;
    %Calculate H parameters
    signalH = fspecial('gaussian',signalSize,signalSize/3);
    backH = fspecial('gaussian',backSize,backSize/3);
end

%Iterate through images
for f = 1:length(fieldnames(img_data))

    %% Make Masks
    %Determine z-size
    clear maskmat
    if dfmt == 1
        z_size = size(img_data.(f_label{f}).data{1},1)./n_chans;
    elseif dfmt == 2
        z_size = size(img_data.(f_label{f}),1)./n_chans;
    end

    %Gaussian filter actin image
    if gs == 1

        %Get raw actin image
        if dfmt == 1
            actin_ortho_raw = ortho_data.(f_label{f}).data{1}{chan_i(1),1};
        elseif dfmt == 2
            actin_ortho_raw = ortho_data.(f_label{f}){chan_i(1),1};
        end

        % calculate background
        background = imfilter(actin_ortho_raw,backH,'symmetric');

        % subtract background and rescale
        actin_ortho = actin_ortho_raw - background;

        % set anything that became negative to 0
        actin_ortho(actin_ortho<0) = 0;
        actin_ortho = mat2gray(actin_ortho);

        % filter noise
        actin_ortho = imfilter(actin_ortho,signalH,'symmetric');
    else
        if dfmt == 1
            actin_ortho = ortho_data.(f_label{f}).data{1}{chan_i(1),1};
        elseif dfmt == 2
            actin_ortho = ortho_data.(f_label{f}){chan_i(1),1};
        end
    end

    %Get threshold values for actin and nuc channels if manual
    if a_t == 1
```

```
        [~, thresh(1)] =
imthresh_rnk(mat2gray(actin_ortho,scale_vals{1}),'Cyto Thresh',0.01);
        if ph == 2
            if dfmt == 1
                [~, thresh(2)] =
imthresh_rnk(mat2gray(ortho_data.(f_label{f}).data{1}{chan_i(2),1},scale_vals
{2}),'Nuc Thresh',0.1);
            elseif dfmt == 2
                [~, thresh(2)] =
imthresh_rnk(mat2gray(ortho_data.(f_label{f}){chan_i(2),1},scale_vals{2}),'Nu
c Thresh',0.1);
            end
        else
            if dfmt == 1
                [~, thresh(2)] =
imthresh_rnk(mat2gray(ortho_data.(f_label{f}).data{1}{chan_i(2),1},scale_vals
{2}),'Nuc Thresh',0.1);
            elseif dfmt == 2
                [~, thresh(2)] =
imthresh_rnk(mat2gray(ortho_data.(f_label{f}){chan_i(2),1},scale_vals{2}),'Nu
c Thresh',0.1);
            end
        end
    end

    %Build thresholded data matrices
    for z = 1:z_size

        %Gaussian filter actin image
        if gs == 1

            %Get raw actin image
            if dfmt == 1
                actin_z_raw = img_data.(f_label{f}).data{1}{(z-
1)*n_chans+chan_i(1),1};
            elseif dfmt == 2
                actin_z_raw = img_data.(f_label{f}){(z-
1)*n_chans+chan_i(1),1};
            end

            % calculate background
            background = imfilter(actin_z_raw,backH,'symmetric');

            % subtract background and rescale
            actin_z = actin_z_raw - background;

            % set anything that became negative to 0
            actin_z(actin_z<0) = 0;
            actin_z = mat2gray(actin_z);
            % filter noise
            actin_z = imfilter(actin_z,signalH,'symmetric');
        else
            if dfmt == 1
                actin_z = img_data.(f_label{f}).data{1}{(z-
1)*n_chans+chan_i(1),1};
            elseif dfmt == 2
                actin_z = img_data.(f_label{f}){(z-1)*n_chans+chan_i(1),1};
            end
        end

        %Binarize and clean up cyto and nuc masks
        if dfmt == 1
            img_curr_z = {mat2gray(actin_z,scale_vals{1})...
                mat2gray(img_data.(f_label{f}).data{1}{(z-
1)*n_chans+chan_i(2),1},scale_vals{2})};
        elseif dfmt == 2
            img_curr_z = {mat2gray(actin_z,scale_vals{1})...
                mat2gray(img_data.(f_label{f}){(z-
1)*n_chans+chan_i(2),1},scale_vals{2})};
        end

        for mask_i = 1:2

            %Binarize, close holes, and remove spurs
            img_temp = im2bw(img_curr_z{mask_i},thresh(mask_i));
            img_temp = bwmorph(img_temp, 'close');
            mask_temp = bwmorph(img_temp, 'spur');

            %Update 3D mask
            maskmat{mask_i}(:,:,z) = mask_temp;
        end
    end


    %Initialize filter mask for vol/PAL if necessary
    if fltr == 1
        fltrvoxelIdx = [];
        fltr_mask = zeros(1024,1024,z_size);
    end


    %Iterate through mask types (cyto and nuc) again to identify clusters
    %and sort by size
    mask_n = {'cyto' 'nuc'};
    mask_vis = zeros(1024,1024,3); %Initialize mask visualizer
    for mask_i = 2:-1:1 %Cyto=1, nuc=2 (do nuc first)

        %Identify 3D clusters
        CC = bwconncomp(maskmat{mask_i},26);
        allStats =
regionprops3(CC,'Volume','PrincipalAxisLength','Orientation','VoxelIdxList');

        count = 0;
        voxelIdx.(mask_n{mask_i}) = [];

        %Iterate through clusters, volume exclude, and store
        for k=1:CC.NumObjects
            if allStats.Volume(k)/(zoom(f)^2) >= vol_limits{mask_i}(1) &&
allStats.Volume(k)/(zoom(f)^2) <= vol_limits{mask_i}(2)

                count = count + 1;

                %Store voxels
                voxelIdx.(mask_n{mask_i}) = [voxelIdx.(mask_n{mask_i})
allStats.VoxelIdxList{k}'];

                %Add to randomly colored cyto mask
                if mask_i == 1
                    clr = rand(1,3);
                    cyto_test = zeros(1024,1024,z_size);
cyto_test(setdiff(allStats.VoxelIdxList{k},voxelIdx.nuc)) = 1;
                    for c = 1:3
                        mask_vis(:,:,c) = mask_vis(:,:,c) +
max(cyto_test,[],3).*clr(c);
                    end
                end

                %Get morpho data for current mask
                if cut == 1
                    if mask_i == 2
                        orientation(count) = allStats.Orientation(k);
                        vol(count) = allStats.Volume(k)/zoom(f)^2;

                        %Principal axis ratio
                        PAR_temp = allStats.PrincipalAxisLength(k,:);
%                         [~, z_i] = min(PAR_temp);
%                         PAR_temp(z_i) = PAR_temp(z_i)*5;
                        PAR(count) = max(PAR_temp);

                        %Store individual nuclear voxel lists for extraction
                        %later
                        voxelIdxCell.nuc{count} = allStats.VoxelIdxList{k}';
                    end
                else
                    orientation(count) = allStats.Orientation(k);
                    vol(count) = allStats.Volume(k)/zoom(f)^2;

                    %Principal axis ratio
                    PAR_temp = allStats.PrincipalAxisLength(k,:);
```

```
%                     [~, z_i] = min(PAR_temp);
%                     PAR_temp(z_i) = PAR_temp(z_i)*5;
                    PAR(count) = max(PAR_temp);

                    %Store individual nuclear voxel lists for extraction
                    %later
                    voxelIdxCell.nuc{count} = allStats.VoxelIdxList{k}';
                end

                %Store mask of objects who don't meet cyto volume/PAL
                %criteria
                if fltr == 1 && mask_i == 1
                    if vol(count) < min_max_filt_thresh(1) && PAR(count) <
min_max_filt_thresh(2)
                        fltrvoxelIdx = [fltrvoxelIdx
allStats.VoxelIdxList{k}'];
                    end
                end
            end
        end

%         %Make filter mask and apply to cyto maskmat
%         if fltr == 1
%             [Xfltr,Yfltr,~] = ind2sub([1024 1024 z_size],fltrvoxelIdx);
%             fltr_ind = sub2ind([1024 1024],Xfltr,Yfltr);
%             fltr_mask = zeros(1024,1024);
%             fltr_mask(fltr_ind) = 1;
%         end


        %Store nuc data
        if mask_i == 2
            data_out.(f_label{f}).cluster_vol.(mask_n{mask_i}) = vol;
            data_out.(f_label{f}).orientation.(mask_n{mask_i}) = orientation;
            data_out.(f_label{f}).PAR.(mask_n{mask_i}) = PAR;
        end

        %If not cutting the cyto mask, assign to output now
        if cut == 0
            if mask_i == 1
                data_out.(f_label{f}).cluster_vol.(mask_n{1}) = vol;
                data_out.(f_label{f}).orientation.(mask_n{1}) = orientation;
                data_out.(f_label{f}).PAR.(mask_n{1}) = PAR;
            end
        end
    end

    %Remove nuc indices from cyto voxel index list
    voxel_i.nuc = voxelIdx.nuc;
    voxel_i.cyto = setdiff(voxelIdx.cyto,voxelIdx.nuc);
    if fltr == 1
        voxel_i.cyto = setdiff(voxelIdx.cyto,fltrvoxelIdx);
    else
        voxel_i.cyto = voxelIdx.nuc;
    end

    %% Cut and remove cyto clusters
    if cut == 1

        %Display ortho projection of finalized masks for cutting
        nuc_test = zeros(1024,1024,z_size); nuc_test(voxel_i.nuc) = 1;
        for c = 1:3
            mask_vis = mask_vis + max(nuc_test,[],3); %Nuc in white
        end

        h_fig = figure(1);
        set(h_fig,'Units','Normalized','Outerposition',[0 0 0.6 1]);
        imshow(mask_vis);
        title('Right Click to Cut (Enter when Done)');

        %Draw cuts
        button = 0;
        cutMask = zeros(1024,1024);
        while isempty(button) ~= 1

            %Collect user input
            [x,y,button] = ginputc(1,'Color','w','LineStyle',':');

            if button == 3 %Right click

                [cutMask_temp, mask_vis] = mask_cut(x,y,[1024
1024],mask_vis);
                cutMask = cutMask + cutMask_temp;

                figure(1); imshow(mask_vis);
                set(h_fig,'Units','Normalized','Outerposition',[0 0 0.6 1]);
            end
        end
        close all

        %Update cyto mask matrix
        for z = 1:z_size
            temp_mask = maskmat{1}(:,:,z) - cutMask;

            %Change negative numbers to 0
            temp_mask(temp_mask < 0) = 0;
            maskmat{1}(:,:,z) = temp_mask;
        end

        %Re-run cyto clustering
    CC = bwconncomp(maskmat{1},26);
    allStats =
regionprops3(CC,'Volume','PrincipalAxisLength','Orientation','Centroid','Voxe
lIdxList');

    count = 0;
    voxelIdx.(mask_n{1}) = [];

    %Iterate through clusters, volume exclude, and store
    mask_vis = zeros(1024,1024,3); %Re-initialize mask visualizer
    clear vol PAR orientation %Clear output variables
    for k=1:CC.NumObjects
      if allStats.Volume(k)/(zoom(f)^2) >= vol_limits{1}(1) &&
allStats.Volume(k)/(zoom(f)^2) <= vol_limits{1}(2)
        count = count + 1;
        vol(count) = allStats.Volume(k)/zoom(f)^2;
        voxelIdx.(mask_n{1}) = [voxelIdx.(mask_n{1})
allStats.VoxelIdxList{k}'];
        orientation(count) = allStats.Orientation(k);

        PAR_temp = allStats.PrincipalAxisLength(k,:);
%         [~, z_i] = min(PAR_temp);
%         PAR_temp(z_i) = PAR_temp(z_i)*5;
        PAR(count) = max(PAR_temp);

        %Get cell/cluster centroids and individual voxel lists for
        %extraction later
        cellCentroids(count,:) = allStats.Centroid(k,:);
        voxelIdxCell.cyto{count} = allStats.VoxelIdxList{k}';

        %Add to randomly colored cyto mask
        clr = rand(1,3);
        cyto_test = zeros(1024,1024,z_size);
cyto_test(setdiff(allStats.VoxelIdxList{k},voxelIdx.nuc)) = 1;
        for c = 1:3
          mask_vis(:,:,c) = mask_vis(:,:,c) +
max(cyto_test,[],3).*clr(c);
        end
      end
    end

    data_out.(f_label{f}).cluster_vol.(mask_n{1}) = vol;
    data_out.(f_label{f}).orientation.(mask_n{1}) = orientation;
    data_out.(f_label{f}).PAR.(mask_n{1}) = PAR;

    %Remove nuc indices from cyto voxel index list
    voxel_i.cyto = setdiff(voxelIdx.cyto,voxelIdx.nuc);

    %Display ortho projection of finalized masks for cutting
    nuc_test = zeros(1024,1024,z_size); nuc_test(voxel_i.nuc) = 1;
```

```
        for c = 1:3
            mask_vis = mask_vis + max(nuc_test,[],3); %Nuc in white
        end

        %% Remove clusters
        h_fig = figure(1);
        set(h_fig,'Units','Normalized','Outerposition',[0 0 0.6 1]);
        imshow(mask_vis);
        title('Left Click to Exclude Clusters');

        button = 0;
        while isempty(button) ~= 1

            %Collect user input
            [x,y,button] = ginputc(1,'Color','w','LineStyle',':');

            % left click to remove data for a cell cluster
            if button == 1

                %Find cell centroid that's closest to click
                [value,cellIndex] = min(sqrt((cellCentroids(:,1)-
x).^2+(cellCentroids(:,2)-y).^2));

                %Convert indices of deleted cell to 3D subscripts
                [Xcyto,Ycyto,~] = ind2sub([1024 1024
z_size],voxelIdxCell.cyto{cellIndex});

                %Find nuclei overlapping with the selected actin structure
                nucIndex = [];
                Xnuc = []; Ynuc = [];
                for n = 1:length(voxelIdxCell.nuc)
                    if
~isempty(intersect(voxelIdxCell.cyto{cellIndex},voxelIdxCell.nuc{n}))
                        nucIndex = [nucIndex n];

                        %Convert indices of deleted nuclei to 3D subscripts
                        [Xnuc_temp,Ynuc_temp,~] = ind2sub([1024 1024
z_size],voxelIdxCell.nuc{n});
                        Xnuc = [Xnuc Xnuc_temp];
                        Ynuc = [Ynuc Ynuc_temp];
                    end
                end

                %Re-compile masks
                voxel_i.cyto =
setdiff(voxel_i.cyto,voxelIdxCell.cyto{cellIndex});
                for n = 1:length(nucIndex)
                    voxel_i.nuc =
setdiff(voxel_i.nuc,voxelIdxCell.nuc{nucIndex(n)});
                end
                %Mark selected data indices in outputs
                %Cyto
                data_out.(f_label{f}).cluster_vol.(mask_n{1})(cellIndex) =
NaN;
                data_out.(f_label{f}).orientation.(mask_n{1})(cellIndex) =
NaN;
                data_out.(f_label{f}).PAR.(mask_n{1})(cellIndex) = NaN;

                %Nuc
                data_out.(f_label{f}).cluster_vol.(mask_n{2})(nucIndex) =
NaN;
                data_out.(f_label{f}).orientation.(mask_n{2})(nucIndex) =
NaN;
                data_out.(f_label{f}).PAR.(mask_n{2})(nucIndex) = NaN;

                %Show new mask
                delete_ind_cyto = sub2ind([1024 1024],Xcyto,Ycyto);
                delete_ind_nuc = sub2ind([1024 1024],Xnuc,Ynuc);
                for c = 1:3
                    mask_vis_temp = mask_vis(:,:,c);
                    mask_vis_temp([delete_ind_cyto delete_ind_nuc]) = 0;
                    mask_vis(:,:,c) = mask_vis_temp;
                end
                imshow(mask_vis);
            end
        end

        %Remove deleted data
        for mask_i = 1:2
            data_out.(f_label{f}).cluster_vol.(mask_n{mask_i}) =...
                data_out.(f_label{f}).cluster_vol.(mask_n{mask_i})...
                (~isnan(data_out.(f_label{f}).cluster_vol.(mask_n{mask_i})));
            data_out.(f_label{f}).orientation.(mask_n{mask_i}) =...
                data_out.(f_label{f}).orientation.(mask_n{mask_i})...
                (~isnan(data_out.(f_label{f}).orientation.(mask_n{mask_i})));
            data_out.(f_label{f}).PAR.(mask_n{mask_i}) =...
                data_out.(f_label{f}).PAR.(mask_n{mask_i})...
                (~isnan(data_out.(f_label{f}).PAR.(mask_n{mask_i})));
        end

        if gm == 1
            imshow(g_img{ceil(rand.*6)});
            text(20,20,'***LOOKS GUCCI***','FontSize',25,'Color',[0 1 0]);
            pause(0.7);
        end

        close all
    end
    %% Quantify COI intensity
    if ph == 2

        %Iterate through channels
        for ch = ph+1:length(chan_i)

            %Get data from COI (scaled per wrap inputs)
            for z = 1:z_size
                if dfmt == 1
                    COI_data(:,:,z) =
mat2gray(img_data.(f_label{f}).data{1}{(z-
1)*n_chans+chan_i(ch),1},scale_vals{ch});
                elseif dfmt == 2
                    COI_data(:,:,z) = mat2gray(img_data.(f_label{f}){(z-
1)*n_chans+chan_i(ch),1},scale_vals{ch});
                end
            end

            %Get mean pixel intensity within cyto and nuc masks
            data_out.(f_label{f}).COI_int.(COI_n{ch-ph}).cyto =
mean(mean(mean(COI_data(voxel_i.cyto))));
            data_out.(f_label{f}).COI_int.(COI_n{ch-ph}).nuc =
mean(mean(mean(COI_data(voxel_i.nuc))));
        end
    elseif ph == 1

            %Get data from COI (scaled per wrap inputs)
            for z = 1:z_size
                if dfmt == 1
                    COI_data(:,:,z) =
mat2gray(img_data.(f_label{f}).data{1}{(z-
1)*n_chans+chan_i(1),1},scale_vals{1});
                elseif dfmt == 2
                    COI_data(:,:,z) = mat2gray(img_data.(f_label{f}){(z-
1)*n_chans+chan_i(1),1},scale_vals{1});
                end
            end

            %Get mean pixel intensity within cyto and nuc masks
            data_out.(f_label{f}).COI_int.(COI_n{1}).cyto =
mean(mean(mean(COI_data(voxel_i.cyto))));
            data_out.(f_label{f}).COI_int.(COI_n{1}).nuc =
mean(mean(mean(COI_data(voxel_i.nuc))));
    end
end
```

A12 Picrosirius red quant

```
%Redness Quant
%Bobby Kent
%2/6/2023
%
%Script that determines the redness of an RGB image by calculating the
%ratio of the red intensity to the sum of red, green, and blue intensities
%for each pixel.
%
%Mask style:
%   - Drawn masks are drawn manually. Best for solid slices.
%   - Thresholded masks are generated as a function of the redness value at
%   each pixel to eliminate all regions of the image not containing sample.
%   Best for samples with a lot of holes.
%
%User selects the ROI by drawing a polygon.
%
%Email bobbykent14@gmail.com with questions.

clear
clc
close all

%% User Settings

%Brigntness scaling (applied to all images)
b_scale = 2;

%Additional scaling for drawing (to help see boundaries better)
b_scale_addtl = 1;

%Mask style
% m_s = 1; %Drawn
% m_s = 2; %Thresholded
m_s = 3; %Draw and threshold

%Threshold style (irrelevent if drawing)
% t_i = 1; %Manual
t_i = 2; mask_thresh = 0.08; %Automatic

%Output .xls name
outputXlsName = 'FD_screen_redness_temp.xls';

%R G or B
quantclr = 1; %1 for R, 2 for G, 3 for B

%% Redness Quant
%Select images
filenames_pre = uigetfile('*.tif','MultiSelect','On');
```

```
if ~iscell(filenames_pre) %Make an array even if n = 1
    filenames{1} = filenames_pre;
else
    filenames = filenames_pre;
end

%Assign header to output matrix
mat_out{1,2} = 'Redness (AU)';

%Iterate through images
for f = 1:length(filenames)

    %Assign filename to output matrix
    mat_out{f+1,1} = filenames{f};

    %Load image
    img_raw = imread(filenames{f});
    img_scale = img_raw.*b_scale; %Scale

    %Make mask
    if m_s == 1 %Draw mask

        mask = draw_mask_scale(filenames{f},b_scale);
        mask = 1-mask(:,:,1); %Invert mask and take a single plane
        mask_i = find(mask==1);

    elseif m_s == 2 %Threshold mask

        %Convert to double
        dbl_img = im2double(img_scale);

        %Get normalized matrix of standard deviations across R/G/B
        img_std = std(dbl_img,[],3);
        img_std_norm = (img_std-min(img_std))/(max(max(img_std))-
min(min(img_std)));

        %Make mask and fill holes
        if t_i == 1 %Manual
            [~, mask_thresh] = imthresh_rnk(img_std_norm,'Mask Thresh',0.1);
        end
        mask = im2bw(img_std_norm,mask_thresh);
        mask = bwmorph(mask, 'close');
        mask = bwmorph(mask, 'spur');

%         %Check mask
%         h_fig = figure(1);
%         set(h_fig,'Units','Normalized','Outerposition',[0 0 1 1]);
%         subplot(1,2,1);
%         imshow(mask);
%         subplot(1,2,2);
%          imshow(img_scale);
%          title(filenames{f});
%          ginput(1);

        mask_i = find(mask==1);

    elseif m_s == 3 %Draw and threshold

        polymask = draw_mask_scale(filenames{f},b_scale*b_scale_addtl);
        polymask = 1-polymask(:,:,1); %Invert mask and take a single plane

        %Convert to double
        dbl_img = im2double(img_scale);

        %Get normalized matrix of standard deviations across R/G/B
        img_std = std(dbl_img,[],3);
        img_std_norm = (img_std-min(img_std))/(max(max(img_std))-
min(min(img_std)));

        %Make mask and fill holes
        if t_i == 1 %Manual
             [~, mask_thresh] = imthresh_rnk(img_std_norm,'Mask Thresh',0.1);
        end
        mask = im2bw(img_std_norm,mask_thresh);
        mask = bwmorph(mask, 'close');
        mask = bwmorph(mask, 'spur');
        mask = mask.*polymask;

        mask_i = find(mask==1);
    end

    %Map indices to array
    [x_i,y_i] = ind2sub([1022 1356],mask_i);

    %Calculate redness in ROI
    for j = 1:length(x_i)
        redness(j) =
img_scale(x_i(j),y_i(j),quantclr)./sum(img_scale(x_i(j),y_i(j),:));
    end
    mat_out{f+1,2} = mean(redness);
end

%Write xls file
xlswrite(outputXlsName,mat_out);
close all
```

A13 Birefringence quant

```
%Birefringence Angle Quant
%Bobby Kent
%2/6/2023
%
%Script that determines the luminance of the average pixel in a circular
%ROI in the center of a series of images sweeping through 90 degrees.
%
%User must set the interval based on the number of images taken.
%
%Run while in a folder containing only the images for a given angle sweep
%(in order).
%
%Email bobbykent14@gmail.com with questions.

clear
clc
close all

%% User Settings

%Brigntness scaling (applied to all images)
b_scale = 8;

%Angle interval (degrees)
a_int = 5;

%ROI radius (pixels)
radius = 400;

%Output .xls name
outputXlsName = 'birefringence_temp.xls';

%% Birefringence vs Angle Quant
%Get image names
d = dir;
for i = 3:length(d)
    filenames{i-2} = d(i).name;
end

%Load sample image to get xy size
img_test = imread(filenames{1});
xy_sz = size(img_test);

%Assign headers to output matrix
cf = pwd;
slash_i = find(cf=='\');
mat_out{1,2} = cf(slash_i(end)+1:end);
```

```
%Set up angle vector
angles = 0:a_int:90;

%Generate mask indices
[xx,yy] = meshgrid(1:xy_sz(2),1:xy_sz(1));
mask = false(xy_sz(1),xy_sz(2));
mask = mask | hypot(xx - ceil(xy_sz(2)/2), yy - ceil(xy_sz(1)/2)) <= radius;
mask_i = find(mask==1);
[x_i,y_i] = ind2sub([xy_sz(1) xy_sz(2)],mask_i);

%Iterate through files
for a_i = 1:length(angles)

    %Assign angle to output matrix
    mat_out{a_i+1,1} = angles(a_i);

    img_raw = imread(filenames{a_i});
    img_scale = img_raw.*b_scale;

    %Calculate luminance in ROI
    for j = 1:length(x_i)
        lum(j) = 0.2126*img_scale(x_i(j),y_i(j),1) + 
0.7152*img_scale(x_i(j),y_i(j),1) + 0.0722*img_scale(x_i(j),y_i(j),1);
    end
    lum_mn(a_i) = mean(lum);
end

%Normalize luminance such that the max value = 1 and the min value = 0
% lum_mn_norm = (lum_mn - min(lum_mn))/(max(lum_mn)-min(lum_mn)); %Normalize
lum_mn_norm = lum_mn; %Don't normalize
for i = 1:length(angles)
    mat_out{i+1,2} = lum_mn_norm(i);
end

%Write to .xls file
cd ..
cd ..
xlswrite(outputXlsName,mat_out);
cd birefringence
```

A14 Birefringence delta and full width half max calculator

```
%Delta and FWHM
%Bobby Kent
%9/19/23
%
%Script that calculates the delta and FWHM from PSR birefringece vs.
%deviation curves.
%
%Email bobbykent14@gmail.com with questions.

clear
clc

%% Set data columns to analyze
rng = [9:14];

%% Run quant
%Get data
filename = uigetfile('*.xls');
data = xlsread(filename);

%Get desired columns
data_curr = data(1:19,rng);

%Define independent variable (deviation in degrees)
x = -45:5:45;

%Iterate through columns
for i = 1:length(rng)

    %Get delta
    mat_out(i,1) = max(data_curr(:,i)) - min(data_curr(:,i));

    %Get FWHM
    f = fit(x',data_curr(:,i),'gauss2');
    mat_out(i,2) = 2*sqrt(log(2))*f.c1;
end
```

Bibliography

Abercrombie, M., Heaysman, J.E., & Pegrum, S.M. (1971). The locomotion of fibroblasts in culture. Iv. Electron microscopy of the leading lamella. Exp Cell Res, *67*, 359-367.

Agrawal, A., Rahbar, N., & Calvert, P.D. (2013). Strong fiber-reinforced hydrogel. Acta Biomater, *9*, 5313-5318.

Akhmetshina, A., Dees, C., Pileckyte, M., Szucs, G., Spriewald, B.M., Zwerina, J., Distler, O., Schett, G., & Distler, J.H. (2008). Rho-associated kinases are crucial for myofibroblast differentiation and production of extracellular matrix in scleroderma fibroblasts. Arthritis Rheum, *58*, 2553-2564.

Arvind, V., Howell, K., & Huang, A.H. (2021). Reprogramming adult tendon healing using regenerative neonatal regulatory t cells. BioRxiv.

Awad, H.A., Boivin, G.P., Dressler, M.R., Smith, F.N., Young, R.G., & Butler, D.L. (2003). Repair of patellar tendon injuries using a cell-collagen composite. J Orthop Res, *21*, 420-431.

Baghy, K., Iozzo, R.V., & Kovalszky, I. (2012). Decorin-tgfbeta axis in hepatic fibrosis and cirrhosis. J Histochem Cytochem, *60*, 262-268.

Baker, B.M., & Mauck, R.L. (2007). The effect of nanofiber alignment on the maturation of engineered meniscus constructs. Biomaterials, *28*, 1967-1977.

Baker, B.M., Shah, R.P., Silverstein, A.M., Esterhai, J.L., Burdick, J.A., & Mauck, R.L. (2012). Sacrificial nanofibrous composites provide instruction without impediment and enable functional tissue formation. Proc Natl Acad Sci U S A, *109*, 14176-14181.

Baker, B.M., Trappmann, B., Wang, W.Y., Sakar, M.S., Kim, I.L., Shenoy, V.B., Burdick, J.A., & Chen, C.S. (2015). Cell-mediated fibre recruitment drives extracellular matrix mechanosensing in engineered fibrillar microenvironments. Nat Mater, *14*, 1262-1268.

Baldwin, M.J., Mimpen, J.Y., Cribbs, A.P., Stace, E., Philpott, M., Dakin, S.G., Carr, A.J., & Snelling, S.J. (2021). Electrospun scaffold micro-architecture induces an activated transcriptional phenotype within tendon fibroblasts. Front Bioeng Biotechnol, *9*, 795748.

Bankhead, P., Loughrey, M.B., Fernandez, J.A., Dombrowski, Y., McArt, D.G., Dunne, P.D., McQuaid, S., Gray, R.T., Murray, L.J., Coleman, H.G., James, J.A., Salto-Tellez, M., &

Hamilton, P.W. (2017). Qupath: Open source software for digital pathology image analysis. Sci Rep, *7*, 16878.

Barsby, T., Bavin, E.P., & Guest, D.J. (2014). Three-dimensional culture and transforming growth factor beta3 synergistically promote tenogenic differentiation of equine embryo-derived stem cells. Tissue Eng Part A, *20*, 2604-2613.

Bartoschek, M., & Pietras, K. (2018). Pdgf family function and prognostic value in tumor biology. Biochem Biophys Res Commun, *503*, 984-990.

Bas, O., De-Juan-Pardo, E.M., Chhaya, M.P., Wunner, F.M., Jeon, J.E., Klein, T.J., & Dietmar, W.H. (2015). Enhancing structural integrity of hydrogels by using highly organised melt electrospun fibre constructs. Eur Polym J, *72*, 451-463.

Beckett, L.E., Lewis, J.T., Tonge, T.K., & Korley, L.T.J. (2020). Enhancement of the mechanical properties of hydrogels with continuous fibrous reinforcement. ACS Biomater Sci Eng, *6*, 5453-5473.

Bernard-Beaubois, K., Hecquet, C., Houcine, O., Hayem, G., & Adolphe, M. (1997). Culture and characterization of juvenile rabbit tenocytes. Cell Biol Toxicol, *13*, 103-113.

Best, K.T., Korcari, A., Mora, K.E., Nichols, A.E., Muscat, S.N., Knapp, E., Buckley, M.R., & Loiselle, A.E. (2021). Scleraxis-lineage cell depletion improves tendon healing and disrupts adult tendon homeostasis. Elife, *10*.

Best, K.T., & Loiselle, A.E. (2019). Scleraxis lineage cells contribute to organized bridging tissue during tendon healing and identify a subpopulation of resident tendon cells. FASEB J, *33*, 8578-8587.

Bhattacharyya, S., Midwood, K.S., & Varga, J. (2022). Tenascin-c in fibrosis in multiple organs: Translational implications. Semin Cell Dev Biol, *128*, 130-136.

Bi, Y., Ehirchiou, D., Kilts, T.M., Inkson, C.A., Embree, M.C., Sonoyama, W., Li, L., Leet, A.I., Seo, B.M., Zhang, L., Shi, S., & Young, M.F. (2007). Identification of tendon stem/progenitor cells and the role of the extracellular matrix in their niche. Nat Med, *13*, 1219-1227.

Bian, L., Zhai, D.Y., Tous, E., Rai, R., Mauck, R.L., & Burdick, J.A. (2011). Enhanced msc chondrogenesis following delivery of tgf-beta3 from alginate microspheres within hyaluronic acid hydrogels in vitro and in vivo. Biomaterials, *32*, 6425-6434.

Blitz, E., Sharir, A., Akiyama, H., & Zelzer, E. (2013). Tendon-bone attachment unit is formed modularly by a distinct pool of scx- and sox9-positive progenitors. Development, *140*, 2680-2690.

Bornfeldt, K.E., Raines, E.W., Graves, L.M., Skinner, M.P., Krebs, E.G., & Ross, R. (1995). Platelet-derived growth factor. Distinct signal transduction pathways associated with migration versus proliferation. Ann N Y Acad Sci, *766*, 416-430.

Breidenbach, A.P., Dyment, N.A., Lu, Y., Rao, M., Shearn, J.T., Rowe, D.W., Kadler, K.E., & Butler, D.L. (2015). Fibrin gels exhibit improved biological, structural, and mechanical properties compared with collagen gels in cell-based tendon tissue-engineered constructs. Tissue Eng Part A, *21*, 438-450.

Burridge, K., Fath, K., Kelly, T., Nuckolls, G., & Turner, C. (1988). Focal adhesions: Transmembrane junctions between the extracellular matrix and the cytoskeleton. Annu Rev Cell Biol, *4*, 487-525.

Butler, D.L., Juncosa-Melvin, N., Boivin, G.P., Galloway, M.T., Shearn, J.T., Gooch, C., & Awad, H.A. (2007). Functional tissue engineering for tendon repair: A multidisciplinary strategy using mesenchymal stem cells, bioscaffolds, and mechanical stimulation. J Orthop Res, *1*, 1-9.

Cai, J., Liu, J., Xu, J., Li, Y., Zheng, T., Zhang, T., Han, K., Chen, S., Jiang, J., Wu, S., & Zhao, J. (2023). Constructing high-strength nano-micro fibrous woven scaffolds with native-like anisotropic structure and immunoregulatory function for tendon repair and regeneration. Biofabrication, *15*.

Carisey, A., Tsang, R., Greiner, A.M., Nijenhuis, N., Heath, N., Nazgiewicz, A., Kemkemer, R., Derby, B., Spatz, J., & Ballestrem, C. (2013). Vinculin regulates the recruitment and release of core focal adhesion proteins in a force-dependent manner. Curr Biol, *23*, 271-281.

Castilho, M., Hochleitner, G., Wilson, W., van Rietbergen, B., Dalton, P.D., Groll, J., Malda, J., & Ito, K. (2018). Mechanical behavior of a soft hydrogel reinforced with three-dimensional printed microfibre scaffolds. Sci Rep, *8*, 1245.

Chen, Y., Jiang, L., Lyu, K., Lu, J., Long, L., Wang, X., Liu, T., & Li, S. (2022). A promising candidate in tendon healing events-pdgf-bb. Biomolecules, *12*.

Chung, C., & Burdick, J.A. (2009). Influence of three-dimensional hyaluronic acid microenvironments on mesenchymal stem cell chondrogenesis. Tissue Eng Part A, *15*, 243-254.

Chung, E., & Son, Y. (2014). Crosstalk between mesenchymal stem cells and macrophages in tissue repair. Tiss Eng Regen Med, *11*, 431-438.

Cochran, B.H., Reffel, A.C., & Stiles, C.D. (1983). Molecular cloning of gene sequences regulated by platelet-derived growth factor. Cell, *33*, 939-947.

Crosio, G., & Huang, A.H. (2022). Innate and adaptive immune system cells implicated in tendon healing and disease. Eur Cell Mater, *43*, 39-52.

Dahlin, R.L., Ni, M., Meretoja, V.V., Kasper, F.K., & Mikos, A.G. (2014). Tgf-beta3-induced chondrogenesis in co-cultures of chondrocytes and mesenchymal stem cells on biodegradable scaffolds. Biomaterials, *35*, 123-132.

Datta, S.S., Abbaspourrad, A., Amstad, E., Fan, J., Kim, S.H., Romanowsky, M., Shum, H.C., Sun, B., Utada, A.S., Windbergs, M., Zhou, S., & Weitz, D.A. (2014). 25th anniversary article:

Double emulsion templated solid microcapsules: Mechanics and controlled release. Adv Mater, *26*, 2205-2218.

Davidson, C.D., Jayco, D.K.P., Matera, D.L., DePalma, S.J., Hiraki, H.L., Wang, W.Y., & Baker, B.M. (2020a). Myofibroblast activation in synthetic fibrous matrices composed of dextran vinyl sulfone. Acta Biomater, *105*, 78-86.

Davidson, C.D., Jayco, D.K.P., Wang, W.Y., Shikanov, A., & Baker, B.M. (2020b). Fiber crimp confers matrix mechanical nonlinearity, regulates endothelial cell mechanosensing, and promotes microvascular network formation. J Biomech Eng, *142*.

de la Durantaye, M., Piette, A.B., van Rooijen, N., & Frenette, J. (2014). Macrophage depletion reduces cell proliferation and extracellular matrix accumulation but increases the ultimate tensile strength of injured achilles tendons. J Orthop Res, *32*, 279-285.

de Vos, R.J., Weir, A., van Schie, H.T., Bierma-Zeinstra, S.M., Verhaar, J.A., Weinans, H., & Tol, J.L. (2010). Platelet-rich plasma injection for chronic achilles tendinopathy: A randomized controlled trial. JAMA, *303*, 144-149.

Deepthi, S., Jeevitha, K., Sundaram, M.N., Chennazhi, K.P., & Jayakumar, R. (2015). Chitosan-hyaluronic acid hydrogel coated poly(caprolactone) multiscale bilayer scaffold for ligament regeneration. Chem Eng J, *260*, 478-485.

del Pozo, M.A., Price, L.S., Alderson, N.B., Ren, X.D., & Schwartz, M.A. (2000). Adhesion to the extracellular matrix regulates the coupling of the small gtpase rac to its effector pak. EMBO J, *19*, 2008-2014.

DePalma, S.J., Davidson, C.D., Stis, A.E., Helms, A.S., & Baker, B.M. (2021). Microenvironmental determinants of organized ipsc-cardiomyocyte tissues on synthetic fibrous matrices. Biomater Sci, *9*, 93-107.

Diba, M., Polini, A., Petre, D.G., Zhang, Y., & Leeuwenburgh, S.C.G. (2018). Fiber-reinforced colloidal gels as injectable and moldable biomaterials for regenerative medicine. Mater Sci Eng C Mater Biol Appl, *92*, 143-150.

Drakonaki, E.E., Allen, G.M., & Watura, R. (2016). Ultrasound-guided intervention in the ankle and foot. Br J Radiol, *89*, 20150577.

Du, X., Cai, L., Xie, J., & Zhou, X. (2023). The role of tgf-beta3 in cartilage development and osteoarthritis. Bone Res, *11*, 2.

Duscher, D., & Schiffman, M.A. (2019). *Regenerative medicine and plastic surgery: Skin and soft tissue, bone, cartilage, muscle, tendon, and nerves*. Charm, Switzerland: Springer International Publishing.

Dyment, N.A., Hagiwara, Y., Matthews, B.G., Li, Y., Kalajzic, I., & Rowe, D.W. (2014). Lineage tracing of resident tendon progenitor cells during growth and natural healing. PLoS One, *9*, e96113.

Dyment, N.A., Liu, C.F., Kazemi, N., Aschbacher-Smith, L.E., Kenter, K., Breidenbach, A.P., Shearn, J.T., Wylie, C., Rowe, D.W., & Butler, D.L. (2013). The paratenon contributes to scleraxis-expressing cells during patellar tendon healing. PLoS One, *8*, e59944.

Efird, W.M., Fletcher, A.G., Draeger, R.W., Spang, J.T., Dahners, L.E., & Weinhold, P.S. (2018). Deferoxamine-soaked suture improves angiogenesis and repair potential after acute injury of the chicken achilles tendon. Orthop J Sports Med, *6*, 2325967118802792.

El Khatib, M., Mauro, A., Di Mattia, M., Wyrwa, R., Schweder, M., Ancora, M., Lazzaro, F., Berardinelli, P., Valbonetti, L., Di Giacinto, O., Polci, A., Camma, C., Schnabelrauch, M., Barboni, B., & Russo, V. (2020). Electrospun plga fiber diameter and alignment of tendon biomimetic fleece potentiate tenogenic differentiation and immunomodulatory function of amniotic epithelial stem cells. Cells, *9*.

Engler, A.J., Sen, S., Sweeney, H.L., & Discher, D.E. (2006). Matrix elasticity directs stem cell lineage specification. Cell, *126*, 677-689.

English, A., Azeem, A., Spanoudes, K., Jones, E., Tripathi, B., Basu, N., McNamara, K., Tofail, S.A.M., Rooney, N., Riley, G., O'Riordan, A., Cross, G., Hutmacher, D., Biggs, M., Pandit, A., & Zeugolis, D.I. (2015). Substrate topography: A valuable in vitro tool, but a clinical red herring for in vivo tenogenesis. Acta Biomater, *27*, 3-12.

Erisken, C., Zhang, X., Moffat, K.L., Levine, W.N., & Lu, H.H. (2013). Scaffold fiber diameter regulates human tendon fibroblast growth and differentiation. Tissue Eng Part A, *19*, 519-528.

Fearon, A., Dahlstrom, J.E., Twin, J., Cook, J., & Scott, A. (2014). The bonar score revisited: Region of evaluation significantly influences the standardized assessment of tendon degeneration. J Sci Med Sport, *17*, 346-350.

Font Tellado, S., Balmayor, E.R., & Van Griensven, M. (2015). Strategies to engineer tendon/ligament-to-bone interface: Biomaterials, cells and growth factors. Adv Drug Deliv Rev, *94*, 126-140.

Font Tellado, S., Chiera, S., Bonani, W., Poh, P.S.P., Migliaresi, C., Motta, A., Balmayor, E.R., & van Griensven, M. (2018). Heparin functionalization increases retention of tgf-beta2 and gdf5 on biphasic silk fibroin scaffolds for tendon/ligament-to-bone tissue engineering. Acta Biomater, *72*, 150-166.

Ford, A.J., & Rajagopalan, P. (2018). Measuring cytoplasmic stiffness of fibroblasts as a function of location and substrate rigidity using atomic force microscopy. ACS Biomater Sci Eng, *4*, 3974-3982.

Frazier, C.H., & Clark, E.M. (1980). Major tendon repairs with dacron vascular graft suture. Orthopedics, *3*, 323-325.

Freedman, B.R., Kuttler, A., Beckmann, N., Nam, S., Kent, D., Schuleit, M., Ramazani, F., Accart, N., Rock, A., Li, J., Kurz, M., Fisch, A., Ullrich, T., Hast, M.W., Tinguely, Y., Weber, E., & Mooney, D.J. (2022). Enhanced tendon healing by a tough hydrogel with an adhesive side and high drug-loading capacity. Nat Biomed Eng, *6*, 1167-1179.

Fukuma, Y., Tokunaga, T., Tanimura, S., Yoshimoto, Y., Mashimo, T., Kaneko, T., Tian, X., Ideo, K., Yonemitsu, R., Matsushita, K., Sugimoto, K., Yugami, M., Hisanaga, S., Nakamura, T., Uehara, Y., Masuda, T., Shukunami, C., Karasugi, T., & Miyamoto, T. (2023). Potential function of scx+/sox9+ cells as progenitor cells in rotator cuff tear repair in rats. Biochem Biophys Res Commun, *676*, 84-90.

Furumatsu, T., Shukunami, C., Amemiya-Kudo, M., Shimano, H., & Ozaki, T. (2010). Scleraxis and e47 cooperatively regulate the sox9-dependent transcription. Int J Biochem Cell Biol, *42*, 148-156.

Garvin, J., Qi, J., Maloney, M., & Banes, A.J. (2003). Novel system for engineering bioartificial tendons and application of mechanical load. Tissue Eng, *9*, 967-979.

George, N.S., Bell, R., Paredes, J.J., Taub, P.J., & Andarawis-Puri, N. (2021). Superior mechanical recovery in male and female mrl/mpj tendons is associated with a unique genetic profile. J Orthop Res, *39*, 1344-1354.

Gigante, A., Cesari, E., Busilacchi, A., Manzotti, S., Kyriakidou, K., Greco, F., Di Primio, R., & Mattioli-Belmonte, M. (2008). Collagen i membranes for tendon repair: Effect of collagen fiber orientation on cell behavior. J Orthop Res, *27*, 826-832.

Glousman, R., Shields, C., Jr., Kerlan, R., Jobe, F., Lombardo, S., Yocum, L., Tibone, J., & Gambardella, R. (1988). Gore-tex prosthetic ligament in anterior cruciate deficient knees. Am J Sports Med, *16*, 321-326.

Grashoff, C., Hoffman, B.D., Brenner, M.D., Zhou, R., Parsons, M., Yang, M.T., McLean, M.A., Sligar, S.G., Chen, C.S., Ha, T., & Schwartz, M.A. (2010). Measuring mechanical tension across vinculin reveals regulation of focal adhesion dynamics. Nature, *466*, 263-266.

Gunes, O.C., Albayrak, A.Z., Tasdemir, S., & Sendemir, A. (2020). Wet-electrospun phbv nanofiber reinforced carboxymethyl chitosan-silk hydrogel composite scaffolds for articular cartilage repair. J Biomater Appl, *35*, 515-531.

Gunes, O.C., Kara, A., Baysan, G., Bugra Husemoglu, R., Akokay, P., Ziylan Albayrak, A., Ergur, B.U., & Havitcioglu, H. (2022). Fabrication of 3d printed poly(lactic acid) strut and wet-electrospun cellulose nano fiber reinforced chitosan-collagen hydrogel composite scaffolds for meniscus tissue engineering. J Biomater Appl, *37*, 683-697.

Harvey, T., Flamenco, S., & Fan, C.M. (2019). A tppp3(+)pdgfra(+) tendon stem cell population contributes to regeneration and reveals a shared role for pdgf signalling in regeneration and fibrosis. Nat Cell Biol, *21*, 1490-1503.

Hati, A.G., Bassett, D.C., Ribe, J.M., Sikorski, P., Weitz, D.A., & Stokke, B.T. (2016). Versatile, cell and chip friendly method to gel alginate in microfluidic devices. Lab Chip, *16*, 3718-3727.

Hettiaratchi, M.H., Miller, T., Temenoff, J.S., Guldberg, R.E., & McDevitt, T.C. (2014). Heparin microparticle effects on presentation and bioactivity of bone morphogenetic protein-2. Biomaterials, *35*, 7228-7238.

Hettiaratchi, M.H., & Shoichet, M.S. (2019). Modulated protein delivery to engineer tissue repair. Tissue Eng Part A, *25*, 925-930.

Hiraki, H.L., Matera, D.L., Rose, M.J., Kent, R.N., Todd, C.W., Stout, M.E., Wank, A.E., Schiavone, M.C., DePalma, S.J., Zarouk, A.A., & Baker, B.M. (2021). Magnetic alignment of electrospun fiber segments within a hydrogel composite guides cell spreading and migration phenotype switching. Front Bioeng Biotechnol, *9*, 679165.

Hocking, A.M. (2015). The role of chemokines in mesenchymal stem cell homing to wounds. Adv Wound Care (New Rochelle), *4*, 623-630.

Howell, K., Chien, C., Bell, R., Laudier, D., Tufa, S.F., Keene, D.R., Andarawis-Puri, N., & Huang, A.H. (2017). Novel model of tendon regeneration reveals distinct cell mechanisms underlying regenerative and fibrotic tendon healing. Sci Rep, *7*, 45238.

Huang, A.H., Lu, H.H., & Schweitzer, R. (2015). Molecular regulation of tendon cell fate during development. J Orthop Res, *33*, 800-812.

Huang, A.H., Stein, A., Tuan, R.S., & Mauck, R.L. (2009). Transient exposure to transforming growth factor beta 3 improves the mechanical properties of mesenchymal stem cell-laden cartilage constructs in a density-dependent manner. Tissue Eng Part A, *15*, 3461-3472.

Huang, X., Yang, N., Fiore, V.F., Barker, T.H., Sun, Y., Morris, S.W., Ding, Q., Thannickal, V.J., & Zhou, Y. (2012). Matrix stiffness-induced myofibroblast differentiation is mediated by intrinsic mechanotransduction. Am J Respir Cell Mol Biol, *47*, 340-348.

Huang, Y.C., & Liu, T.J. (2012). Mobilization of mesenchymal stem cells by stromal cell-derived factor-1 released from chitosan/tripolyphosphate/fucoidan nanoparticles. Acta Biomater, *8*, 1048-1056.

Iannace, S., Sabatini, G., Ambrosio, L., & Nicolais, L. (1995). Mechanical behaviour of composite artificial tendons and ligaments. Biomaterials, *16*, 675-680.

Ideo, K., Tokunaga, T., Shukunami, C., Takimoto, A., Yoshimoto, Y., Yonemitsu, R., Karasugi, T., Mizuta, H., Hiraki, Y., & Miyamoto, T. (2020). Role of scx+/sox9+ cells as potential progenitor cells for postnatal supraspinatus enthesis formation and healing after injury in mice. PLoS One, *15*, e0242286.

Ionescu, L.C., Lee, G.C., Sennett, B.J., Burdick, J.A., & Mauck, R.L. (2010). An anisotropic nanofiber/microsphere composite with controlled release of biomolecules for fibrous tissue engineering. Biomaterials, *31*, 4113-4120.

Islam, A., Mbimba, T., Younesi, M., & Akkus, O. (2017). Effects of substrate stiffness on the tenoinduction of human mesenchymal stem cells. Acta Biomater, *58*, 244-253.

James, R., Kesturu, G., Balian, G., & Chhabra, A.B. (2008). Tendon: Biology, biomechanics, repair, growth factors, and evolving treatment options. J Hand Surg Am, *33*, 102-112.

Javanshir, S., Younesi Soltani, F., Dowlati, G., Parham, A., & Naderi-Meshkin, H. (2020). Induction of tenogenic differentiation of equine adipose-derived mesenchymal stem cells by platelet-derived growth factor-bb and growth differentiation factor-6. Mol Biol Rep, *47*, 6855-6862.

Jenkins, T.L., Meehan, S., Pourdeyhimi, B., & Little, D. (2017). (*) meltblown polymer fabrics as candidate scaffolds for rotator cuff tendon tissue engineering. Tissue Eng Part A, *23*, 958-967.

Johnstone, B., Hering, T.M., Caplan, A.I., Goldberg, V.M., & Yoo, J.U. (1998). In vitro chondrogenesis of bone marrow-derived mesenchymal progenitor cells. Exp Cell Res, *238*, 265-272.

Jones, M.E., Mudera, V., Brown, R.A., Cambrey, A.D., Grobbelaar, A.O., & McGrouther, D.A. (2003). The early surface cell response to flexor tendon injury. J Hand Surg Am, *28*, 221-230.

Jordan, A.M., Kim, S.E., Van de Voorde, K., Pokorski, J.K., & Korley, L.T.J. (2017). In situ fabrication of fiber reinforced three-dimensional hydrogel tissue engineering scaffolds. ACS Biomater Sci Eng, *3*, 1869-1879.

Józsa, L.G., & Kannus, P. (1997). *Human tendons: Anatomy, physiology, and pathology*. Champaign, IL: Human Kinetics.

Kaji, D.A., Howell, K.L., Balic, Z., Hubmacher, D., & Huang, A.H. (2020). Tgfbeta signaling is required for tenocyte recruitment and functional neonatal tendon regeneration. Elife, *9*.

Kaji, D.A., Montero, A.M., Patel, R., & Huang, A.H. (2021). Transcriptional profiling of mesc-derived tendon and fibrocartilage cell fate switch. Nat Commun, *12*, 4208.

Kallenbach, J.G., Freeberg, M.A.T., Abplanalp, D., Alenchery, R.G., Ajalik, R.E., Muscat, S., Myers, J.A., Ashton, J.M., Loiselle, A., Buckley, M.R., van Wijnen, A.J., & Awad, H.A. (2022). Altered tgfb1 regulated pathways promote accelerated tendon healing in the superhealer mrl/mpj mouse. Sci Rep, *12*, 3026.

Kashiwagi, K., Mochizuki, Y., Yasunaga, Y., Ishida, O., Deie, M., & Ochi, M. (2004). Effects of transforming growth factor-beta 1 on the early stages of healing of the achilles tendon in a rat model. Scand J Plast Reconstr Surg Hand Surg, *38*, 193-197.

Kastelic, J., Galeski, A., & Baer, E. (1978). The multicomposite structure of tendon. Connect Tissue Res, *6*, 11-23.

Katsumi, A., Milanini, J., Kiosses, W.B., del Pozo, M.A., Kaunas, R., Chien, S., Hahn, K.M., & Schwartz, M.A. (2002). Effects of cell tension on the small gtpase rac. J Cell Biol, *158*, 153-164.

Kauwe, M. (2017). Acute achilles tendon rupture: Clinical evaluation, conservative management, and early active rehabilitation. Clin Podiatr Med Surg, *34*, 229-243.

Kent, R.N., Said, M., Busch, M.E., Poupard, E.R., Tsai, A., Xia, J., Matera, D.L., Wang, W.Y., DePalma, S.J., Hiraki, H.L., Killian, M.L., Abraham, A.C., Shin, J.W., Huang, A.H., Shikanov, A., & Baker, B.M. (2022). Physical and soluble cues enhance tendon progenitor cell invasion into injectable synthetic hydrogels. Adv Funct Mater, *32*.

Killian, M.L., Cavinatto, L., Galatz, L.M., & Thomopoulos, S. (2012). The role of mechanobiology in tendon healing. J Shoulder Elbow Surg, *21*, 228-237.

Kishore, V., Bullock, W., Sun, X., Van Dyke, W.S., & Akkus, O. (2012). Tenogenic differentiation of human mscs induced by the topography of electrochemically aligned collagen threads. Biomaterials, *33*, 2137-2144.

Koh, J.L., Szomor, Z., Murrell, G.A., & Warren, R.F. (2002). Supplementation of rotator cuff repair with a bioresorbable scaffold. Am J Sports Med, *30*, 410-413.

Lantto, I., Heikkinen, J., Flinkkila, T., Ohtonen, P., Siira, P., Laine, V., & Leppilahti, J. (2016). A prospective randomized trial comparing surgical and nonsurgical treatments of acute achilles tendon ruptures. Am J Sports Med, *44*, 2406-2414.

Lee, C.H., Lee, F.Y., Tarafder, S., Kao, K., Jun, Y., Yang, G., & Mao, J.J. (2015). Harnessing endogenous stem/progenitor cells for tendon regeneration. J Clin Invest, *125*, 2690-2701.

Lemme, N.J., Li, N.Y., DeFroda, S.F., Kleiner, J., & Owens, B.D. (2018). Epidemiology of achilles tendon ruptures in the united states: Athletic and nonathletic injuries from 2012 to 2016. Orthop J Sports Med, *6*, 2325967118808238.

Li, D., Ma, X., & Zhao, T. (2020). Mechanism of tgf-beta(3) promoting chondrogenesis in human fat stem cells. Biochem Biophys Res Commun, *530*, 725-731.

Li, X., Pongkitwitoon, S., Lu, H., Lee, C., Gelberman, R., & Thomopoulos, S. (2019a). Ctgf induces tenogenic differentiation and proliferation of adipose-derived stromal cells. J Orthop Res, *37*, 574-582.

Li, Y., Dai, G., Shi, L., Lin, Y., Chen, M., Li, G., & Rui, Y. (2019b). The potential roles of tendon stem/progenitor cells in tendon aging. Curr Stem Cell Res Ther, *14*, 34-42.

Li, Y., Liu, X., Liu, X., Peng, Y., Zhu, B., Guo, S., Wang, C., Wang, D., & Li, S. (2022). Transforming growth factor-beta signalling pathway in tendon healing. Growth Factors, *40*, 98-107.

Lieberman, J.R., Lozman, J., Czajka, J., & Dougherty, J. (1988). Repair of achilles tendon ruptures with dacron vascular graft. Clin Orthop Relat Res, 204-208.

Lim, Y., Lee, M., Jeong, H., & Kim, H. (2017). Involvement of pi3k and mmp1 in pdgf-induced migration of human adipose-derived stem cells. Dev Reprod, *21*, 167-180.

Liu, H., Xu, J., Lan, Y., Lim, H.W., & Jiang, R. (2021). The scleraxis transcription factor directly regulates multiple distinct molecular and cellular processes during early tendon cell differentiation. Front Cell Dev Biol, *9*, 654397.

Long, H., Vos, B.E., Betz, T., Baker, B.M., & Trappmann, B. (2022). Nonswelling and hydrolytically stable hydrogels uncover cellular mechanosensing in 3d. Adv Sci (Weinh), *9*, e2105325.

Lui, P.P. (2015). Stem cell technology for tendon regeneration: Current status, challenges, and future research directions. Stem Cells Cloning, *8*, 163-174.

Macdougall, L.J., Perez-Madrigal, M.M., Arno, M.C., & Dove, A.P. (2018). Nonswelling thiol-yne cross-linked hydrogel materials as cytocompatible soft tissue scaffolds. Biomacromolecules, *19*, 1378-1388.

Majima, T., Irie, T., Sawaguchi, N., Funakoshi, T., Iwasaki, N., Harada, K., Minami, A., & Nishimura, S.I. (2007). Chitosan-based hyaluronan hybrid polymer fibre scaffold for ligament and tendon tissue engineering. Proc Inst Mech Eng H, *221*, 537-546.

Malandain, N., Sanz-Fraile, H., Farre, R., Otero, J., Roig, A., & Laromaine, A. (2023). Cell-laden 3d hydrogels of type i collagen incorporating bacterial nanocellulose fibers. ACS Appl Bio Mater, *6*, 3638-3647.

Manning, C.N., Kim, H.M., Sakiyama-Elbert, S., Galatz, L.M., Havlioglu, N., & Thomopoulos, S. (2011). Sustained delivery of transforming growth factor beta three enhances tendon-to-bone healing in a rat model. J Orthop Res, *29*, 1099-1105.

Manning, C.N., Martel, C., Sakiyama-Elbert, S.E., Silva, M.J., Shah, S., Gelberman, R.H., & Thomopoulos, S. (2015). Adipose-derived mesenchymal stromal cells modulate tendon fibroblast responses to macrophage-induced inflammation in vitro. Stem Cell Res Ther, *6*, 74.

Mao, A.S., Shin, J.W., Utech, S., Wang, H., Uzun, O., Li, W., Cooper, M., Hu, Y., Zhang, L., Weitz, D.A., & Mooney, D.J. (2017). Deterministic encapsulation of single cells in thin tunable microgels for niche modelling and therapeutic delivery. Nat Mater, *16*, 236-243.

Martino, M.M., Briquez, P.S., Guc, E., Tortelli, F., Kilarski, W.W., Metzger, S., Rice, J.J., Kuhn, G.A., Muller, R., Swartz, M.A., & Hubbell, J.A. (2014). Growth factors engineered for super-affinity to the extracellular matrix enhance tissue healing. Science, *343*, 885-888.

Matera, D.L., DiLillo, K.M., Smith, M.R., Davidson, C.D., Parikh, R., Said, M., Wilke, C.A., Lombaert, I.M., Arnold, K.B., Moore, B.B., & Baker, B.M. (2020). Microengineered 3d pulmonary interstitial mimetics highlight a critical role for matrix degradation in myofibroblast differentiation. Sci Adv, *6*.

Matera, D.L., Lee, A.T., Hiraki, H.L., & Baker, B.M. (2021). The role of rho gtpases during fibroblast spreading, migration, and myofibroblast differentiation in 3d synthetic fibrous matrices. Cell Mol Bioeng, *14*, 381-396.

Matera, D.L., Wang, W.Y., Smith, M.R., Shikanov, A., & Baker, B.M. (2019). Fiber density modulates cell spreading in 3d interstitial matrix mimetics. ACS Biomat Sci Eng, *5*, 2965-2975.

Matsumoto, N., Horibe, S., Nakamura, N., Senda, T., Shino, K., & Ochi, T. (1998). Effect of alignment of the transplanted graft extracellular matrix on cellular repopulation and newly synthesized collagen. Arch Orthop Trauma Surg, *117*, 215-221.

Mauck, R.L., Yuan, X., & Tuan, R.S. (2006). Chondrogenic differentiation and functional maturation of bovine mesenchymal stem cells in long-term agarose culture. Osteoarthritis Cartilage, *14*, 179-189.

McBeath, R., Pirone, D.M., Nelson, C.M., Bhadriraju, K., & Chen, C.S. (2004). Cell shape, cytoskeletal tension, and rhoa regulate stem cell lineage commitment. Dev Cell, *6*, 483-495.

Mellstrom, K., Heldin, C.H., & Westermark, B. (1988). Induction of circular membrane ruffling on human fibroblasts by platelet-derived growth factor. Exp Cell Res, *177*, 347-359.

Miranda-Nieves, D., & Chaikof, E.L. (2017). Collagen and elastin biomaterials for the fabrication of engineered living tissues. ACS Biomater Sci Eng, *3*, 694-711.

Mo, X.T., Guo, S.C., Xie, H.Q., Deng, L., Zhi, W., Xiang, Z., Li, X.Q., & Yang, Z.M. (2009). Variations in the ratios of co-cultured mesenchymal stem cells and chondrocytes regulate the expression of cartilaginous and osseous phenotype in alginate constructs. Bone, *45*, 42-51.

Mohanraj, B., Duan, G., Peredo, A., Kim, M., Tu, F., Lee, D., Dodge, G.R., & Mauck, R.L. (2019). Mechanically-activated microcapsules for 'on-demand' drug delivery in dynamically loaded musculoskeletal tissues. Adv Funct Mater, *29*.

Moshiri, A., Oryan, A., & Meimandi-Parizi, A. (2015). Synthesis, development, characterization and effectiveness of bovine pure platelet gel-collagen-polydioxanone bioactive graft on tendon healing. J Cell Mol Med, *19*, 1308-1332.

Murray, P.J., Allen, J.E., Biswas, S.K., Fisher, E.A., Gilroy, D.W., Goerdt, S., Gordon, S., Hamilton, J.A., Ivashkiv, L.B., Lawrence, T., Locati, M., Mantovani, A., Martinez, F.O., Mege, J.L., Mosser, D.M., Natoli, G., Saeij, J.P., Schultze, J.L., Shirey, K.A., Sica, A., Suttles, J., Udalova, I., van Ginderachter, J.A., Vogel, S.N., & Wynn, T.A. (2014). Macrophage activation and polarization: Nomenclature and experimental guidelines. Immunity, *41*, 14-20.

Murthi, A.M., Vosburgh, C.L., & Neviaser, T.J. (2000). The incidence of pathologic changes of the long head of the biceps tendon. J Shoulder Elbow Surg, *9*, 382-385.

Neuman, R.E., & Logan, M.A. (1950). The determination of hydroxyproline. J Biol Chem, *184*, 299-306.

Ni, M., Rui, Y.F., Tan, Q., Liu, Y., Xu, L.L., Chan, K.M., Wang, Y., & Li, G. (2013). Engineered scaffold-free tendon tissue produced by tendon-derived stem cells. Biomaterials, *34*, 2024-2037.

Nichols, A.E.C., Wagner, N.W., Ketonis, C., & Loiselle, A.E. (2023). Epitenon-derived cells comprise a distinct progenitor population that contributes to both tendon fibrosis and regeneration following acute injury. bioRxiv.

Nilsson-Helander, K., Silbernagel, K.G., Thomee, R., Faxen, E., Olsson, N., Eriksson, B.I., & Karlsson, J. (2010). Acute achilles tendon rupture: A randomized, controlled study comparing surgical and nonsurgical treatments using validated outcome measures. Am J Sports Med, *38*, 2186-2193.

Nirmalanandhan, V.S., Dressler, M.R., Shearn, J.T., Juncosa-Melvin, N., Rao, M., Gooch, C., Bradica, G., & Butler, D.L. (2007). Mechanical stimulation of tissue engineered tendon constructs: Effect of scaffold materials. J Biomech Eng, *129*, 919-923.

Nirmalanandhan, V.S., Rao, M., Shearn, J.T., Juncosa-Melvin, N., Gooch, C., & Butler, D.L. (2008). Effect of scaffold material, construct length and mechanical stimulation on the in vitro stiffness of the engineered tendon construct. J Biomech, *41*, 822-828.

Nivedhitha Sundaram, M., Deepthi, S., Mony, U., Shalumon, K.T., Chen, J.P., & Jayakumar, R. (2019). Chitosan hydrogel scaffold reinforced with twisted poly(l lactic acid) aligned microfibrous bundle to mimic tendon extracellular matrix. Int J Biol Macromol, *122*, 37-44.

No, Y.J., Castilho, M., Ramaswamy, Y., & Zreiqat, H. (2020a). Role of biomaterials and controlled architecture on tendon/ligament repair and regeneration. Adv Mater, *32*, e1904511.

No, Y.J., Tarafder, S., Reischl, B., Ramaswamy, Y., Dunstan, C., Friedrich, O., Lee, C.H., & Zreiqat, H. (2020b). High-strength fiber-reinforced composite hydrogel scaffolds as biosynthetic tendon graft material. ACS Biomater Sci Eng, *6*, 1887-1898.

Orr, S.B., Chainani, A., Hippensteel, K.J., Kishan, A., Gilchrist, C., Garrigues, N.W., Ruch, D.S., Guilak, F., & Little, D. (2015). Aligned multilayered electrospun scaffolds for rotator cuff tendon tissue engineering. Acta Biomater, *24*, 117-126.

Padilla, S., Sanchez, M., Vaquerizo, V., Malanga, G.A., Fiz, N., Azofra, J., Rogers, C.J., Samitier, G., Sampson, S., Seijas, R., Elorriaga, R., Taunton, J., Boehm, F., Prado, R., Cugat, R., & Anitua, E. (2021). Platelet-rich plasma applications for achilles tendon repair: A bridge between biology and surgery. Int J Mol Sci, *22*.

Pajarinen, J., Lin, T., Gibon, E., Kohno, Y., Maruyama, M., Nathan, K., Lu, L., Yao, Z., & Goodman, S.B. (2019). Mesenchymal stem cell-macrophage crosstalk and bone healing. Biomaterials, *196*, 80-89.

Pan, X.S., Li, J., Brown, E.B., & Kuo, C.K. (2018). Embryo movements regulate tendon mechanical property development. Philos Trans R Soc Lond B Biol Sci, *373*.

Park, D., Wershof, E., Boeing, S., Labernadie, A., Jenkins, R.P., George, S., Trepat, X., Bates, P.A., & Sahai, E. (2020). Extracellular matrix anisotropy is determined by tfap2c-dependent regulation of cell collisions. Nat Mater, *19*, 227-238.

Parsons, J.R., Weiss, A.B., Schenk, R.S., Alexander, H., & Pavlisko, F. (1989). Long-term follow-up of achilles tendon repair with an absorbable polymer carbon fiber composite. Foot Ankle, *9*, 179-184.

Patel, D., Sharma, S., Screen, H.R.C., & Bryant, S.J. (2018). Effects of cell adhesion motif, fiber stiffness, and cyclic strain on tenocyte gene expression in a tendon mimetic fiber composite hydrogel. Biochem Biophys Res Commun, *499*, 642-647.

Praemer, A., Furner, S., & Rice, D.P. (1999). *Musculoskeletal conditions in the united states*: American Academy of Orthopedic Surgeons.

Price, L.S., Leng, J., Schwartz, M.A., & Bokoch, G.M. (1998). Activation of rac and cdc42 by integrins mediates cell spreading. Mol Biol Cell, *9*, 1863-1871.

Pruett, L., Jenkins, C., Singh, N., Catallo, K., & Griffin, D. (2021). Heparin microislands in microporous annealed particle scaffolds for accelerated diabetic wound healing. Adv Funct Mater, *31*.

Pryce, B.A., Brent, A.E., Murchison, N.D., Tabin, C.J., & Schweitzer, R. (2007). Generation of transgenic tendon reporters, scxgfp and scxap, using regulatory elements of the scleraxis gene. Dev Dyn, *236*, 1677-1682.

Purcell, B.P., Lobb, D., Charati, M.B., Dorsey, S.M., Wade, R.J., Zellars, K.N., Doviak, H., Pettaway, S., Logdon, C.B., Shuman, J.A., Freels, P.D., Gorman, J.H., 3rd, Gorman, R.C., Spinale, F.G., & Burdick, J.A. (2014). Injectable and bioresponsive hydrogels for on-demand matrix metalloproteinase inhibition. Nat Mater, *13*, 653-661.

Qiao, Z., Lian, M., Han, Y., Sun, B., Zhang, X., Jiang, W., Li, H., Hao, Y., & Dai, K. (2021). Bioinspired stratified electrowritten fiber-reinforced hydrogel constructs with layer-specific induction capacity for functional osteochondral regeneration. Biomaterials, *266*, 120385.

Qu, F., Holloway, J.L., Esterhai, J.L., Burdick, J.A., & Mauck, R.L. (2017). Programmed biomolecule delivery to enable and direct cell migration for connective tissue repair. Nat Commun, *8*, 1780.

Rajpar, I., & Barrett, J.G. (2019). Optimizing growth factor induction of tenogenesis in three-dimensional culture of mesenchymal stem cells. J Tissue Eng, *10*, 2041731419848776.

Ratcliffe, A., Butler, D.L., Dyment, N.A., Cagle, P.J., Jr., Proctor, C.S., Ratcliffe, S.S., & Flatow, E.L. (2015). Scaffolds for tendon and ligament repair and regeneration. Ann Biomed Eng, *43*, 819-831.

Ravishankar, P., Ozkizilcik, A., Husain, A., & Balachandran, K. (2021). Anisotropic fiber-reinforced glycosaminoglycan hydrogels for heart valve tissue engineering. Tissue Eng Part A, *27*, 513-525.

Richmond, J.C., Manseau, C.J., Patz, R., & McConville, O. (1992). Anterior cruciate reconstruction using a dacron ligament prosthesis. A long-term study. Am J Sports Med, *20*, 24-28.

Rinker, T.E., Philbrick, B.D., Hettiaratchi, M.H., Smalley, D.M., McDevitt, T.C., & Temenoff, J.S. (2018). Microparticle-mediated sequestration of cell-secreted proteins to modulate chondrocytic differentiation. Acta Biomater, *68*, 125-136.

Rinoldi, C., Costantini, M., Kijenska-Gawronska, E., Testa, S., Fornetti, E., Heljak, M., Cwiklinska, M., Buda, R., Baldi, J., Cannata, S., Guzowski, J., Gargioli, C., Khademhosseini, A., & Swieszkowski, W. (2019a). Tendon tissue engineering: Effects of mechanical and biochemical stimulation on stem cell alignment on cell-laden hydrogel yarns. Adv Healthc Mater, *8*, e1801218.

Rinoldi, C., Fallahi, A., Yazdi, I.K., Campos Paras, J., Kijenska-Gawronska, E., Trujillo-de Santiago, G., Tuoheti, A., Demarchi, D., Annabi, N., Khademhosseini, A., Swieszkowski, W., & Tamayol, A. (2019b). Mechanical and biochemical stimulation of 3d multilayered scaffolds for tendon tissue engineering. ACS Biomater Sci Eng, *5*, 2953-2964.

Ritger, P.L., & Peppas, N.A. (1987a). A simple equation for description of solute release ii. Fickian and anomalous release from swellable devices. J Control Rel, *5*, 37-42.

Ritger, P.L., & Peppas, N.A. (1987b). A simple equation for desctiption of solute release i. Fickian and non-fickian release from non-swellable devices in the form of slabs, spheres, cylinders, or discs. J Control Rel, *5*, 23-36.

Rittie, L. (2017). Method for picrosirius red-polarization detection of collagen fibers in tissue sections. Methods Mol Biol, *1627*, 395-407.

Sakabe, T., Sakai, K., Maeda, T., Sunaga, A., Furuta, N., Schweitzer, R., Sasaki, T., & Sakai, T. (2018). Transcription factor scleraxis vitally contributes to progenitor lineage direction in wound healing of adult tendon in mice. J Biol Chem, *293*, 5766-5780.

Sakiyama-Elbert, S.E., & Hubbell, J.A. (2000). Development of fibrin derivatives for controlled release of heparin-binding growth factors. J Control Release, *65*, 389-402.

Sandbo, N., & Dulin, N. (2011). Actin cytoskeleton in myofibroblast differentiation: Ultrastructure defining form and driving function. Transl Res, *158*, 181-196.

Sapudom, J., Mohamed, W.K.E., Garcia-Sabate, A., Alatoom, A., Karaman, S., Mahtani, N., & Teo, J.C. (2020). Collagen fibril density modulates macrophage activation and cellular functions during tissue repair. Bioengineering (Basel), *7*.

Schoenenberger, A.D., Foolen, J., Moor, P., Silvan, U., & Snedeker, J.G. (2018). Substrate fiber alignment mediates tendon cell response to inflammatory signaling. Acta Biomater, *71*, 306-317.

Schweitzer, R., Chyung, J.H., Murtaugh, L.C., Brent, A.E., Rosen, V., Olson, E.N., Lassar, A., & Tabin, C.J. (2001). Analysis of the tendon cell fate using scleraxis, a specific marker for tendons and ligaments. Development, *128*, 3855-3866.

Scott, A., Danielson, P., Abraham, T., Fong, G., Sampaio, A.V., & Underhill, T.M. (2011). Mechanical force modulates scleraxis expression in bioartificial tendons. J Musculoskelet Neuronal Interact, *11*, 124-132.

Seppa, H., Grotendorst, G., Seppa, S., Schiffmann, E., & Martin, G.R. (1982). Platelet-derived growth factor in chemotactic for fibroblasts. J Cell Biol, *92*, 584-588.

Sharma, P., & Maffulli, N. (2006). Biology of tendon injury: Healing, modeling and remodeling. J Musculoskelet Neuronal Interact, *6*, 181-190.

Shimada, A., Wada, S., Inoue, K., Ideno, H., Kamiunten, T., Komatsu, K., Kudo, A., Nakamura, Y., Sato, T., Nakashima, K., & Nifuji, A. (2014). Efficient expansion of mouse primary tenocytes using a novel collagen gel culture method. Histochem Cell Biol, *142*, 205-215.

Siadat, S.M., Silverman, A.A., DiMarzio, C.A., & Ruberti, J.W. (2021). Measuring collagen fibril diameter with differential interference contrast microscopy. J Struct Biol, *213*, 107697.

Singh, M.N., Hemant, K.S., Ram, M., & Shivakumar, H.G. (2010). Microencapsulation: A promising technique for controlled drug delivery. Res Pharm Sci, *5*, 65-77.

Sorkin, M., Huber, A.K., Hwang, C., Carson, W.F.t., Menon, R., Li, J., Vasquez, K., Pagani, C., Patel, N., Li, S., Visser, N.D., Niknafs, Y., Loder, S., Scola, M., Nycz, D., Gallagher, K., McCauley, L.K., Xu, J., James, A.W., Agarwal, S., Kunkel, S., Mishina, Y., & Levi, B. (2020). Regulation of heterotopic ossification by monocytes in a mouse model of aberrant wound healing. Nat Commun, *11*, 722.

Soroceanu, A., Sidhwa, F., Aarabi, S., Kaufman, A., & Glazebrook, M. (2012). Surgical versus nonsurgical treatment of acute achilles tendon rupture: A meta-analysis of randomized trials. J Bone Joint Surg Am, *94*, 2136-2143.

Sorrenti, S.J. (2006). Achilles tendon rupture: Effect of early mobilization in rehabilitation after surgical repair. Foot Ankle Int, *27*, 407-410.

Spiller, K.L., Nassiri, S., Witherel, C.E., Anfang, R.R., Ng, J., Nakazawa, K.R., Yu, T., & Vunjak-Novakovic, G. (2015). Sequential delivery of immunomodulatory cytokines to facilitate the m1-to-m2 transition of macrophages and enhance vascularization of bone scaffolds. Biomaterials, *37*, 194-207.

Sridharan, R., Cavanagh, B., Cameron, A.R., Kelly, D.J., & O'Brien, F.J. (2019). Material stiffness influences the polarization state, function and migration mode of macrophages. Acta Biomater, *89*, 47-59.

Stegemann, H., & Stalder, K. (1967). Determination of hydroxyproline. Clin Chim Acta, *18*, 267-273.

Stoll, C., John, T., Endres, M., Rosen, C., Kaps, C., Kohl, B., Sittinger, M., Ertel, W., & Schulze-Tanzil, G. (2010). Extracellular matrix expression of human tenocytes in three-dimensional air-liquid and plga cultures compared with tendon tissue: Implications for tendon tissue engineering. J Orthop Res, *28*, 1170-1177.

Strange, D.G., Tonsomboon, K., & Oyen, M.L. (2014). Mechanical behaviour of electrospun fibre-reinforced hydrogels. J Mater Sci Mater Med, *25*, 681-690.

Subbiah, R., Cheng, A., Ruehle, M.A., Hettiaratchi, M.H., Bertassoni, L.E., & Guldberg, R.E. (2020). Effects of controlled dual growth factor delivery on bone regeneration following composite bone-muscle injury. Acta Biomater, *114*, 63-75.

Sugg, K.B., Lubardic, J., Gumucio, J.P., & Mendias, C.L. (2014). Changes in macrophage phenotype and induction of epithelial-to-mesenchymal transition genes following acute achilles tenotomy and repair. J Orthop Res, *32*, 944-951.

Sugg, K.B., Markworth, J.F., Disser, N.P., Rizzi, A.M., Talarek, J.R., Sarver, D.C., Brooks, S.V., & Mendias, C.L. (2018). Postnatal tendon growth and remodeling require platelet-derived growth factor receptor signaling. Am J Physiol Cell Physiol, *314*, C389-C403.

Sugimoto, Y., Takimoto, A., Akiyama, H., Kist, R., Scherer, G., Nakamura, T., Hiraki, Y., & Shukunami, C. (2013). Scx+/sox9+ progenitors contribute to the establishment of the junction between cartilage and tendon/ligament. Development, *140*, 2280-2288.

Sunwoo, J.Y., Eliasberg, C.D., Carballo, C.B., & Rodeo, S.A. (2020). The role of the macrophage in tendinopathy and tendon healing. J Orthop Res, *38*, 1666-1675.

Szczesny, S.E., Driscoll, T.P., Tseng, H.Y., Liu, P.C., Heo, S.J., Mauck, R.L., & Chao, P.G. (2017). Crimped nanofibrous biomaterials mimic microstructure and mechanics of native tissue and alter strain transfer to cells. ACS Biomater Sci Eng, *3*, 2869-2876.

Tan, G.K., Pryce, B.A., Stabio, A., Brigande, J.V., Wang, C., Xia, Z., Tufa, S.F., Keene, D.R., & Schweitzer, R. (2020). Tgfbeta signaling is critical for maintenance of the tendon cell fate. Elife, *9*.

Tan, Q., Lui, P.P., & Rui, Y.F. (2012). Effect of in vitro passaging on the stem cell-related properties of tendon-derived stem cells-implications in tissue engineering. Stem Cells Dev, *21*, 790-800.

Tarafder, S., Brito, J.A., Minhas, S., Effiong, L., Thomopoulos, S., & Lee, C.H. (2019a). In situ tissue engineering of the tendon-to-bone interface by endogenous stem/progenitor cells. Biofabrication, *12*, 015008.

Tarafder, S., Ricupero, C., Minhas, S., Yu, R.J., Alex, A.D., & Lee, C.H. (2019b). A combination of oxo-m and 4-ppbp as a potential regenerative therapeutics for tendon injury. Theranostics, *9*, 4241-4254.

Tatara, A.M., & Mikos, A.G. (2016). Tissue engineering in orthopaedics. J Bone Joint Surg Am, *98*, 1132-1139.

Tempfer, H., Kaser-Eichberger, A., Lehner, C., Gehwolf, R., Korntner, S., Kunkel, N., Wagner, A., Gruetz, M., Heindl, L.M., Schroedl, F., & Traweger, A. (2018). Bevacizumab improves achilles tendon repair in a rat model. Cell Physiol Biochem, *46*, 1148-1158.

Testa, S., Costantini, M., Fornetti, E., Bernardini, S., Trombetta, M., Seliktar, D., Cannata, S., Rainer, A., & Gargioli, C. (2017). Combination of biochemical and mechanical cues for tendon tissue engineering. J Cell Mol Med, *21*, 2711-2719.

Thomopoulos, S., Parks, W.C., Rifkin, D.B., & Derwin, K.A. (2015). Mechanisms of tendon injury and repair. J Orthop Res, *33*, 832-839.

Thomopoulos, S., Zaegel, M., Das, R., Harwood, F.L., Silva, M.J., Amiel, D., Sakiyama-Elbert, S., & Gelberman, R.H. (2007). Pdgf-bb released in tendon repair using a novel delivery system promotes cell proliferation and collagen remodeling. J Orthop Res, *25*, 1358-1368.

Thrivikraman, G., Jagiello, A., Lai, V.K., Johnson, S.L., Keating, M., Nelson, A., Schultz, B., Wang, C.M., Levine, A.J., Botvinick, E.L., & Tranquillo, R.T. (2021). Cell contact guidance via sensing anisotropy of network mechanical resistance. Proc Natl Acad Sci U S A, *118*.

Tidball, J.G., & Spencer, M.J. (1993). Pdgf stimulation induces phosphorylation of talin and cytoskeletal reorganization in skeletal muscle. J Cell Biol, *123*, 627-635.

Trappmann, B., Baker, B.M., Polacheck, W.J., Choi, C.K., Burdick, J.A., & Chen, C.S. (2017). Matrix degradability controls multicellularity of 3d cell migration. Nat Commun, *8*, 371.

Triantafillopoulos, I.K., Banes, A.J., Bowman, K.F., Jr., Maloney, M., Garrett, W.E., Jr., & Karas, S.G. (2004). Nandrolone decanoate and load increase remodeling and strength in human supraspinatus bioartificial tendons. Am J Sports Med, *32*, 934-943.

United states bone and joint initiative: The burden of musculoskeletal disease in the united states, fourth edition. (2016). American Academy of Orthopedic Surgeons.

Utech, S., Prodanovic, R., Mao, A.S., Ostafe, R., Mooney, D.J., & Weitz, D.A. (2015). Microfluidic generation of monodisperse, structurally homogeneous alginate microgels for cell encapsulation and 3d cell culture. Adv Healthc Mater, *4*, 1628-1633.

van der Vlist, A.C., Breda, S.J., Oei, E.H.G., Verhaar, J.A.N., & de Vos, R.J. (2019). Clinical risk factors for achilles tendinopathy: A systematic review. Br J Sports Med, *53*, 1352-1361.

Vinci, M., Box, C., & Eccles, S.A. (2015). Three-dimensional (3d) tumor spheroid invasion assay. J Vis Exp, e52686.

Visser, J., Melchels, F.P., Jeon, J.E., van Bussel, E.M., Kimpton, L.S., Byrne, H.M., Dhert, W.J., Dalton, P.D., Hutmacher, D.W., & Malda, J. (2015). Reinforcement of hydrogels using three-dimensionally printed microfibres. Nat Commun, *6*, 6933.

Voleti, P.B., Buckley, M.R., & Soslowsky, L.J. (2012). Tendon healing: Repair and regeneration. Annu Rev Biomed Eng, *14*, 47-71.

Walia, B., & Huang, A.H. (2019). Tendon stem progenitor cells: Understanding the biology to inform therapeutic strategies for tendon repair. J Orthop Res, *37*, 1270-1280.

Wang, W.Y., Kent, R.N., 3rd, Huang, S.A., Jarman, E.H., Shikanov, E.H., Davidson, C.D., Hiraki, H.L., Lin, D., Wall, M.A., Matera, D.L., Shin, J.W., Polacheck, W.J., Shikanov, A., & Baker, B.M. (2021a). Direct comparison of angiogenesis in natural and synthetic biomaterials reveals that matrix porosity regulates endothelial cell invasion speed and sprout diameter. Acta Biomater, *135*, 260-273.

Wang, W.Y., Lin, D., Jarman, E.H., Polacheck, W.J., & Baker, B.M. (2020). Functional angiogenesis requires microenvironmental cues balancing endothelial cell migration and proliferation. Lab Chip, *20*, 1153-1166.

Wang, W.Y., Pearson, A.T., Kutys, M.L., Choi, C.K., Wozniak, M.A., Baker, B.M., & Chen, C.S. (2018a). Extracellular matrix alignment dictates the organization of focal adhesions and directs uniaxial cell migration. APL Bioeng, *2*, 046107.

Wang, Y., Chen, X., Cao, W., & Shi, Y. (2014). Plasticity of mesenchymal stem cells in immunomodulation: Pathological and therapeutic implications. Nat Immunol, *15*, 1009-1016.

Wang, Y., Jin, S., Luo, D., He, D., Shi, C., Zhu, L., Guan, B., Li, Z., Zhang, T., Zhou, Y., Wang, C.Y., & Liu, Y. (2021b). Functional regeneration and repair of tendons using biomimetic scaffolds loaded with recombinant periostin. Nat Commun, *12*, 1293.

Wang, Z., Lee, W.J., Koh, B.T.H., Hong, M., Wang, W., Lim, P.N., Feng, J., Park, L.S., Kim, M., & Thian, E.S. (2018b). Functional regeneration of tendons using scaffolds with physical anisotropy engineered via microarchitectural manipulation. Sci Adv, *4*, eaat4537.

Wee, J., Kim, H., Shin, S.J., Lee, T., & Lee, S.Y. (2022). Influence of mechanical and tgf-beta3 stimulation on the tenogenic differentiation of tonsil-derived mesenchymal stem cells. BMC Mol Cell Biol, *23*, 3.

Weitkamp, J.T., Woltje, M., Nusspickel, B., Schmidt, F.N., Aibibu, D., Bayer, A., Eglin, D., Armiento, A.R., Arnold, P., Cherif, C., Lucius, R., Smeets, R., Kurz, B., & Behrendt, P. (2021). Silk fiber-reinforced hyaluronic acid-based hydrogel for cartilage tissue engineering. Int J Mol Sci, *22*.

Williams, I.F., Craig, A.S., Parry, D.A.D., Goodship, A.E., Shah, J., & Silver, I.A. (1985). Development of collagen fibril organization and collagen crimp patterns during tendon healing. Int J Biol Macromol, *7*, 275-282.

Wipff, P.J., Rifkin, D.B., Meister, J.J., & Hinz, B. (2007). Myofibroblast contraction activates latent tgf-beta1 from the extracellular matrix. J Cell Biol, *179*, 1311-1323.

Wojciak, B., & Crossan, J.F. (1993). The accumulation of inflammatory cells in synovial sheath and epitenon during adhesion formation in healing rat flexor tendons. Clin Exp Immunol, *93*, 108-114.

Wong, C.Y., Al-Salami, H., & Dass, C.R. (2018). Microparticles, microcapsules and microspheres: A review of recent developments and prospects for oral delivery of insulin. Int J Pharm, *537*, 223-244.

Wren, T.A., Yerby, S.A., Beaupre, G.S., & Carter, D.R. (2001). Mechanical properties of the human achilles tendon. Clin Biomech (Bristol, Avon), *16*, 245-251.

Wu, F., Nerlich, M., & Docheva, D. (2017a). Tendon injuries: Basic science and new repair proposals. EFORT Open Rev, *2*, 332-342.

Wu, G., Deng, X., Song, J., & Chen, F. (2018). Enhanced biological properties of biomimetic apatite fabricated polycaprolactone/chitosan nanofibrous bio-composite for tendon and ligament regeneration. J Photochem Photobiol B, *178*, 27-32.

Wu, S., Peng, H., Li, X., Streubel, P.N., Liu, Y., & Duan, B. (2017b). Effect of scaffold morphology and cell co-culture on tenogenic differentiation of hadmsc on centrifugal melt electrospun poly (l-lactic acid) fibrous meshes. Biofabrication, *9*, 044106.

Xie, Y., Zhang, F., Akkus, O., & King, M.W. (2022). A collagen/pla hybrid scaffold supports tendon-derived cell growth for tendon repair and regeneration. J Biomed Mater Res B Appl Biomater, *110*, 2624-2635.

Xiong, Y., Mi, B.B., Lin, Z., Hu, Y.Q., Yu, L., Zha, K.K., Panayi, A.C., Yu, T., Chen, L., Liu, Z.P., Patel, A., Feng, Q., Zhou, S.H., & Liu, G.H. (2022). The role of the immune microenvironment in bone, cartilage, and soft tissue regeneration: From mechanism to therapeutic opportunity. Mil Med Res, *9*, 65.

Yang, G., Lin, H., Rothrauff, B.B., Yu, S., & Tuan, R.S. (2016). Multilayered polycaprolactone/gelatin fiber-hydrogel composite for tendon tissue engineering. Acta Biomater, *35*, 68-76.

Yang, Z., Cao, H., Gao, S., Yang, M., Lyu, J., & Tang, K. (2017). Effect of tendon stem cells in chitosan/beta-glycerophosphate/collagen hydrogel on achilles tendon healing in a rat model. Med Sci Monit, *23*, 4633-4643.

Yao, L., Bestwick, C.S., Bestwick, L.A., Maffulli, N., & Aspden, R.M. (2006). Phenotypic drift in human tenocyte culture. Tissue Eng, *12*, 1843-1849.

Yin, H., Caceres, M.D., Yan, Z., Schieker, M., Nerlich, M., & Docheva, D. (2019). Tenomodulin regulates matrix remodeling of mouse tendon stem/progenitor cells in an ex vivo collagen i gel model. Biochem Biophys Res Commun, *512*, 691-697.

Yin, Z., Chen, X., Chen, J.L., Shen, W.L., Hieu Nguyen, T.M., Gao, L., & Ouyang, H.W. (2010). The regulation of tendon stem cell differentiation by the alignment of nanofibers. Biomaterials, *31*, 2163-2175.

Yoon, J.P., Lee, C.H., Jung, J.W., Lee, H.J., Lee, Y.S., Kim, J.Y., Park, G.Y., Choi, J.H., & Chung, S.W. (2018). Sustained delivery of transforming growth factor beta1 by use of absorbable alginate scaffold enhances rotator cuff healing in a rabbit model. Am J Sports Med, *46*, 1441-1450.

Younesi, M., Islam, A., Kishore, V., Anderson, J.M., & Akkus, O. (2014). Tenogenic induction of human mscs by anisotropically aligned collagen biotextiles. Adv Funct Mater, *24*, 5762-5770.

Young, R.G., Butler, D.L., Weber, W., Caplan, A.I., Gordon, S.L., & Fink, D.J. (1998). Use of mesenchymal stem cells in a collagen matrix for achilles tendon repair. J Orthop Res, *16*, 406-413.

Yu, Y., & Chau, Y. (2012). One-step "click" method for generating vinyl sulfone groups on hydroxyl-containing water-soluble polymers. Biomacromolecules, *13*, 937-942.

Zajac, F.E. (1989). Muscle and tendon: Properties, models, scaling, and application to biomechanics and motor control. Crit Rev Biomed Eng, *17*, 359-411.

Zhu, J., Li, J., Wang, B., Zhang, W.J., Zhou, G., Cao, Y., & Liu, W. (2010). The regulation of phenotype of cultured tenocytes by microgrooved surface structure. Biomaterials, *31*, 6952-6958.

Zimmermann, J.A., Hettiaratchi, M.H., & McDevitt, T.C. (2017). Enhanced immunosuppression of t cells by sustained presentation of bioactive interferon-gamma within three-dimensional mesenchymal stem cell constructs. Stem Cells Transl Med, *6*, 223-237.